

Signal Extraction and Optical Design for an Advanced Gravitational Wave Interferometer

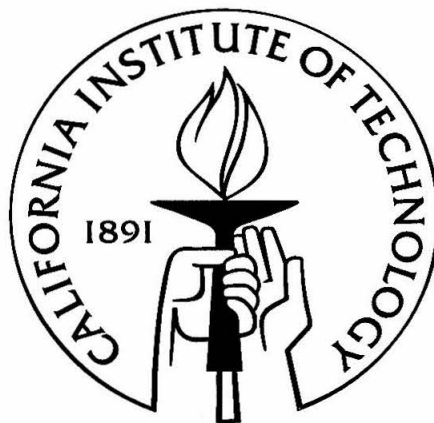
Thesis by

James E. Mason

In Partial Fulfillment of the Requirements

for the Degree of

Doctor of Philosophy



California Institute of Technology
Pasadena, California

2001

(Submitted February 23, 2001)

© 2001

James E. Mason

All Rights Reserved

Abstract

The LIGO project is two 4 km baseline interferometers which are currently being constructed in the quest to directly detect gravitational radiation. Concurrent with this effort is research aimed at increasing the strain sensitivity of the initial interferometers to $2.5 \times 10^{-23}/\sqrt{\text{Hz}}$. The optical configuration, which defines the detector gain and bandwidth, is one such area of research. Resonant sideband extraction (RSE) is the configuration which is proposed for advanced LIGO. RSE allows for much more freedom in the optimization of the detector response compared to the initial configuration.

The principle of RSE is examined in the context of a three mirror coupled cavity. The effect of optical losses on the design of an RSE interferometer is discussed. Two model optimizations of the interferometer design are done: one for binary inspiral sources and one for periodic sources at 1 kHz.

An optical heterodyne signal extraction scheme is proposed to sense the deviation of the mirrors away from their nominal positions, and to read out the gravitational wave signal. The scheme is applied to the two model interferometers previously designed, and its performance is analyzed for each case. Allowable residual deviations of the common mode degrees of freedom are also derived.

A tabletop prototype of an RSE interferometer has been constructed to demonstrate both the viability of the proposed signal extraction scheme and the tunability of the RSE interferometer. Good agreement on both counts is found between the measured experimental data and the modeled predictions.

The coupling of laser frequency and amplitude noise into the gravitational wave readout port is analyzed for the RSE configuration assuming the proposed gravitational wave signal readout scheme. Specifications for the allowable laser frequency and amplitude noise, as well as allowable residual deviations of the differential mode degrees of freedom, are derived for the two model interferometers.

Acknowledgements

I'm a little amazed that I made it this far.

As an undergraduate, Drs. Clyde Zaidins, Ned Davies, and Randy Tagg were great inspirations. They taught well, challenged me, and went out of their way to encourage me to go further. They made the effort to be not just professors, but mentors. I also had the great fortune to work with the gravity group at JILA – Tuck Stebbins, Peter Bender, Jim Faller, Dave Newell, and Sam Richman. This was my first taste of research, and it couldn't have been with a better, more supportive group of people. Tuck especially deserves a word of thanks for his invaluable support and guidance, as well as his impeccable fashion sense.

I feel very fortunate to have been able to do my graduate studies at Caltech. Although it seemed at times as if I were out on a limb when the tree had been taken away, I still am proud to have done my thesis there. Caltech is very supportive of its graduates, and has afforded me the chance to work with some very brilliant and inspiring people. I must confess my great admiration for Dr. Rochus Vogt. Although he acted as my advisor for a very short time, I appreciated his support, and admired his strength of character and attitude. I also thank Dr. Ken Libbrecht for taking me on at a difficult time. A great deal of gratitude goes to my elders in the LIGO grad office, Torrey Lyons and Aaron Gillespie, for their support and (whether they knew it or not) mentorship. Seiji Kawamura, Andy Kuhnert, Bob Spero, Jenny Logan and Alex Abramovici have also taught me a great deal, not only about interferometry but about doing science. It was a great loss to me that I couldn't have worked with them longer. Phil Willems has been a tremendous source of help and guidance, and he's been great person to work with in these last years. His Herculean efforts in proofing this thesis should not go unremarked. He read the whole thing *twice*. Nergis Mavalvala has always been a font of wisdom and pillar of support. Do *not* believe her modesty, sincere as it may be. She's brilliant.

Of course, one couldn't last six and a half years of grad school without some fun and games. It would be too tedious to categorize everyone in their place, so I'll just list names. Josh Bliss. Rick Jenet. Torrey, Maggie, Aaron, Ruth, Eric, Heather, and Steve. Malik Rahkmanov. Matt Evans. Arthur Street. Teviet Creighton. Dave Vernooy. Christina Hood. Penelope Kneebone. Brian Kern and Genna Helmberger. Steve Kaye. YAMA. Brad Behr. Gautam Vasisht. Mike Hrynevych. Theo and Sally ten Brummelaar. Anyone who ever played (and brought beer) for Trout Fishing in America. I'm sure there are more, excuse me if I can't remember. I've nothing but the fondest thoughts for you all.

I love my coffee cup. Thank god for epoxy.

To the source, thanks to my Dad, who fostered in me that quality of curiosity that a scientist needs. Thanks to my sister and brother, Nancy and Dave, for *being* my sister and brother, and looking out for me for all those years.

Frank Kusumoto is my best friend in the whole world. I miss Denver a lot, and he's a large part of that. Mike Jackson would probably pummel me senseless if I didn't mention his name here. Besides, he's a great friend, even when he's turning me upside down and shaking the change out of my pockets. Danielle Simmance, Donna Hickey-Jackson, Joni Zisman, Christiana Warvi, Tony, Hennessey, Michelle, Ero, Matt, Jill, Julie, and the host of other Denverites that were there when I came back – thanks. Also, life would be a little bit paler if it weren't for Pete's Kitchen, and the best damn breakfast burrito in the world.

Probably the hardest thing in the last few years has been living apart from the love of my life, Sharon Ziperovich. I'll be there in just a bit. And I'm not leaving, this time.

To Barney, the best cat in the world. I miss you terribly.

1988-2000

Contents

Abstract	iii
Acknowledgements	iv
1 Prologue	1
1.1 General Relativity	1
1.2 The Search for Gravitational Waves	3
1.2.1 Resonant Bar Detectors	3
1.2.2 Interferometers	3
1.3 Interferometer Sensitivity	5
1.3.1 Seismic Noise	5
1.3.2 Thermal Noise	7
1.3.3 Optical Noise	10
1.3.4 Interferometer Configuration	12
1.4 The Goal of this Work	16
2 Resonant Sideband Extraction	19
2.1 Frequency Response	19
2.1.1 The Three Mirror Coupled Cavity	22
2.1.2 RSE Transfer Functions	31
2.2 Practical Limitations	35
2.2.1 Power Recycling	36
2.2.2 Transfer Function Limitations	39
2.2.3 Implications	41
2.3 Detector Optimization for RSE	44
2.3.1 Narrowband Response	45

2.3.2	Optimized Broadband	48
3	Signal Extraction	52
3.1	Optically Heterodyned Signals	52
3.1.1	DC Signal	55
3.1.2	Frequency Dependent Signal	58
3.1.3	Phasor Diagrams	60
3.1.4	<i>Twiddle</i>	65
3.2	The RSE Interferometer	67
3.2.1	Asymmetry	69
3.2.2	Detuned Interferometer	73
3.2.3	Additional Sidebands	75
3.2.4	Proposed Signal Extraction Scheme	76
3.3	Signal Sensitivity	79
3.3.1	Reflected and Pickoff Signals	81
3.3.2	Dark Port Signals	88
3.4	Matrix of Discriminants	92
3.4.1	Optimized Broadband	93
3.4.2	Narrowband RSE	98
3.5	Conclusions	102
4	The RSE Tabletop Prototype Experiment	104
4.1	Prototype Design	104
4.1.1	Optics	106
4.1.2	Lengths and Frequencies	108
4.1.3	Electro-Optics	109
4.1.4	Mirror Mounting	112
4.1.5	Electronics	115
4.2	Input Optics and the Mach-Zender	118
4.3	Arm Cavities	119
4.3.1	Visibility	119

4.3.2	Mode Matching	120
4.4	Experimental Process	123
4.4.1	Fabry-Perot Michelson	124
4.4.2	Dual-Recycled Michelson	126
4.4.3	RSE	129
4.4.4	Systematic Errors	131
4.5	Data and Results	133
4.5.1	Dual-Recycled Michelson	133
4.5.2	RSE	136
4.5.3	Gravitational Wave Transfer Function	140
4.6	Conclusions	144
5	Laser Noise Couplings in RSE	147
5.1	Conceptual Motivation	148
5.1.1	Balanced Sidebands	148
5.1.2	Unbalanced Sidebands	151
5.2	Figure of Merit	152
5.3	Input Noise	154
5.3.1	Laser Frequency Noise	155
5.3.2	Laser Amplitude Noise	156
5.4	Readout	157
5.5	Transmission of Light	157
5.5.1	The General Transmission Function	158
5.5.2	The Carrier	160
5.5.3	RF Sidebands	164
5.6	Calculation of the Measured Noise	168
5.6.1	Broadband RSE	168
5.6.2	Detuned RSE	169
5.7	Analysis	172
5.7.1	Optimized Broadband RSE	173

5.7.2	Narrowband RSE	176
5.7.3	Conclusion	179
A	The Fabry-Perot Cavity	181
A.1	The Reflected Field	182
A.1.1	Cavity Coupling	184
A.1.2	Cavity Approximations	186
A.1.3	Fabry-Perot Cavity Difference	189
A.2	The Pickoff Field	191
A.3	The Transmitted Field	193
A.4	Derivatives	194
A.5	Additional Losses	195
B	Transmission of the RSE Interferometer	197
B.1	The General Transmission Equation	197
B.1.1	Dual-Recycled Michelson – Coupled Cavity	198
B.2	The Carrier Equation	199
B.3	The RF Sideband Equation	203
C	Cross-Coupled 2×2 Plant	206
C.1	Diagonal Plant	208
C.2	Ill-Conditioned Plant	209
C.2.1	System Performance	210
C.2.2	Transfer Function Measurement	211
D	Schematics of the Prototype Electronics	213
D.1	Feedback Electronics	213
D.2	RF Electronics	214
	Bibliography	226

List of Figures

1.1	Internal thermal noise for fused silica and sapphire.	9
2.1	RSE interferometer optical layout.	20
2.2	Equivalent three mirror coupled cavity for differential signals.	21
2.3	Tile plot for coupled cavity with an under-coupled signal cavity.	23
2.4	Coupled cavity transmittance with an under-coupled signal cavity.	25
2.5	Peak frequency and bandwidth vs. detuning.	28
2.6	Tile plot for a coupled cavity with an over-coupled signal cavity.	30
2.7	Coupled cavity transmittance with an over-coupled signal cavity.	31
2.8	The effect of a field incident on a moving mirror.	31
2.9	Arm cavity power as a function of ITM transmittance.	37
2.10	The effect of losses in the signal cavity.	40
2.11	Cavity reflectivity as a function of one mirror's transmittance.	42
2.12	1 kHz narrowband optimization.	47
2.13	1 kHz shot noise limited sensitivity	48
2.14	<i>bench.m</i> optimization for neutron binary coalescence.	51
3.1	Signal extraction in the inphase demodulation.	61
3.2	Signal extraction in the quadrature demodulation.	62
3.3	Generation of the signal phasors.	63
3.4	Unbalanced RF sidebands in the phasor picture.	64
3.5	Example configuration for <i>Twiddle</i>	65
3.6	The optical layout of the RSE interferometer.	67
3.7	The Michelson "mirror."	68
3.8	The power/signal coupled cavity.	69
3.9	Power/signal coupled cavity transmittance as a function of asymmetry.	73
3.10	Power and signal cavity spectral schematics.	77

3.11	Signal cavity spectral schematic for a detuned RSE interferometer.	78
3.12	A single cavity representation of the RSE interferometer.	82
3.13	Variation of the frequency of peak sensitivity with demodulation phase for narrowband RSE.	91
3.14	Variation of the frequency of peak sensitivity with demodulation phase for optimized broadband.	92
4.1	Layout of the optical table for the RSE experiment.	105
4.2	Calibration of photodiode/mixer gain.	111
4.3	Fast piezo mirror actuator.	113
4.4	Block diagram of the feedback electronics.	115
4.5	Block diagram of the RF frequency generation board.	117
4.6	Mode matching as a function of cavity loss, given a measured visibility.	121
4.7	Experimental setup for the Φ_+ and Φ_- demodulation phase optimization.	125
4.8	Experimental setup for transfer function measurements in the dual- recycled Michelson.	134
4.9	Dual-recycled Michelson transfer function measurements.	135
4.10	RSE transfer function data for the minor degrees of freedom.	138
4.11	RSE transfer function data at the pickoff 81 MHz port.	139
4.12	Raw data of the Φ_- transfer function measurement of the Fabry-Perot Michelson.	141
4.13	Measurement of the RSE gravitational wave transfer function, relative to the same measurement in the FPM.	142
4.14	RSE transfer function of Figure 4.13, as well as one with an offset added to the ϕ_s signal.	143
4.15	RSE transfer function sensitivity to demodulation phase.	145
5.1	Phasor representation of gravitational wave signal generation.	149
5.2	Phasor representation of frequency noise generation.	149
5.3	Phasor representation of amplitude noise generation.	150
5.4	Phasor representation of second order amplitude noise generation.	151

5.5	Amplitude noise with unbalanced sidebands.	152
5.6	The RSE interferometer optical layout.	158
5.7	Ratio of RSE DC carrier gain to LIGO I DC carrier gain.	162
5.8	Carrier noise sideband transmission for broadband RSE relative to LIGO I.	165
5.9	Optimized broadband noise coupling at 300 Hz.	173
5.10	Optimized broadband noise coupling.	174
5.11	Individual carrier and RF sideband contributions to the total measured noise.	175
5.12	1 kHz narrowband RSE noise coupling evaluated at 1 kHz.	176
5.13	Noise coupling of a 1 kHz narrowband RSE interferometer.	177
5.14	Individual carrier and RF sideband contributions to the total measured noise.	178
A.1	Fabry-Perot cavity.	181
A.2	Cavity reflectivity examples.	183
A.3	Cavity reflectivity as a function of the front mirror reflectance.	185
A.4	Arm cavity reflectivity as a function of frequency.	187
A.5	Difference between cavity approximation and exact formula.	188
A.6	Comparison of the approximate cavity difference Eq. (A.26) with the exact equation Eq. (A.21).	192
A.7	Cavity power gain as a function of front mirror reflectance.	193
C.1	Block diagram of a 2×2 control system.	206
D.1	PZT compensation schematics: Overview.	215
D.2	PZT compensation schematics: Channel 1 input.	216
D.3	PZT compensation schematics: Channel 2 input.	217
D.4	PZT compensation schematics: Adder.	218
D.5	PZT compensation schematics: Fast PZT network.	219
D.6	PZT compensation schematics: Slow PZT network.	220

D.7	Michelson compensation board.	221
D.8	High voltage fast PZT driver.	222
D.9	High voltage slow PZT driver.	223
D.10	RF frequency generation board.	224
D.11	Four-way RF phase shifter and amplification board.	225

List of Tables

2.1	Comparison of broadband RSE with and without power recycling, assuming 10 ppm coating loss.	43
2.2	Comparison of broadband RSE with and without power recycling, assuming 25 ppm coating loss.	43
2.3	1 kHz optimization parameters.	46
2.4	Revised 1 kHz optimization parameters.	47
2.5	Optical parameters of an interferometer optimized by <i>bench.m</i> for neutron star binary coalescences.	50
2.6	Power recycled Fabry-Perot Michelson optimization by <i>bench.m</i> for neutron star binary coalescences.	50
2.7	Broadband RSE interferometer optimization by <i>bench.m</i> for neutron star binary coalescences.	51
3.1	Matrix of discriminants for an optimized broadband interferometer.	94
3.2	Variation of phase gains with changing asymmetry.	95
3.3	Matrix of discriminants for an optimized broadband interferometer, with optimized asymmetry.	96
3.4	Optical and physical parameters for optimized broadband interferometer.	97
3.5	Common mode residual requirements for the optimized broadband interferometer.	97
3.6	Matrix of discriminants for a 1 kHz narrowband RSE interferometer.	99
3.7	Optical and physical parameters for 1 kHz narrowband interferometer.	99
3.8	Common mode residual requirements for the 1 kHz narrowband interferometer.	100
4.1	Calibration of the readout gains of the signal ports.	112

4.2	Effective response of the mirror actuators used in the transfer function measurements.	114
4.3	Measured beam parameters for the light input into the main interferometer.	122
4.4	Measurement of the ETM radii of curvature.	122
4.5	Powers in the dual-recycled Michelson experiment.	129
4.6	Demodulation phase change between the Fabry-Perot Michelson and dual-recycled Michelson experiments.	129
4.7	Uncertainties in parameters used in the model predictions of the matrix of discriminants.	132
4.8	Dual-recycled Michelson matrix of discriminants.	135
4.9	Matrix of discriminants for RSE.	139
5.1	Spectral components due to amplitude and frequency noise.	157

Chapter 1

Prologue

1.1 General Relativity

On the 25th of November, 1914, Albert Einstein presented to the Prussian Academy the final, definitive form of his General Theory of Relativity. In this theory, Einstein found a way to present the laws of physics independent of the frame in which the laws were expressed, and thereby found a description of the structure of space-time of the universe. This structure is conveniently described as a “curvature” of space-time. In turn, curvature tells matter how to move, and the distribution of matter tells space-time how to curve. This simple, yet deeply revealing statement indicates the new paradigm in which gravity is to be understood. Gravity is simply the manifestation of space-time curvature.

General Relativity is a deep, subtle, and difficult theory. Answers to questions do not come easily. However, the efforts of many great thinkers in the past 86 years have managed to astound and amaze the world with predictions of fantastic objects such as black holes, and even more fantastic possibilities, such as worm holes and time travel.

Although the results which have been predicted have come only after tremendous effort, even more difficult have been some of the experimental tests which could verify such a fantastic theory. There are many reasons for this – the curvature is very small where we live, the strength of gravitational coupling is 40 orders of magnitude weaker than electromagnetism. Yet, the experimentalists press on, seeking truths in very small numbers.

Perhaps one of the most fascinating results of Einstein’s fantastic theory is the prediction that the curvature of space-time in which we live can be perturbed by ripples generated by very massive, compact sources. Much like the waves on a pond

into which a stone has been dropped, these ripples, or gravitational waves, propagate outwards through the universe, producing minute perturbations of the curvature in which we sit. Since curvature generates gravity, which is the same as acceleration, these ripples should in principle be observable by monitoring the relative acceleration of test particles due to the tidal forces produced by the gravitational wave.

A “Newtonian/quadrupole” approximation to Einstein’s field equations gives an estimate for the size of these space-time perturbations as a strain $h = \Delta l/l$ of space.

$$h \simeq \frac{G}{c^4} \frac{\ddot{Q}}{r} \quad (1.1)$$

where G is Newton’s gravitational constant, c is the speed of light, Q is the object’s quadrupole moment, and r is the distance to the source. For waves of any appreciable magnitude, the quadrupole moment must be quite large, approximately $Q \simeq ML^2$, where M is the mass of the object and L is the scale of its size. The second derivative is then $\ddot{Q} \simeq 2Mv^2 \simeq 4E_{\text{kin}}^{\text{ns}}$ where v is the internal velocity of the mass distribution and $E_{\text{kin}}^{\text{ns}}$ is the kinetic energy of the non-spherical part of the mass distribution. This gives the estimation

$$h \simeq \frac{1}{c^2} \frac{4G(E_{\text{kin}}^{\text{ns}}/c^2)}{r} \quad (1.2)$$

For very large objects, such as colliding neutron stars, each with roughly a solar mass, $E_{\text{kin}}^{\text{ns}}$ is roughly the mass of the sun, so the strain h from objects in the Virgo cluster (at 15 Mpc) would be roughly $h \sim 10^{-20}$. For two objects 4 km apart, this corresponds to 0.04 fm, or roughly 1/100th of the width of a nucleus over two and a half miles. Perhaps even more disheartening is the estimation that the sensitivity would have to be yet another magnitude greater to see only a few events of any kind in one year, based on our current knowledge of the universe, and predictions of the rarity of these types of events.

1.2 The Search for Gravitational Waves

1.2.1 Resonant Bar Detectors

This type of extreme measurement is fuel for visionaries. In the late 1950s, Joseph Weber began a quest for developing a detector to measure gravitational radiation.[1] Weber ultimately chose a large cylindrical aluminum bar, based on the idea that the tidal forces due to gravitational radiation would excite the normal modes of the bar. Detection of the excitation of the resonant mode of the bar was initially accomplished by using piezoelectric transducers. Resonant bar research is still an active field, and the fundamental concept remains largely unchanged. The greatest progress has been in the development of very sensitive transducers to monitor the mode of the bar, methods for reducing the number of spurious events, as well as methods for reducing the thermal noise of the bar by cryogenics.

1.2.2 Interferometers

One drawback to resonant bar detectors is that their sensitivity is limited to very narrow bandwidths. The year 1962 saw the introduction of a new concept, by two theorists in the Soviet Union, Mikhail Gertsenshtein and V.I. Pustovoit, ([2] referenced by Thorne in [3]) in which an interferometer could be used to detect gravitational radiation. This idea languished behind the Iron Curtain, and it wasn't until the late 60s that Rai Weiss [4] and Robert Forward [5] also realized the potential for Michelson interferometers in gravitational wave detection.¹ The basic idea is that a Michelson interferometer can measure the differential displacement of the end mirrors (the "test masses") of the Michelson due to the tidal forces of the gravitational radiation using the exceptionally good ruler of laser light. The frequency response of an interferometer, unlike bars, is flat from DC (0 Hz) out to a frequency characterized by the time the light spends in the arms of the Michelson. The past 30 years has seen the development of various optical tricks which increase the signal sensitivity (with mirrors,

¹[5] indicates that Weber had suggested such a technique in a telephone conversation with Forward in 1964.

but no smoke). These tricks have led to numerous leaps and bounds in the limits of strain sensitivity, from $\simeq 2 \times 10^{-16}/\sqrt{\text{Hz}}$ above 2 kHz,[6] by Forward in 1978, to $7.5 \times 10^{-21}/\sqrt{\text{Hz}}$ around 450 Hz, at the Caltech 40 m prototype in the mid-90s.[7]

There are currently many research efforts worldwide which are developing large scale interferometers for gravitational wave observation. Almost all of the detectors, including LIGO,[8] VIRGO,[9] and TAMA[10] are adopting a power recycled Fabry-Perot Michelson configuration as their first detector. This interferometer uses Fabry-Perot cavities in the arms to increase the integration time of the detector to roughly 1/100th of a second. In addition, the Michelson itself is held at a dark fringe, so that all of the light returning from the arms goes back toward the laser. This is where “power recycling” comes in. An additional partially transmitting mirror, called the power recycling mirror, is placed between the laser and the Fabry-Perot Michelson. It is positioned such that the light returning from the Michelson which reflects from it back into the interferometer, is in phase with the incoming light from the laser, which transmits through it. By choosing the transmittance of this mirror appropriately, all of the returning light from the arms can be sent back into the interferometer. This increases the amount of light in the interferometer by the power recycling gain, typically a factor of 10–100. Both LIGO and VIRGO are multi-kilometer efforts; LIGO has 4 km arms and VIRGO is 3 km. The TAMA project in Tokyo is an order of magnitude smaller, at 300 m, due to space constraints on the campus of the NAO. The joint Scottish/German effort, GEO600,[11] is taking a slightly different approach in which the signal integration time is increased, not by adding Fabry-Perot cavities in the arms, but rather by adding a single mirror at the output of the interferometer. This mirror recycles the signal in much the same way as the power recycling mirror recycles the laser power. The GEO600 effort will use both power and signal recycling, a configuration known as dual-recycling.

1.3 Interferometer Sensitivity

Concurrent with the construction of the first generation LIGO detector (LIGO I) is the work of an international collaboration, the LIGO Scientific Collaboration (LSC), to develop the next generation interferometer, LIGO II.[12] The planned improvements lead to nearly an order of magnitude increase in the sensitivity across the bandwidth, as well as extending the bandwidth to lower frequencies. To understand how this is to be accomplished requires some description of the limits to the sensitivity of the detector, and how that sensitivity is shaped. In brief, the sensitivity is defined by the noise which limits the measurement (seismic, thermal, and shot noise), as well as the gain of the interferometer. LIGO II will use improved technology and materials to reduce the noise due to seismic and thermal noise. Increased laser power will reduce shot noise. An advanced interferometer configuration will shift the maximum gain of the detector away from DC into the bandwidth of interest by placing a mirror at the output, similar to the original GEO600 interferometer. This will generally be referred to as a signal tuned interferometer.

1.3.1 Seismic Noise

The measurement of the gravitational wave is accomplished by monitoring the relative distance between the surfaces of two test masses. Any other force which disturbs the center of mass or the surface of the mass itself makes the measurement ambiguous – it is unclear whether the disturbance is due to the gravitational wave or the noise force. A ground-based interferometer must be, at some level, mechanically coupled to the earth, hence the masses are subject to seismically driven vibrations. The dominant part of the seismic power spectrum is at low frequencies. This varies, sometimes by an order of magnitude or more around the world, but a moderately quiet site will have a spectrum of roughly $x(f) = 10^{-8}\text{m}/\sqrt{\text{Hz}} \times (1\text{Hz}/f)^2$.

Techniques for reducing the effects of seismic noise have long been known, and yet new designs and approaches continue to improve vibration isolation. Two different approaches have been taken: passive and active.

At the heart of passive techniques is the inertial response of a mass on a spring. Passive isolation takes advantage of the fact that above the resonant frequency, f_0 , of the mass-spring system, the response of the mass to driving forces decreases by $(f_0/f)^2$. Systems with lower resonant frequencies give higher isolation at a given frequency. These passive systems can also be staged by suspending one isolation system from the isolated stage of a previous system. The total isolation then is the product of each mass-spring system, or $(f_0/f)^{2n}$, where n is the number of stages (assuming the same resonant frequency). Clever mechanical designs have been able to reduce the resonant frequency to well below 100 mHz in structures roughly 1 meter in scale.[13]

Active isolation techniques, on the other hand, employ a bootstrapping method. A proof mass is placed on the platform being isolated. The proof mass must be more inertial than the platform it sits on, usually by being itself a mass on a spring. Monitoring the relative displacement, velocity, or acceleration between the platform and the proof mass generates an error signal when the platform has suffered a disturbance to its state. Feedback control systems are used to correct the error signal, locking the position of the platform to the inertial reference of the proof mass. The level of isolation is proportional to the closed-loop gain of the system, assuming sensor noise is low enough. The limits to the closed-loop gain, hence the isolation, are the sensor's bandwidth and noise. This type of system, similar to passive systems, can also be arranged in stages. An advantage to staging the isolation is that loop gain in each stage can be more modest, which is sometimes forced by the available bandwidths and mechanical resonances of the structure.

LIGO I uses a simple, multi-layer passive isolation system which places a "wall" in the seismic noise spectrum at roughly 40 Hz. The proposed LIGO II seismic isolation is largely active.[14] A "quiet hydraulic" system is used externally to the vacuum chambers which house the test masses. This external system has large dynamic range, and is used primarily to take out long time scale drifts and disturbances. A two-stage active isolation system inside the test mass chambers is supported by the external system through bellows. The active system isolates an optical table in all six

degrees of freedom, from which the test mass is hung as the lower mass of a quadruple pendulum. This design is expected to move the seismic wall to ≈ 10 Hz.

1.3.2 Thermal Noise

The second fundamental noise source is due to the fact that the masses are at finite temperature. Finite temperature dictates that the atoms which comprise the masses, as well as the wires which suspend the masses, vibrate. Vibrations of the test mass atoms cause the surfaces of the mirrors to vibrate, generating a signal. The vibrations of the wires which support the test mass shake the mirror, similarly to seismic noise. Thermal noise which affects the surface of the test mass itself is referred to as “internal thermal noise,” while the thermal noise from the suspension wires is called “pendulum thermal noise.”

Internal Thermal Noise

The “Fluctuation-Dissipation Theorem” describes the physical mechanism for the existence of thermal noise.[15] The theorem states that for an object in equilibrium with the environment, the path through which energy can dissipate out of the object, hence cool the object, is the same path through which the environmental energy can enter into the object, thus driving the vibrations. The traditional way to think about the internal thermal noise of the test mass is to recognize that, for every mode of an object, equipartition gives $k_B T/2$ of energy. The energy is frequency independent, so it drives the mode across the entire bandwidth of its response. The larger the mechanical Q of the mode, the more of this energy is concentrated around the resonant frequency, while the noise level at all other frequencies is lower. The total noise of the mass is calculated by characterizing the modes of the test mass, and summing their contributions. The power spectrum of the fluctuations of the surface of the test mass due to a single mode is given by [16]

$$S_{x_n}(f) = \frac{4k_B T}{\alpha_n m 2\pi f} \left[\frac{\omega_n^2 \phi_n(f)}{((2\pi f)^2 - \omega_n^2)^2 + \omega_n^4 \phi_n(f)^2} \right] \quad (1.3)$$

The various terms are defined as follows: the subscript n indicates the mode, ω_n is the resonant frequency, m is the mass of the object, α_n is the effective mass coefficient for the n th mode, k_B is Boltzmann's constant, T is the temperature, and $\phi_n(f)$ is the "loss function" for the n th mode. This loss function is a model of the method through which dissipation occurs. The assumption for internal loss is that ϕ_n is independent of frequency, equivalent to the inverse of the mechanical Q of the mode. This is referred to as "Brownian noise" by Braginsky.[17] It should be noted that a different approach proposed by Levin provides a more powerful method of calculating thermal noise, and in fact, is more physically satisfying than this description.[18]

The fact that the tails of the resonances of the masses are what lie in the relevant bandwidth for LIGO (< 1 kHz) motivates the goal to use materials with the highest mechanical Q 's. LIGO I is using fused silica, which has Q 's of 10^6 , while LIGO II intends to use sapphire which has Q 's of 10^8 .

Recent work has uncovered yet another source of fluctuations of the surface of the test mass, known as "thermoelastic noise." [17] The thermal diffusivity $D = \kappa_{th}/(C_V\rho)$ (κ_{th} is the coefficient of thermal conductivity, C_V is the specific heat at constant volume, and ρ is the material density) defines the time in which heat can diffuse across a distance r_0 , which is defined by the radius of the Gaussian power profile of the laser light incident on the test mass. For sapphire masses with a spot size of 4 cm, this is approximately 100 seconds. Temperature fluctuations will not average out over the sampled surface of the test mass during the characteristic time of a gravitational wave (0.01 sec). However, the size of the mass divided by the speed of sound in the mass is a much shorter time scale than the characteristic time of a gravitational wave, so oscillations of stress and strain in the test mass effectively respond immediately. This suggests that the temperature fluctuations, since they are not averaged out, will immediately jiggle the surface of the test mass via the thermal expansion coefficient. The temperature fluctuations arise due to the fundamental statistical nature of the particles making up the test mass at finite temperature. Exact calculations indicate

that the power spectrum of this “thermoelastic noise” is

$$S_x(f) = \frac{8(1 + \sigma)^2}{\sqrt{2\pi}} \frac{\alpha_l^2 \kappa_{th} k_B T^2}{C_V^2 \rho^2 r_0^3 (2\pi f)^2} C_{FTM}^2 \quad (1.4)$$

The test mass material parameters, σ and α_l , are the Poisson ratio and the linear thermal expansion coefficient, respectively. Neglecting the term C_{FTM} , the expression gives the noise for a test mass which is infinite in radius and length. Liu and Thorne worked out the geometrical correction factor C_{FTM} , which is of order unity.[19]

The thermoelastic noise is worse for sapphire than for fused silica, due to its higher expansion coefficient. However, the Brownian thermal noise of silica is significantly worse than that of sapphire, and masks its own thermoelastic noise. The total noise for sapphire can be optimized by increasing the spot size, thereby balancing the decrease in thermoelastic noise (by $r_0^{-3/2}$) against the increase in losses due to diffraction past the edge of the mirror. The total noise for sapphire is better than silica for most of the bandwidth, as shown in Figure 1.1. The optimization done is for a 14 cm radius mass of thickness 12 cm, and a spot size of 5.4 cm.

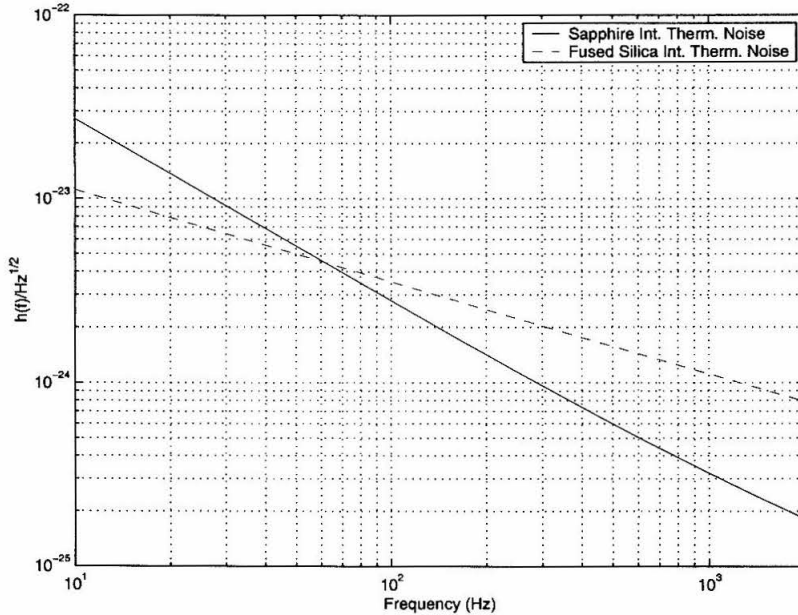


Figure 1.1: Internal thermal noise equivalent to strain for fused silica and sapphire.

Pendulum Thermal Noise

The test masses themselves are not free masses, but rather are suspended from wires as pendulums. This is needed to support the masses in earth's gravitational field, as well as being a good way to further isolate the masses from seismic vibrations. However, the same issues of internal thermal noise plague the wires which suspend the masses. The result is that minute vibrations of the wires, due to their thermal noise, shake the test masses, contributing to the thermal noise sensitivity limit.

A great deal of research has gone into developing fibers which not only have low thermal noise, but whose coupling to test mass displacement is likewise minimized. Issues such as fiber material, surface losses, non-linear thermo-elastic losses, fiber geometry, and the method of attachment have all played a role in the development of the proposed suspension for LIGO II. This proposal includes the use of fused silica ribbons which are silicate bonded to the test masses. The current prediction for pendulum thermal noise is that it will only contribute to the sensitivity limit in a small region around 10 Hz.

1.3.3 Optical Noise

Both thermal and seismic noise influence the position of the surface of the test mass. The last of the fundamental noise sources is a limitation of the measurement process itself. The measurement process involves the interaction of light with the test masses, and the subsequent counting of the signal photons by a photodetector. This has traditionally been thought of in terms of two uncorrelated sources - the Poissonian statistics of the counting of photons, otherwise known as "shot noise," and the Poissonian statistics of the force on the test masses from photons, known as "radiation pressure noise." [4, 15] One critical assumption about the radiation pressure noise in interferometers without a signal mirror is that the fluctuations in the power of the two arms of the interferometer are anti-correlated. This semi-classical approach generated a "lively but unpublished controversy" regarding the existence of the fluctuating radiation pressure. [20] The controversy was put to rest by Caves, who demonstrated

rigorously that the radiation pressure fluctuations are, in fact, anti-correlated.[21] Caves' analysis indicated that the source of the fluctuations for both shot and radiation pressure noise is the vacuum fluctuations which enter the interferometer from the output port of the beamsplitter. Shot and radiation pressure noise are manifestations of the two quadratures of the vacuum. The square-law photodiode measures the product of the amplitudes of the vacuum and the coherent light from the laser.

Increasing the laser power increases the shot noise sensitivity while the radiation pressure noise sensitivity decreases. In LIGO I, 6 watts of light are incident on the interferometer, and radiation pressure noise is negligible. In LIGO II, however, roughly 120 watts of power are planned, which makes radiation pressure an important factor.

The shot noise spectral density is flat, while the radiation pressure amplitude spectral density has a $1/f$ shape. At a given frequency, the quadrature sum of the shot and radiation pressure noise can be minimized by using the right amount of power. This defines the "standard quantum limit." [22]

$$h_{SQL}(f) = \sqrt{\frac{8\hbar}{(2\pi f)^2 mL^2}} \quad (1.5)$$

The mass of the test mass is m , and L is the length of the interferometer arms. This is actually a locus of the optimum strain spectral density at frequency f assuming the optimized input power for that frequency,

$$P_{SQL} = \frac{mL^2(2\pi f)^4}{4\omega_0} \quad (1.6)$$

where ω_0 is the angular frequency of the light. This limit makes the assumption that the shot noise and the radiation pressure noise are uncorrelated.

Recent work has discovered that there *are* correlations in the radiation pressure noise in signal tuned interferometers.[23, 24] This discovery follows an analysis of the interferometer which includes the mechanical response of the interferometer. Radiation pressure fluctuations cause forces on a test mass, which in turn generates a

back-action force on the incident field. These perturbations to the optical field are then recycled by the signal mirror back into the interferometer, which correlates the radiation pressure noise with itself at different times.² The standard quantum limit is no longer relevant for this type of interferometer. In fact, the added correlations actually improve the sensitivity, beating the standard quantum limit in some frequency ranges.

The result is that the semi-classical approach does not generate an accurate prediction for the optical noise in signal tuned interferometers. In fact, where the semi-classical approach generates one peak in the sensitivity at a frequency shifted from DC, the proper opto-mechanical analysis uncovers a second peak in the sensitivity curve, at a lower frequency, while the first peak in sensitivity is changed very little, if at all. It is in this new peak in the sensitivity that the standard quantum limit is surpassed.

Unfortunately, the level of thermal noise that is expected for a LIGO II detector is very near the standard quantum limit. Thermal noise then will largely mask this second resonance of the opto-mechanical system. As a result, the total noise, when summing the optical, thermal, and seismic noises in quadrature, is only mildly altered from the semi-classical predictions. Because of its mild effect on the noise, and because of the timing of these results relative to the conclusion of this thesis work, these results will not be taken into account here. The semi-classical approach, in which the noise is considered independent of the frequency response of the detector, will be used. It must be remarked, though, that future analyses of interferometers will need to take the proper quantum mechanical approach in order to properly understand the optical noise limited sensitivity of any configuration.

1.3.4 Interferometer Configuration

The last factor which sets sensitivity is the interferometer's frequency response. This goes hand in hand with the optical noise, but is independent of thermal and seismic

²This is true except for the two special cases in which the signal cavity is exactly resonant or anti-resonant.

noise. Thermal and seismic noise disturb the test masses directly, while optical noise sets a limit on the smallness of the observable measurement. Hence, a configuration that increases the gain of the gravitational wave signal increases the detector sensitivity relative to the optical noise. A “shot noise limited sensitivity” is defined as the strain that generates a measured signal equivalent to the shot noise, which is found by dividing the shot noise by the transfer function from gravitational wave signal input to interferometer output. By studying optical configurations, the hope is to increase the interferometer’s gain, as well as tailor the frequency response in regions dominated by shot noise.

Two factors define the ultimate sensitivity of the detector: the energy stored in the detector, and the detector bandwidth. This is summed up nicely in Mizuno’s sensitivity theorem.[25]

$$\tilde{h}_0 \geq \sqrt{\frac{2\hbar\lambda}{\pi c} \frac{\Delta f_{\text{bw}}}{\mathcal{E}}} \quad (1.7)$$

The bandwidth and the energy stored are represented by Δf_{bw} and \mathcal{E} , respectively. Clearly, having a narrower bandwidth, and/or more energy stored conspires to increase the sensitivity. It should be noted that this gives a *lower bound*, and factors such as losses in the signal output can degrade the ultimate sensitivity.

The bandwidth of LIGO I is defined by the Fabry-Perot cavities in the arms – the frequency response of a Fabry-Perot cavity is well approximated by a low-pass filter. The cavity’s pole frequency is called the “cavity pole.” This pole is a function of the reflectivities of the mirrors and the length of the cavity. In LIGO, the end mirror has a reflectivity very nearly unity, and so the cavity pole is set by the choice of the input mirror of the Fabry-Perot cavity alone. One problem with this is that the bandwidth is centered at DC, but clearly the seismic and thermal noises prevent any access to this frequency band of highest sensitivity.

The energy stored in the interferometer is limited by the losses. These losses are a combination of the losses in the arm cavities plus the losses in the power recycling cavity. The latter are typically far larger than the former, due to the large loss mechanisms that exist there – AR coating reflectivities and absorption of substrates.

Scatter and absorption of coatings, which exist in both the arms and power recycling cavities, are typically much smaller. The input mirrors of the arm cavities set the total loss, given the mechanisms mentioned. This is because the input mirror sets the arm cavity loss, which in turn sets the amount of light returning to be power recycled. This factor decides the level of power recycling, which in turn sets the losses in the power recycling cavity. The total losses are then the light power circulating in the power recycling and arm cavities times their respective round trip loss factor.

Resonant Sideband Extraction

The technique of signal recycling was first suggested by Meers in 1988.[26] Signal recycling adds a “signal mirror” at the output of the interferometer to increase the signal integration time, which amplifies the measured signal. The signal shouldn’t be integrated indefinitely – the oscillatory nature of the gravitational wave causes an attenuation of the measured signal if it’s integrated for much more than half the wave period. In general, then, dual-recycling is to be used for detectors whose arms alone can’t integrate the signal long enough, that is, their bandwidth is too large.

Adding the signal mirror gives two more parameters which can be varied for interferometer design – the mirror transmittance, as well as the average propagation phase between the signal mirror and the two arms. This propagation phase defines a “signal cavity.” When this phase is anti-resonant, the interferometer’s response is narrowed and the signal integration time is increased. This is referred to as broadband dual-recycling due to the fact that the peak sensitivity is at DC, and the bandwidth is typically chosen such that the widest range of gravitational wave frequencies are accessible (similar to LIGO I). If the phase is “detuned” away from this point, the peak sensitivity shifts to frequencies away from DC. With the appropriate choice of signal mirror and phase, the interferometer can be designed to have a very narrowband response at a gravitational wave frequency of interest, which increases the sensitivity, by the sensitivity theorem. This ability to manipulate the frequency response allows a great deal more freedom in optimizing the interferometer’s sensitivity than the LIGO I configuration.

The LIGO interferometers are large enough such that reaching the maximum storage time isn't a problem. As a matter of fact, the bandwidth could be made much smaller, increasing the storage time. This wouldn't be good for the integration of the signal, but it would be good for the energy stored in the detector. Increased storage time in the arms causes more of the light to be lost through the arm loss mechanisms, which are much smaller than the loss mechanisms in the power recycling cavity. The less light returning from the arms, the less efficiently light is lost due to the large power recycling losses, and the more light energy is stored. In 1993, Mizuno realized that the same signal mirror that Meers proposed to recycle the signal could be used to more efficiently "extract" the signal from a high storage time arm cavity.[27] By choosing the propagation phase defined by the signal mirror to be resonant, the band of frequencies resonant with the signal cavity transmit more efficiently, and so the storage time for signals in the arms is *decreased*. This is known as resonant sideband extraction, or RSE.

The issue of the losses in the power recycling cavity is actually somewhat more complicated than the simple linear losses at AR coatings and scatter and absorption in the substrates. The absorption in the substrates will heat the test masses with a temperature distribution similar to the Gaussian intensity profile of the beam. This temperature gradient forms a lens in the substrate via the dependence of the index of refraction on temperature. The lenses created by the substrates of the optics are sources of loss due to the fact that they change the profile of the beam, causing scattering of light out of the fundamental spatial mode into higher order modes of the modified cavity.[28] RSE addresses this issue simply by taking more light out of the power cavity and placing it in the arm cavities where these effects should be smaller.[25]

Similar to dual-recycling, detuning the signal cavity phase away from resonance will generate frequency responses which have peak sensitivities at frequencies away from DC. Thus, RSE allows the design of a detector which can store more light in the arms, while optimizing the shape of the transfer function with respect to shot noise and the desired gravitational wave source.

Another feature of signal tuned interferometers is the potential to reduce the amount of stray light leaking out the dark port of the interferometer. The imperfect interference of light at the beamsplitter, or “contrast defect,” has many sources: misalignments of the return beams from the two arms, mismatch of wavefront curvatures due to differing arm mirror curvatures, optics which have imperfect surface figures, as well as mismatched lensing in the two arms. The ability of the signal mirror to reduce these effects was anticipated by Meers [26], and was analyzed by Bochner in his thesis.[29] There are several results. First, the concept of “wavefront healing,” in which light scattered into higher order modes is re-introduced into the fundamental mode, was confirmed. However, Bochner points out that this effect is negligible compared to the losses due to high angle scattering from realistically deformed optics. Broadband dual-recycling is effective at suppressing higher order modes at the dark port, which reduces the amount of stray light at the photodiode; however, it amplifies fundamental mode losses due to arm mismatches. Detuned interferometers, as well as broadband RSE interferometers, reduce fundamental mode losses, but tend to amplify higher order mode losses. The addition of an “output mode cleaner” at the dark port, through which only the fundamental mode is transmitted, is part of the proposal for LIGO II, and would significantly reduce the power at the photodiode due to higher order modes.

1.4 The Goal of this Work

Some of the features and operation of signal tuned interferometers have been experimentally verified. A suspended test mass dual-recycled interferometer has been built, and the frequency responses of detuning have been demonstrated, as well as an improvement of the contrast defect.[30] A tabletop RSE prototype has been built, demonstrating the enhanced sensitivity at frequencies above the arm cavity bandwidth.[31] A tabletop prototype has tested the power recycled Fabry-Perot Michelson.[32] Compared to the proposal for LIGO II,[12] there are still many untested elements.

The LIGO II proposal is for an RSE interferometer, with power recycling. The arm cavity optics, which define the thermal noise, are proposed to be sapphire. The input power at the interferometer is 120 watts. The method of signal extraction to control the mirrors, and most importantly, read out the gravitational wave signal, is an optical heterodyne technique, in which radio frequency (RF) sidebands are added to the input light.³ Modulation is performed at the detection photodiodes by the square-law detection where the beat-note between the carrier and RF sidebands is measured. The electronic signal from the photodiode is subsequently demodulated electronically. The two predominant methods for coupling the RF sideband light to the output of the interferometer where it can beat against the gravitational wave signal have been “external modulation,”[33] and “Schnupp modulation” or “frontal modulation.”[34] The proposal in LIGO II is to use Schnupp modulation. The demonstration of the suspended dual-recycled interferometer used Schnupp modulation, and optical heterodyning for control of all mirrors, but did not include arm cavities. The experimental demonstration of RSE used external modulation, no power recycling, and employed some dither locking for some of the degrees of freedom of the interferometer. The tabletop power recycled Fabry-Perot Michelson used Schnupp modulation, and all optically heterodyned signal extraction, but did not have a signal mirror.

In this thesis, the primary goal is to propose an optically heterodyned signal extraction scheme for a power-recycled signal tuned RSE interferometer using Schnupp modulation for use in LIGO II. A tabletop prototype will demonstrate the feasibility of such a design, as well as also demonstrate the detuning of RSE. Chapter 2 will discuss in greater detail the principle of RSE, as well as try to understand some of the limitations to the design of such a detector. Some optimizations for narrowband sources and binary coalescences will be examined. It will be shown that optimization via the sensitivity theorem occasionally breaks down, due to the fact that the equality in Eq. (1.7) seldom can be reached because of losses. Chapter 3 will discuss the principles of optical heterodyne signal extraction, both mathematically and conceptually.

³The current proposal plans to use DC offset locking, or homodyne detection, for the gravitational wave readout. However, this has never been tested at the sensitivity levels anticipated, and so the heterodyne readout scheme (which has been tested) is being kept as a backup.

A scheme for controlling the five degree of freedom system of RSE will be proposed, and this scheme will be applied to the optimizations from Chapter 2. Chapter 4 will describe the design and implementation of the tabletop prototype. The results of the measurement of the control system and the detuned frequency response are presented. Chapter 5 examines how frequency and amplitude noise of the input laser light can propagate through an imperfect RSE interferometer and generate measured noise in the gravitational wave signal port, thus potentially reducing the detector's sensitivity. Based on expectations for the levels of imperfections in a LIGO II interferometer, specifications for the level of frequency and amplitude stability of the input laser light are derived.

Chapter 2

Resonant Sideband Extraction

The concept of resonant sideband extraction (RSE) was realized by Jun Mizuno in 1993.[27] It is a Michelson based interferometer with Fabry-Perot cavities in the arms, and an additional mirror placed at the output of the Michelson. The addition of the output, or “signal mirror” allows more freedom in choosing the interferometer optics. This freedom can be used to optimize the distribution of losses in the interferometer, and thus increase the stored light energy. Another feature is that the frequency response can be optimized for various gravitational wave signals of interest. The combination of these features is the focus of this Chapter.

Section 2.1 will discuss the transfer function for gravitational wave signals when the signal mirror is added at the output of the interferometer. This will be done in the context of the simpler, idealized configuration of the three mirror coupled cavity. Section 2.2 will investigate some of the practical limitations to the implementation of an optical design, mostly due to the effect of losses in the interferometer. Section 2.3 will examine two particular astrophysical sources, and make a first pass at designing an interferometer whose frequency response is optimized for those sources.

2.1 Frequency Response

The optical layout of an RSE interferometer is shown in Figure 2.1. This is a Michelson based interferometer, with Fabry-Perot cavities in the arms. Each Fabry-Perot cavity is comprised of the input test mass (ITM) at the input, and the end test mass (ETM) at the end of the cavity. Each cavity is also resonant at the carrier frequency. The arm cavities are designed to be equal, which is a good approximation in reality, and an assumption in this chapter. The end mirrors typically are the highest reflectors available, such that the losses due to transmission through these mirrors is minimized.

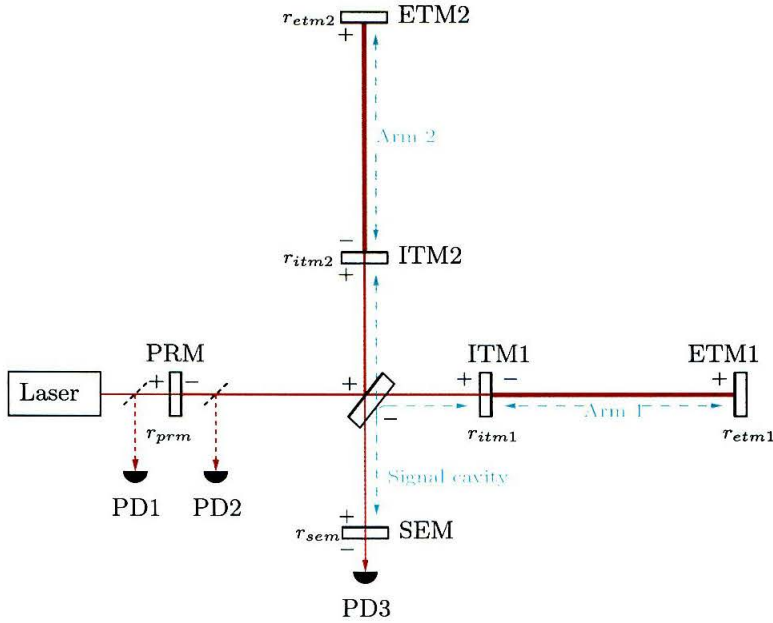


Figure 2.1: RSE interferometer optical layout. Signs indicate reflectivity convention used. Each r_i associated with a mirror has a t_i as well. Signal cavity and arm cavities indicated by dashed lines.

The beamsplitter is 50/50 in reflectance/transmittance, and is positioned such that all the light returning from the arms constructively interferes in the direction returning to the laser. This implies that none of the carrier light goes to the output, which is known as the “dark fringe” condition. The power recycling mirror (PRM), which sits between the laser and the interferometer, is a partially transmitting mirror. It is positioned such that, as the returning light is reflected, it is in phase with the fresh light from the laser. The “right” choice of mirror transmittance sets up a boundary condition such that all of the light from the laser goes back into the interferometer, and none returns to the laser. The signal extraction mirror (SEM) at the output of the interferometer is the feature of RSE and of all signal-tuned interferometers.

When the beamsplitter is held on a dark fringe, no light exits the interferometer towards the signal mirror, and all of the light (minus any losses and transmittance though the end mirrors) returns toward the laser. If the end mirrors of the cavities in the arms of the interferometer are shifted in a common mode fashion, the interference

at the beamsplitter remains unchanged, and all of the light still goes back towards the laser. If the mirrors are moved differentially, the interference at the output is no longer perfectly destructive, and some light leaks out. For very small phase shifts, the amount of light returning to the laser is effectively unchanged. This means that the dark fringe condition effectively diagonalizes the response of the detector into common and differential modes. No information about differential motion of the end mirrors goes back towards the laser, and likewise, no common mode information exits the output of the interferometer.

When a mirror is added at the output, otherwise known as the “dark port,” differential signals are the only ones which sense its presence due to the diagonalization by the dark fringe. If the arms of the interferometer are equal, then the two equal but oppositely signed signals in the arms experience the same arm cavity, and after being summed at the beam splitter, the same signal cavity. For the purposes of analyzing the interferometer’s response to differential arm signals, the rather complicated configuration of Figure 2.1 can be reduced to the 3 mirror coupled cavity of Figure 2.2. The transmissivity of this configuration is given by Eq. (2.1).

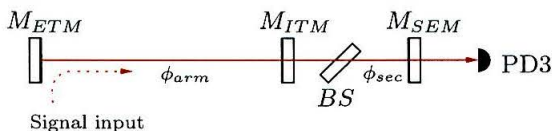


Figure 2.2: Equivalent three mirror coupled cavity for differentially modulated signals generated in the arms. The effect of losses in the beamsplitter, as well as in the ITM substrates, can be included in an effective signal mirror reflectivity and transmissivity, r'_{sem} and t'_{sem} .

$$t_{cc}(f) = \frac{t_{itm}t'_{sem}e^{-i(2\pi f(\tau_a+\tau_s)+\phi_{dt})/2}}{1 - r_{itm}r_{etm}e^{-i2\pi f\tau_a} - r_{itm}r'_{sem}e^{-i(2\pi f\tau_s+\phi_{dt})} + r_{etm}r'_{sem}A_{itm}e^{-i(2\pi f(\tau_a+\tau_s)+\phi_{dt})}} \quad (2.1)$$

The characteristic times $\tau_a = 2l_{arm}/c$ and $\tau_s = 2l_{sec}/c$ are the round trip travel times in the arm and signal cavities. The quantity A_{itm} represents 1 minus the losses of the ITM coating. The frequency f is relative to a carrier frequency which is resonant in the arms, and off-resonant in the signal cavity by the round-trip phase ϕ_{dt} , otherwise

known as the detuning phase. The losses associated with the beamsplitter and the ITM substrate are incorporated into the signal mirror parameters in the following way.

$$\begin{aligned} r'_{sem} &= A_{sub}A_{bs} r_{sem} \\ t'_{sem} &= \sqrt{A_{sub}A_{bs}} t_{sem} \end{aligned} \tag{2.2}$$

The quantities A_{bs} and A_{sub} represent $1 - L_{bs}$ and $1 - L_{sub}$, or 1 minus the losses of the beamsplitter and the ITM substrates, respectively. These substitutions were arrived at by reducing the full equations for the configuration of Figure 2.1; however, they can be intuitively arrived at by considering that the light from the arm cavity propagates through the substrate with a transmission of $\sqrt{1 - L_{sub}}$, and then through the beamsplitter with a transmission of $\sqrt{1 - L_{bs}}$.¹ This loss of light can be modeled as a reduced transmission of the signal mirror. For the light reflected from the signal mirror, these losses are likewise experienced again, hence these factors are squared.

2.1.1 The Three Mirror Coupled Cavity

It's useful to examine some properties of three mirror coupled cavities. Properties of simple Fabry-Perot cavities are assumed, and are outlined in Appendix A.

Under-coupled Signal Cavity

It will be assumed for this section that $T_{sem} > T_{itm}$. First, simply consider the coupled cavity transmission as a function of its phases. The magnitude of the transmissivity is plotted as a function of these phases in Figure 2.3. This particular example has an ETM transmittance of 10%, an ITM of 20%, and a signal mirror of 60%. These aren't particularly practical numbers for a LIGO interferometer, but they illustrate some of the features of a coupled cavity system. The case where the ITM has a higher transmittance than the SEM will be discussed later. Notice first that the

¹The 50% transmission of the beamsplitter is ignored, since it is constructively summing the light from both arms.

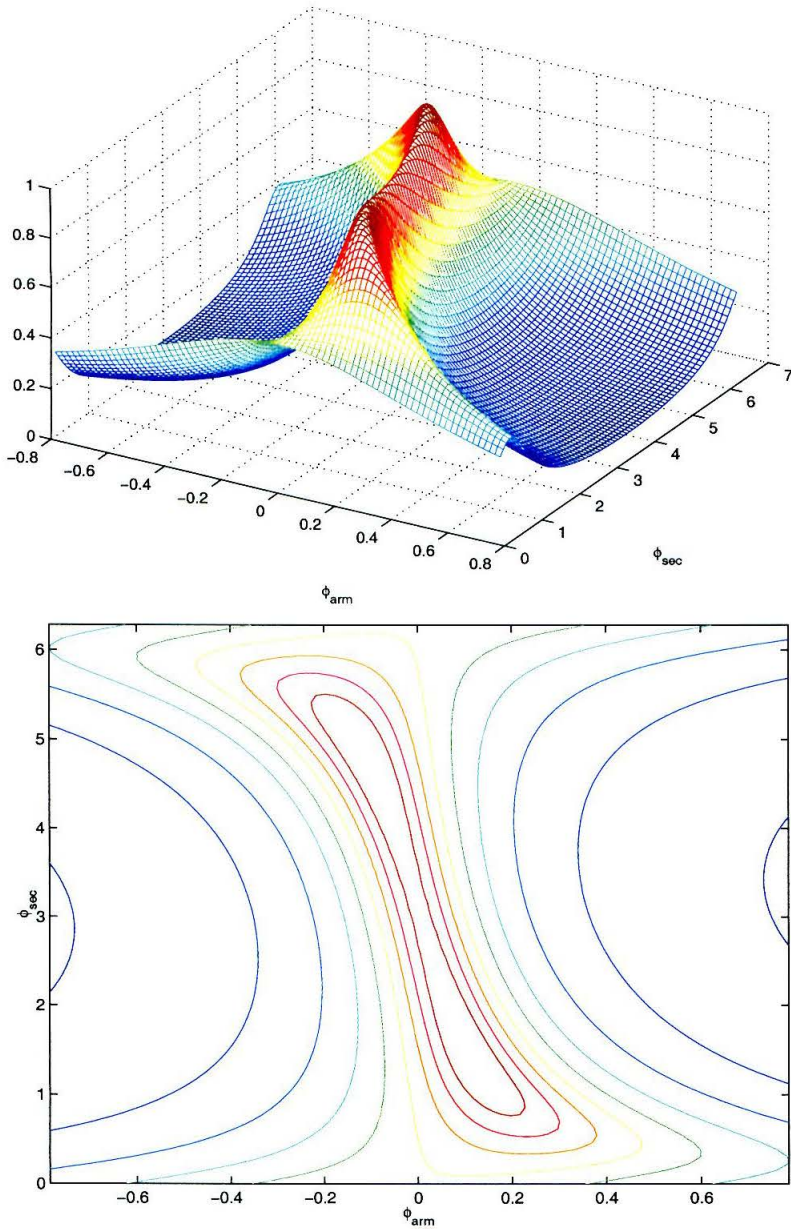


Figure 2.3: Tile plot for a coupled cavity which has the following mirror transmittances: an ETM of 10%, an ITM of 20%, and a SEM of 60%.

highest transmittance does not occur at the point where the cavities are resonant. Rather, it occurs at points where the individual cavities are off-resonant. One way to think about this is that, viewed from the arm cavity, the off-resonance of the signal

cavity induces a phase shift upon reflection. The arm cavity can then be off-resonant itself by an equal and opposite amount, thus restoring the resonance of the coupled cavity. Recalling single cavity physics, the transmittance of a cavity approaches its peak at a point known as “optimal coupling,” when the transmittance of the input mirror matches the losses of the cavity. To a good approximation, this is equivalent to matching the reflectivity of the mirrors. The view from the arm cavity “sees” the reflectivity of the signal cavity change as its phase varies. At some point, it could be expected that an off-resonance reflectivity might match the reflectivity of the end mirror of the arm cavity better than if the signal cavity was exactly on resonance, improving the transmissivity. This method of decomposing a complicated optical configuration, like the three mirror coupled cavity, into a single cavity model is quite useful, and will come up again.

Eq. (2.1) is explicitly a function of frequency. The phases are both related to the frequency by the individual lengths of the cavities.

$$\phi_{arm} = 2\pi f\tau_a \quad (2.3)$$

$$\phi_{sec} = 2\pi f\tau_s + \phi_{dt} \quad (2.4)$$

Clearly, as the frequency is varied, a line is drawn through the ϕ_{arm} - ϕ_{sec} plane whose slope is l_{sec}/l_{arm} and whose y-intercept is ϕ_{dt} . This line picks out the frequency response of the coupled cavity system as the value of the transmissivity along the line. As the detuning phase ϕ_{dt} is microscopically varied, this line moves vertically in the ϕ_{arm} - ϕ_{sec} plane, and the frequency which most efficiently propagates through the coupled cavity system changes. An example of the transmission as a function of frequency is shown in Figure 2.4. RSE is technically the point where $\phi_{dt} = 0$, dual-recycling is the point where $\phi_{dt} = \pi$, and the dotted line is the transmission of the simple arm cavity. The addition of the signal mirror at the RSE point clearly increases the bandwidth over that of the simple arm cavity, where the bandwidth is

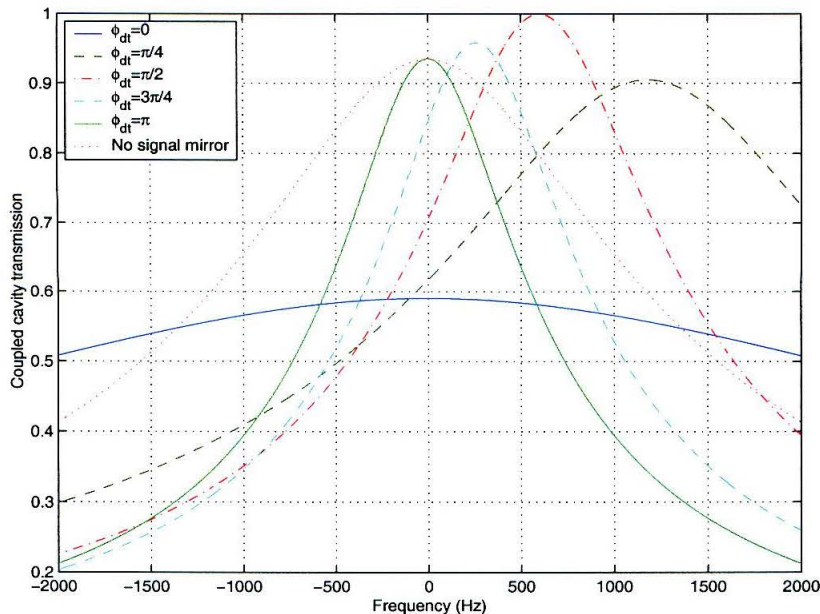


Figure 2.4: Transmissivity of a three mirror coupled cavity as a function of frequency and detuning. The arm length is 4000 m, the signal cavity is 6 m. The optics are the same as in Figure 2.3.

defined as the half width at half maximum.

$$\Delta f_{3 \text{ dB}} = \frac{c}{4l} \frac{1}{\mathcal{F}} \quad (2.5)$$

Appealing to the notion that the signal cavity is a “compound mirror,” when the signal cavity is resonant, its reflectivity is lower than the ITM alone. The effective finesse of the arm cavity is decreased, hence the bandwidth is increased over that of the simple arm cavity. As the signal cavity is tuned off resonance, its reflectivity increases. The effective finesse of the arm increases, hence the bandwidth decreases to the minimum value at the dual-recycling point, which is much narrower than the simple arm cavity alone.

The resonant frequency is a fairly complicated function of the detuning phase. There is a useful simplification that can be made which gives some reasonable approximations. If the length of the signal cavity is very short compared to the length

of the first cavity, then for a range of frequencies which satisfy $f < c/(2l_{arm})$, the phase of the signal cavity $2\pi f\tau_s \ll 2\pi f\tau_a$, so the dynamics of the coupled cavity are dominated by the phase of the arm cavity, and $2\pi f\tau_s \approx 0$. The signal cavity acts like a mirror, called a “compound mirror,” with a complex reflectivity, whose magnitude and phase are a function of the detuning phase only. The phase shift upon reflection from this compound mirror changes the resonant frequency of the coupled cavity system. The frequency response in the short signal cavity limit is now a horizontal line across the diagram, where detuning phase indicates the height of this line. In this sense, the horizontal axis is equivalent to frequency. A subtle feature here: the arm cavities are still resonant at the carrier frequency for light which has come from the laser because of the diagonalization of the interferometer by the dark fringe. This carrier light from the laser doesn’t “know” anything of the existence of the signal mirror or signal cavity. Only light which is differentially generated in the arms will propagate to the signal cavity. The resonant frequency as a function of the detuning phase is easily found by simply looking at the phase of the reflection of the signal cavity as viewed by the arm.

$$f_p = \frac{c}{4\pi l_{arm}} \arctan \left(\frac{T_{itm} r'_{sem} \sin(\phi_{dt})}{r_{itm}(1 + A_{itm} R'_{sem}) - r'_{sem}(2R_{itm} + T_{itm}) \cos(\phi_{dt})} \right) \quad (2.6)$$

Conversely, the required detuning to achieve peak sensitivity at some target frequency f_{tar} is approximated by taking a derivative of the magnitude of Eq. (2.1), and is found to be

$$\phi_{dt_0} = \arctan \left(\frac{T_{itm} \sin(2\pi f_{tar} \tau_a)}{r_{itm}(1 + A_{itm}) - (2R_{itm} + T_{itm}) \cos(2\pi f_{tar} \tau_a)} \right) \quad (2.7)$$

where it’s been assumed that the end mirrors of the arm cavities have unity reflectivity. This detuning phase actually isn’t the detuning which gives a peak frequency at f_{tar} ; it is the detuning that maximizes the amplitude of the transmission function at f_{tar} , which is a subtly different thing. Generally, the height of the transmission peak tends to increase with increasing detuning (see Figure 2.4), so a higher sensitivity at a

particular frequency can be achieved by a slightly larger detuning. This shifts the frequency of best sensitivity to a lower value.

Following the derivation of Mizuno in which the denominator function of Eq. (2.1) is expanded to first order in frequency around the carrier frequency, the true peak frequency and bandwidth for a given detuning and target frequency can be approximated by

$$f_p \simeq f_{tar} + \Im \{E(f_{tar}, \phi_{dt_0})\} / (4\pi l_{arm}/c) \quad (2.8)$$

$$\Delta f_{3dB} \simeq |\Re \{E(f_{tar}, \phi_{dt_0})\}| / (2\pi l_{arm}/c) \quad (2.9)$$

where the function $E(f, \phi)$ is defined

$$E(f, \phi) = 1 - \frac{1 - r'_{sec} r_{itm} e^{-i2\phi}}{r_{itm} e^{-i2\pi f \tau_a} - A_{itm} r'_{sem} e^{-i2\pi f \tau_a + \phi}} \quad (2.10)$$

These approximations work best when the Q is high, that is $f/\Delta f_{3dB} \gg 1$. Figure 2.5 shows the peak frequency and bandwidth as a function of the detuning phase for the same optics in Figure 2.4.

In these cases, the peak frequency is seen to increase from DC to some maximum frequency, at which point the trend reverses and the peak frequency drifts back to DC. The highest peak frequency is found by taking a derivative of Eq. (2.6).²

$$f_{p_{max}} = \frac{c}{4\pi l_{arm}} \arctan \left(\frac{r'_{sem} T_{itm}}{\sqrt{(R_{itm} - A_{itm} R'_{sem})(1 - R_{itm} R'_{sem})}} \right) \quad (2.11)$$

The fact that there is a peak frequency is consequence of the under-coupled nature of the signal cavity. The phase on reflection of an under-coupled cavity starts at zero on resonance, deviates some amount away from zero, then slowly comes back, in the same fashion as in Figure 2.5.

It's interesting to compare the peak frequency to the RSE bandwidth at zero

²More precisely, taking the derivative of the argument of the arctangent. Maximizing f is the same as maximizing $\tan(\pi f \tau_a)$.

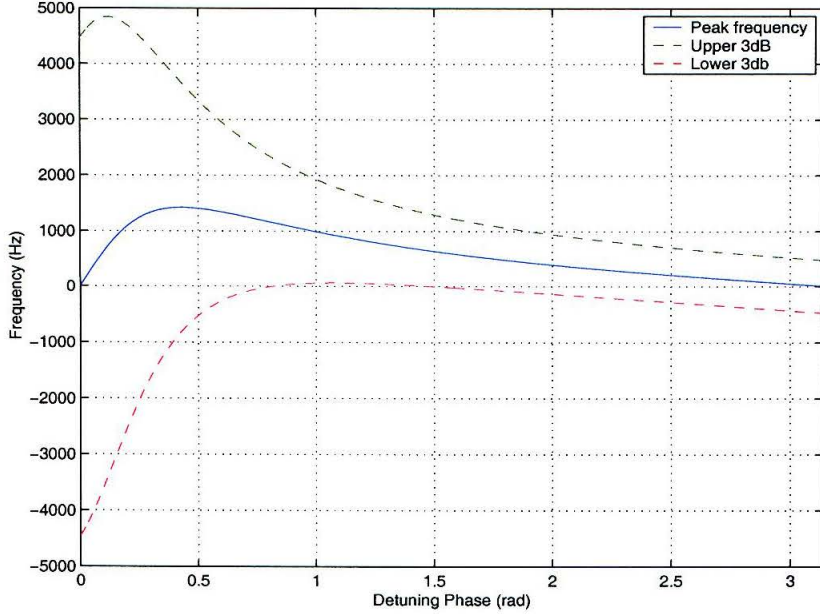


Figure 2.5: Peak frequency and bandwidth as a function of detuning for the mirrors of Figure 2.3.

detuning, f_{bb} .

$$f_{bb} \approx \frac{c}{4\pi l_{arm}} \frac{(1 - r_{itm})(1 + r'_{sem})}{\sqrt{(1 - r_{itm}r'_{sem})(r_{itm} - r'_{sem})}} \quad (2.12)$$

In the limit that the peak frequency is much less than the cavity free spectral range, $f_{pmax} \ll c/(2l_{arm})$, the losses of the ITM are small, $A_{itm} \approx 1$, and the reflectivities of the ITM and signal mirror are fairly close to unity, then the ratio of the maximum peak frequency to the RSE bandwidth can be found to be

$$\frac{f_{pmax}}{f_{bb}} \approx \frac{r'_{sem}}{2} \quad (2.13)$$

This indicates that the highest detunable frequency will always be less than half the bandwidth of RSE. Stated another way, if an interferometer is designed to have its particular RSE bandwidth at some frequency f_{bb} , subsequent detuning of this interferometer cannot access frequencies higher than roughly half this value.

These examples have been somewhat typical of the features of the three mirror

coupled cavity, although the examples have been limited to the case where the signal cavity is short and the signal mirror has a larger transmittance than the ITM.

Over-Coupled Signal Cavity

If the relation between the signal mirror and ITM is reversed, then the signal cavity is over-coupled, and the sign upon reflection is negative. The resonant frequency for differentially generated signals will be not at DC, but at half the cavity free spectral range. The tile plot for the over-coupled signal cavity is shown in Figure 2.6. RSE again corresponds to $\phi_{sec} = 0$ and dual-recycling to $\phi_{sec} = \pi$. In the short cavity limit, varying the detuning phase from RSE to dual-recycling shifts the peak frequency shifts from the far right, at the cavity half free spectral range, across the entire range of frequencies down to DC, which is in the middle, as shown in Figure 2.7. This is also expected due to the over-coupled nature of the signal cavity, for which the phase upon reflection sweeps from $+\pi$ to 0 as the phase of the cavity sweeps from resonance to anti-resonance. This is entirely acceptable if the interferometer is to be designed as a detuned interferometer. The RSE broadband point is not especially usable, since it's centered about roughly 18.75 kHz for arm cavities of 4000 m. However, the maximum peak frequency limitations of Eq. (2.11) obviously don't exist in this case.

One more consequence of having the RSE peak frequency at half the free spectral range is that it tends to be easier to access very narrowband detunings at high frequencies. The bandwidth of the detuning is a function of the reflectivity of the signal cavity. As the signal cavity is detuned away from resonance, the reflectivity rises, narrowing the bandwidth. The amount of detuning to reach a frequency of interest below 1 kHz from the "broadband" frequency of 18.75 kHz is quite large, and typically the signal cavity will be quite anti-resonant. The implication is that the bandwidth of the detuned RSE interferometer will be near its minimum, which can be quite small. For the under-coupled signal cavity, some care must be applied to make the RSE bandwidth f_{bb} much higher than the desired detuning frequencies. Experience with modeling these transfer functions has shown that the range of frequencies when the bandwidth is narrow relative to the peak frequency tends to be about a factor of

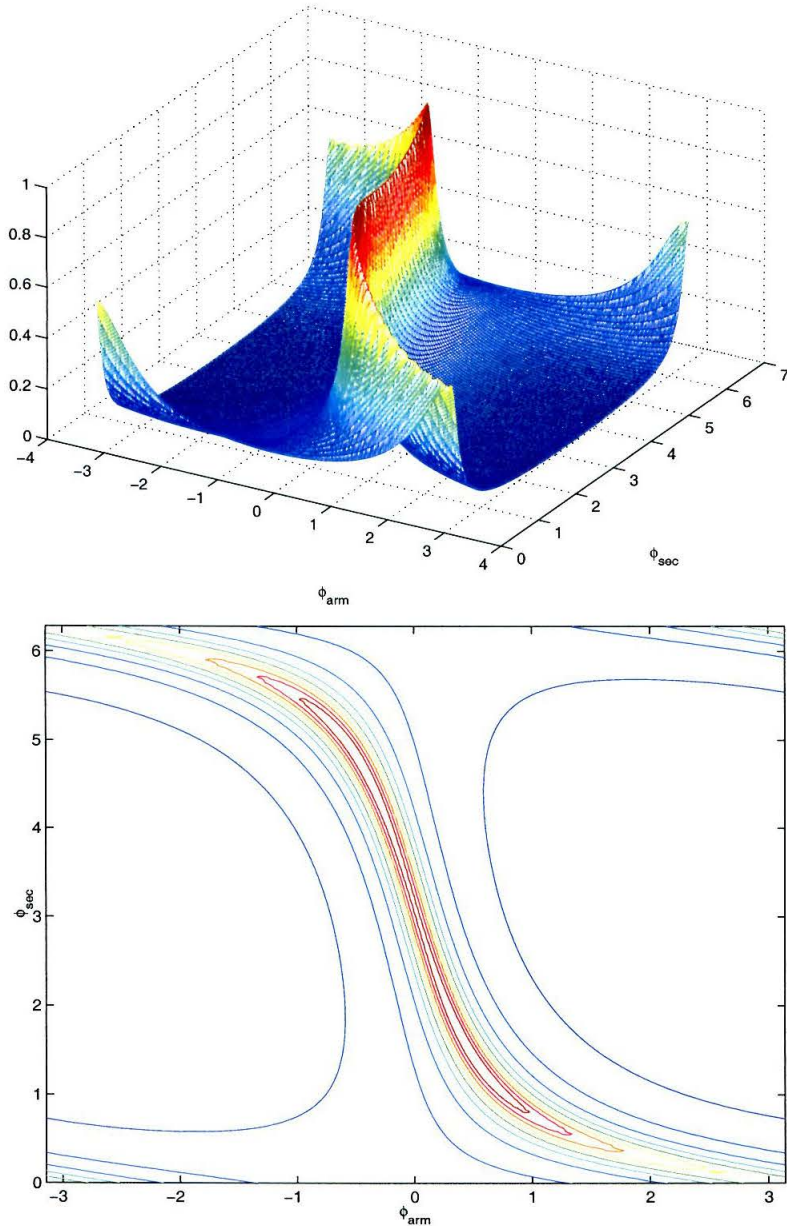


Figure 2.6: This tile plot has an ETM of 10%, a ITM of 60%, and SEM of 20%.

4 or more below the peak frequency f_{pmax} . Hence f_{pmax} would need to be quite high to access high frequency, narrowband detunings.

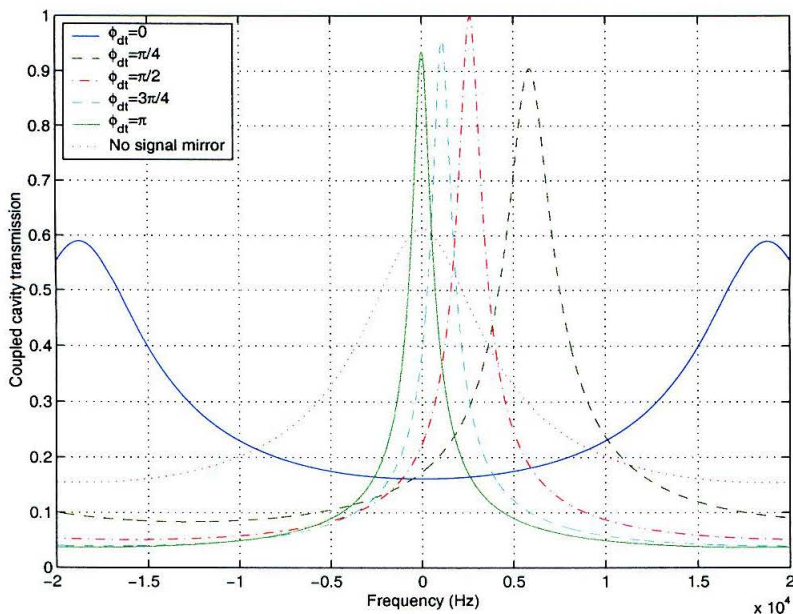


Figure 2.7: Transmissivity of a three mirror coupled cavity as a function of frequency and detuning. The signal cavity is over-coupled. The arm length is 4000 m, the signal cavity is 6 m. The optics are the same as in Figure 2.6.

2.1.2 RSE Transfer Functions

The effect of the gravitational wave on the end mirrors can be interpreted as a tidal force causing the mirrors to move relative to the beamsplitter. The motion of the mirrors phase modulates the fields incident on the mirror, as seen in Figure 2.8. It's assumed for this analysis that the mirror motion is sinusoidal at frequency $\omega = 2\pi f$. If the incident field at the dashed line is given by E_i , then the field returning from

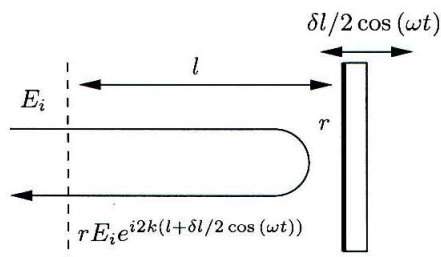


Figure 2.8: The effect of a field incident on a moving mirror.

the mirror is

$$\begin{aligned}
E_r &= r E_i e^{i2k(l+\delta l/2 \cos(\omega t))} \\
&\approx r E_i e^{i2kl} (1 + ik\delta l \cos(\omega t)) \\
&\approx r E_i e^{i2kl} (1 + ik\delta l/2 e^{i\omega t} + ik\delta l/2 e^{-i\omega t})
\end{aligned} \tag{2.14}$$

The approximation is a Taylor series assuming a very small modulation of the mirror position ($\delta l \ll k$). In this limit, the phase modulation of the light adds small signal sidebands on either side of the incident frequency, with amplitudes $irk\delta l/2$ relative to the input field. These occasionally are referred to as “audio sidebands,” since the frequencies of interest tend to be in the 10 to 1000 Hz bandwidth. In terms of strain, the amplitude $\delta l/2 = h l_{arm}$.

Eq. (2.14) shows that the size of the signal sidebands is directly proportional to the amplitude of the light incident on the arm cavity end mirror. This is a product of the light incident on the arm cavity times the amplitude gain of the arm. The light incident on the arm is itself a product of the amplitude gain of the power recycling cavity times the light incident from the laser.

$$E_{arm} = \frac{1}{\sqrt{2}} g_{pr} g_{arm} E_l \tag{2.15}$$

where E_l is the incident amplitude of the laser light on the interferometer. The quantity E_{arm} is the amplitude in a single arm, and the factor of $1/\sqrt{2}$ comes from the beamsplitter.

Thus, signal sidebands are generated which then propagate through this coupled cavity system via Eq. (2.1) at plus and minus the frequency of the input signal. There are several readout methods that can be used. One method uses a homodyne readout, in which some carrier light is also present along with the audio sidebands at the output photodiode. The power measured by the square-law photodiode detector is proportional to

$$P_{PD} \propto |E_0|^2 + 2\Re \{ (E_{-f}^* E_0 + E_0^* E_{+f}) e^{-i2\pi f t} \} \tag{2.16}$$

where it's been assumed that the power in the signal sidebands is negligible. The signal of interest is the second part, and the signal sideband fields can be expressed in terms of Eq. (2.1) and Eq. (2.14), where it has been assumed that the mirror reflectivity $r_{etm} \approx 1$.

$$E_{+f} = ikl_{arm}h |E_{arm}|t_{cc}(+f) \quad (2.17)$$

$$E_{-f} = ikl_{arm}h |E_{arm}|t_{cc}(-f) \quad (2.18)$$

Substitution into the second term of Eq. (2.16) and some algebra gives a measured signal voltage as

$$V_{signal} = Z_{imp} \frac{\eta e}{h\nu_0} 2kl_{arm}h \Re \left\{ \tilde{H}(f) e^{-i2\pi ft} \right\} \quad (2.19)$$

where Z_{imp} is the transimpedance of the photodiode in amps to volts, η is the quantum efficiency of the photodiode in number of electrons to number of photons, e is the electric charge, $h\nu_0$ is the energy of a carrier photon. The transfer function $\tilde{H}(f)$ is defined as

$$\tilde{H}(f) = |E_{arm}| |E_0| (it_{cc}(+f))^* e^{i\phi_0} + (it_{cc}(-f)) e^{-i\phi_0} \quad (2.20)$$

where ϕ_0 is the phase of the carrier field E_0 .

If the phase of the carrier can be chosen arbitrarily, it can be seen that the output *at a particular frequency* can be maximized by choosing the carrier phase such that both terms have the same overall phase. This can be found to be $2\phi_0 = \arg(t_{cc}(+f)) + \arg(t_{cc}(-f)) + \pi$. This carrier phase defines a maximum transfer function

$$|\tilde{H}_{max}(f)| = |E_{arm}| |E_0| (|t_{cc}(-f)| + |t_{cc}(+f)|) \quad (2.21)$$

If $t_{cc}(+f)^* = -t_{cc}(-f)$, then this holds true for all frequencies. This condition is met at resonance (RSE or dual-recycling), but fails for all detunings. Hence, all real transfer functions will be less than or equal to Eq. (2.21). The transfer function $\tilde{H}_{max}(f)$ defines a theoretically ideal transfer function which, in general, is not reached at all frequencies.

The shot noise current spectral density is given by the standard formula

$$S_i(f) = 2e\bar{I} \quad (2.22)$$

where $S_i(f)$ is the one-sided current noise power spectral density and \bar{I} is the average current from the photodiode. The shot noise voltage spectral density includes a factor of the transimpedance. The average current is due to the carrier local oscillator, assuming no other light is present at the dark port.

$$\bar{I} = \frac{|E_0|^2 \eta e}{h\nu_0} \quad (2.23)$$

A little bit of algebra gives the strain spectral density equivalent to shot noise as

$$\tilde{h}(f) = \frac{1}{l_{arm}} \sqrt{\frac{\hbar c \lambda}{2\pi \eta P_{arms}}} \frac{1}{|\tilde{H}'(f)|} \quad (2.24)$$

where the normalized transfer function $\tilde{H}'(f)$ has been defined as

$$\tilde{H}'(f) = t_{cc}^*(-f)(ie^{i\phi_0}) + t_{cc}(+f)(ie^{i\phi_0})^* \quad (2.25)$$

and $P_{arms} = 2|E_{arm}|^2$ is the total power in the arm cavities.

For practical readout schemes, there are two main classes, homodyne and heterodyne detection. If a homodyne scheme such as offset locking is implemented, the carrier “local oscillator” is generated by offsetting the arms from resonance by some very small amount, allowing a small bit of light to leak out the dark port. In this case, the phase of the E_0 field isn’t controllable.³ The frequency f at which the transfer function Eq. (2.25) is maximized is dependent on the phases of the transmission functions.

³The field generated in this fashion is typically orthogonal to the leakage field due to arm mismatch, which is a result to be shown in Chapter 5. In this way, one could *conceivably* control the phase of the local oscillator by changing the amplitude of the offset field, since the local oscillator is then a combination of the (unintentional) mismatch field and the orthogonal offset field. Another possibility is outlined in [35], where output optics are added to shift the phase of the signal in such a way as to cancel the phase of the transmission.

Heterodyne detection, in which RF sidebands present at the dark port are used as local oscillators for the signal sidebands, is discussed in Chapter 3. The measured photovoltage is electronically demodulated at a phase β , and subsequently low-pass filtered. The output is given in Eq. (3.19), where the carrier field E_0 is set to zero for the dark port case (the notation is modified for this context).

$$\tilde{H}(f) \propto -t_{cc}(-f)^*(E_-e^{-i\beta} + E_+e^{i\beta}) + t_{cc}(+f)(E_-e^{-i\beta} + E_+e^{i\beta})^* \quad (2.26)$$

This is similar to Eq. (2.20) with the substitution $E_0 \rightarrow (E_-e^{-i\beta} + E_+e^{i\beta})$.⁴ In this case, the demodulation phase of this local oscillator is controllable, and the signal can be maximized at a particular frequency to match Eq. (2.21). One downside of this technique is that the signal to noise in a heterodyne readout is typically larger than in the homodyne case, such that the achievable signal to noise isn't as good.[36, 37, 38]

Ultimately, the details of a particular readout scheme need to be analyzed properly, which would include the efficiency of the readout and the noise characteristics of the readout as well. However, it's simpler and sufficient in this context of comparison, as well as a first pass at optimization, to utilize an ideal transfer function of Eq. (2.21). Likewise, the ideal case of Eq. (2.24) will be used when referring to a "shot noise limited sensitivity."

2.2 Practical Limitations

The transfer function of the interferometer is actually a function of many parameters. Thus far, the focus has been on the flexibility afforded by signal tuned RSE to the optical designer to optimize the interferometer frequency response, given by the transmission function of Eq. (2.1). This gives a shape of the response, as well as the gain normalized to a unit amplitude signal. The next step is to determine the actual gain achievable, which is a function of the amount of light in the arm cavities. This

⁴It should be noted, however, that the actual magnitude of the measured signal is decreased by a factor of two. This is due to the fact that, in demodulation, the signal at Ω is mixed by Ω , which then splits the signal into two parts, one at DC, which is measured, and one at 2Ω , which is filtered and discarded.

depends on the choice of ITM, upon which the power recycling mirror transmittance depends. Thus, the ITM plays a role both in the stored energy and in the signal tuning.

Optimization of the interferometer's transfer function increases the signal gain, but noise sources such as thermal and seismic noise place fundamental limits on the detector's ability to resolve any such signal. In some cases, especially at lower frequencies, optimization of the transfer function gain may constrain the optical design far more than necessary by gaining sensitivity where thermal or seismic noise would dominate. In this section, thermal and seismic noise will be neglected in order to develop a little intuition about some of the practical limitations to detector design.

2.2.1 Power Recycling

Power recycling is the method used to make the most efficient use of the laser light as possible.[39] When the Fabry-Perot Michelson is thought of as a compound mirror, the concept of power recycling is fairly easy to understand. The carrier is optimally coupled into the interferometer when the transmittance of the power recycling mirror is equal to the losses of the Fabry-Perot Michelson. This also corresponds to the maximum power both stored in the power recycling cavity, and incident on the arms. Hence, the amount of power in the arms is maximized.

One of the freedoms afforded by adding the signal mirror is the ability to store more light in the arm cavities. This tends to increase the energy stored in the interferometer. Without the signal mirror, the only parameter with which to tune the frequency response of the interferometer is the ITM transmittance. This sets the total arm losses, which in turn sets the power recycling gain to one fixed value. However, with the signal mirror, the ability to make the signal bandwidth much broader than the arm cavity bandwidth alone frees up the choices for the arm cavity ITM. Since the largest sources of loss in the interferometer are the anti-reflection (AR) coatings of the ITM substrates and the beamsplitter,⁵ all of which are in the power cavity, the

⁵In the case of sapphire ITMs, the loss associated with substrate absorption is also very high.

total losses can be decreased by reducing the power recycling gain. More light is in the arms as a result, which can be seen in Figure 2.9. This curve is generated using

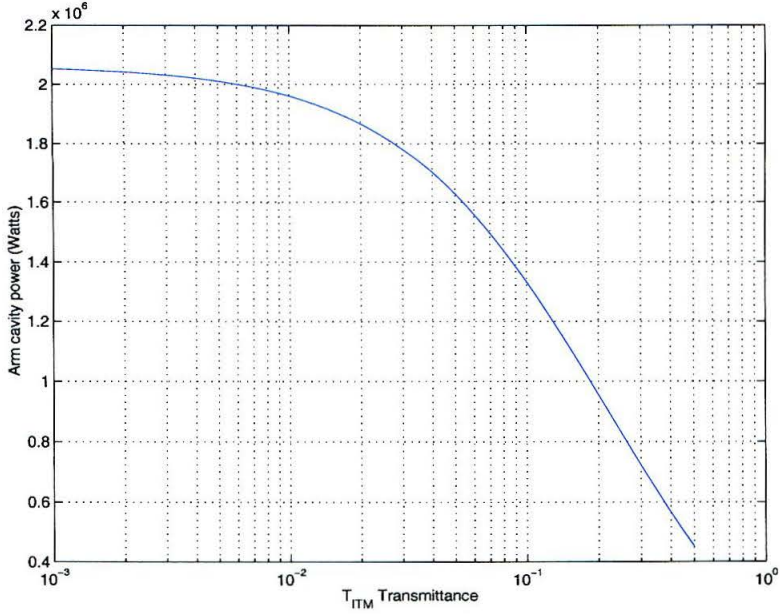


Figure 2.9: Arm cavity power as a function of transmittance. Assumed are average losses of 25 ppm, AR coating losses of 300 ppm, sapphire substrates with 480 ppm loss, and a power mirror matched to 1% carrier reflectance.

Eq. (2.15). The power is the square of this, doubled for the total in both arms.

$$P_{arms} = (g_{pr}g_{arm})^2 P_{inc} \quad (2.27)$$

where P_{inc} is the incident carrier power. Each arm individually has half this amount.

The amplitude gains for the power recycling cavity as well as the arm cavity are given by

$$g_{pr} = \frac{t_{prm}}{1 - r_{prm}r_{Michelson}} \quad (2.28)$$

$$g_{arm} = \frac{t_{itm}}{1 - r_{itm}r_{etm}} \quad (2.29)$$

The reflectivity parameters used are found in the following way. The power cavity

mirror is calculated based on the model of the power recycling cavity as a cavity whose end mirror is the Fabry-Perot Michelson. For the carrier and ideal optics, this is simply the reflectivity of the arm cavities. This reflectivity is then modified by the losses of the substrates and AR coatings in the much the same way as in Eq. (2.2).

$$r_{\text{Michelson}} = r_{\text{cavity}} A_{\text{sub}} A_{\text{ITM}_{\text{AR}}} A_{\text{BS}_{\text{AR}}} \quad (2.30)$$

Given the desired 1% power reflectivity,⁶ the power mirror reflectivity can be calculated as

$$r_{\text{prm}} = -\frac{\sqrt{0.01} + r_{\text{Michelson}} A_{\text{prm}}}{1 + \sqrt{0.01} r_{\text{Michelson}}} \quad (2.31)$$

Figure 2.9 shows the effect of decreasing the transmittance of the ITM, and the effect it has on the power available for gravitational wave signal extraction. Clearly, decreasing the transmittance of the ITM increases the amount of power stored in the arm cavities.

There is one significant effect which has been ignored to this point. Losses have been assumed to be a constant, independent of incident power. In fact, it's well known that those losses heat the mirrors, causing deformations and lensing, which further increases the losses. Two reasons justify ignoring lensing at this point.

First, this non-linear effect is somewhat mitigated by the arm/power coupled cavity.[29] The insensitivity of the carrier to thermal lensing in the power recycling cavity is due to the fact that the resonance of the carrier in the power cavity depends on the resonance in the arms. The arm cavities are over-coupled, which generates a sign flip upon reflection. The power cavity alone has to be an anti-resonant cavity for the carrier, which attains resonance only when the carrier resonates in the arms. When the optics are lensed in the power cavity, they change the spatial mode structure of the cavity. Ordinarily, changing the mode structure of the power cavity would cause more carrier light to be scattered into higher order modes, which effectively are

⁶This number has two purposes. One, some carrier light is needed in reflection to give adequate control signals in the reflection port. Second, the optimal coupling point is not robust to changing losses in the interferometer. Choosing a point slightly on the over-coupled side of optimal coupling balances the need for high power with significant decrease in sensitivity to parameter drift.

losses. The arms, however, are very stable cavities with very little lensing, and they effectively enforce their mode structure on the power cavity, with little regard for the thermal lensing. There is a decrease in power, though, due to the initial coupling of the input light into the interferometer, but the scatter which would occur in the power cavity can't happen because the spatial higher order modes aren't resonant.

Second, LIGO II plans to use some type of thermal compensation on the beam-splitter and ITMs.[12] These take the form of either passive heating rings, which would act to reduce the thermal gradients in the masses, or active heating, in which a CO₂ laser beam is scanned through the volume of the mass, heating it. A Schack-Hartmann wavefront sensing scheme is used to measure the thermal gradients, and feedback is applied to the scan of the beam to smooth them out. While it's not currently known which method would be used, there is enough confidence in at least the passive technique that a factor of 10 reduction in lensing could be achieved.

2.2.2 Transfer Function Limitations

The transfer functions that can be achieved with RSE also are dependent on the ITM transmittance, as well as the beamsplitter and substrate losses, since they form the effective signal mirror reflectivity and transmissivity, seen in Eq. (2.2). The effect of the losses in the signal cavity can be quite detrimental. Referring back to Eq. (2.1), if the approximation $r_{itm}^2 \approx A_{itm} = r_{itm}^2 + t_{itm}^2$ is made for ITMs of low transmittance, then the transmissivity can be factored as follows.

$$t_{cc}(f) = \frac{t_{itm}e^{-i2\pi f\tau_a/2}}{1 - r_{itm}r_{etm}e^{-i2\pi f\tau_a}} \frac{t'_{sem}e^{-i(2\pi f\tau_s + \phi_{dt})/2}}{1 - r_{itm}r'_{sem}e^{-i(2\pi f\tau_s + \phi_{dt})}} \quad (2.32)$$

This shows that the transmissivity is akin to a product of the individual arm and signal cavities. Examining the second term in the product of Eq. (2.32), if the ITM has a very low transmittance, as suggested by the previous section, then $r_{itm} \approx 1$ for this term. The signal half of the transmissivity is given (on resonance) by

$$t'_{sec} = \frac{t'_{sem}}{1 - r'_{sem}} \quad (2.33)$$

This is not the transmissivity of a cavity, but rather the transmissivity from inside the cavity. Figure 2.10 shows this evaluated for the case in which the losses of the substrates and AR coatings are included (roughly 1100 ppm), and case in which they're not. For signal mirror transmittances below 1%, the losses dominate the

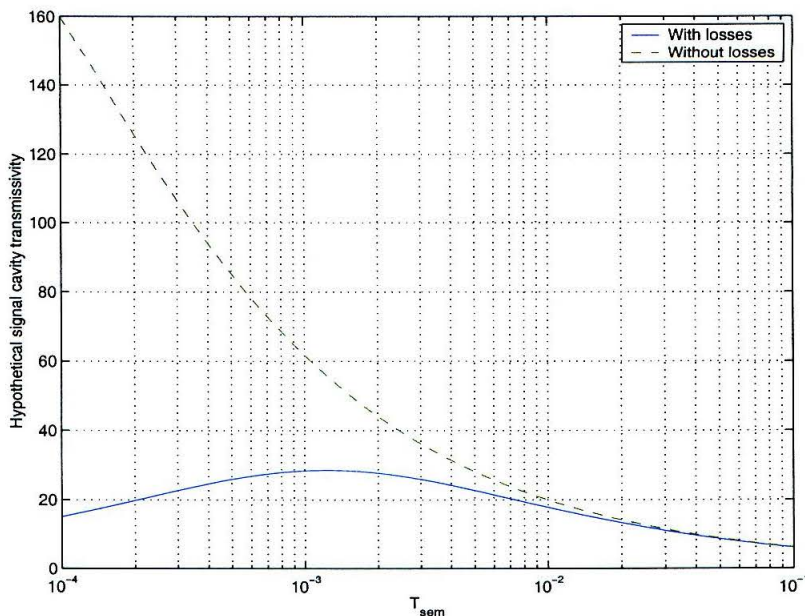


Figure 2.10: The effect of internal losses on the signal cavity’s transmissivity for the “idealized” case of Eq. (2.33). This is the transmissivity from *inside* the signal cavity, hence the values $\gg 1$.

signal transmittance. Similar to the way in which losses in the power cavity decrease the amount of light power stored in the interferometer, losses in the signal cavity decrease the amplitude of the signal sidebands as they propagate to the dark port photodiode. In both cases, this effect is minimized by power or signal mirrors of higher transmittance. In the case of the power mirror, this is done by using an ITM of low transmittance. The signal mirror, however, needs to be chosen by astrophysical considerations, although Figure 2.10 shows that it would be preferable to keep this value $T_{sem} \gtrsim 1\%$ when the ITM transmittance is low. On the other hand, if the transmittance of the ITM is increased, the effect of the losses in the signal cavity decreases. A proper optimization would find a balance of these two effects.

2.2.3 Implications

The two preceding sections suggest that T_{sem} should be high, and T_{itm} should be low. Of course, a proper numerical optimization should be done for whatever type of signal the interferometer is designed to detect, and the effects of loss will naturally be built into the optimization routine. However, it's worthwhile to try and draw some conclusions about the result of these effects and how they might impact the range of optics that might reasonably be used, given the intuitive understanding of this interferometer.

In the case that the desired detector bandwidth is wide, for both detuned and broadband operation, the reflectivity of the signal cavity must be relatively low. Assume a broadband bandwidth of 300 Hz. The free spectral range is about 37.5 kHz for 4 km arms, so the finesse of the arm cavity for signals would need to be about 65. This implies

$$65 \approx \frac{\pi}{1 - r_{sec}} \quad (2.34)$$

$$r_{sec} \approx 95\% \quad (2.35)$$

Figure 2.11 shows the signal cavity reflectivity (on resonance) for an ITM transmittance of $T_{itm} = 0.01\%$, $T_{itm} = 0.1\%$, and $T_{itm} = 1.0\%$, as a function of the signal mirror transmittance. For a reflectivity of 95% and $T_{itm} = 0.1\%$, the signal mirror can have a transmittance around 4%, which is an acceptable number for the losses expected.

An interesting feature of Figure 2.11 is that the functional shape of the signal cavity reflectivity remains the same for different ITM transmittances – only the position moves back and forth. It can be concluded, then, that in order to maintain the same signal cavity reflectivity, and hence the same signal bandwidth, a decrease in the ITM transmittance must be accompanied by a similar fractional decrease in the signal mirror transmittance. Using the example in the previous paragraph, if T_{itm} is reduced by an order of magnitude to 0.01%, the signal mirror transmittance which

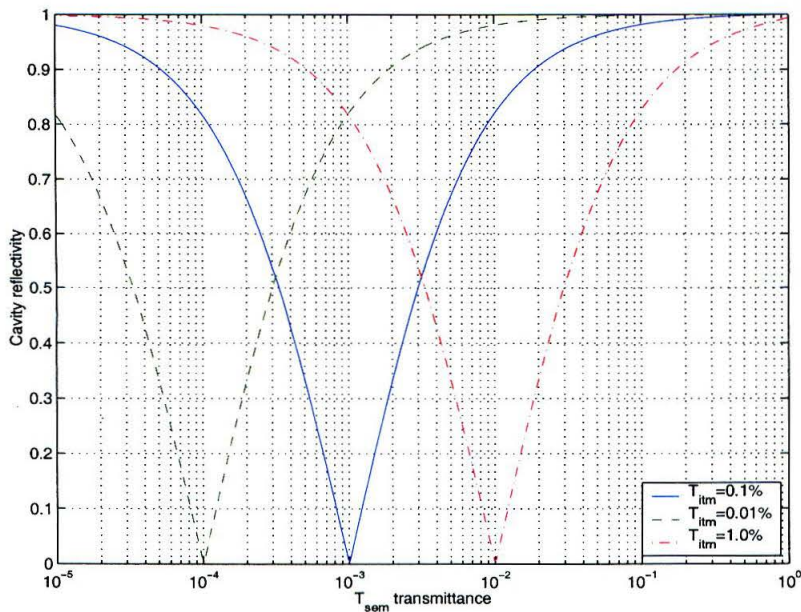


Figure 2.11: Signal cavity reflectivity as a function of signal mirror transmittance. Three ITMs are modeled: $T_{itm} = 0.01\%$, $T_{itm} = 0.1\%$, and $T_{itm} = 1.0\%$.

gives 95% reflectivity likewise drops an order of magnitude to about 0.4%. The noteworthy result of this is that Figure 2.10 indicates a decrease in the signal of about 30% due to signal cavity losses, but Figure 2.9 doesn't indicate a similar increase in the power stored in the arms. Overall, the sensitivity will decrease with increasing arm cavity finesse.

The broadband RSE interferometer is considered as an example of the signal and arm cavity loss tradeoff. Non-power recycled RSE will be compared to the case where the power recycled RSE interferometer is optimized for greatest sensitivity. This comparison addresses an early promise of RSE, which suggested that it may be possible to do away with the power recycling mirror altogether. In both cases, the optical parameters are chosen to allow 1% of the carrier light to return to the laser, and the signal mirror is chosen such that the internal thermal noise is equal to the shot noise at the 3 dB point of the shot noise sensitivity. The ITM substrates are assumed to be sapphire, with 500 ppm loss, and the AR coating loss of the ITMs and beamsplitter is assumed to be 300 ppm each. There is some uncertainty regarding

the coating losses of the arm cavity optics – numbers between 10 and 25 ppm have been quoted.[40] The 10 ppm case is summarized in Table 2.1. Clearly, the sensitivity

	With PR	Without PR
T_{itm}	1.0%	55 ppm
T_{sem}	42%	0.20%
T_{prm}	1.7%	None
Coating losses	10 ppm	10 ppm
DC sensitivity ($h/\sqrt{\text{Hz}}$)	0.89×10^{-24}	1.40×10^{-24}

Table 2.1: Comparison between broadband RSE with and without power recycling. 10 ppm coating losses are assumed.

without power recycling suffers considerably due to signal cavity losses, being about a factor of 1.6 times less than power recycled RSE. Cubing this factor indicates that the volume of space that the interferometer can probe is nearly a factor of four greater with power recycling.

This factor, however, is very sensitive to the actual losses of the arm cavities, as demonstrated by the case when the coating losses are 25 ppm. These results are summarized in Table 2.2. The difference between RSE with and without power

	With PR	Without PR
T_{itm}	1.0%	75 ppm
T_{sem}	50%	0.37%
T_{prm}	3.1%	None
Coating losses	25 ppm	25 ppm
DC sensitivity ($h/\sqrt{\text{Hz}}$)	1.08×10^{-24}	1.22×10^{-24}

Table 2.2: Comparison between broadband RSE with and without power recycling. 25 ppm coating losses are assumed.

recycling isn't nearly so pronounced, due to the increase in arm cavity losses. The volume of space probed is 1.4 times greater with power recycling, which isn't to be sneezed at, but it certainly isn't as compelling as the factor of four difference with the 10 ppm coating losses. Clearly, better knowledge of the coating losses is needed. If it's expected that the optics will be very good, power recycling becomes a necessity.

For high frequency response, both the under-coupled and over-coupled signal cavities are considered. It's first noted that the tendencies might favor an under-coupled signal cavity, since the effects outlined suggest such an arrangement of mirrors (T_{sem} high, T_{itm} low). However, in the under-coupled case, Eq. (2.13) shows that all detuned frequencies come below the broadband RSE bandwidth frequency. High detuning frequencies imply a higher RSE bandwidth at resonance. For sensitivity at 1 kHz, a 5 kHz RSE bandwidth will probably be necessary, implying an effective finesse of the arm/signal cavity of about 4. The signal cavity reflectivity which permits this wide a bandwidth is about 20%. To keep the signal mirror above 1%, the ITM transmittance must be at least 0.7%. At this point, the stored power isn't degraded much. However, modeling such configurations has shown that the high frequency bandwidths in these cases still tend to be fairly large.

The other option is the over-coupled signal cavity, in which case T_{sem} is low and T_{itm} is high. As the transmittance of the ITM increases, the losses of the carrier increase, as in Figure 2.9, due to the re-tuning of the power mirror. However, the effect of the losses in the signal cavity decreases, because its finesse is decreasing. This particular case, as noted earlier, is more amenable to high frequency response, due to the fact that the peak frequency at RSE is already at half the arm free spectral range. Compared to the under-coupled case, the over-coupled signal cavity probably will generate better high frequency signal response.

2.3 Detector Optimization for RSE

The optimization problem is quite complicated – many factors influence the detector sensitivity. In addition, as seen, the choice of ITM does not act independently, since it can both increase the stored energy of the detector, and yet cause excessive signal losses when the signal mirror is chosen for a specific astrophysical reason. Thus using the sensitivity theorem as an optimizing strategy doesn't always work. As a result, the only reliable method of optimization is numerical, in which as many relevant effects are accounted for as possible. Some work has already been done regarding

“acceptable” ITM parameters. Ken Strain has suggested that a reasonable range for the ITM transmittance would be roughly 0.1% to a couple percent.[41] Below 0.1%, technical difficulties with the implementation of such high finesse cavities come into play. Above a few percent, thermal lensing and non-linear effects can dominate.⁷

Different strategies for optimization are used depending on the type of gravitational wave source being considered. This section will examine two types of sources. First, pulsars with a bump or wobble are strongly periodic, and are good candidates for an interferometer with a very narrow bandwidth. Second, a pair of massive compact objects, such as two neutron stars, two black holes, or a black hole-neutron star system are expected to radiate gravitational radiation over a wide band of frequencies as their orbits decay and the objects coalesce. In this case, the interferometer’s frequency response is optimized via a convolution with the expected source spectrum over a reasonable range of ITM and SEM optics, as well as detunings.

2.3.1 Narrowband Response

After the birth of a neutron star from a supernova event, the crust begins to cool and crystallize. The neutron star will maintain most of the angular momentum of the progenitor star, and so typically will be spinning. The solid crust will settle down to the typical oblate axisymmetric spheroid with some poloidal ellipticity, ϵ_p . At this point, two possibilities arise.[42] First, if the principle axis deviates from the spin axis by a “wobble angle” θ_w , then waves can be generated at a frequency of $f_{rot} + f_{prec}$, where f_{rot} is the rotational frequency, and f_{prec} is the precessional frequency of the wobble. Second, the crust may solidify with some slight deviation from axisymmetry about the principle axis characterized by an equatorial ellipticity e_e , which would generate waves at $2f_{rot}$. The strength of such waves is estimated to be

$$h \sim 6 \times 10^{-25} \left(\frac{f_{rot}}{500 \text{ Hz}} \right)^2 \left(\frac{1 \text{ kpc}}{r} \right) \left(\frac{\epsilon_e \text{ or } \theta_w \epsilon_p}{10^{-6}} \right) \quad (2.36)$$

⁷This is somewhat ITM material-dependent. For example, fused silica has such low absorption that the coating losses in the arm cavities dominate the high finesse arm cavity interferometers. Sapphire, on the other hand, has very high absorption, so coating losses are insignificant, but the lensing is about an order of magnitude less.

Although this is a tiny signal, its strong periodicity helps. Integration of the signal for time τ will increase the effective signal strength relative to the noise in the detector by $\sqrt{n} = \sqrt{f\tau}$ or the square root of the number of cycles. A third of a year at 1 kHz would increase the effective signal by about 10^5 . This is clearly the type of source which lends itself to a search with a narrowband signal tuned interferometer, where the detector's response is significantly enhanced at a frequency where the thermal noise is small. For example, at 1 kHz, sapphire optics limit the sensitivity to $3 \times 10^{-25}/\sqrt{\text{Hz}}$. An optimization can be done, initially neglecting thermal noise. After optimization, the thermal noise can be verified to be less than the shot noise, or else the bandwidth can be broadened until the shot noise is not dominated by thermal noise.

A Matlab code was written which made a lattice of pairs of ITM and SEM transmittances. For each particular pair, the detuning was determined by Eq. (2.7), the power in the arms is calculated using Eq. (2.27), and this is multiplied with the value of the transfer function evaluated at the target frequency using Eq. (2.1). The resulting matrix of values is normalized by the largest value, and the corresponding pair of ITM/SEM transmittances are found.

An example is shown in the Figure 2.12, for an optimization at 1 kHz. Table 2.3 gives the parameters for best sensitivity. This particular optimization has a huge

T_{itm}	14.0%
T_{sem}	0.25%
T_{prm}	0.50%
Power Recycling Gain	260
Δf_3 dB	6 Hz

Table 2.3: Optical parameters for optimized shot noise sensitivity at 1 kHz for sapphire optics.

power recycling gain, and a correspondingly high ITM transmittance. As mentioned before, non-linear effects will probably generate larger losses that aren't modeled here. An upper bound of ITM is suggested to be a few percent, so a cutoff is placed at $T_{itm} = 2\%$, and the solution by the code is given in Table 2.4.

The shot noise limited sensitivities for these two cases are shown in Figure 2.13.

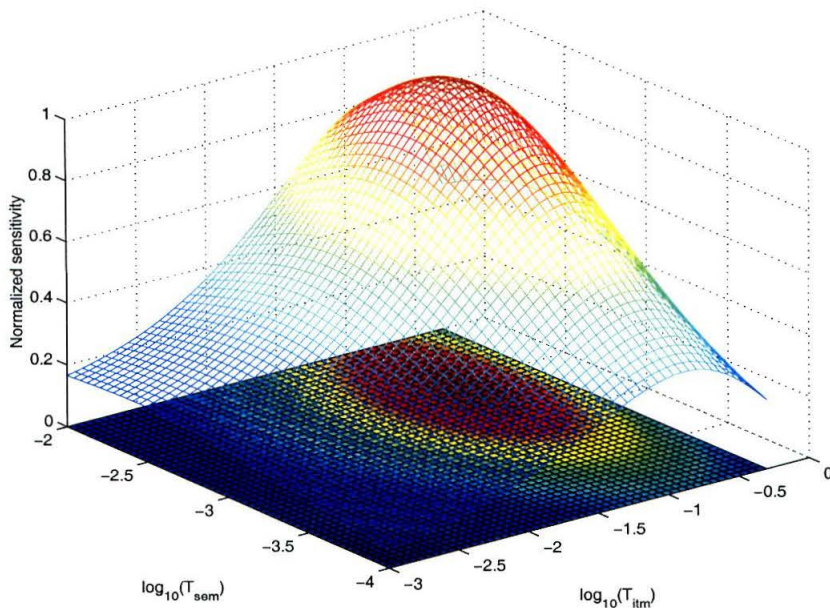


Figure 2.12: Optimization for 1 kHz shot noise sensitivity. 25 ppm losses are assumed per coating, 300 ppm losses are assumed for AR coatings, and 480 ppm losses are assumed for (sapphire) substrates.

T_{itm}	2.0%
T_{sem}	0.25%
T_{prm}	1.7%
Power Recycling Gain	70
Δf_3 dB	40 Hz

Table 2.4: 1 kHz optimization parameters given maximum ITM transmittance of 2%.

It is noted that the thermal noise in both cases is less than the shot noise. Furthermore, this clearly is a case when the losses of the signal cavity strongly dominate the frequency response, forcing a much higher ITM transmittance than would be indicated by maximizing energy storage alone. By Figure 2.9, the original solution would sacrifice a factor of 2 or more in stored energy.

The optimum bandwidth for such a periodic source would be very small (Krolak, *et al.*, suggests about 3 Hz [43]). However, the ignorance about the population of such sources is extremely high. Thus, it is not likely that a known source at a

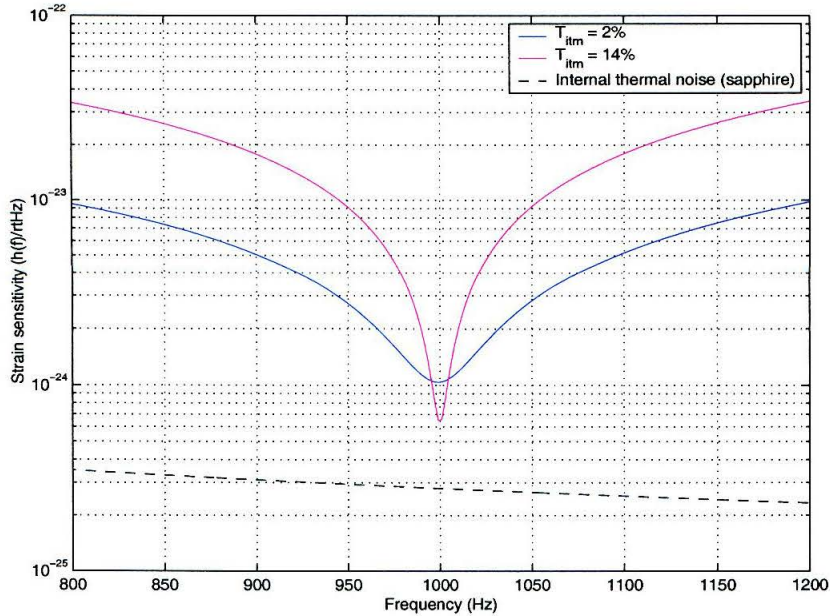


Figure 2.13: 1 kHz shot noise limited sensitivity for the two cases discussed in this section.

particular frequency would be targeted. A suggested search would instead broaden the bandwidth to 50 Hz, and step through a wide range of frequencies in week-long searches.[12] This is also consistent with the 2% ITM solution.

2.3.2 Optimized Broadband

The idea of an “optimized broadband” detector is to use the ability of RSE to gain extra sensitivity over a sizeable bandwidth at higher frequencies. The low frequency limiting noise sources, seismic and thermal, effectively place limits that constrain gravitational wave observation to frequencies above 10 Hz. However, a broadband detector has its greatest sensitivity at DC, which wastes the maximum sensitivity from 0 to 10 Hz. It’s conceivable that RSE would allow the design of a detuned interferometer which has a fairly broad linewidth, and a peak frequency somewhere in the mid 100’s of Hz. This would allow the shot noise to be tailored such that more of the available sensitivity at higher frequencies liberated by thermal noise would be

accessible.

Probably the most commonly cited wideband source of gravitational waves is the neutron star-neutron star binary coalescence. This is a broadband source which sweeps through most if not all of the bandwidth of the detector. The lowest order approximation to the spectrum of this waveform is given by [44]

$$\tilde{h}(f) = \frac{Q}{D} \mathcal{M}^{5/6} f^{-7/6} \exp[i\Psi(f)] \quad (2.37)$$

The various quantities are defined as follows. Q is a geometrical factor relating the physical orientation of the detector relative to the direction and inclination of the source, as well as to the polarization of the wave. D is the distance to the source. \mathcal{M} is the “chirp mass,” and Ψ are

$$\mathcal{M} = \frac{(M_1 M_2)^{3/5}}{(M_1 + M_2)^{1/5}} \quad (2.38)$$

$$\Psi(f) = 2\pi f t_c - \phi_c - \frac{\pi}{4} + \frac{3}{4} (8\pi \mathcal{M} f)^{-5/3} \quad (2.39)$$

The M_i 's are the masses of the two objects, ϕ_c and t_c refer to the formal collision phase and time when the radius of the inspiral goes to zero.

The integrated signal to noise of a source such as this up to some cut-off frequency f is given by

$$(S/N)^2(f) \equiv 4 \int_0^f \frac{|\tilde{h}(f')|^2}{S_n(f')} df' \quad (2.40)$$

$$\propto \int_0^f \frac{f'^{-7/3}}{S_n(f')} df' \quad (2.41)$$

The spectral density of the noise, $S_n(f)$, is from the contributions due to the seismic, thermal, and optical noise equivalent to strain, summed in quadrature. The optical noise is where the RSE transfer function comes in, as in Eq. (2.24).

A Matlab code, *bench.m* (copyright), has been developed by Sam Finn to optimize the SNR given by Eq. (2.40) over a set of optical parameters.[45, 46] The output is a figure of merit, or “score,” which is a distance r_0 , such that the expected number of

sources the interferometer would see with a SNR greater than 8 is the volume $(4/3)\pi r_0^3$ times the neutron star binary inspiral rate density.⁸ Obviously the parameters which maximize this distance are best suited for detection of this type of source.

Ken Strain at Glasgow University has done this optimization for an RSE interferometer with sapphire optics.[47] Certain issues, such as the non-linear thermal sources of loss in the interferometer were handled by setting limits on allowable powers, which was done partly with the aid of another Matlab code called *Melody*,[48] and partly intuitively based on lengthy experience. The result is the set of parameters in Table 2.5. The output of *bench.m* is shown in Figure 2.14. The score that *bench.m* gives

T_{itm}	0.5%
T_{sem}	5.0%
T_{prm}	8.0%
Detuning	0.09 rad (round trip)
Power Recycling Gain	17

Table 2.5: Parameters for an optimized broadband interferometer.

for this configuration is $r_0 = 202$ Mpc.

For comparison, a power recycled Fabry-Perot Michelson (PRFPM) was also analyzed, assuming the same input power. The ITM and signal mirrors were varied to optimize the score for each. The PRFPM optimizes to a score of 158 Mpc, so an optimized broadband interferometer samples roughly 2.4 times more volume than without a signal mirror. The parameters for this interferometer are in Table 2.6. The power recycling factor is quite high, so the score reported is probably a bit optimistic, due to non-linear losses.

T_{itm}	5.0%
T_{sem}	None
T_{prm}	1.0%
Power Recycling Gain	159

Table 2.6: Parameters for a power recycled Fabry-Perot Michelson interferometer.

⁸In the comments included with *bench.m*, Finn indicates this score is not rigorous, but meant mostly as a means to compare different optical configurations.

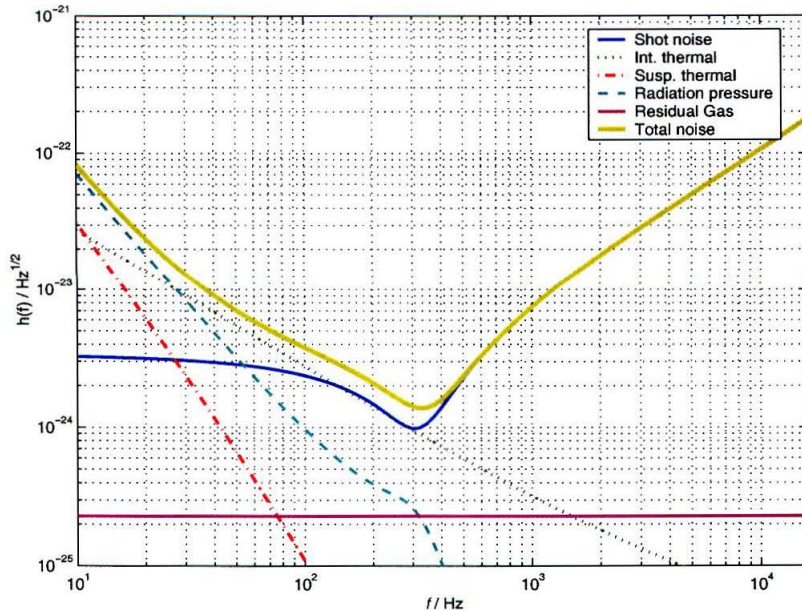


Figure 2.14: Contributions to the final optimized broadband sensitivity.

Similarly, *bench.m* was used to maximize the binary inspiral signal to noise for a broadband RSE ($\phi_{dt} = 0$) interferometer. The resulting score wasn't much better than the PRFPM configuration, at 169 Mpc. These values are in Table 2.7 below. The optimized broadband interferometer samples about a 1.7 times greater volume

T_{itm}	1.0%
T_{sem}	30%
T_{prm}	3.8%
Detuning	0 rad (broadband)
Power Recycling Gain	33

Table 2.7: Parameters for an RSE broadband interferometer.

of space, which is still a significant amount, considering the expected rarity of these events.

Chapter 3

Signal Extraction

The addition of a mirror at the anti-symmetric port gives a great deal more freedom to the optical designer to optimize the sensitivity of the detector to various source signals. However, it also complicates the interferometer. As with the other mirrors, the position of the signal mirror is crucial, and so a control system must be developed to monitor and maintain its position. Unfortunately, this is not a simple matter, as this new degree of freedom is not decoupled from the other degrees of freedom. Even more taxing is the fact that, when the interferometer is detuned, the signals needed to control the various degrees of freedom become even more cross-coupled, and a great deal more care must be exercised in establishing the control system.

Section 3.1 will develop the mathematical model of the signal extraction technique, which utilizes an optical heterodyne. In addition, this technique will be conceptually described in terms of phasor diagrams, which are useful for developing some intuition for how signals are generated. Section 3.2 will then discuss some of the issues which impact the design of the interferometer in order to implement a control system for the five degree of freedom RSE interferometer. This is in contrast to Chapter 2, in which the interferometer design was strictly motivated by astrophysical considerations. A specific proposal for a signal extraction scheme and its implementation is discussed. In Section 3.3, analytical formulas for the signal extraction scheme are derived, and in Section 3.4, these formulas are applied to design control systems for the interferometers designed in Section 2.3.

3.1 Optically Heterodyned Signals

The technique of using an optical heterodyne in making interferometric measurements is quite common. The description here largely follows the thesis of Martin Regehr,

although a slightly more general approach is taken.[32]

A carrier in the interferometer has some signal impressed upon it, usually by some modulation of its amplitude or phase. At the detection photodiodes, the carrier is “mixed” with a local oscillator, usually a radio frequency (RF) modulated sideband of the carrier. This allows the measurement of the signal to occur at the frequency of the RF modulated sideband, where the noise of the laser light should be shot noise limited, and where the noise of the front end electronics should be low. Power fluctuations at the modulation frequency, which are the measurable quantities, are then solely due to signals of interest, and are not contaminated by the intensity noise of the carrier.[15] It’s also of note that an optical heterodyne signal extraction provides gain to the signal by the amplitude of the local oscillator.[25] This controllable gain can be used to enhance the signal relative to the various non-fundamental noise sources of the measurement, such as electronic noise of the photo-detection process, or optical noise due to the presence of “junk” light at the photodiode. Another way to view this is that the input referred noise is improved by providing more gain at an earlier stage. This section will go over the fundamentals of the optical heterodyne techniques used for gravitational wave detection.

In a general description, two electric fields are separated by the modulation frequency, Ω . These two fields are incident on the interferometer, which can be thought of as a black-box, linear operator which propagates the fields to the detection photodiodes. The “transmission functions” will describe this propagation. These are complex, frequency dependent numbers which characterize the gains of the transmission as well as the phase shifts involved. It is assumed that they depend only on the reflectivities and transmissivities of the optics, as well as the optical path length propagation phases. Higher order transverse spatial modes are ignored. The field incident on the photodiode is described as

$$E_{PD} = (E_1 + E_2 e^{i\Omega t}) e^{i\omega t} \quad (3.1)$$

where ω represents the frequency of the laser light. The power measured by the

photodiode is proportional to

$$|E_{PD}|^2 = |E_1|^2 + |E_2|^2 + 2\Re \{E_1 E_2^* e^{i\Omega t}\} \quad (3.2)$$

This measured power is converted to a voltage, which is subsequently electronically demodulated in a mixer at Ω . This is equivalent to multiplying Eq. (3.2) by a square wave at Ω with unity amplitude, and a phase known as the “demodulation phase.” A square wave is spectrally comprised of a fundamental frequency at Ω , and many weaker odd harmonics. Multiplication with Eq. (3.2) generates frequency components at sums and differences of the spectral components involved. This mixer output is low-pass filtered at a frequency $\omega_p \ll \Omega$, which removes all high frequency components, leaving only the term proportional to $\Re \{E_1 E_2^*\}$.

The most common application of this technique uses phase modulation of the input light, which generates frequency components at plus and minus the modulation frequency Ω . The amount of modulation placed on the input light is typically small, so the approximation of sidebands to first order is acceptable. The field incident on the interferometer is written as

$$E_i = E_l (J_0(\Gamma) + iJ_1(\Gamma)e^{i\Omega t} + iJ_1(\Gamma)e^{-i\Omega t})e^{i\omega t} \quad (3.3)$$

where E_l is the amplitude of the light from the laser, the J_i 's are Bessel functions of the first kind, and Γ is the modulation depth. The measured power at the photodiode is proportional to

$$|E_{PD}|^2 = |E_0|^2 + |E_+|^2 + |E_-|^2 + 2\Re\{(E_-^* E_0 + E_0^* E_+)e^{i\Omega t}\} + 2\Re\{E_-^* E_+ e^{i2\Omega t}\} \quad (3.4)$$

The fields incident on the photodiode are defined as

$$\begin{aligned} E_0 &= t_0 J_0(\Gamma) E_l \\ E_+ &= t_+ i J_1(\Gamma) E_l \\ E_- &= t_- i J_1(\Gamma) E_l \end{aligned} \quad (3.5)$$

The t_i 's are the transmission functions from the input of the interferometer to the photodiode. The additional component at 2Ω doesn't affect the signal extraction process. Multiplying this by a square wave at Ω generates frequency components at Ω and higher, which are subsequently removed by the low-pass filter. Generally, though, if a complicated spectrum is incident on the photodiode, some care should be taken to make sure all inter-modulation products are accounted for when deriving the signals.

3.1.1 DC Signal

The process of mixing and low pass filtering can be mathematically described as a product with a cosine at the demodulation frequency Ω with phase β , which is then averaged over period T , equal to the period of the modulation.[32]

$$V_{out}(t) = \frac{1}{T} \int_{t-T}^t |E_{PD}|^2 \cos(\Omega t' + \beta) dt' \quad (3.6)$$

$$= \Re \{ E_1^* E_2 e^{-i\beta} \} \quad (3.7)$$

This is assuming the detected power of Eq. (3.2), from which it can be seen that a factor of 2 in the signal has been lost. This is because the multiplication at Ω down-converts the half signal to DC, but also up-converts half the signal to 2Ω , where it's lost in the low pass filter.

Some care must be taken in extending this to the phase modulated case, where there are two RF sidebands. Eq. (3.7) assumes that E_1 is at a lower frequency than E_2 which has consequences on the sign of the demodulation phase. If E_1 were at a higher frequency, the demodulation phase would have the opposite sign in the exponential. The demodulated signal for phase modulated input light of Eq. (3.4) is

$$V_{out}(t) = \Re \{ E_-^* E_0 e^{-i\beta} + E_0^* E_+ e^{-i\beta} \} \quad (3.8)$$

$$= \Re \{ E_0 (E_- e^{i\beta} + E_+ e^{-i\beta})^* \} \quad (3.9)$$

The demodulation phase $\beta = 0$ is usually referred to as the “inphase” demodulation, and $\beta = \pi/2$ is the “quadrature” demodulation. The signal at a specific photodiode at a specific demodulation phase will be referred to as a “signal port.”

Signal Sensitivity

Eq. (3.7) is proportional to the measured voltage as the fields evolve due to the motion of the mirrors in the interferometer. When the interferometer is locked, the deviation away from a nominal DC value (typically 0), due to the fluctuation in a degree of freedom, will be small. A Taylor series expansion around the lock point indicates that the first derivative gives the “gain” of the signal relative to the degree of freedom with which the derivative is taken. A matrix, known as the “matrix of discriminants,” can be formed which gives the derivatives at each signal port with respect to every degree of freedom. The photodiode will be referred to by the letter of the transmission function which propagates the light from the input to the photodiode. The matrix element at the photodiode which has a transmission function “ t ” for the j th degree of freedom is given by

$$M_{t,j} = |E_l|^2 a_1 a_2 \Im \left\{ \frac{\partial t_1}{\partial \phi_j} t_2^* e^{i\beta t} + t_1 \frac{\partial t_2^*}{\partial \phi_j} e^{i\beta t} \right\} \quad (3.10)$$

It should be noted at this time that there will be three photodiodes used, and the transmission functions will be indicated by r , for the reflected photodiode, p for the pickoff photodiode, and d for the dark port photodiode. The subscript t in this instance should not be confused with the transmissivity of a mirror. The subscript of β_t likewise indicates the photodiode output to which the demodulation is applied. The subscripts of M will indicate the photodiode and degree of freedom, respectively. Two things have been assumed here. First, the amplitudes E_1 and E_2 incident on the photodiode are taken to be $E_l a_1 t_1$ and $E_l a_2 t_2$, respectively, where the t_i ’s are the transmission functions, and the a_i ’s are the input field amplitudes relative to the amplitude of the laser light, E_l . Second, it’s assumed that the relative phase of a_1 and a_2 is $\pi/2$. Casting the matrix element in this form has the utility of relating the

signal sensitivity to the interferometer transmission functions. The actual values of the incident field amplitudes are then constant scaling factors for all matrix elements of a single signal port.

The phase modulated input field has a matrix described by

$$M_{t,j} = |E_l|^2 J_0 J_1 \Im \left\{ \frac{\partial t_0}{\partial \phi_j} (t_- e^{i\beta t} + t_+ e^{-i\beta t})^* + t_0 \left(\frac{\partial t_-}{\partial \phi_j} e^{i\beta t} + \frac{\partial t_+}{\partial \phi_j} e^{-i\beta t} \right)^* \right\} \quad (3.11)$$

A row in the matrix of discriminants shows the relative DC sensitivity of a signal port to the degrees of freedom of the interferometer. This can be used to decide which signal ports should be used to control each of the degrees of freedom.

Examples

A couple of examples, using the phase modulated input fields, are good pedagogical tools for developing some intuition about what these demodulated signals are measuring. It's first assumed that E_0 is real. The RF sidebands are assumed equal, $E_+ = E_-$, and imaginary. The derivatives of the carrier and RF sidebands are assumed to be imaginary and real, respectively. This is true for fields which are incident on an interferometer which has strictly resonant or anti-resonant conditions.¹

The measured inphase ($\beta = 0$) signal is

$$V_I(t) = \Re \{ E_0 (E_- + E_+)^* \} \quad (3.12)$$

The matrix element associated with this is found to be

$$M_{t,j} \propto 2\Im \left\{ \frac{\partial t_0}{\partial \phi_j} t_+^* + t_0 \frac{\partial t_+}{\partial \phi_j} \right\} \quad (3.13)$$

$$\propto 2t_0 t_+ \left(\frac{1}{-it_0} \frac{\partial t_0}{\partial \phi_j} - \frac{1}{-it_+} \frac{\partial t_+}{\partial \phi_j} \right) \quad (3.14)$$

The quantity $\frac{1}{-it_k} \frac{\partial t_k}{\partial \theta}$ is easily recognized as the derivative of the phase of t_k with respect to the parameter θ . This indicates that the inphase demodulation is sensitive

¹In general, there may also be an overall phase factor which can be removed, maintaining the assumption of real carrier and imaginary RF sidebands.

to the difference in the rates of change of phase between the carrier and the RF sidebands. Another way to say this is that the inphase demodulation measures the differential phase modulation of the carrier and RF sidebands relative to each other.

The quadrature demodulation is orthogonal to the inphase demodulation, $\beta = \pi/2$. The measured signal is

$$V_Q(t) = \Im\{E_0(E_+^* - E_-^*)\} \quad (3.15)$$

and its associated matrix element is

$$M_{t,j} \propto t_0 \left(\frac{\partial t_+}{\partial \phi_j} - \frac{\partial t_-}{\partial \phi_j} \right) \quad (3.16)$$

Here, it's seen that the quadrature demodulation measures the differential amplitude modulation of the two RF sidebands.

It will be seen later that the assumptions about the relative phases of the carrier and RF sidebands incident on the photodiode typically do not hold for detuned interferometers. However, the concepts embodied in these simple examples are generally useful.

3.1.2 Frequency Dependent Signal

This section will assume the light incident on the interferometer is phase modulated, so the measured power is given by Eq. (3.4). Extension of these results to the two-frequency measured power of Eq. (3.2) is easily found by simply setting the terms associated with one of the RF sidebands to zero, and dealing with the assumption that the relative phase between the DC carrier and RF sidebands is $\pi/2$.

Deriving the frequency dependent signal requires the knowledge of how signals are generated, and model for how they're detected. The generation of signal sidebands due to mirror motion was described in Chapter 2, shown in Figure 2.8 and derived in Eq. (2.14). Detection is a more complicated function now that the light incident on the photodiode includes the audio sidebands. For full generality, it's assumed that

the modulation of the mirror is applied to the carrier and both RF sidebands, which produces two audio sidebands on each incident field at frequency $\pm\omega_g$. There are nine field components incident on the photodiode.

$$\begin{aligned}
E_{PD} = & E_{0+}e^{i\omega_g t} + E_{00} + E_{0-}e^{-i\omega_g t} + \\
& E_{++}e^{i(\Omega+\omega_g)t} + E_{+0}e^{i\Omega t} + E_{+-}e^{i(\Omega-\omega_g)t} + \\
& E_{-+}e^{i(-\Omega+\omega_g)t} + E_{-0}e^{-i\Omega t} + E_{--}e^{i(-\Omega-\omega_g)t}
\end{aligned} \tag{3.17}$$

The overall carrier $e^{i\omega t}$ phase has been dropped, and the subscripts are ordered to indicate first, the RF sidebands or the carrier (+ indicating the $+\Omega$ RF sideband, 0 indicating the carrier, etc.), and second, which order audio sideband. E_{+-} is then the lower audio sideband of the upper RF sideband.

The power measured by the photodiode will have, as in the DC case, power at DC, Ω and 2Ω , as well as components close to these frequencies. Demodulation and subsequent low-pass filtering only picks out the components in the bandwidth defined by the low pass filter around Ω , so these are the only components of interest. The low-pass frequency is assumed to be much greater than the frequencies of signals considered. It's also assumed that products between the signal sidebands are negligible.

$$\begin{aligned}
|E_{PD}|^2_{\text{DC}} = & 2\Re\{E_{++}E_{00}^*e^{i(\Omega+\omega_g)t} + E_{-+}E_{00}^*e^{i(-\Omega+\omega_g)t} + \\
& E_{+-}^*E_{00}e^{i(-\Omega+\omega_g)t} + E_{--}^*E_{00}e^{i(\Omega+\omega_g)t} + \\
& E_{+0}E_{0-}^*e^{i(\Omega+\omega_g)t} + E_{-0}E_{0-}^*e^{i(-\Omega+\omega_g)t} + \\
& E_{+0}^*E_{0+}e^{i(-\Omega+\omega_g)t} + E_{-0}E_{0-}^*e^{i(-\Omega+\omega_g)t}\}
\end{aligned} \tag{3.18}$$

Applying Eq. (3.6), the demodulated signal is

$$\begin{aligned}
V_{out}(t) = & \Re\{[E_{00}^*(E_{++}e^{i\beta} + E_{-+}e^{-i\beta}) + E_{00}(E_{--}^*e^{i\beta} + E_{+-}^*e^{-i\beta}) + \\
& E_{0+}(E_{-0}^*e^{i\beta} + E_{+0}^*e^{-i\beta}) + E_{0-}^*(E_{+0}e^{i\beta} + E_{-0}e^{-i\beta})]e^{i\omega_g t}\}
\end{aligned} \tag{3.19}$$

If it's assumed that the mirror motion is $\delta l(t) = \Re\{(1/k)e^{i\omega_g t}\}$, the factor of k scales

out of the amplitude of the audio sidebands (Eq. (2.14)). Equivalently, this also can be thought of as the direct phase modulation of the light incident on the mirror with amplitude 1 rad. The signal sideband amplitudes are proportional to the individual transmission functions *from the mirror to the photodiode*, evaluated at frequency ω_g , as well as the amplitude of the light incident on the mirror, as indicated by Eq. (2.14). Eq. (3.19) can be written more clearly as

$$\begin{aligned} V_{out}(t) &= \Re \left\{ |\tilde{H}(\omega_g)| e^{i \arg(\tilde{H}(\omega_g))} \delta l e^{i \omega_g t} \right\} \\ &= |\tilde{H}(\omega_g)| |\delta l| \cos(\omega_g t + \arg(\tilde{H}(\omega_g))) \end{aligned} \quad (3.20)$$

where the complex transfer function is defined as

$$\begin{aligned} \tilde{H}(\omega_g) \equiv \frac{V_{out}(\omega_g)}{\delta l(\omega_g)} &= E_{00}^* (E_{++} e^{i\beta} + E_{-+} e^{-i\beta}) + E_{00} (E_{--}^* e^{i\beta} + E_{+-}^* e^{-i\beta}) + \\ &E_{0+} (E_{-0}^* e^{i\beta} + E_{+0}^* e^{-i\beta}) + E_{0-}^* (E_{+0} e^{i\beta} + E_{-0} e^{-i\beta}) \end{aligned} \quad (3.21)$$

Units are in $W/(\lambda/2\pi)$ when $\delta l = k$.

Although this transfer function was derived for phase modulations applied by mirror motion, it's equally valid for any sort of phase noise or amplitude noise, as long as the corresponding amplitudes of these disturbances are dealt with appropriately. Typically this involves being careful about the dimensions and the relative phases (factors of i and such) of the audio sidebands.

3.1.3 Phasor Diagrams

Phasor diagrams are an extremely useful graphical aid to the intuition when thinking about optical heterodyne signal extraction. Discussion again will assume the phase modulated spectrum of Eq. (3.3). Referring back to Eq. (3.9), the real part of each term in the brackets can be seen to be the scalar product of two vectors whose real and imaginary parts make up the basis of the vector space.

$$\Re\{ab^*\} = \Re\{a\}\Re\{b\} + \Im\{a\}\Im\{b\} = \vec{a} \cdot \vec{b} \quad (3.22)$$

The carrier phasor is made stationary by factoring the carrier frequency out. The RF sidebands are rotating either clockwise or counter-clockwise relative to the carrier, depending on whether they're lower or upper sidebands. Examining Eq. (3.9) again, the process of demodulation fixes the RF sidebands at some point in their rotation characterized by the demodulation phase β . A change in demodulation phase generates a static rotation of the sidebands in the opposite sense, as evidenced by the conjugation of the demodulation rotation on the lower sideband. Therefore, the process of signal extraction can be thought of as the scalar product of the carrier vector with the resultant RF sideband vector, at a point in their rotation which is controlled by the demodulation phase.

Eqs. (3.14) and (3.16) can be revisited in terms of phasor diagrams. Phase modulated light generates RF sidebands which are orthogonal to the carrier, as seen in Eq. (3.3) by the factor of i in their amplitudes. Thus, the RF sideband phasors start out both parallel to each other and orthogonal to the carrier. This is a more useful definition the “inphase” demodulation since it relates to the state of the RF sidebands relative to the carrier, rather than simply a numerical value for β , and will be used as the functional definition for the rest of this thesis. Signal extraction is shown in Figure 3.1. Since the unperturbed resultant RF sideband and the carrier

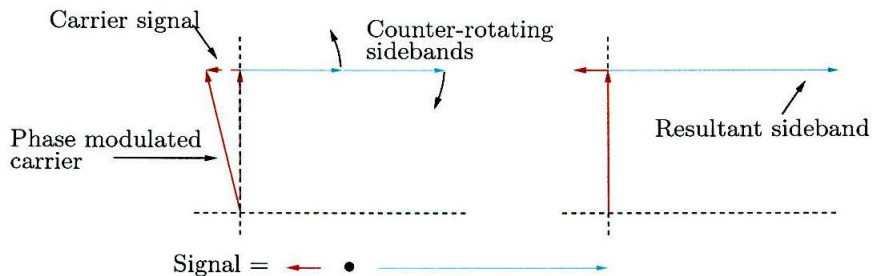


Figure 3.1: Signal extraction in the inphase demodulation.

phasors are orthogonal to each other, no signal is measured. If any of the phasors is amplitude modulated, it can be seen that there still would be no signal. However, if the carrier is phase modulated, as shown in the figure, there is now a component of the carrier parallel to the resultant RF sideband phasor, and so the scalar product

is non-zero. This is the basic form of the Pound-Drever cavity locking technique, in which the carrier resonates in a cavity, and the RF sidebands are excluded. Length fluctuations of the cavity cause phase fluctuations of the carrier to first order, while the RF sidebands remain unperturbed. If the RF sidebands are also in the cavity, all frequencies will experience the same phase modulation, that is to say, the resultant RF sideband will be rotated by the same amount as the carrier, and no signal would be measured. A third situation of interest is if the cavity is dispersive and all frequencies are resonant. Then the phase shift for a cavity length perturbation is different for the carrier and the RF sidebands, and the phasors are rotated by different amounts. A signal will be measured, either larger or smaller than if the sidebands are excluded from the cavity, depending on the direction of the phase shifts. This all goes back to the interpretation of Eq. (3.14), which stated that the inphase demodulation is sensitive to *relative* phase modulations between the carrier and RF sidebands.

In the quadrature demodulation, the RF sideband phasors are rotated by a quarter of a cycle, such that they're anti-parallel. The resultant sideband vector is null, so clearly any perturbation to the carrier doesn't generate a signal. In fact, about the only way a signal can be measured is when the amplitude of the RF sidebands is differentially modulated. The applicability for this demodulation phase is, for

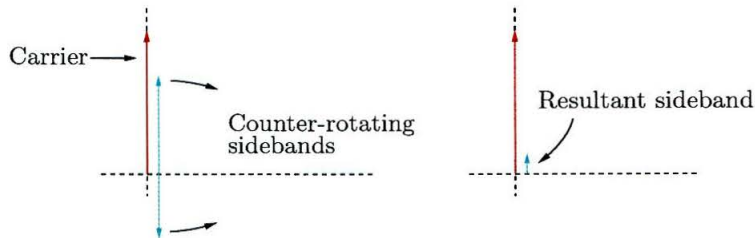


Figure 3.2: Signal extraction in the quadrature demodulation.

example, in an asymmetric Michelson interferometer when the carrier is dark at the output. With the asymmetry, the two RF sidebands have some non-zero amplitude at the output. When the interferometer is pushed away from the dark fringe, one sideband will grow in amplitude, while the other will shrink, causing a differential amplitude modulation, consistent with the interpretation of Eq. (3.16). Another

possible use of the quadrature demodulation is for cavity locking, in which the carrier is resonant, but the RF sidebands are slightly off-resonant. Subsequent perturbations to the length of the cavity causes their amplitudes to be differentially modulated, and so generate signals in the quadrature demodulation.

The “signal” in these cases is due to an additional phasor which is either normal or parallel to the original phasor, depending on whether the perturbation is in phase or amplitude, respectively. This signal phasor will in general have some time dependence, which can be decomposed into its Fourier components. In the case of phase modulation, the original phasor is rotationally dithered, tracing out a swinging length phasor normal to the original. Amplitude modulation causes the original phasor to grow and shrink, generating a swinging length phasor parallel to the original phasor. These swinging length phasors can be decomposed into two counter-rotating phasors, rotating at the frequency of the perturbation. This is shown in Figure 3.3. A clear

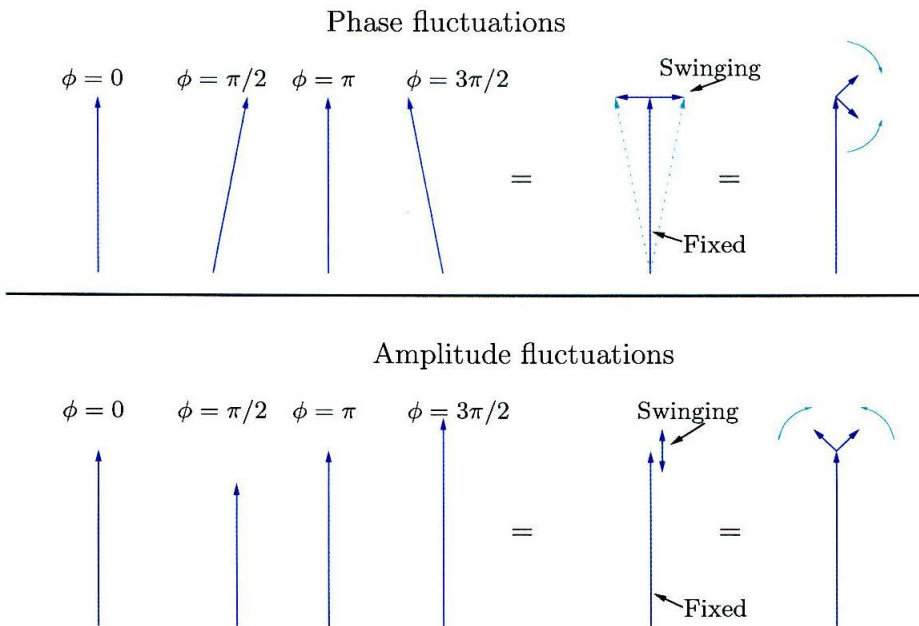


Figure 3.3: Generation of the signal phasors.

example of this is the phase modulation of the input light which is decomposed into a carrier plus the two counter-rotating RF sidebands. This picture can be extended

further to generate the second order sidebands as well, although it will typically be assumed that the perturbations are small enough that the second order effects can be ignored.

In general, it's possible that the RF sidebands aren't equal in magnitude or phase. The input light certainly has equal RF sidebands; however, the transmission functions which propagate them to the photodiode may not be the same. In this case, the RF sidebands are unbalanced. The resultant RF sideband no longer is a swinging length vector, but rather, it traces out an ellipse at the modulation frequency Ω , shown in Figure 3.4. Clearly, even without any perturbations, the value of the scalar product

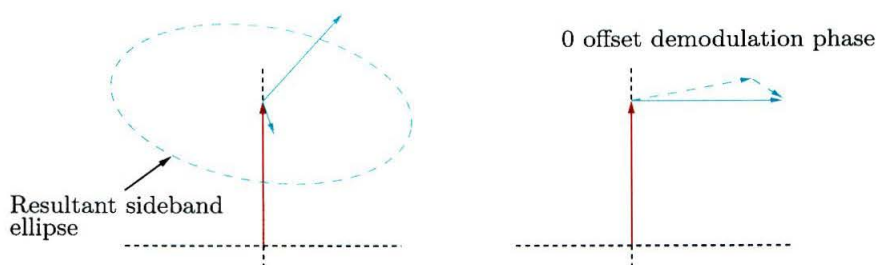


Figure 3.4: Unbalanced RF sidebands. The RF sideband resultant traces out an ellipse as a function of demodulation phase. The only non-zero output from this configuration is at the demodulation represented on the right, where the resultant is orthogonal (as well as the phase 180° rotated from this).

is non-zero for all demodulation phases except two, when the resultant is normal to the carrier. The presence of a DC offset for arbitrary demodulation phase can in principle be nulled by a summed electronic offset after demodulation. This would have the benefit of a clear interpretation of any non-zero output being due to signal. However, it's also clear that the value of the DC offset is entirely dependent on the state of the phasors remaining stable. For example, drifts in alignment, modulation depth, etc., would cause the required voltage offset to be periodically re-evaluated. In order to avoid complications as much as possible, attention will be confined to the demodulation phase in which the resultant is normal to the carrier, and the optical offset is zero. This is seen in Figure 3.4 to be the functional definition of the inphase demodulation.

In this situation, signal extraction isn't nearly as clear. In the balanced sideband case, the inphase demodulation would only be sensitive to phase modulations. When the RF sidebands are unbalanced, however, an amplitude modulation of the two RF sidebands can also generate a signal phasor which has a component parallel to the carrier. On the other hand, the only type of measurable signal impressed upon the carrier is still due to phase modulations, since the resultant RF sideband is orthogonal to the carrier.

3.1.4 *Twiddle*

Twiddle is a Mathematica program which was originally written by Martin Regehr in order to calculate the frequency response of an interferometer to mirror motions.[32] *Twiddle* works by building a set of linear equations which relate the fields incident on, and propagating away from, an arbitrary set of optics and light sources, through the propagation phases which connect the optics. The user has a set of commands with which to define the interferometer optics as well as the propagation paths. An example is shown in Figure 3.5. The fields at a mirror, for example, are related by

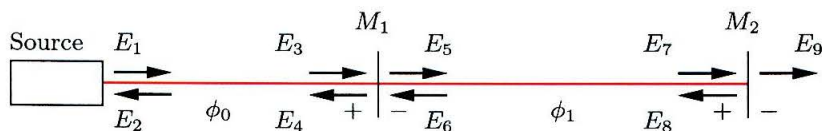


Figure 3.5: Example configuration for *Twiddle*.

$$E_4 = r_1 E_3 + t_1 E_6 \quad (3.23)$$

$$E_5 = t_1 E_3 - r_1 E_6$$

These fields are connected to the other mirrors and light sources by propagation phases, such as

$$E_3 = E_1 e^{-i\phi_0} \quad (3.24)$$

$$E_6 = E_8 e^{-i\phi_1}$$

The source amplitude is set by the user.

$$E_1 = E_{input} \quad (3.25)$$

When all the fields and their connections are specified, a matrix M can be built into a matrix equation as

$$M \begin{pmatrix} E_1 \\ E_2 \\ \vdots \\ E_9 \end{pmatrix} = \begin{pmatrix} E_{input} \\ 0 \\ \vdots \\ 0 \end{pmatrix} \quad (3.26)$$

Given a user-defined input spectrum of carrier and RF sidebands, *Twiddle* solves this equation for the field amplitudes E_{1-9} of each of the input spectrum components.

Twiddle then simulates mirror motion via the model in Eq. (2.14) by “injecting” audio sidebands at the mirror chosen by the user to be shaken. It’s assumed that this motion is much smaller than the wavelength of the light. These audio sidebands are taken to be new “sources” of light for the equations defined by the M matrix. The propagation of these audio sidebands to a specified location in the interferometer is then solved for by including the frequency dependence in the propagation phases of Eq. (3.24). *Twiddle* solves this audio sideband equation for a user specified number of points in a frequency range also specified by the user. At each frequency point, the model in Eq. (3.21) is used to calculate the value of the transfer function at that frequency.

The version developed by Regehr is very robust, and makes very few assumptions about the interferometer in calculating the transfer function. The current state of the model has been updated, and many new features have been added by myself, Hiro Yamamoto, and Osamu Miyakawa. Some of the new features include support for arbitrary sets of RF sidebands, calculation of the DC matrix of discriminants, and signal sweeps, in which a mirror is swept linearly through some arbitrary displacement, rather than dithered back and forth by a small amount.

Twiddle is the standard model which was used throughout this thesis to design

and test ideas and analytical formulas relating to signal extraction schemes. It was also extensively used in the tabletop prototype experiment of Chapter 4 to predict the state of the interferometer as well as design and debug the experiment. It is available through the STAIC website.[49]

3.2 The RSE Interferometer

Figure 3.6 shows the RSE interferometer, along with the labels relevant to this section. There are five longitudinal degrees of freedom in RSE. “Longitudinal” indicates that

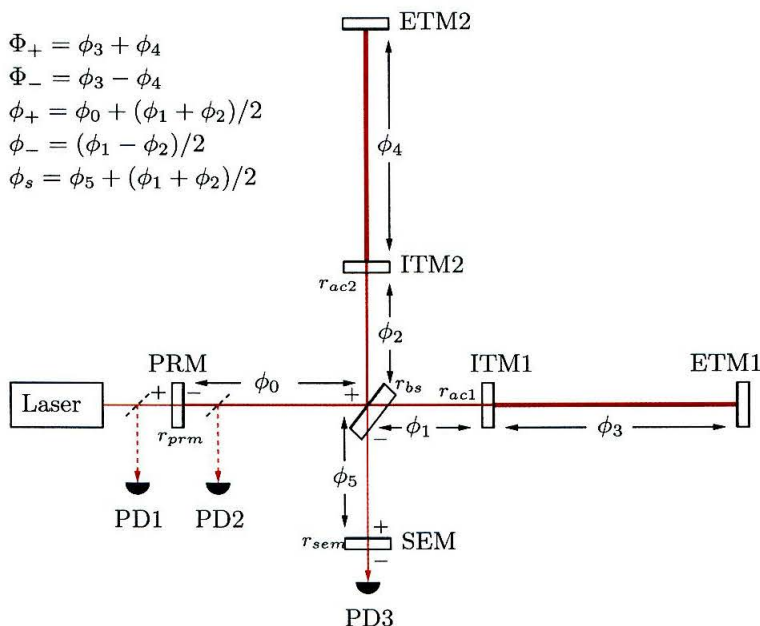


Figure 3.6: The optical layout of the RSE interferometer. r_{prm} , r_{bs} , and r_{sem} are the reflectivities of the power recycling mirror, the beamsplitter, and the signal mirror, respectively. r_{ac1} and r_{ac2} are the reflectivities of the inline and perpendicular arm cavities. Sign conventions for the mirrors are indicated.

the degree of freedom is along the axis of the laser beam, as opposed to the angular degrees of freedom, which are related to the tilting motions of the mirrors. The five degrees of freedom are comprised of four cavity phases plus the dark fringe Michelson condition. The four cavities are the power recycling cavity and signal extraction cavity, as well as the two arm cavities. The two arm cavities are represented in terms

of their sum and difference, or “common” and “differential” modes. The degrees of freedom are represented by Φ_+ , Φ_- , ϕ_+ , ϕ_- , and ϕ_s in Figure 3.6, where they’re expressed explicitly in terms of the connection phases from optic to optic. The phases are all assumed to be round-trip phases.

The three photodiodes represented measure the reflected fields at PD1, the pickoff fields in the power recycling cavity at PD2, and the dark port fields at PD3. The interferometer can be simplified somewhat by treating the arms of the interferometer as compound mirrors with complex, frequency dependent reflectivities. The result is a dual-recycled Michelson, with the arm cavities frequency responses folded into the complex reflectivities of the end mirrors of the Michelson, r_{ac1} and r_{ac2} . This can be simplified another step further by noting that the Michelson itself behaves like a complex-functioned, frequency dependent mirror. The four input-output relations

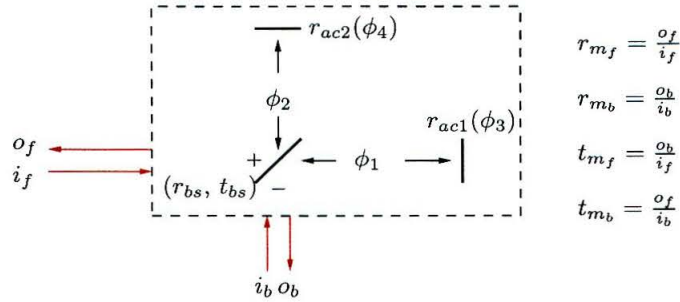


Figure 3.7: The Michelson “mirror.” Phases and sign conventions are indicated. Phases are round-trip. The beamsplitter reflectivity and transmissivity are r_{bs} and t_{bs} , respectively.

shown in Figure 3.7 can be easily found to be²

$$\begin{aligned} r_{m_f} &= r_{bs}^2 r_{ac2}(\phi_4) e^{i\phi_-} + t_{bs}^2 r_{ac1}(\phi_3) e^{-i\phi_-} \\ r_{m_b} &= t_{bs}^2 r_{ac2}(\phi_4) e^{i\phi_-} + r_{bs}^2 r_{ac1}(\phi_3) e^{-i\phi_-} \\ t_{m_f} &= t_{m_b} = r_{bs} t_{bs} (r_{ac2}(\phi_4) e^{i\phi_-} - r_{ac1}(\phi_3) e^{-i\phi_-}) \end{aligned} \quad (3.27)$$

²Each of these terms actually also has an overall phase factor of $e^{-i(\phi_1 + \phi_2)/2}$. This phase factor is taken out of these expressions, and added to the power and signal cavities to which the Michelson mirror is connected. This is the source of the “ $(\phi_1 + \phi_2)/2$ ” terms in the definitions of those degrees of freedom indicated in Figure 3.6.

The f and b subscripts indicate from which direction the Michelson is being looked at, “front” or “back.” Front is taken to be the side the laser light sees first.

It’s worth noting how these formulas simplify when the arm cavities are equal, $r_{ac1} = r_{ac2} = r_{ac}$, and the beamsplitter mismatch is zero (but with non-zero losses), $r_{bs}^2 = t_{bs}^2$ and $A_{bs} = 1 - L_{bs} = r_{bs}^2 + t_{bs}^2$.

$$\begin{aligned} r_{m_f} &= r_{m_b} = A_{bs} r_{ac} \cos(\phi_-) \\ t_{m_f} &= t_{m_b} = i A_{bs} r_{ac} \sin(\phi_-) \end{aligned} \quad (3.28)$$

Hence the Michelson mirror reflectivity and transmissivity is a function of the phase ϕ_- .

Modeling the Michelson as a mirror, the interferometer takes on the form of a three mirror coupled cavity, with the input and output mirrors being the power and signal mirrors, and the coupling mirror being the Michelson mirror. The cavities are the power and signal cavities, and all other phases are then folded into the response of the Michelson mirror.

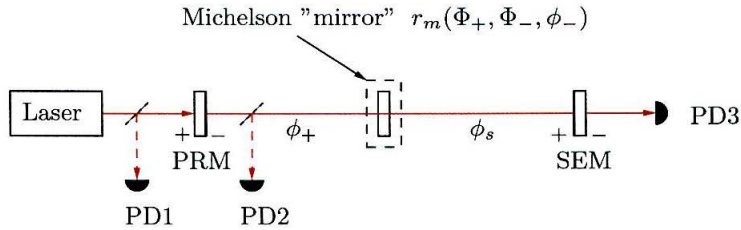


Figure 3.8: The power/signal coupled cavity system. The Michelson degree of freedom, ϕ_- , as well as the arm cavity degrees of freedom, Φ_+ and Φ_- , are included in the Michelson mirror quantities, r_{m_f} , r_{m_b} , and t_{m_f} .

3.2.1 Asymmetry

Figure 3.8 reduces to a single cavity for LIGO I, whose end mirror is the Michelson mirror. The carrier and RF sidebands are resonant in this cavity, and the carrier is held on a dark fringe in the Michelson. The Michelson phase ϕ_- for the RF sidebands,

however, is given by

$$\phi_- = \frac{\Omega_{mod}(l_1 - l_2)}{c} = \frac{\Omega_{mod}\delta}{c} \quad (3.29)$$

where δ is a macroscopic asymmetry, also known as the ‘‘Schnupp asymmetry.’’ Coupling of RF sideband power to the dark port is accomplished by choosing the asymmetry such that the transmittance of the Michelson is roughly equal to the transmittance of the power mirror, $\sin(\phi_-)^2 \approx T_{PRM}$, since the RF sidebands are not resonant in the arms ($r_{ac} \approx 1$). This makes the power cavity nearly optimally coupled for the RF sidebands. Because the RF sidebands are used at the dark port as the local oscillator (LO) for the gravitational wave signal, it’s important that the amount of power present due to the RF sidebands is large compared to any other source of ‘‘junk’’ light. Junk light generates shot noise without adding sensitivity to signal, so it’s desired that the dominant source of shot noise will be due to the presence of the RF sidebands. Sources of junk light are contrast defect and higher order transverse spatial modes.

RSE is a bit more complicated, since the sidebands now need to transmit through a coupled cavity system. Consider first the broadband RSE case, where the carrier is resonant in the signal cavity. There are a couple of options. First, the asymmetry can be made large enough such that the reflectivity of the Michelson is zero. The coupled cavity is effectively reduced to a single cavity with the power and signal mirrors acting as its input and output mirrors. If the power and signal cavity mirrors have similar enough transmittances, the total transmitted power can be fairly good. The asymmetry is set by the following equation.

$$\phi_- = \frac{\Omega_{mod}\delta}{c} = \pi/2 \quad (3.30)$$

$$\delta = \frac{\lambda_{mod}}{4} \quad (3.31)$$

The lengths of the power and signal cavity are chosen such that the round trip phase for the RF sidebands satisfies a resonant condition. Given the sign convention used in Figure 3.8, resonance is satisfied by a round trip phase equal to an odd integer π ,

due to the sign from the power recycling mirror.

$$\left(\phi_{carrier_{prc}} + \phi_{carrier_{sec}} \pm \frac{2\pi 2(l_{prc} + l_{sec})f_{mod}}{c} + 2\frac{\pi}{2} \right) = (2n + 1)\pi \quad (3.32)$$

$$l_{prc} + l_{sec} = n' \frac{\lambda_{mod}}{2} \quad (3.33)$$

The round-trip carrier phases are some integer 2π in the broadband case. Of note is the final factor of $\pi/2$. This comes from the fact that the Michelson, although the magnitude of its transmission is unity, adds a phase of $\pi/2$ for each transmission, as evidenced by the factor of i in Eq. (3.28).

In general, though, the transmittance of the power and signal mirrors can be different enough that the transmittance of the coupled cavity on the bright fringe can become quite low. In this case the asymmetry must be properly matched in the coupled cavity system. One way to think about this is that, viewed from the power cavity, the signal cavity, formed by the Michelson and the signal mirror, looks like a mirror. The asymmetry is chosen such that the transmittance of the signal cavity compound mirror again is approximately equal to the transmittance of the power mirror, which then optimally couples the sideband transmission to the dark port. The general solution can be quite complex. As evidenced by the tile plot of Figure 2.3, this can involve off-resonant cavities, such that there are three variables to solve for: the asymmetry and the phases of the power and signal cavities. Simpler, analytical solutions can be found by setting the individual cavities on resonance or anti-resonance. There are two solutions for the reflectivity, $r_{prm} = \pm r_{sec}$, since a resonant cavity reflectivity can have either sign.

The first solution assumes the power and signal cavity are both resonant for the RF sidebands. Solving this equality gives

$$\delta = \frac{c}{\Omega_{mod}} \arccos \left(A_{bs} \frac{r_{prm} + r_{sem}}{1 + r_{prc} r_{sem} A_{bs}^2} \right) \quad (3.34)$$

This usually is a fairly small number, on the order of a couple centimeters for typical mirrors and modulation frequencies in the 10's of MHz. The value of the Michelson

transmittance is then higher than either the power or signal mirrors. This allows a certain consistency, that being that both cavities, as viewed from the other, appear to be under-coupled. The sign on reflection is then positive, and the resonance of the cavities is preserved.

The second solution has a much larger asymmetry, such that the Michelson has a transmittance near unity. How the solution is found depends on which mirror, power or signal, has the higher transmittance. First assume the power mirror has the higher transmittance. Since a resonant cavity has a higher transmission than either of the single mirrors, the signal cavity can be made to match its transmission to the power mirror. However, with a large asymmetry, the signal cavity is over-coupled, and the sign flip from the signal cavity requires that the power cavity be anti-resonant without this particular effect. This is in the same manner as the resonance condition for the carrier in the power cavity. In this case, the solution is

$$\delta = \frac{c}{\Omega_{mod}} \arccos \left(A_{bs} \frac{r_{sem} - r_{prm}}{1 - r_{prm} r_{sem} A_{bs}^2} \right) \quad (3.35)$$

If the situation is reversed, that is the power mirror has a lower transmittance than the signal mirror, the solution is found to be

$$\delta = \frac{c}{\Omega_{mod}} \arccos \left(A_{bs} \frac{r_{prm} - r_{sem}}{1 - r_{prm} r_{sem} A_{bs}^2} \right) \quad (3.36)$$

As an example, the transmittance of the coupled cavity system is shown in Figure 3.9 as a function of the asymmetry. This plot uses the power and signal mirrors for the optimized broadband interferometer, with the power mirror transmittance of $T_{prm} = 8.6\%$ and a signal cavity mirror transmittance of $T_{sem} = 5\%$. The frequency of the RF sidebands is at $f_{mod} = 81$ MHz, and the losses are assumed to be zero.

Designing to the point of optimal coupling is, in fact, not a good practice. Optics invariably have characteristics (losses, reflectivities) which are not exactly what were ordered. Furthermore, losses can change in time. The desire to have strong transmission to the dark port does constrain the asymmetry to a value close to the optimal

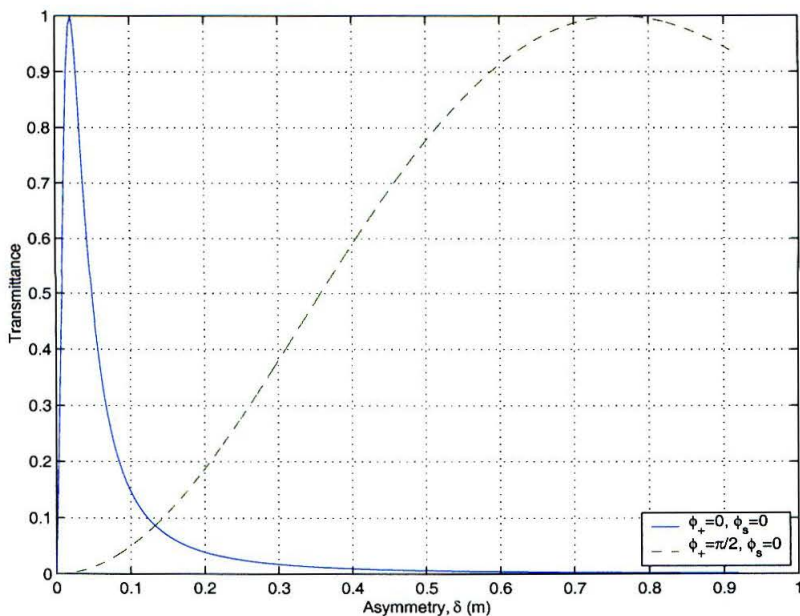


Figure 3.9: Power/signal coupled cavity transmittance as a function of asymmetry. The phases of the power and signal cavities are indicated as one-way phases in the legend. $T_{prm} = 8.6\%$, $T_{sem} = 5\%$, and the RF modulation frequency is 81 MHz.

asymmetry, so these formulas give a reasonable starting point.

3.2.2 Detuned Interferometer

The state of the RF sidebands in the interferometer is further muddled by detuned operation, where the signal cavity is off resonant for the carrier. In this case, it is not possible in general to resonate both the upper and lower RF sidebands equally in the coupled cavity. This is because the sideband phases are

$$\phi_{\pm SB} = \phi_{carrier} \pm \frac{\Omega_{mod} 2l}{c} \quad (3.37)$$

The carrier phase in the signal cavity is some fraction between 0 and 1 of $\pi/2$. For the upper and lower sidebands to “see” the same cavity system, their phases need to be equal. Additionally, the total phase needs to be some integer multiple of π for

resonance, for both upper and lower RF sidebands.

$$\pm \frac{\Omega_{mod} 2l}{c} = n\pi - \phi_{dt} \quad (3.38)$$

where ϕ_{dt} is the detuning phase, and n an integer. A solution for this is generally not possible for both RF sidebands. Significant RF sideband power is still needed at the dark port for good signal to noise in the gravitational wave signal port. The typical solution is then to optimize for one of the RF sidebands at the expense of the other. This can be done in one of two ways.

First, the frequency of the modulation can be varied numerically to find a solution which optimizes the transmission of one of the RF sidebands. In general, the solution is one of the off-axis points of a tile plot. The RF sideband isn't exactly resonant in either cavity individually, but is resonant in the coupled cavity system.[50] If the detuning changes, the RF sideband frequency can likewise be re-optimized.

The second solution is a modification of Eq. (3.38). It's assumed that a solution for the broadband RSE interferometer is found, and both RF sidebands have acceptably high transmittance to the dark port. When the interferometer is detuned, the length of the signal cavity can be shifted in such a way that Eq. (3.38) is satisfied for one of the RF sidebands. The phase shift of the detuning is canceled by the macroscopic length shift of the cavity, and the transmittance for one of the RF sidebands is the same as in the broadband case. Eq. (3.39) shows the length shift for keeping the lower RF sideband on resonance.

$$\Delta l_{sec} = -\phi_{dt} \frac{c}{\Omega_{mod}} \quad (3.39)$$

For the small detunings expected in RSE, this is typically on the order of a few centimeters.

Both of these methods have advantages and disadvantages. In the frequency shift solution, the interferometer is left unperturbed, and the change in detuning can in principle be done dialing the knob which changes the modulation frequency. This also leaves the possibility that the detuning can be done dynamically, that is the interferometer frequency response can be changed in time to attempt to match a

signal.[51] One main disadvantage involves the use of a mode cleaner. The mode cleaner is a Fabry-Perot cavity through which the modulated laser light propagates before it's incident on the interferometer. This cavity provides some frequency and amplitude stability, a reduction in beam jitter, and rejection of light in higher order transverse spatial modes (hence the name "mode cleaner"). However, it's critical that the modulation frequencies match the free spectral range of the mode cleaner to high precision due to frequency–amplitude noise coupling. If the modulation frequency is shifted, the mode cleaner length would correspondingly have to be changed.

The advantage of the macroscopic length shift is that it's entirely compatible with a mode cleaner. For any significant new detuning, the macroscopic position of the signal mirror ideally would need to be changed. This can potentially be done without breaking vacuum, for example if the suspension of the signal mirror could be mounted on a rail. However, it is unlikely that the interferometer could be dynamically detuned. Shifting its position by such distances would most likely cause the interferometer to lose lock. On the other hand, it is expected that the operation of the interferometer won't require frequent detuning, especially in the optimized broadband case.

3.2.3 Additional Sidebands

The problem of RF sideband transmission to the dark port for the gravitational wave readout and control of Φ_- has been discussed in the previous subsections. There are still four additional degrees of freedom to measure.

LIGO I is adequately controlled with a single set of phase modulated RF sidebands at some frequency f_1 . There are several factors which force the addition of another set of RF sidebands in RSE. First, the dark port photodiode isn't sensitive to any of the degrees of freedom besides the differential modes Φ_- and ϕ_- at the f_1 demodulation frequency. This leaves the reflected and pickoff photodiodes to provide the cavity signals ϕ_+ , ϕ_s , and Φ_+ . In the broadband RSE interferometer, where the RF sidebands are balanced, only the inphase demodulation measures the phase shift

due to the fluctuating length of a cavity.³ This leaves two signal ports, one from each of the reflected and the pickoff photodiodes, for three cavity signals. At the dark port, only one of the differential signals can be used, typically Φ_- . ϕ_- could still be found in the quadrature demodulation at either the pickoff or reflected photodiode, much the same as in LIGO I. In a detuned RSE interferometer, however, the restriction that there is only one demodulation phase per photodiode per demodulation frequency limits the total number of signal ports to two for the four degrees of freedom besides Φ_- .

Clearly there is a need for another RF frequency, at some frequency f_2 . This provides two more demodulation frequencies, one at f_2 , which measures the beat between the new RF sidebands and the carrier, as well as at $f_1 - f_2$, which measures the beat between the two sets of RF sidebands. At the reflected and pickoff photodiodes, there are now six signal ports for four degrees of freedom, assuming that the only signal taken at the dark port photodiode is Φ_- .

3.2.4 Proposed Signal Extraction Scheme

The choices for the specific implementation of a control scheme are numerous. The scheme proposed by this thesis was chosen for the following reasons. First, it was considered necessary to keep the modulation frequencies fixed, and at frequencies which are integer multiples in order to pass them through a single mode cleaner. Fixed frequencies then imply a macroscopic change in the length of the signal cavity to accompany a change in detuning, as in Eq. (3.39). Second, it was decided to keep the asymmetry as small as possible. This was mostly chosen in order to minimize frequency noise considerations. The method of choosing the modulation frequencies is as follows.

There are many combinations of frequencies and lengths which can be used in the interferometer. The requirements generally are that, in the power recycling cavity, the RF sideband frequencies are odd integer multiples of half the cavity's free spectral

³This assumes the RF sidebands are exactly on resonance in the individual cavities.

range. This ensures the carrier frequency is at an anti-resonant node, such that resonance is satisfied when the arm cavities resonate as well.

$$f_1 = (2n_1 + 1) \frac{f_{f_{sr_{prc}}}}{2} \quad (3.40)$$

where n_1 is an integer, and $f_{f_{sr_{prc}}} = c/(2l_{prc})$. This argument applies to each of the modulation frequencies, with a different integer, n_2 for the second RF sideband. Clearly the difference of the two frequencies will be some integer multiple of the free spectral range.

It's desired that one of the RF sideband frequencies resonates in the signal cavity, while the other does not. The non-resonant RF sideband then acts as a local oscillator for the resonant RF sideband, thus providing a signal extraction port for the ϕ_s degree of freedom. An example solution is shown in Figure 3.10, where $f_2 = 3f_1$. For

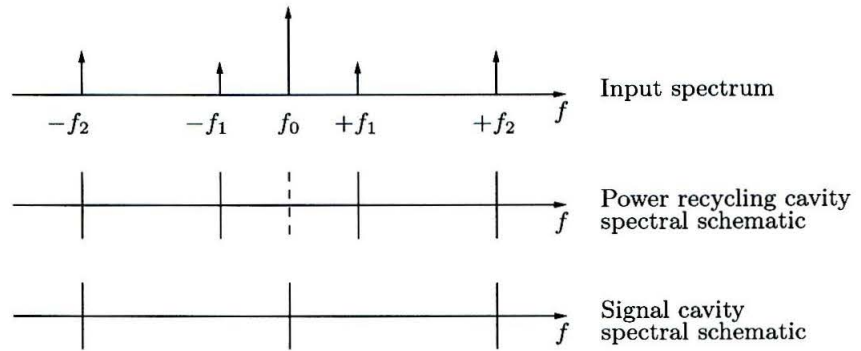


Figure 3.10: Power and signal cavity spectral schematic for broadband RSE. The RF sidebands are related by $f_2 = 3f_1$.

broadband RSE, some care must be taken as to which frequency is resonant in the signal cavity. For example, in the $f_2 = 3f_1$ case, clearly if f_1 were resonant in the signal cavity, f_2 would be resonant as well.

The constraint on which frequency is resonant in the signal cavity doesn't usually apply to a detuned RSE interferometer. Since both the frequency of one of the RF sidebands, and the frequency of the detuning must be resonant in the signal cavity,⁴

⁴Note that this is not the detuned frequency for the gravitational wave.

the hash marks corresponding to the signal cavity resonance won't usually line up with the integrally related RF sidebands, as shown in Figure 3.11.

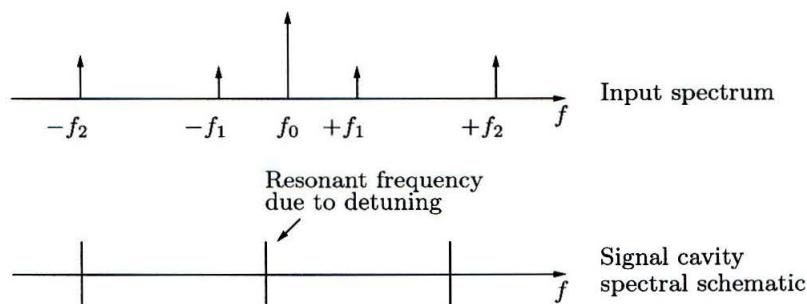


Figure 3.11: Signal cavity spectral schematic for a detuned RSE interferometer.

In this thesis, the proposal is then to use fixed RF sideband frequencies at f and $3f$. Although the interferometers designed in Chapter 2 were both detuned interferometers, the possibility of use in a broadband interferometer chooses the $3f$ modulation frequency as the one which is to propagate to the dark port for gravitational wave detection. Furthermore, the $3f$ RF sidebands will be phase modulated sidebands, again, primarily useful for a broadband RSE interferometer.

The additional RF sidebands at f are then needed, as mentioned in the previous section, to generate signals for some of the “auxiliary” degrees of freedom, ϕ_+ , ϕ_- , and ϕ_s . Cross-coupling with the arm degrees of freedom is usually a difficult issue when considering these modes. It would be useful to restrict attention to the demodulation at $2f$ (or possibly $4f$), which measures the beat note between the f and $3f$ RF sidebands, because neither experiences the arm cavities. Since the $3f$ RF sidebands are phase modulated, one option is that the RF sidebands at f would need to be amplitude modulated so that the relative phases between the two RF sidebands is $\pi/2$.⁵ Another alternative would be to use a single sideband (SSB) for the RF sideband at f . This second option is what will be used in this thesis. If there are RF sidebands at $\pm f$, the demodulation at $2f$ will specifically measure the beat between $-3f$ and $-f$, as well as $+f$ and $+3f$ (as well as $-f$ and $+f$, but that will be ignored

⁵This is important only in a broadband interferometer. In a detuned interferometer, it wouldn't matter, since the relative phases aren't preserved when the frequencies are off-resonant.

for the moment). One of these pairs isn't particularly useful in generating the measured signal for the signal extraction cavity since only one of the $3f$ RF sidebands is resonant there. It was also found through modeling that the use of the SSB RF sideband at f tended to generate a more diagonal control matrix, compared to amplitude modulated RF sidebands. The preferred method for generating the single sideband would probably be to phase-lock a second, less powerful, laser at a frequency shifted by f relative to the main laser which has been phase modulated at $3f$.

3.3 Signal Sensitivity

The process of deriving a set of signals with which to control the interferometer has a couple of steps. The first step is to derive the matrix of discriminants, Eqs. (3.10) and (3.11). The second step is to see if there's any method to optimize this matrix to produce a control matrix, or plant, which is as diagonal as possible.

Matrix of Discriminants

There are two types of signals in this scheme. The first measures the signal due to the beat of the carrier and the phase modulated (PM) RF sidebands. This will be referred to as the "PM output." The second signal arises from the beat between the lower phase modulated RF sideband and the single RF sideband (SSB). This will be referred to as the "SSB output."

The PM output signals in all three photodiodes will be dominated by the arm cavity degrees of freedom, Φ_+ and Φ_- . Due to the nature of the diagonalization of common and differential mode signals by the dark fringe condition, these two signals are separated, Φ_+ showing up primarily in the reflected and pickoff signal ports, and Φ_- dominant in the dark port signal port. This is the ideal case, and some deviation from this rule will occur due to imperfections in the matching of the arm cavities and mismatch in the beamsplitter. However, with high quality optics, these effects are small, and are ignored. When analyzing the reflected and pickoff signal ports, only Φ_+ , ϕ_+ , ϕ_- , and ϕ_s will be considered. At the dark port signal port, which is

sensitive to differential signals, only Φ_- and ϕ_- will be considered.

The SSB output signals have little influence from the arm cavities, so Φ_+ and Φ_- can be ignored. The SSB output signals in the dark port are also significantly smaller than the ones found in the reflection and pickoff ports since they would require transmission of the non-resonant SSB through the signal cavity. As a result, analysis of the SSB output will only be done in the reflected and pickoff signal ports.

It is necessary to find the appropriate demodulation phase such that the PM and the SSB outputs are zero because of the unbalanced RF sidebands. The one port in which this isn't true is the dark port. The PM output does not have any DC offset because there is no carrier present. It should be pointed out that determination of demodulation phase is primarily for the purpose of modeling. Experimental determination of appropriate demodulation phase cannot be done in any reliable way by theoretically calculating what the demodulation phase should be.

In the ideal interferometer, the calculation of the demodulation phase takes on a fairly simple form. First, consider the PM output.

$$V = |E_i|^2 J_0 J_1 \Im \{ t_0 (t_- e^{i\beta} + t_+ e^{-i\beta})^* \} \quad (3.41)$$

The carrier is exactly on resonance, except in the signal cavity, in which there is no carrier light. The field transmission function for the carrier is then a purely real function. The demodulation phase is chosen such that this measured signal is zero, which implies $\Im \{ t_- e^{i\beta} + t_+ e^{-i\beta} \} = 0$. Solving, the demodulation phase is

$$\beta_t^P = -\arctan \left(\frac{\Im \{ t_- + t_+ \}}{\Re \{ t_- - t_+ \}} \right) \quad (3.42)$$

The P superscript indicates that the demodulation phase is applied to the PM output signal, while the t subscript indicates which photodiode output is being considered, being the label for the transmission function from the input of the interferometer to that particular photodiode, as indicated by t_- and t_+ .

A similar analysis can be applied to the SSB output. In this case, the lower RF

sideband has been made to be exactly resonant in both the power and signal cavities, so its transmission function is likewise purely real.

$$\beta_t^S = \arctan \left(\frac{\Im \{t_s\}}{\Re \{t_s\}} \right) \quad (3.43)$$

The subscript s will be used to indicate the transmission function corresponding to the SSB, similar to the way in which $+$ and $-$ indicate the transmission functions for the upper and lower PM RF sidebands.

Optimization

Astrophysical considerations have driven the choice of the optics as well as the carrier resonance in the interferometer, so methods of optimization must largely be restricted to things which affect the sidebands. Phases are the quantities which affect the transmission functions of the interferometer, so the “knobs” that can be turned are either modulation frequencies and/or path lengths. Attention in this thesis is restricted to the case in which the modulation frequencies remain fixed, once chosen, and the lower RF sideband remains resonant in both the power and signal cavities, as a function of detuning. This fixes the lengths of the power and signal cavity relative to the RF sidebands, which leaves the asymmetry as the only flexible length parameter.

3.3.1 Reflected and Pickoff Signals

The simplified RSE interferometer of Figure 3.8 can be simplified even further to a single cavity, the power recycling cavity, when considering the fields actually incident on the various photodiodes. The front mirror is the power mirror, and the back mirror is the compound mirror formed by the signal cavity which has the Michelson mirror as its front mirror and the signal mirror as its back mirror. The fields then are the reflected, pickoff, and transmitted fields of a single cavity, with the appropriate substitutions. Sensitivity to a particular degree of freedom at a particular photodiode can then be formed from the simple relations found for a single cavity. For the reflected and pickoff signals, the derivatives with respect to the degrees of freedom take the

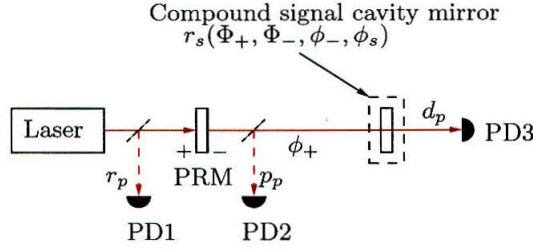


Figure 3.12: A single cavity representation of the RSE interferometer. The subscripts on the photodiode transmission functions r_p , p_p , and d_p indicate application of a cavity reflectivity, pickoff, and transmitted fields of this power recycling cavity. The subscript s on the end mirror indicates the reflectivity of a cavity applied to the signal cavity.

form of the following products.

$$\begin{aligned}
 \frac{\partial r_p}{\partial \Phi_+} &= \frac{\partial r_p}{\partial r_s} \frac{\partial r_s}{\partial r_m} \frac{\partial r_m}{\partial r_{ac}} \frac{\partial r_{ac}}{\partial \Phi_+} \\
 \frac{\partial r_p}{\partial \phi_+} &= \frac{\partial r_p}{\partial \phi_+} \\
 \frac{\partial r_p}{\partial \phi_-} &= \frac{\partial r_p}{\partial r_s} \frac{\partial r_s}{\partial r_m} \frac{\partial r_m}{\partial \phi_-} \\
 \frac{\partial r_p}{\partial \phi_s} &= \frac{\partial r_p}{\partial r_s} \frac{\partial r_s}{\partial \phi_s}
 \end{aligned} \tag{3.44}$$

Specifically, these are for the reflected signals at the photodiode characterized by the transmission function r_p . The subscript p is to indicate that the transmission function is for the effective single power recycling cavity. Similarly, the subscript s refers to the signal cavity, formed by the Michelson mirror and the signal mirror. The subscript m indicates the reflectivity and transmissivity of the Michelson mirror. The pickoff signals are formed by replacing r_p subscript with p_p .

Individual Derivatives

The transmission functions to the reflected and pickoff photodiodes, relative to the input, are given by

$$r_p = r_{prm} + \frac{T_{prm}r_s e^{-i\phi_+}}{1 + r_{prm}r_s e^{-i\phi_+}} = \frac{r_{prm} + A_{prm}r_s e^{-i\phi_+}}{1 + r_{prm}r_s e^{-i\phi_+}} \quad (3.45)$$

$$p_p = \frac{t_{prm}r_s e^{-i\phi_+}}{1 + r_{prm}r_s e^{-i\phi_+}} \quad (3.46)$$

These are explicitly functions of ϕ_+ only, so derivatives with respect to all other degrees of freedom require the functional dependence of the compound signal cavity mirror, as well as the derivative of r_p with respect to r_s . *All transmission functions and derivatives thereof are evaluated at the phases of the carrier in a broadband RSE.* The exponentials left in the formulas are set to 1 for the carrier, except for the signal cavity phase, which is replaced by the detuning phase. The phases need to be subsequently evaluated for the RF sidebands. The derivatives with respect to ϕ_+ are

$$\frac{\partial r_p}{\partial \phi_+} = \frac{-iT_{prm}r_s e^{-i\phi_+}}{(1 + r_{prm}r_s e^{-i\phi_+})^2} \quad (3.47)$$

$$\frac{\partial p_p}{\partial \phi_+} = \frac{-it_{prm}r_s e^{-i\phi_+}}{(1 + r_{prm}r_s e^{-i\phi_+})^2} \quad (3.48)$$

and the derivative with respect to the end mirror is

$$\frac{\partial r_p}{\partial r_s} = \frac{T_{prm}e^{-i\phi_+}}{(1 + r_{prm}r_s e^{-i\phi_+})^2} \quad (3.49)$$

The signal cavity reflectivity is

$$r_s = \frac{r_m - A_m r_{sem} e^{-i\phi_s}}{1 - r_m r_{sem} e^{-i\phi_s}} \quad (3.50)$$

It can be noted that, for the carrier, r_s reduces to r_m regardless of the detuning. The only explicit dependence in r_s is the signal cavity degree of freedom, ϕ_s . Both arm cavity degrees of freedom, Φ_+ and Φ_- , as well as ϕ_- , are wrapped up in the Michelson

compound mirror. The derivatives of r_s with respect to r_m and ϕ_s are

$$\frac{\partial r_s}{\partial r_m} = \frac{1 - A_m r_{sem}^2 e^{-i2\phi_s}}{(1 - r_m r_{sem} e^{-i\phi_s})^2} \quad (3.51)$$

$$\frac{\partial r_s}{\partial \phi_s} = \frac{it_m^2 r_{sem} e^{-i\phi_s}}{(1 - r_m r_{sem} e^{-i\phi_s})^2} \quad (3.52)$$

$$(3.53)$$

Finally, the arm cavities are expressed as sums and differences,

$$r_{ac} = \frac{r_{ac1} + r_{ac2}}{2} \quad (3.54)$$

$$\Delta r_{ac} = \frac{r_{ac1} - r_{ac2}}{2} \quad (3.55)$$

In this analysis, the two arms are assumed to be equal. Hence, evaluated at DC, r_{ac} is simply equal to a single arm cavity, while Δr_{ac} is equal to 0. To express the derivative of the Michelson mirror with respect to the arm cavity degrees of freedom, the following relations are needed.

$$\begin{aligned} \frac{\partial}{\partial \Phi_+} &= \frac{\partial}{\partial \phi_3} + \frac{\partial}{\partial \phi_4} \\ \frac{\partial}{\partial \Phi_-} &= \frac{\partial}{\partial \phi_3} - \frac{\partial}{\partial \phi_4} \end{aligned} \quad (3.56)$$

so that

$$\begin{aligned} \frac{\partial r_{ac}}{\partial \Phi_+} &= \frac{\partial}{\partial \Phi_+} \left(\frac{r_{ac1} + r_{ac2}}{2} \right) = \frac{\partial r_{ac}(\phi_{ac})}{\partial \phi_{ac}} \\ \frac{\partial r_{ac}}{\partial \Phi_-} &= \frac{\partial}{\partial \Phi_-} \left(\frac{r_{ac1} + r_{ac2}}{2} \right) = 0 \\ \frac{\partial \Delta r_{ac}}{\partial \Phi_+} &= \frac{\partial}{\partial \Phi_+} \left(\frac{r_{ac1} - r_{ac2}}{2} \right) = 0 \\ \frac{\partial \Delta r_{ac}}{\partial \Phi_-} &= \frac{\partial}{\partial \Phi_-} \left(\frac{r_{ac1} - r_{ac2}}{2} \right) = \frac{\partial r_{ac}(\phi_{ac})}{\partial \phi_{ac}} \end{aligned} \quad (3.57)$$

r_{ac} is the reflectivity of a single arm cavity, whose internal path phase is ϕ_{ac} .

$$\frac{\partial r_{ac}}{\partial \phi_{ac}} = \frac{iT_{itm}e^{-i\phi_{ac}}}{(1 - r_{itm}e^{-i\phi_{ac}})^2} \quad (3.58)$$

It's been assumed here that the end mirror has very nearly unity reflection, $r_{etm} \approx 1$.

Writing the Michelson reflectivity and transmissivity in the following way indicates the functional dependence necessary for taking derivatives with respect to the arm cavity degrees of freedom. It's assumed for this purpose that the beamsplitter is matched, that is $r_{bs} = t_{bs}$.

$$r_m = A_{bs}(r_{ac}(\Phi_+) \cos(\phi_-) - i\Delta r_{ac}(\Phi_-) \sin(\phi_-)) \quad (3.59)$$

$$t_m = A_{bs}(i r_{ac}(\Phi_+) \sin(\phi_-) - \Delta r_{ac}(\Phi_-) \cos(\phi_-)) \quad (3.60)$$

The losses of the Michelson are expressed in the term A_m ,

$$A_m = A_{bs}^2 r_{ac}(\Phi_+)^2 \quad (3.61)$$

This is simply equal to r_m^2 for the carrier.

Every matrix element then will be a function of the derivatives of the fields at either the pickoff or the reflected port. These derivatives are found by applying the rules of Eq. (3.44). Frequently, a useful way to describe the sensitivity is to normalize the derivative of a field with the field itself as $\frac{1}{-it} \frac{\partial t}{\partial \theta}$. This quantity gives the derivative of the phase of the complex quantity t with respect to some general parameter θ . When θ is the cavity phase, this is known as either the internal or external phase gain,⁶ depending on whether the field in question is the pickoff or reflected field. This notion is somewhat generalized here to include derivatives of the power recycling cavity transmission functions with respect to *any* of the degrees of

⁶In other literature, these have been referred to as the bounce number, and augmented bounce number, respectively.[32]

freedom.

$$N' = \frac{1}{-ir_c} \frac{\partial r_c}{\partial \phi} \quad (3.62)$$

$$N = \frac{1}{-ip_c} \frac{\partial p_c}{\partial \phi} \quad (3.63)$$

N' is the external phase gain, and N is the internal phase gain. Subscripts will be used in order to indicate which field (carrier or RF sideband) the derivative refers to, as well as the degree of freedom by which the derivative is taken.

Signal Sensitivity

The matrix elements, Eqs. (3.10) and (3.11) won't typically be as nice as the examples discussed in Section 3.1.1. The upper PM RF sideband and the SSB RF sideband tend to be somewhat off resonant. Their corresponding transmission functions and phase gains are complex. Simplification of the matrix elements as in Eq. (3.14) and Eq. (3.16) isn't possible, because the $\Re\{\}$ argument needs to be kept, which makes it a little harder to understand the dependencies of the matrix elements.

The general matrix formula for the PM and SSB outputs can be re-arranged in the following fashion with a bit of algebra.

$$M_{r,j}^P = -|E_l|^2 J_0 J_1 r_{p,0} \Re \left\{ r_{p,-}^* (N'_{0,j} - N_{-,j}^*) e^{-i\beta_r^P} + r_{p,+}^* (N'_{0,j} - N_{+,j}^*) e^{i\beta_r^P} \right\} \quad (3.64)$$

$$M_{r,j}^S = -|E_l| J_1 a_s \Re \left\{ r_{p,-} r_{p,s}^* (N'_{-,j} - N_{s,j}^*) e^{i\beta_r^S} \right\} \quad (3.65)$$

The power cavity reflectivity r_p now have an additional subscript to indicate whether it refers to the carrier (0), the upper PM RF sideband (+), the lower PM RF sideband (-), or the SSB RF sideband (s). The variable a_s is the amplitude of the SSB relative to the laser output amplitude, assumed to be real. These formulas apply to the matrix elements of the reflected photodiode, where the phase gain N' is evaluated for the various degrees of freedom. The substitutions $N' \rightarrow N$ and $r_p \rightarrow p_p$ supply the matrix elements for all signal ports of the pickoff photodiode, $M_{p,j}^P$ and $M_{p,j}^S$.

The Φ_+ degree of freedom is actually fairly simple, due to the fact that the RF

sidebands are very insensitive to the arm cavity modes, relative to the carrier sensitivity. The N and N' 's associated with the RF sidebands are 0, to good approximation.

$$M_{r,\Phi_+}^P = r_{p,0} N'_{0,\Phi_+} \Re \left\{ r_{p,-} e^{i\beta_r^P} + r_{p,+} e^{-i\beta_r^P} \right\} \quad (3.66)$$

$$M_{p,\Phi_+}^P = p_{p,0} N_{0,\Phi_+} \Re \left\{ p_{p,-} e^{i\beta_p^P} + p_{p,+} e^{-i\beta_p^P} \right\} \quad (3.67)$$

$$M_{r,\Phi_+}^S = 0 \quad (3.68)$$

$$M_{p,\Phi_+}^S = 0 \quad (3.69)$$

The constants $-|E_l|^2 J_0 J_1$ and $-|E_l|^2 J_1 a_s$ have been dropped, since they're common to every element in the PM output and SSB output matrices, respectively.

The ϕ_+ degree of freedom affects every frequency involved in the interferometer, since all frequencies are meant to resonate in the power cavity. The matrix elements associated with this degree of freedom are

$$M_{r,\phi_+}^P = r_{p,0} \Re \left\{ r_{p,-}^* (N'_{0,\phi_+} - N_{-, \phi_+}^*) e^{-i\beta_r^P} + r_{p,+}^* (N'_{0,\phi_+} - N_{+, \phi_+}^*) e^{i\beta_r^P} \right\} \quad (3.70)$$

$$M_{p,\phi_+}^P = p_{p,0} \Re \left\{ p_{p,-}^* (N_{0,\phi_+} - N_{-, \phi_+}^*) e^{-i\beta_p^P} + p_{p,+}^* (N_{0,\phi_+} - N_{+, \phi_+}^*) e^{i\beta_p^P} \right\} \quad (3.71)$$

$$M_{r,\phi_+}^S = \Re \left\{ r_{p,-} r_{p,s}^* (N'_{-, \phi_+} - N_{s, \phi_+}^*) e^{i\beta_r^S} \right\} \quad (3.72)$$

$$M_{p,\phi_+}^S = \Re \left\{ p_{p,-} p_{p,s}^* (N_{-, \phi_+} - N_{s, \phi_+}^*) e^{i\beta_p^S} \right\} \quad (3.73)$$

Both the reflected and pickoff photodiodes see the carrier on a bright fringe due to the reflectivity of the Michelson being $\propto \cos(\phi_-)$. The derivative of the carrier field with respect to the ϕ_- degree of freedom is zero. For the PM output signals, this allows some simplification of the formula.

$$M_{r,\phi_-}^P = r_{p,0} \Im \left\{ \frac{\partial r_{p,-}^*}{\partial \phi_-} e^{-i\beta_r^P} + \frac{\partial r_{p,+}^*}{\partial \phi_-} e^{i\beta_r^P} \right\} \quad (3.74)$$

$$M_{p,\phi_-}^P = p_{p,0} \Im \left\{ \frac{\partial p_{p,-}^*}{\partial \phi_-} e^{-i\beta_p^P} + \frac{\partial p_{p,+}^*}{\partial \phi_-} e^{i\beta_p^P} \right\} \quad (3.75)$$

$$M_{r,\phi_-}^S = \Re \left\{ r_{p,-} r_{p,s}^* (N'_{-, \phi_-} - N_{s, \phi_-}^*) e^{i\beta_r^S} \right\} \quad (3.76)$$

$$M_{p,\phi_-}^S = \Re \left\{ p_{p,-} p_{p,s}^* (N_{-, \phi_-} - N_{s, \phi_-}^*) e^{i\beta_p^S} \right\} \quad (3.77)$$

The ϕ_s degree of freedom is quite simple. First, the carrier is completely insensitive to this degree of freedom because of the dark fringe condition - no carrier light is in the signal cavity. Second, the upper RF sideband is largely non-resonant in the signal cavity. So both N and N' associated with the upper RF sideband as well as the single sideband can be set to 0.

$$M_{r,\phi_s}^P = -r_{p,0}r_{p,-}N'_{-, \phi_s} \cos(\beta_r^P) \quad (3.78)$$

$$M_{p,\phi_s}^P = -p_{p,0}p_{p,-}N_{-, \phi_s} \cos(\beta_p^P) \quad (3.79)$$

$$M_{r,\phi_s}^S = r_{p,-}N'_{-, \phi_s} \Re \left\{ r_{p,s}^* e^{i\beta_r^S} \right\} \quad (3.80)$$

$$M_{p,\phi_s}^S = p_{p,-}N_{-, \phi_s} \Re \left\{ p_{p,s}^* e^{i\beta_p^S} \right\} \quad (3.81)$$

3.3.2 Dark Port Signals

The PM output at the dark port is particularly simple. Since there's no DC carrier present, the only possible measured signal will be due to signals impressed on the carrier. Derivatives with respect to the RF sidebands can be ignored. Furthermore, since the carrier is on a dark fringe, only signals which can perturb that dark fringe condition appear, namely the Φ_- and ϕ_- degrees of freedom.

The derivatives with respect to the field at the dark port take on the following products.

$$\begin{aligned} \frac{\partial d_p}{\partial \Phi_-} &= \frac{\partial d_p}{\partial t_s} \frac{\partial t_s}{\partial t_m} \frac{\partial t_m}{\partial \Delta r_{ac}} \frac{\partial \Delta r_{ac}}{\partial \Phi_-} \\ \frac{\partial d_p}{\partial \phi_-} &= \frac{\partial d_p}{\partial t_s} \frac{\partial t_s}{\partial t_m} \frac{\partial t_m}{\partial \phi_-} \end{aligned} \quad (3.82)$$

These equations use the fact that some of the partial derivatives are zero,

$$\frac{\partial d_p}{\partial r_s} = \frac{\partial t_s}{\partial r_m} = 0 \quad (3.83)$$

which follows from the fact that

$$\frac{\partial r_m}{\partial \Phi_-} = \frac{\partial r_m}{\partial \phi_-} = 0 \quad (3.84)$$

Individual Derivatives

The field at the dark port, relative to the input, is

$$d_p = \frac{t_{prm} t_s e^{-i\phi_+/2}}{1 + r_{prm} r_s e^{-i\phi_+}} \quad (3.85)$$

where the transmissivity of the signal cavity is given by

$$t_s = \frac{t_m t_{sem} e^{-i\phi_s/2}}{1 - r_m r_{sem} e^{-i\phi_s}} \quad (3.86)$$

The derivatives in Eq. (3.82) are seen to be all quite trivial.

Signal Sensitivity

The matrix terms at the dark port take on a fairly simple form.

$$M_{d,\Phi_-}^P = \Im \left\{ \frac{\partial d_{p,0}}{\partial \Phi_-} (d_{p,-} e^{i\beta_d^P} + d_{p,+} e^{-i\beta_d^P})^* \right\} \quad (3.87)$$

and

$$M_{d,\phi_-}^P = \Im \left\{ \frac{\partial d_{p,0}}{\partial \phi_-} (d_{p,-} e^{i\beta_d^P} + d_{p,+} e^{-i\beta_d^P})^* \right\} \quad (3.88)$$

Using Eq. (3.82), it can be seen that the ratio between these two matrix elements is roughly $|\frac{\partial \Delta r_{ac}}{\partial \Phi_-}|$.

Demodulation Phase at the Dark Port

The constraints placed on the demodulation phase in the reflected and pickoff signal ports don't apply at the dark port. From a controls perspective, the first guess about the demodulation phase would be to maximize the DC sensitivity to the Φ_- degree of freedom. However, this also is the gravitational wave readout signal, and so more

care must be applied to this question.

In general, the dependence of the gravitational wave transfer function on demodulation phase is fairly complex. Appealing to Eq. (3.21), and noting that the DC carrier $E_{00} = 0$,

$$|\tilde{H}_{d,\Phi_-}^P(\omega_g)| = |E_{0+}(E_{-0}e^{-i\beta} + E_{+0}e^{i\beta})^* + E_{0-}^*(E_{-0}e^{-i\beta} + E_{+0}e^{i\beta})| \quad (3.89)$$

This can be maximized for any particular frequency component by using the transmission function for the upper and lower signal sidebands. The actual solution is quite complicated and not particularly interesting. Furthermore, the technique of maximization over the bandwidth will depend on the gravitational wave signal of interest. A periodic source will maximize at a single frequency, while a signal with a broad bandwidth will require a maximization of the convolution of the transfer function Eq. (3.89) with the gravitational wave source. However, some limiting cases can be of interest.

As the frequency approaches DC, the magnitudes of the transmission functions t_{0+} and t_{0-} (these t 's are for the transmission of the gravitational wave audio sidebands) approach a common value, call it $t_{0,DC}$. The DC gain is proportional to

$$|H(0)| \propto \Re \{ (E_{-0}^*e^{i\beta} + E_{+0}^*e^{-i\beta})e^{-i\arg(t_{0,DC})} \} \quad (3.90)$$

The phase which maximizes the DC gain is given by

$$\beta = \arctan \frac{\Im \{ (E_{-0} - E_{+0})e^{-i\arg(t_{0,DC})} \}}{\Re \{ (E_{-0} + E_{+0})e^{-i\arg(t_{0,DC})} \}} \quad (3.91)$$

Another case of interest is around the peak frequency. In the detuned interferometer, the narrowband peaking around a particular frequency of interest only accentuates one of the two audio sidebands. Typically the magnitude of the transmission function for the audio sideband which isn't accentuated is much smaller than its complement. Assuming this, the term involving the smaller transmission function can be dropped. The phase of larger transmission function is common and so can be

dropped. It can then be seen that maximizing the transfer function in the bandwidth around the peak is equivalent to maximizing the RF sideband phasor.

$$\beta = \frac{\arg(E_{-0}) - \arg(E_{+0})}{2} \quad (3.92)$$

Another consequence of the choice of demodulation phase is its effect on the value and magnitude of the peak frequency. For a given demodulation phase, the frequency response is the projection of the signal ellipse traced out by the upper and lower gravitational wave phasors on the resultant RF sideband phasor. The orientation and major axis of this ellipse varies with frequency. It's imaginable that the frequency which has the largest projection on the RF sideband resultant may vary as a function of demodulation phase. This is shown in the following figures. Figure 3.13 shows the case for the narrow band interferometer.

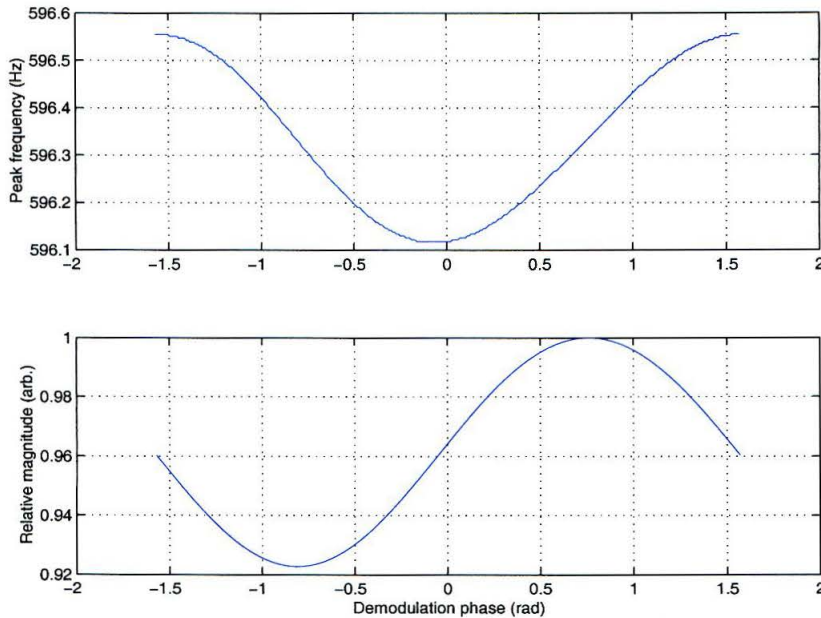


Figure 3.13: Variation of the peak sensitivity frequency with demodulation phase. Also plotted is the relative magnitude of the transfer function with demodulation phase. This case is for a narrowband RSE interferometer, with $T_{itm} = 0.5\%$ and $T_{sem} = 0.2\%$.

The effect on the peak frequency is small in this case, roughly 0.5 Hz variation.

The magnitude likewise doesn't suffer too much, about 8% degradation. Using the demodulation phase to change the peak frequency doesn't appear to be too effective.

Figure 3.14 shows the case for the optimized broadband interferometer. There's a much stronger dependence of the peak frequency on demodulation phase, showing roughly 30 Hz variation. However, the corresponding sensitivity likewise varies strongly, with as much as 60% degradation.

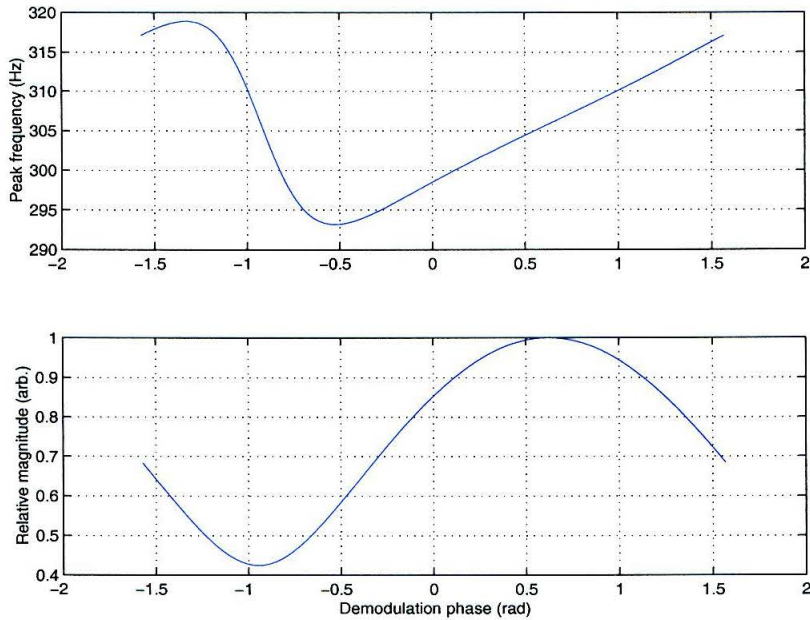


Figure 3.14: Same as Figure 3.13, for an optimized broadband interferometer. The ITMs are $T_{itm} = 0.5\%$ and the signal mirror is $T_{sem} = 5\%$.

3.4 Matrix of Discriminants

In Chapter 2, two candidate RSE interferometers were described, and the optics for each configuration were specified. The first configuration analyzed with respect to its matrix of discriminants is the optimized broadband RSE, and second is the 1 kHz narrowband RSE interferometer.

3.4.1 Optimized Broadband

A set of optics for the optimized broadband interferometer was derived in Section 2.3.2 from the *bench.m* program. Best overall sensitivity to neutron-neutron binary coalescence was found with an interferometer whose ITM transmittances are 0.5% and a signal mirror transmittance of 5%. The power mirror is chosen to couple 99% of the input carrier power into the interferometer, erring on the over-coupled side. This sets the power mirror transmittance at roughly 8.5%. This number can vary somewhat depending on the actual losses in the interferometer. The detuning phase to optimize the frequency response is 0.09 rad.

RF frequencies $f = 27$ MHz and $3f = 81$ MHz are used (this matches with the tabletop experiment in Chapter 4) to satisfy the $f_2 = 3f_1$ signal extraction scheme, as well as to keep the RF frequencies below 100 MHz. A free spectral range of 18 MHz will resonate the PM sidebands and the single RF sideband, as well as setting the power cavity on anti-resonance for the carrier. The length corresponding to this is 8.328 m. The signal cavity, at broadband, is chosen to be consistent with a free spectral range of $81/5 = 16.2$ MHz, corresponding to 9.253 m. With a detuning of 0.09 radians, the length shift necessary is 2.65 cm, setting the signal cavity length to 9.279 m.

The asymmetry which optimally couples the 81 MHz sideband is, from Eq. (3.34), 1.83 cm. Given this, the matrix of discriminants is calculated and presented in Table 3.1. First, it can be noted that the comparison between the analytical formulas and the results of *Twiddle* is quite good. Disparities can be attributed to assumptions about the sensitivity of the RF sidebands to the arm cavities, as in the Φ_- signal in the reflected and pickoff 81 MHz ports, as well as the Φ_+ signal in the 54 MHz ports. The discrepancy of the ϕ_s signals in the reflected and pickoff 81 ports can be attributed to the assumption of the lack of sensitivity of the non-resonant RF sideband in the ϕ_s cavity.

The signals for the arm cavity degrees of freedom are without competition. The presence of other signals will contaminate the performance of these degrees of freedom,

	Φ_+	Φ_-	ϕ_+	ϕ_-	ϕ_s
Refl 81	2400 2400	0 -0.0006	-1.7 -1.7	-0.51 -0.51	0.37 0.34
Pick 81	96000 96000	0 -0.09	54 54	-71 -71	51 47
Dark 81	0 0	-77 -77	0 0	-0.097 -0.097	0 0
Refl 54	0 0	0 0	-0.25 -0.25	-0.014 -0.015	-0.35 -0.35
Pick 54	0 0	0 0	-6.3 -6.4	-0.057 -0.055	9.6 9.7

Table 3.1: Matrix of discriminants for an optimized broadband interferometer. Numbers in bold are predictions from *Twiddle*, while normal text numbers are generated from the analytical formulas of this Chapter.

but it's noted that the coupling is typically small; less than part per thousand.

The ϕ_- signal is not the dominant signal in any port. However, in the pickoff 81 port, only the Φ_+ matrix element is larger. Analysis of an ill-conditioned 2×2 submatrix similar to the one defined by the Φ_+/ϕ_- matrix elements in the reflected and pickoff 81 signal ports was a large part of the thesis of Regehr.[32] He showed that such a plant can be stable, and how to set specifications for loop gains such that system performance degradation due to the cross coupling is minimized. Some of his results are repeated in Appendix C, and will be returned to later.

The SSB output signals, which are used for ϕ_+ and ϕ_s , are also somewhat ill-conditioned. It might be expected that this would occur due to the fact that, analyzed independently, the signal cavity has a higher finesse than the power cavity. This implies that the phase gain is larger for ϕ_s , and so it would dominate the ϕ_+ signal.

This matrix has been derived assuming an asymmetry which optimally couples the resonant PM RF sideband to the dark port. It was noted earlier that this probably isn't the best choice, due to the sensitive dependence of the state of that RF sideband with respect to variation in losses. In response, the asymmetry should be changed to reduce the transmittance to some non-maximum, but still acceptable level. The dependence of the matrix terms on the asymmetry will be examined.

The signal cavity is fairly non-resonant for the upper PM RF sideband and the SSB. Variation of the asymmetry, which changes the reflectivity of the front mirror of this cavity, doesn't affect these sidebands much. Increasing the asymmetry does decrease the transmittance of the coupled cavity for the lower PM RF sideband and lowers the effective finesse of both the power and signal cavities. This also increases the amount of reflected light, while decreasing the light at the pickoff. The internal phase gains for the lower PM RF sideband with respect to the power and signal cavities then stay relatively the same, because both the derivative and the transmission function decrease. The external phase gains, however, decrease because the derivatives decrease, while the transmission function increases. The asymmetry can be increased enough such that, in reflection, N'_{-, ϕ_s} decreases below $N'_{-, \phi_+} - N'_{s, \phi_+} \approx N'_{s, \phi_+}$ (see Eq. (3.80) and Eq. (3.72)). Thus, the ϕ_+ signal can be made dominant in the reflected SSB output port, diagonalizing the control of ϕ_+ and ϕ_s . Table 3.2 shows this trend.

Asymmetry (cm)	$N'_{-, \phi_+} - N'_{s, \phi_+}$	N'_{-, ϕ_s}	$N_{-, \phi_+} - N_{s, \phi_+}$	N_{-, ϕ_s}	$ d_- ^2$
1.8	640 + 96	1000	24 - 48	41	98%
3.0	20 + 95	77	15 - 48	58	82%
6.0	1 + 96	16	5 - 48	88	33%

Table 3.2: Variation of phase gains with asymmetry. Overall signs haven't been preserved. The final column is the transmittance of the lower PM RF sideband to the dark port.

Increasing the asymmetry increases the diagonalization of the plant for ϕ_+ and ϕ_s , but it also decreases the RF sideband power at the dark port. The question arises: how much power is needed at the dark port? For the proposed schemes, the power recycling factor is roughly 15. It's anticipated that advanced LIGO II will have about 120 Watts of carrier power incident on the power mirror, which implies (conservatively) about 2000 Watts incident on the beamsplitter. Experiments in Garching have shown that contrast defects on the order of 10^{-4} can be achieved.[30] This estimates that about 0.2 Watts of "junk" light will be incident on the photodiode. It would be desired that the power due to the RF sidebands be at least a factor of

10 more than this. With a transmittance of 100%, this implies a modulation depth of at least 0.27. At the 30% transmittance with a 6 cm asymmetry, the necessary modulation depth increases to about 0.5. The decrease in carrier amplitude, and hence, gravitational wave sensitivity, is about 4%, with a corresponding decrease in the probed volume of space of about 11%. This is just on the edge of being acceptable. There are other factors which come into play, however. One is the fact that LIGO II proposes to use an output mode cleaner, which can improve the contrast by a factor of approximately 100.[52] If this is the case, then the 6 cm asymmetry with a smaller modulation depth will certainly be acceptable.

The matrix with the 6 cm asymmetry is shown in Table 3.3. The optical and

	Φ_+	Φ_-	ϕ_+	ϕ_-	ϕ_s
Refl 81	170	0	0.0030	-0.26	0.017
ϕ_-	170	-0.0003	0.0033	-0.26	0.017
Pick 81	37000	0	-16	-37	2.4
Φ_+	37000	-0.05	-16	-37	2.4
Dark 81	0	71	0	0.089	0
Φ_-	0	71	0	0.089	0
Refl 54	0	0	0.83	0.017	0.11
ϕ_+	0	0	0.84	0.015	0.12
Pick 54	0	0	-1.7	-0.040	-3.1
ϕ_s	0	0	-1.7	-0.034	3.2

Table 3.3: Matrix of discriminants for an optimized broadband interferometer, with the optimized asymmetry of 6 cm.

physical parameters used to generate the matrix of Table 3.3 are given in Table 3.4.

The specifications for the acceptable RMS of residual fluctuations in ϕ_+ and Φ_+ are given by the deviation which degrades the carrier power stored by 1%. The requirements on ϕ_s aren't as clear. Two things are affected by a fluctuation in ϕ_s : a decrease in RF sideband power at the dark port, and a change in the transfer function. Fluctuations in RF sideband power don't affect the sensitivity very much, since both the shot noise and signal scale as the RF sideband amplitude. A requirement of < 1% is probably too strict. The changes in the transfer function will place a stricter requirement on the control of ϕ_s . It's taken as a specification that the fluctuation of

Power recycling mirror	$T_{prc} = 8.3\%$	Arm cavity power	780 kW
Signal mirror	$T_{sem} = 5.0\%$	PM RF sideband frequency	81 MHz
ITM	$T_{itm} = 0.5\%$	PM modulation depth	0.2 rad
Average coating loss	37.5 ppm	SSB sideband frequency	27 MHz
ITM substrate loss	480 ppm	SSB input power	1.25 W
Power recycling gain	17	Power recycling length	8.328 m
Detuning phase	0.09 rad	Signal cavity length	9.279 m
Input power	125 W	Asymmetry	6.0 cm

Table 3.4: Optical and physical parameters for optimized broadband interferometer. Average coating loss includes ETM transmittance.

the transfer function at any frequency point be less than 1% in the bandwidth of interest. For the optimized broadband interferometer, the common mode requirements are given in the following table.

Degree of freedom	Residual length	Residual phase
Φ_+	$\delta L_+ \leq 8 \times 10^{-13}$ m	$\delta \Phi_+ \leq 5 \times 10^{-6}$ rad
ϕ_+	$\delta l_+ \leq 1.3 \times 10^{-9}$ m	$\delta \phi_+ \leq 0.008$ rad
ϕ_s	$\delta l_s \leq 8.5 \times 10^{-11}$ m	$\delta \phi_s \leq 0.0005$ rad

Table 3.5: Common mode residual requirements for the optimized broadband interferometer.

First, it's noted that the ϕ_+/ϕ_s submatrix has been adequately diagonalized. The non-diagonal elements of the matrix do couple noise from one control loop into the other. This is examined in Appendix C. The degradation of the performance in each loop is roughly the scaling factor between the two elements in a row – roughly a factor of 1/7 worse in the ϕ_+ loop and a factor 1/2 worse in the ϕ_s loop. The required performance of these two loops, however, is not terribly strict. In fact, the strictest requirement, for ϕ_s , is only a little smaller than the ϕ_+ requirement for LIGO I.[53]

Not only has the ϕ_+/ϕ_s submatrix been fairly well diagonalized, but the state of the ϕ_- degree of freedom has improved as well, although it is still ill-conditioned. The performance of such a coupled system is not significantly degraded with the establishment of a “gain hierarchy,” discussed in [32] and Appendix C, in which the gain of the Φ_+ loop is larger than the ϕ_- loop by the coupling factor. The coupling

factor to Φ_+ , which was ~ 5000 in the reflected 81 port, is now down to about 600. The loop gain in Φ_+ is typically very large, and it's anticipated that a factor of 1000 between these two loop gains is acceptable, since a similar ratio is achieved in ill-conditioned Φ_+/ϕ_+ submatrix in the the LIGO I design.[54]

3.4.2 Narrowband RSE

In Section 2.3.1, a narrowband interferometer with peak sensitivity at 1 kHz was designed. This interferometer has a signal mirror transmittance of 0.25%, an ITM transmittance of 2%, and a detuning of 0.12 rad. The asymmetry which optimally couples the lower RF sideband is quite small, 2.5 mm. This might be expected, since the signal mirror is now highly reflective, and it takes a correspondingly highly reflective front mirror to bring the reflectivity of the signal cavity down to that of the power mirror, which is roughly 2%. The power recycling gain is about 60. The same modulation frequencies are used, hence the power and signal cavities have the same lengths as for broadband RSE. For a detuning of 0.12 rad, the shift in the signal cavity is 3.55 cm.

The matrix found by using these preliminary numbers is quite similar in nature to the first optimized broadband matrix of Table 3.1. Increasing the asymmetry to 1 cm improves the independence of the control for the ϕ_+ and ϕ_s signals. The PM RF sideband transmittance reduced to roughly 15%. With a power recycling gain of 60, there is approximately 7 kW incident on the beamsplitter. Without an output mode-cleaner, a contrast of 10^{-4} generates about 0.7 W of junk light. This would require about 7 watts of PM RF sideband power, in order that the shot noise from the junk light doesn't seriously degrade the interferometer sensitivity. This would be a bit ambitious. However, an output mode cleaner would make the problem significantly more tractable. With an added suppression of 10^{-2} of the contrast defect, the output decreases to 7 mW, and a modulation depth of $\Gamma = 0.2$ generates about 200 mW PM RF sideband power at the dark port, given the 1 cm asymmetry, which is acceptable. The matrix is given in Table 3.6.

	Φ_+	Φ_-	ϕ_+	ϕ_-	ϕ_s
Ref1 81	-31	0	0.35	-0.50	1.2
ϕ_-	-34	-0.003	0.35	-0.52	1.2
Pick 81	230000	0	650	-270	640
Φ_+	230000	-1.4	640	-280	630
Dark 81	0	3.0	0	0.015	0
Φ_-	0	3.0	0	0.015	0
Ref1 54	0	0	2.9	-0.010	1.0
ϕ_+	0	0	3.0	-0.009	1.0
Pick 54	0	0	19	-0.025	110
ϕ_s	0	0	20	-0.025	-110

Table 3.6: Matrix of discriminants for a 1 kHz narrowband RSE interferometer. The asymmetry has been optimized for good signal diagonalization.

Table 3.7 summarizes the optical and physical parameters used to generate the matrix in Table 3.6.

Power recycling mirror	$T_{prc} = 2.0\%$	Arm cavity power	720 kW
Signal mirror	$T_{sem} = 0.25\%$	PM RF sideband frequency	81 MHz
ITM	$T_{itm} = 2.0\%$	PM modulation depth	0.2 rad
Average coating loss	37.5 ppm	SSB sideband frequency	27 MHz
ITM substrate loss	480 ppm	SSB input power	1.25 W
Power recycling gain	60	Power recycling length	8.328 m
Detuning phase	0.12 rad	Signal cavity length	9.288 m
Input power	125 W	Asymmetry	1.0 cm

Table 3.7: Optical and physical parameters for 1 kHz narrowband interferometer. Average coating loss includes ETM transmittance. SSB power is equal to the input PM RF sideband power.

The specifications for the allowable residual common mode fluctuations are given in Table 3.8. The bandwidth over which the fluctuations in ϕ_s are analyzed is the roughly 50 Hz bandwidth around the 1 kHz peak frequency.

First, it's pointed out that the separation of ϕ_+ and ϕ_s is good. The coupling factors are $\lesssim 1/3$. It's seen, though, that the specifications for the allowable fluctuations are about an order of magnitude tighter than for the optimized broadband case. This is not unexpected, since the power and signal cavities are somewhat higher finesse cavities, which amplifies the effect of length fluctuations.

Degree of freedom	Residual length	Residual phase
Φ_+	$\delta L_+ \leq 8.5 \times 10^{-13}$ m	$\delta \Phi_+ \leq 5 \times 10^{-6}$ rad
ϕ_+	$\delta l_+ \leq 3.4 \times 10^{-10}$ m	$\delta \phi_+ \leq 0.002$ rad
ϕ_s	$\delta l_s \leq 7 \times 10^{-12}$ m	$\delta \phi_s \leq 4 \times 10^{-5}$ rad

Table 3.8: Common mode residual requirements for the 1 kHz narrowband interferometer.

The ϕ_- degree of freedom is somewhat more problematic. Both the Φ_+ and the ϕ_s degrees of freedom have larger matrix elements than the term which is to contribute the signal to control ϕ_- . There was no variation of the asymmetry which could rectify this without reducing the transmittance of RF sideband power to the dark port to less than 1%. However, modeling this system indicates that the gain hierarchy can be used independently for both the ϕ_-/Φ_+ and ϕ_-/ϕ_s submatrices. This is largely due to the fact that the Φ_+/ϕ_s submatrix is sufficiently diagonal. The implication, as shown in Appendix C, is that the loop gains need to scale as the coupling to the weaker loop. This is to say, then, that the Φ_+ loop gain needs to be roughly 70 \times larger than the ϕ_- loop gain, and the ϕ_s loop gain needs to be roughly 3 \times larger than the ϕ_- loop gain. If it's assumed that the loop gains will scale as the inverse of the specification for residual fluctuations, then the gain hierarchy in both of the sub-matrices is automatically satisfied. In Chapter 5, the allowable RMS residual deviation of ϕ_- is determined to be 10^{-10} m, so the ratio of the ϕ_s to ϕ_- loop gains needs to be at least 14. The ratio of the ϕ_-/Φ_+ requirements is about 120. Extending the model in Appendix C to a 3 \times 3 system, the plant and feedback is given by

$$P = \begin{pmatrix} 1 & -.0012 & 0.0028 \\ 68.8 & 1 & -2.4 \\ 0.0059 & 0.0022 & 1 \end{pmatrix} \quad (3.93)$$

$$H = \begin{pmatrix} 1200 & 0 & 0 \\ 0 & 10 & 0 \\ 0 & 0 & 140 \end{pmatrix} \quad (3.94)$$

The first two rows in P have been interchanged, relative to Table 3.6. The first row is the pickoff 81 MHz port and the second row is the reflected 81 MHz port. The third row is the pickoff 54 MHz port. The rows have been scaled to the signal which is being used for control, Φ_+ , ϕ_- , and ϕ_s respectively. Due to the scaling of the plant, the values in H represent the loop gains of each loop. The closed loop gain matrix S , which indicates the residual level of disturbance in each degree of freedom relative to the input noise, is given by $S = (1 + H \cdot P)^{-1}$. The residual disturbance in each loop is given by

$$\vec{e} = S \cdot \vec{n} \quad (3.95)$$

where the error and noise vectors are given by

$$\vec{e} = \begin{pmatrix} e_{\Phi_+} \\ e_{\phi_-} \\ e_{\phi_s} \end{pmatrix} \quad (3.96)$$

$$\vec{n} = \begin{pmatrix} n_{\Phi_+} \\ n_{\phi_-} \\ n_{\phi_s} \end{pmatrix} \quad (3.97)$$

The closed loop gain is found to be

$$|S| = \begin{pmatrix} 1 & 0.13 & 0.0008 \\ 0.57 & 1 & 0.18 \\ 0.014 & 0.026 & 1 \end{pmatrix} \quad (3.98)$$

The rows of the matrix S have likewise been scaled to the contributions from the degree of freedom under control in each row. The second row shows the level of coupling to the ϕ_- degree of freedom. Assuming an equal, but otherwise uncorrelated disturbance in each element of \vec{n} , the ϕ_- performance is degraded by about 16%. This is acceptable.

3.5 Conclusions

Designing the RSE interferometer for astrophysical considerations constrains the choices of the optics used, as well as the carrier phases in the interferometer. With this chosen set of optics, the modulation frequencies and macroscopic lengths in the dual-recycled Michelson need to be found which can give an acceptable set of control signals to control the five longitudinal degrees of freedom.

Both a mathematical and conceptual description of the optical heterodyne signal extraction technique traditionally used in gravitational wave interferometers was developed in this Chapter. Two frequencies of light, typically separated by 10's of MHz, are used, one of which has a signal impressed upon it. These are mixed at the photodiode via the square-law detection process. The frequency with no signal acts as a phase reference, or local oscillator, in order to measure the signal modulations on the frequency which carries the signal.

With this in mind, the RSE interferometer was designed. Perhaps the most critical aspect of the design is the strong transmission of the RF sidebands to the dark port for the gravitational wave readout. With the added detunability of the signal cavity, this becomes a more complicated issue when frontal modulation is used. The issues are the state of the RF sidebands in the power/signal coupled cavity, and the size of the asymmetry. It was chosen that the RF sidebands would be resonant in both the power and signal cavities independently for a broadband RSE interferometer. Detuning the signal cavity for the carrier is accompanied by a macroscopic length shift of the signal cavity to effectively null the detuning phase shift for one of the RF sidebands. The asymmetry had three options: a bright fringe, and a large and small asymmetry which both optimally couple the RF sidebands to the dark port. The small asymmetry solution was chosen. An additional modulation was added in order to extract the new signal from the signal extraction cavity. This was chosen to be a single sideband which resonates only in the power recycling cavity, hence it can act as a local oscillator for the RF sideband which resonates in the signal cavity. The design was further constrained to use modulation frequencies which are integrally related to

each other, such that a single mode cleaner can be used after modulation but before they are input into the RSE interferometer.

Given this design, analytical formulas were derived to generate the matrix of discriminants. These were used, along with the *Twiddle* model, to derive the matrix of discriminants for the 5×5 cross-coupled system. This was done for both the optimized broadband and the 1 kHz narrowband RSE interferometers design in Chapter 2. Variation of the asymmetry was used as a tool to improve the diagonality of the matrix. One positive aspect of this design is that the power and signal cavity submatrix could be diagonalized, with no coupling from the arm cavity degrees of freedom. The Michelson degree of freedom, however, remained strongly coupled with the arm cavity common mode, and so a gain hierarchy needs to be used. Furthermore, in the narrowband interferometer, the Michelson signal port is dominated by signals from both the arm cavity common mode and the signal cavity. It was found that a reasonable double gain hierarchy could be established which did not significantly degrade the performance of the Michelson degree of freedom.

Although two designs were “successfully” implemented, the success largely depended on using the asymmetry as an optimization tool. In both cases, the optimal coupling asymmetry presented an ill-conditioned matrix, which was subsequently improved by increasing the asymmetry. It’s very difficult, however, to quantify this technique. In particular, some cases were found (specifically with $T_{prm} < T_{sem}$) in which variation of the asymmetry did very little to improve the conditioning of the matrix. Clearly, in these types of cases, a much more careful analysis would need to be taken to determine whether some type of gain hierarchy could be established to provide a stable system which provides the necessary performance.

Chapter 4

The RSE Tabletop Prototype Experiment

An experimental verification of the proposed signal extraction scheme was demonstrated on an RSE interferometer which was prototyped on an optical table. This chapter describes the experiment and its results. Section 4.1 will describe the physical design of the experiment. Section 4.2 describes the conditioning of the laser light for the interferometer, while Section 4.3 describes the characterization of the arm cavities. The RSE interferometer is a very complicated system, and locking it in the desired state is a difficult task. Section 4.4 describes the process through which the interferometer is aligned and finally locked, with some confidence that the interferometer is in the correct state. Section 4.5 reports the data from the locked RSE interferometer, including the matrix of discriminants and the RSE transfer function.

4.1 Prototype Design

Figure 4.1 shows the optical layout of the RSE tabletop prototype experiment. The placement of the optics in the figure is fairly close to scale. A brief description of the layout is given here, with a more detailed description of the hows and whys of the various optics, lengths, and other components involved in the following subsections. All of the optics are located on a single optical table, a 5' by 12' Newport RS-4000 optical table on Newport I-2000 vibration isolator legs. A free standing clean room cover surrounds the table. The air flow from the HEPA filters in the ceiling of the clean room were turned off for the running of the experiment due to the noise they generated. A patch panel located on the table is the point at which all electronic signals are passed to three racks of electronics and diagnostic equipment (oscilloscopes, spectrum analyzers, etc.).

In between the laser and the power recycling mirror (PRM) are all the conditioning

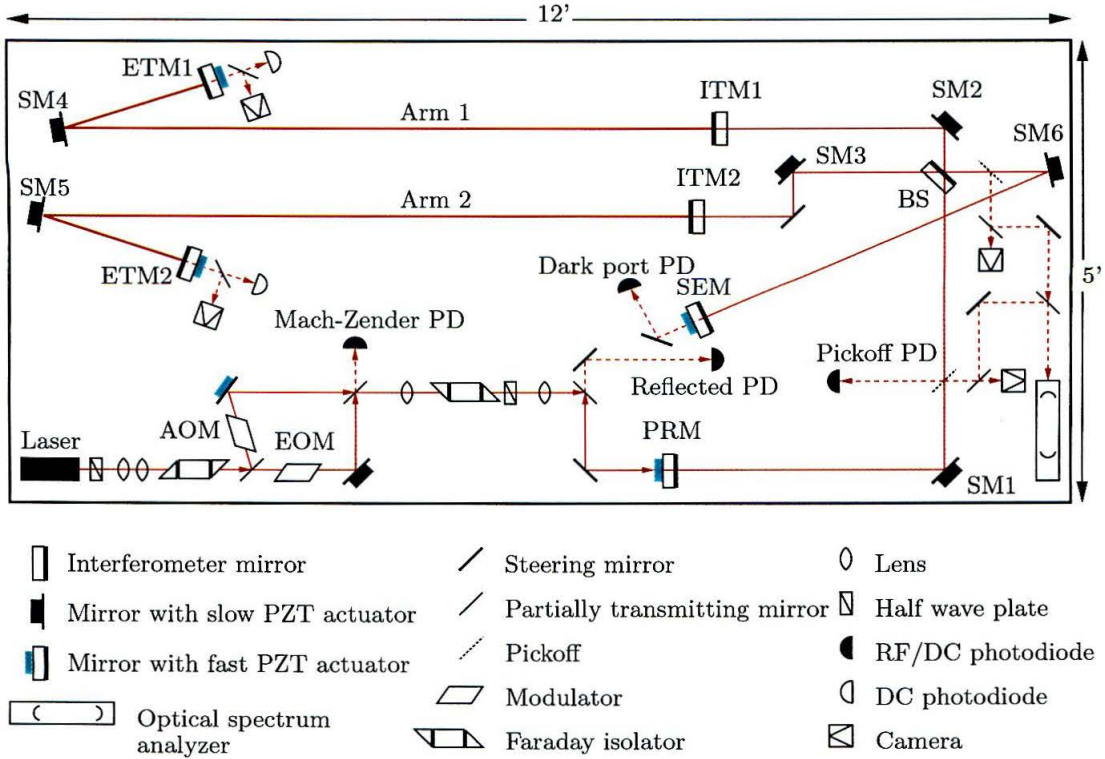


Figure 4.1: Layout of the optical table for the RSE experiment. The dark line of the interferometer mirrors indicates the coated side of the optic. The two beams going to the optical spectrum analyzer do not actually perform any interference. At any one time, one of the beams was blocked so that the other could be analyzed.

optics. Following the beam path from the laser, the first set of two lenses is used to circularize the beam from the laser. Isolation of the laser from back-reflected light is accomplished with the Faraday isolator, in conjunction with the $\lambda/2$ plate between the laser and circularizing lenses. The Mach-Zender interferometer is used to generate the input light spectrum, by phase modulating the light in one path, and frequency shifting the light in the other. Mode matching is performed by the following set of two lenses, and yet another Faraday isolator makes an appearance to isolate the Mach-Zender from the main interferometer. Two steering mirrors, the first partially reflecting, follow the last Faraday isolator, and are used as a periscope to align the input beam into the main interferometer.

The “interferometer mirrors” in the figure are the nominal seven mirrors for RSE.

Two input test masses (ITM) and two end test masses (ETM) form the arms of the interferometer. In addition, there is the beam-splitter (BS), the power recycling mirror (PRM), and the signal extraction mirror (SEM). Many steering mirrors (SM#) are used to fold the light path in order to fit the optical paths onto the table. The steering mirrors also provide convenient points to actuate the various cavity lengths. Two pickoffs are also placed in the beam path inside the interferometer, one in the power recycling cavity, just past SM1, and one in the signal extraction cavity, just past the beam-splitter, before SM6. These pickoffs provide signal and diagnostics.

4.1.1 Optics

Interferometer Optics

The optics are at the core of the design. The main optical components affecting the measurement of the frequency pulling of detuned RSE are the arm cavity ITMs and the signal mirror. Two types of interferometers have been discussed in this thesis, a 1 kHz narrowband and an optimized broadband RSE interferometer. The most generally useful interferometer is the optimized broadband configuration, which is what is tested here.¹

The goal of this experiment was nominally to test RSE, for which the working definition was taken to be a signal tuned interferometer whose ITM transmittances were lower than that of LIGO I. The ITM mirrors chosen for this experiment are CVI PR1-98's with a measured transmittance of $T_{ITM} = 1.65\%$. The ETM mirrors need to have as low a transmittance as possible. Mirrors from REO with 300 ppm transmittance are used.

The signal mirror is a CVI PR1-60, with a measured transmittance of $T_{SEM} = 36\%$. Although this is seemingly quite high, it does give a fairly nice representation of an optimized broadband frequency response.

For the reasonably high losses expected for an interferometer in air, the arm cavities chosen would dictate a power recycling mirror with a transmittance of about

¹In fact, an optimized broadband interferometer configuration is being put forth in the Advanced LIGO proposal.

30%. However, the optical designs considered in this thesis have a PRM which has a higher transmittance than the SEM. This affects how the signals couple together in their respective ports, as well as how the optimization of the matrix of discriminants is accomplished using the asymmetry. In order to be consistent with the designs of this thesis, a CVI PR1-40 with a measured transmittance of $T_{PRM} = 60\%$ was chosen for the PRM. This gives at least some amount of power recycling (approximately 3.5), while also being fairly easy to control.

The beamsplitter is a CVI PR1-50. This is measured to have $R_{BS} = 56\%$ and $T_{BS} = 43\%$.

Mirror Radii of Curvature

The radii of curvature for the mirrors are chosen to achieve the best mode matching of the input light to the interferometer, and so are dependent on the beam radius and the lengths of cavities involved, which is discussed in Section 4.1.2. It was initially desired in the design of this experiment that the beam waist should be as small as reasonably possible. The reason for this relates to aging and losses of the mirrors. In air, dust particles which fall through the beam can be carried by the beam and deposited onto the mirror surface. These particles can occasionally get “baked” onto the surface, and wouldn’t be cleanable by an air duster. A beam with a smaller cross-section was felt to be less susceptible to this problem. Given availability of mirror stock and the optical path lengths involved, a solution was found with a 0.8 mm waist positioned after the beamsplitter at the average of the beamsplitter-ITM distances. Flat ITMs and a 4 m radius of curvature for PRM, SEM, and the ETMs gives a reasonable solution for mode-matching.

Mach-Zender Optics

The purpose of the Mach-Zender is to generate the input spectrum. Most of the light is needed at the Pockels cell, since the carrier light is passed through this device. Only a small amount of light is needed at the AOM, since this generates the SSB RF sideband used for signal extraction. The first beam-splitter in the Mach-Zender is

a CVI W1-1064 window, AR coated one side. The uncoated side reflects about 5%. The recombining beam-splitter is a CVI PR1-50, which has a transmittance of 44% and reflectance of 56%, similar to the main interferometer beam-splitter.

Other Optics

The steering mirrors inside the interferometer should all have as high a reflectance as possible. In the arms, where the losses would be most severely felt, the steering mirrors SM4 and SM5 are REO super-mirrors, with a nominal 15 ppm transmittance and 30 ppm loss. All other steering mirrors are CVI Y1-1064 mirrors, with $R_{SM} > 99.9\%$.

The pickoffs in the power and signal cavities are both CVI W2-1064, two-sided AR coated windows. The reflectivity of each surface is roughly 0.2%. Of the two periscope mirrors used to align the input beam into the interferometer, located just before the PRM, the first is partially transmitting at 1.4% (this is a CVI PR1-99.5 for normal incidence), while the other is a CVI Y1-1064 high reflector.

4.1.2 Lengths and Frequencies

The intent is to measure the RSE transfer function by driving the ETMs through their mirror actuators. PZT response and high voltage electronics bandwidths limit this to a bandwidth $\lesssim 1$ MHz. Hence, the arm cavities need to be as long as reasonably possible so that the peak can be well below 1 MHz with minimal detuning. The arms were chosen to be 2.66 m, which mode matches the input waist (0.8 mm) to the 4 m radius of curvature end mirrors.

The power recycling and signal cavity lengths are chosen to fit the RF sidebands used in the control of the interferometer. The SSB at f is generated by an acousto-optic modulator (AOM), while the PM RF sidebands at $3f$ are generated by a Pockels cell (EOM). Keeping the frequencies below 100 MHz is desirable, since RF electronics and photodiodes are then easier to make and/or more readily available. The lowest frequency AOM found was a 27 MHz frequency shifter, which sets the drive to the Pockels cell at 81 MHz.

The shortest choice for the power recycling cavity length is consistent with a free spectral range of 54 MHz, which is 2.78 m. The nominal signal cavity length for broadband RSE is consistent with a free spectral range of 81 MHz, or 1.85 m. A detuning of 27° , or 0.47 rad, was chosen to give the peak in the frequency response at roughly 130 kHz. This detuning shifts the length of the signal cavity by

$$\delta l = \frac{\phi_{dtc}}{2\pi f_{mod}} = 27.8 \text{ cm} \quad (4.1)$$

This sets the signal cavity length to 2.13 m.

The asymmetry is set to optimize the diagonality of the matrix of discriminants, as discussed in Section 3.4. This was done numerically by varying the asymmetry until a reasonable matrix was found, which was at 27.7 cm.

4.1.3 Electro-Optics

The Laser

The light source is a Lightwave model 126-1064-100, which is a 100 mW NPRO Nd:YAG 1064 nm laser. This model of laser has been measured to have a frequency noise spectrum of roughly $200 \text{ Hz}/\sqrt{\text{Hz}}$ at 100 Hz.[55] Integrating this down to 1 Hz gives an equivalent length noise of roughly 10^{-10} m_{RMS} for cavities on the order of a meter in length, by the relation

$$\frac{\delta f}{f} = \frac{\delta l}{l} \quad (4.2)$$

It was measured that the displacement noise on the table was $\gtrsim 2 \times 10^{-9} \text{ m}_{RMS}$, so frequency noise of the laser isn't a concern.

Modulators

The phase modulator is a New Focus 4003, which has an input circuit resonantly tuned to 81 MHz, and roughly 0.2 rad/V modulation depth. The AOM used to generate the SSB is a Brimrose Corporation AMF-27-5-1064 frequency shifter. The AOM requires +19 dBm of input RF power, and advertises 90% efficiency for the first

order diffracted beam. Although this degraded over time to roughly 50%, 80% was achieved initially. It's assumed this was due to drifts in the alignment of the AOM. Since the amplitude of the single sideband wasn't critical, no attempts were made to re-optimize the alignment.

Faraday Isolators

The isolators are necessary to keep reflected light from one interferometer from coupling backwards to a previous interferometer. Specifically, any light going back into the laser resonator tends to cause the laser to either become noisy or go unstable altogether. Also, it was noticed that light reflected from the main interferometer significantly degraded the control of the Mach-Zender. Isolation is actually accomplished by two components, the Faraday isolator component, which is an Electro-Optics Technology 1845-2 isolator, in conjunction with a CVI QWPM-1064-05-2 half wave plate, to keep the polarization vertical.

Photodiodes

Two different types of photodiodes² are used to generate the signals used to control the interferometer, which are labeled "RF/DC photodiodes" in Figure 4.1. First, two tuned photodiodes built in-house by the LIGO electronics shop were acquired. The transimpedance electronics of one was tuned to 81 MHz, while the other was tuned to 54 MHz. The RF gains were typically a few hundred V/W. The other two photodiodes used were New Focus model 1811 photodiodes. These have a flat frequency response up to the 125 MHz roll-off frequency. They have very high RF gain, roughly 30000 V/W, as they are designed to operate in very low light experiments. Because of this, neutral density filters usually were needed to keep their RF amplifiers from saturating.

The two New Focus 1811 photodiodes were used as the reflected and pickoff photodiodes. The 54 MHz tuned PD is used as the dark port PD, and the 81 MHz tuned PD is used as the Mach-Zender PD. This is somewhat counter to one's notion of how

²In this context, "photodiode" is used to describe both the photodiode element and the associated RF transimpedance electronics.

to do things. The reason is that the gain of the 81 MHz PD was always about an order of magnitude less than the 54 MHz PD, and furthermore it was noticed at some point that the initial tuning of the 81 MHz PD had changed, and whatever advantage the tuning gave to the signal didn't exist anymore. So they were switched.

The measurement of the matrix of discriminants is to be compared to the output of a model, which predicts the watts of signal power at a point in the interferometer, given a normalized displacement of a mirror. Thus, a calibration is needed to characterize the gain from the optic which picks the light out of the main beam to the output of the mixer. The matrix will be measured only at the reflected and pickoff 54 and 81 signal ports, so only these calibrations are needed. The calibration was done by sweeping the Michelson through several fringes, and maximizing the measured demodulated signal with the demodulation phase. Eq. (3.9) gives a model of the optical gain, that is the watts of signal expected, based on a measurement of the laser power and modulation depth. The scale factor which converts this to the volts of the measurement gives the calibration which includes all the effects of the pickoff, neutral density filters, the RF gain of the transimpedance electronics, cable and mixer loss, etc. This is shown in Figure 4.2. The uncertainties are primarily due to the noise of

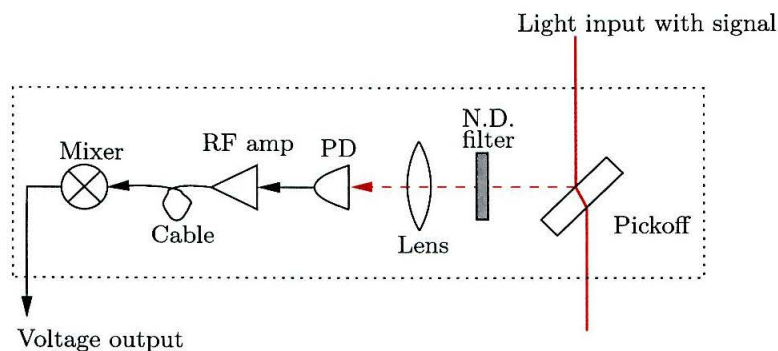


Figure 4.2: Calibration of photodiode/mixer gains. Modeling the signal input at the pickoff (in watts) and measuring the voltage signal out gives a calibration which takes into account all the objects in the dashed box.

the measurement itself ($\leq 5\%$) and the uncertainties in the power contained in the carrier and RF sidebands ($\simeq 5\%$).

	Reflected 81	Reflected 54	Pickoff 81	Pickoff 54
Readout gain (V/W)	6.05 ± 0.3	6.33 ± 0.4	13.5 ± 0.7	26.5 ± 1.5

Table 4.1: Calibration of the readout gains of the signal ports.

The “DC photodiodes” in Figure 4.1 are Thorlabs DET410 photodiodes. These only have a biasing battery, and no transimpedance electronics. A $1\text{k}\Omega$ resistor was used as the transimpedance. These photodiodes are used to monitor the light power stored in the arms.

Cameras

Four cameras were used to monitor power build-up, mode shape, and also a little bit as a fiducial for alignment. The cameras are part of the Radio Shack VSS-400 4-channel observation system, and have a decent sensitivity at 1064 nm. The imaging lens on each camera was removed, and the light was incident directly on the CCD element.

Optical Spectrum Analyzer

A Melles-Griot 13 SAE 006 optical spectrum analyzer was used to monitor the power in each of the RF sidebands and the carrier. Monitoring was done in both the power and signal cavities, using the pickoffs in each cavity to sample the light. Since there was only one spectrum analyzer, the light from both pickoffs was directed into the analyzer, while at any one time, one of the paths was blocked to make a measurement.

4.1.4 Mirror Mounting

Mirror Actuation

Two types of actuators were used in this experiment, a “fast” actuator, with low dynamic range, but high bandwidth, and a “slow” actuator, with large dynamic range, but low bandwidth. The design for the fast mirror actuator was taken from the tabletop wavefront sensing FMI of Mavalvala.[56] This design, shown in Figure 4.3,

has a relatively high usable bandwidth for 1" optics. The first series resonance is

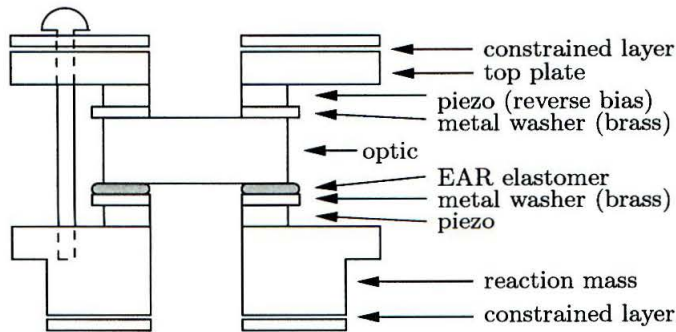


Figure 4.3: Fast piezo mirror actuator. The top plate and reaction mass have a constrained layer of epoxy to damp out resonances. Voltage is applied to the metal washers, the reaction mass and top plate are at ground. The elastomer is used for compliance.

at roughly 50 kHz. The piezos used are PKI 552 actuators from Piezo Kinetics Corporation. The response of these actuators is advertised to be around $0.5 \mu\text{m}/\text{kV}$ per piezo, with a maximum range of $-200\text{V}/+400\text{V}$. The maximum dynamic range, then, is not quite a fringe width (these actuate along the beam path, so the round trip path length is doubled). These actuators are used for the PRM, SEM, ETM1 and ETM2 mirrors, which account for four of the five degrees of freedom (Φ_+ , Φ_- , ϕ_+ , and ϕ_s).

It would take a large stack of these to have the desired dynamic range of a few μm 's (several fringes), so an actuation design which splits the feedback between a low dynamic range, high bandwidth actuator, and a high dynamic range, low bandwidth actuator, was used. The second actuator is a commercial unit, the Burleigh PZAT-80. These have an advertised $6 \mu\text{m}/\text{kV}$ response, with a 0 to $+1000\text{V}$ operating range. Measurements of these actuators showed a roughly 10% spread in the real actuation response at the mid-point of the range (around 500V). More troubling was that the response varied about 20% depending on the bias value. The largest variability of the response was seen at low bias, ≤ 200 volts. These actuators are used on the SM1-6 steering mirrors.

In terms of the degrees of freedom, the actuation of ϕ_+ is accomplished by a

combination of the PRM and SM1 mirrors. ϕ_s uses the SEM and SM6 mirrors. The arm cavity degrees of freedom, Φ_+ and Φ_- , use common and differential combinations of the arm 1 and arm 2 actuation. Arm 1 uses the ETM1 and SM4 mirrors, while arm 2 uses the ETM2 and SM5 mirrors. The Michelson degree of freedom, ϕ_- , is different in that it uses only slow actuators, SM2 and SM3, in a differential mode. The gain of the actuators relevant to the matrix and transfer function measurements is tabulated below.

	ETM1	ETM2	PRM	SEM	SM2
PZT response (nm/V)	0.39	0.30	0.32	0.20	6.0

Table 4.2: Effective response of mirror actuators used in transfer function measurements. For the SM2 piezo, which is a slow piezo tilted 45° to the beam path, the additional factor of $\sqrt{2}$ is included in this gain.

Mirror Mounts

The physical mounts used to hold both the fast and slow mirror actuators are the Newport SL51 gimbal mounts. The beamsplitter uses a Newport SK25.4 high-resolution gimbal mount. It has no actuation for the longitudinal position of the mirror. The ITM mirrors, which also have no longitudinal actuation, use the Newport SL25.4 gimbal mounts.

Coarse alignment of the tilt of the mirrors was done by hand using micrometers on the gimbal mounts. Fine alignment was accomplished using Thorlabs AE0505D16 piezos, which were sandwiched in between the pusher on the gimbal mount and the micrometer. Brass extenders were used to house the alignment piezos, and were taken from Regehr's experiment.[32] Coarse alignment was typically done before the interferometer was locked, while fine alignment was done after lock was acquired by adjusting the voltage applied to the alignment piezos.

4.1.5 Electronics

There are two main parts to the electronics, which are all analog. The first part is the feedback electronics, which filter, condition, and amplify the control signals, and then drive the mirror actuators. The second part is the RF electronics, which are used for generating the input spectrum of light, as well as providing local oscillators (LO) for the demodulation process. This section is meant to be a general description. Schematics are given in Appendix D.

Feedback Electronics

A general outline of the feedback electronics is shown in Figure 4.4. There are some

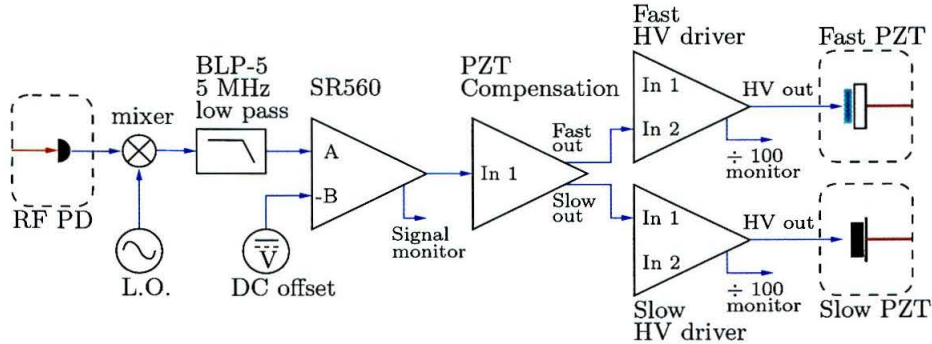


Figure 4.4: Block diagram of the feedback electronics. The elements in dashed boxes are on the optical table. The “-B” input of the SR560’s is used for calibrated offset adjusts, as well as some transfer function measurements. The SR560’s also have a second buffered output used for monitoring signals. The second inputs of the HV drivers also are convenient places for making transfer function measurements, when above unity gain.

modifications to this outline in some cases. The ϕ_{MZ} does not use a SR560 in its feedback. The ϕ_- feedback also doesn’t use a SR560, and furthermore the PZT compensation module is a unique set of electronics, the output of which goes to two slow HV drivers differentially, driving SM2 and SM3. As mentioned before, the feedback to Φ_+ and Φ_- is done as a combination of the actuators in both arms. Feedback for Φ_+ is done by driving both ETMs as well as SM4 and SM5 with the same sign. Feedback for Φ_- is done by driving ETM1 and SM4 with an opposite sign

from ETM2 and SM5. A box of electronics, called the “CM/DM driver,” was built which splits the output of the Φ_+ and Φ_- compensation modules into signals for each of the four actuators in both arms, and then appropriately sums and differences the signals. The output is then directed to the high voltage drivers for ETM1, ETM2, SM4, and SM5. The CM/DM driver also includes test inputs for the Φ_+ and Φ_- modes.

The SR560 amplifiers function not only as amplifiers and filters, but also as convenient points for summing offsets, signal monitoring, and transfer function measurements. They also do a nice job of breaking ground loops.

The PZT compensation modules contain a variable gain and a feedback sign switch. The electronics for splitting the feedback into fast and slow paths is done in these modules. They also contain a switchable boost stage, which adds roughly 500 gain at low frequency. The boost is turned off for acquisition, and turned on once all loops are locked. There is also a switchable integrator in the slow path, which is also left off until lock is acquired.

The high voltage (HV) drivers have $\times 100$ gain. The fast HV driver is capable of driving ± 200 V, while the slow HV driver can output 0 to +1000 V. The slow HV drivers also contain a bias knob, which allows the user to vary the voltage to the slow piezos by hand. All of these HV drivers include test inputs as well as $\div 100$ monitors.

The loop gains for all paths except for ϕ_- have a 10 Hz pole with no boost, and two 10 Hz poles plus a 5 kHz zero with the boost on. When the integrator is turned on, one of these poles moves to DC. Most of these poles and zeros are formed in the PZT compensation electronics. In the exceptions, a 10 Hz pole is removed from the PZT compensation and is implemented in the HV drivers for the fast and slow actuators. Additionally, low pass filtering was done in the SR560's at high frequencies (≥ 30 kHz). The ϕ_- compensation has a single 10 Hz pole, which moves to DC when its integrator was turned on. Additionally, a 2 kHz pole is used to low pass the slow PZT resonances as much as possible. There is no boost stage in the ϕ_- feedback.

RF Electronics

RF electronics serve two purposes. First, they drive the Pockels cell and AOM which generate the RF sidebands on the laser light. Second, they supply the local oscillators for the mixers to demodulate all of the signals, as well as a phase shifter for each LO to control the demodulation phase.

The RF frequencies needed are f , $3f$, and $3f - f$. It's not an absolute necessity that f and $3f$ are *exact* multiples of each other. It is necessary that the third frequency be exactly $3f - f$, and furthermore the phase of $3f - f$ needs to be stable relative to the f and $3f$ frequencies. This is most easily done by generating all three frequencies from a single oscillator, which is done on a single board. A HP8656B synthesized signal generator is used to generate 27 MHz (f). This is split three ways by a power splitter. One path is amplified and sent to the AOM. The second path is frequency doubled using a Mini-Circuits SYK-2, followed by tuned resonant filters to reject the fundamental as well as higher harmonics. The third path uses a circuit which creates a square wave from the 27 MHz input, using a Motorola MC10115 quad line receiver chip. The square wave has odd harmonic components, the first being 81 MHz. Several resonant filters are used then to pass the 81 MHz component, while suppressing all other harmonics. Figure 4.5 shows a block diagram of this board.

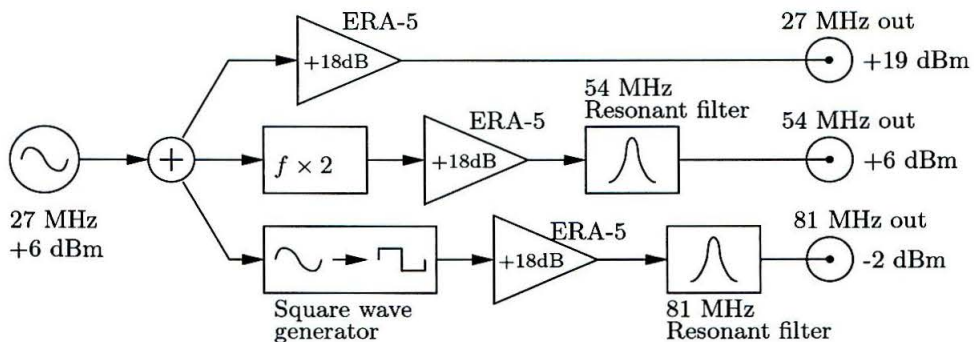


Figure 4.5: Block diagram of the RF frequency generation board.

There are three 54 MHz LO's, three 81 MHz LO's, plus the Pockels cell 81 MHz. A board was designed which splits the input four ways. All four paths are amplified to

output roughly +18 dBm, while three of the four paths include a voltage controlled phase shifter. Two of these were made for the 54 and 81 MHz LO's and Pockels cell drive. The input was taken from the frequency generation board. The voltage controlled phase shifter is a Synergy Microwave PP-924. The input voltage to the phase shifter is controlled by a 10-turn pot on the front panel. The amplification uses Mini-Circuits ERA-1 and ERA-5 monolithic amplifiers. The mixers used are Mini-Circuits ZLW-3SH level 17 mixers.

4.2 Input Optics and the Mach-Zender

This section describes the conditioning of the light incident on the main interferometer, starting from the laser and propagating to the input of the PRM.

The laser output is roughly 110 mW. The beam profile was measured with a Beam-Scan beam profiler. The horizontal waist was found to be 0.20 mm at a distance of 43.1 mm from the output aperture, while the vertical waist was found to be 0.15 mm at a distance of 48.1 mm. Two cylindrical lenses are used to circularize the beam. A solution which places the horizontal and vertical waists at the same location, with the same size, was found using the Gaussian beam lens formula

$$\begin{aligned}\frac{1}{q_2} &= \frac{1}{q_1} - \frac{1}{f} \\ q_i &= z + iz_0 \\ z_0 &= \frac{\pi\omega_0^2}{\lambda}\end{aligned}\tag{4.3}$$

A general rule of thumb which seems to work well is to choose two lenses whose ratio of focal lengths matches the initial ratio of waists. A program was written in *Mathematica* to calculate the waist size and position, relative to the input beam, after the beam is sent through a lens. The program then generates a parametric plot of the new waist size vs. separation, parameterized by the lens position. Data for both horizontal and vertical waists are plotted in the same graph, with the waist separation in the vertical direction increased by the difference in their initial positions.

The intersection of the two plots is a solution which places the same sized waist in the same place. The solution uses $f_H = 226.2$ mm and $f_V = 169.7$ mm lenses, and generates a $\omega_0 = 0.38$ mm waist approximately 38.5 cm from the laser aperture.

The first beamsplitter of the Mach-Zender is a window which transmits about 95% of the incident power. The transmitted light is modulated by the EOM with a modulation depth of $\Gamma = 0.54$. Of the 5% which goes into the reflected path to the AOM, about 50% is diffracted to the first order beam, which is frequency shifted by -27 MHz. An iris, placed near the output beamsplitter of the Mach-Zender, is used to block all other diffracted orders.

The output beamsplitter of the Mach-Zender is roughly 50/50, thus half the light input into the Mach-Zender goes to the interferometer, while the other half is used for control of the Mach-Zender. Demodulation is done at 54 MHz. The importance of control of the Mach-Zender is to suppress any variations in the relative phase between the 27 and 81 MHz sidebands, as relative phase fluctuations between the two RF sidebands will be indistinguishable from the desired signals in the interferometer. The degrees of freedom to be controlled with 54 MHz demodulation are ϕ_+ and ϕ_s . It's expected that the bandwidth needed for these servos will be below 1 kHz, so the bandwidth of the Mach-Zender control is set somewhat larger than this, at 3 kHz.

4.3 Arm Cavities

A reasonably good understanding of the arm cavities is important for generating accurate model predictions. The lack of adequate equipment did not allow a precise characterization of cavity losses and mode matching; however, some simpler measurements were used to place some acceptable constraints on these parameters.

4.3.1 Visibility

Measurements of the power reflected from a cavity in both the resonant and non-resonant state gives information about the losses and mode matching of the cavity.

The reflected powers are used to calculate the cavity visibility, defined as³

$$\mathcal{V} = \frac{V_{bright} - V_{dark}}{V_{bright}} \quad (4.4)$$

V_{bright} is the measured DC voltage with the arms internally blocked, which assumes that the reflectance of the ITM is roughly equal to the reflectivity of the anti-resonant cavity, which is a fairly good approximation when R_{itm} is near 1. V_{dark} is measured when the cavity is locked, and aligned for optimum power build-up. Since the losses and mode matching of the arm cavities is applied to the carrier only, the voltages are corrected for the presence of RF sideband power. This is done by assuming the same amount of RF sideband power in both bright and dark measurements, and calculating this amount as a fraction of the bright measurement (13.8% power in the RF sidebands). This amount is subtracted off of the bright and dark measured voltages. The measured values then are modeled as follows.

$$V_{bright} \propto R_{itm} \quad (4.5)$$

$$V_{dark} \propto (1 - MM) + MM \times R_{cavity} \quad (4.6)$$

MM is the mode matching fraction, and R_{cavity} is the reflectance of the cavity on resonance for the cavity mode, which is a function of the losses. A plot showing the mode matching as a function of the cavity loss is shown in Figure 4.6. This uses the measured visibility of 0.25 ± 0.005 for arm 2, and 0.22 ± 0.005 for arm 1.

4.3.2 Mode Matching

Typically, losses can be easily characterized by measuring the decay time of the cavity. However, with cavities as short as the ones in the prototype, the decay time is on the order of $1 \mu\text{s}$, and the required equipment to modulate the laser's intensity faster than this was not available. So, some tests were done to make an estimate of the

³Note that this is not the normal definition for visibility used in most optics texts. However, it does tend to give a good picture of what the losses of the cavity are, which, in the case of cavities with ideally unity reflectors for end mirrors, does define the ability to resolve a fringe.

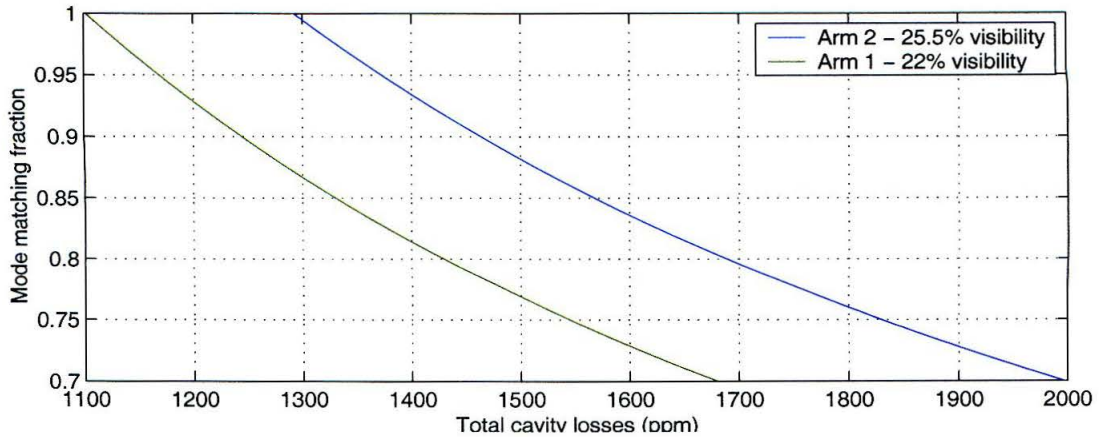


Figure 4.6: Mode matching as a function of cavity loss, given the measured visibilities for arm 1 and arm 2.

modematching, and together with Figure 4.6, estimate the losses.

First, a simple approach was to unlock the cavity from the previous experiment, and sweep it through several fringes, and tabulate the height of the higher order modes (of course the RF modulation was turned off). For arm 2, approximately 84% of the total measured power was in the TEM_{00} mode, with roughly 80% of the remaining 16% in the TEM_{01} mode. If a more careful, painstaking additional alignment was done, arm 1 showed roughly 95% of the power in the 00 mode, while arm 2 was somewhat worse, at around 90% optimum. It's assumed that under normal circumstances, the modematching was more like 85%.

The next approach was to do a theoretical calculation, based on a measurement of the beam profile incident on the cavity and the mirror radii of curvature. First, the waist sizes and positions of the laser light were measured. It is assumed that the light is entirely in the 00 mode, such that the waist size and position completely determine the modal structure of the input light. This is probably a good approximation to the 90% level. Next, the radii of curvature of the mirrors was measured using a fiber optic illuminator, by measuring the distance at which the image of the light source is at the same distance as the light source itself. Surprisingly, the mirrors were significantly off the values ordered from REO. It's not known if this is a result of clamping the

	Waist size (mm)	Waist position (cm)
Horizontal waist	0.80	-27.4
Vertical waist	0.84	+4.3

Table 4.3: Measured beam parameters for the light input into the main interferometer. Waist position is relative to the average power recycling cavity length position, from the power recycling mirror.

mirrors in their actuator mounts, or if the mirrors are simply not the radius that was specified. Table 4.4 summarizes the measured radii, as well as the waist of each arm cavity due to the ETM radius. The mode matching is calculated as an overlap

	Mirror radius (m)	Waist size (mm)
ETM1	5.0 ± 0.3	0.92 ± 0.03
ETM2	5.8 ± 0.3	0.99 ± 0.03
PRM	4.4 ± 0.2	0.85 ± 0.03

Table 4.4: Measured arm ETM radii of curvature, and the resulting cavity mode waists, based on a length of 2.65 m and flat ITMs.

integral between the arm cavity mode from Table 4.4 and the mode of the input light from Table 4.3, where the waist position and size are all that is needed to characterize the fundamental mode.

$$MM = \left| \int_{-\infty}^{\infty} u_{cavity}(x, y, 0) u_{input}^*(x, y, 0) dx dy \right|^2 \quad (4.7)$$

using the Gaussian 00 mode structure

$$\begin{aligned}
u_{00}(x, y, z) &= \sqrt{\frac{2}{\pi}} \frac{1}{\omega(z)} e^{-i\left(\frac{2\pi z}{\lambda} - \eta(z) + \frac{\pi(x^2+y^2)}{\lambda R(z)}\right)} e^{-\left(\frac{x^2+y^2}{\omega(z)^2}\right)} \\
\omega(z) &= \omega_0 \sqrt{1 + z^2/z_0^2} \\
R(z) &= z(1 + z_0^2/z^2) \\
\eta(z) &= \arctan(z/z_0) \\
z_0 &= \pi \omega_0^2 / \lambda
\end{aligned} \quad (4.8)$$

The overlap, or mode matching, between the laser light and arm 1, arm 2, and the

power recycling cavity is 98%, 96%, and 99.6%, respectively. Clearly, the input beam matches the individual cavities quite well.

It's also of interest to calculate the overlap between the sum of the arm cavity modes, and the power recycling cavity, which would give an estimate of the expected coupling of the input light to the power recycled Fabry-Perot interferometer that the carrier light will see.

$$MM = \left| \int_{-\infty}^{\infty} u_{prc}(x, y, 0) \left(\frac{1}{\sqrt{2}} u_{arm_1}^*(x, y, 0) + \frac{1}{\sqrt{2}} u_{arm_2}^*(x, y, 0) e^{i\theta} \right) dx dy \right|^2 \quad (4.9)$$

The term $e^{i\theta}$ arises due to the phase shift to the 00 mode that occurs when the waist is displaced longitudinally along the beam axis.[57] This phase shift is something the control system would null out, which also maximizes the integral. The maximum of this integral is about 97%.

Of course, the theoretical calculations are quite optimistic, and the measured value of approximately 85% modematching is assumed. The losses of the arms are taken to be 1280 ppm for arm 1, and 1520 ppm for arm 2, which includes the transmittance of the ETMs (300 ppm).

4.4 Experimental Process

The experiment goes through several stages before finally locking the RSE configuration. This is necessary to provide some calibration of the demodulation phases, align the optics, and, in general, simply “get one’s bearings.” The imbalance of the RF sidebands in the interferometer makes it necessary to get the demodulation phases and servo gains set right before there would be any hope of acquiring lock. Every instance of locking the RSE interferometer (typically a day-long process) went through the following stages to align the optics and set the phases and offsets before final lock was acquired. Only at the end, with the final transfer function measurement, came a confidence that, in fact, the interferometer was locked correctly. It’s possible that in a more well designed prototype (i.e., one with better mode matching, better

characterized mirrors, alignment servos, etc.) diagnostics such as optical spectrum analyzers and DC power monitoring would give more accurate guideposts for the state of the interferometer. In this case, those diagnostics were still completely invaluable; however, they were taken as only fairly reliable measures, and the ultimate measure of success was in the final measurement of the GW transfer function and its good agreement with the modeled prediction.

4.4.1 Fabry-Perot Michelson

The Fabry-Perot Michelson (FPM) is a fairly straightforward configuration to lock and diagnose. The signal ports used to lock the Φ_+ , Φ_- , and the ϕ_- degrees of freedom are the same as what will be used in locking RSE, namely the reflected 81, the dark port 81, and the pickoff 81 signal ports, respectively.

Several measurements are made on the Fabry-Perot Michelson which give a calibration for the rest of the experiment. First, the demodulation phases for Φ_+ and Φ_- are optimized for their strongest signal. A coarse optimization is done by sweeping an individual arm cavity and making the signal discriminant as large as possible. Lock can be achieved using this method. A finer calibration is done using the HP4395A network analyzer, and a locked interferometer. Figure 4.7 shows the experimental setup. The source of the network analyzer is used to drive the fast piezos of the arms in the differential or common mode by using the CM/DM driver test input, from 10 kHz to 1 MHz. This is also taken to be the input of the transfer function measurement. The output is taken from the mixer output of the degree of freedom under test (Φ_+ or Φ_-). The measurement bandwidth is chosen to be above unity gain so that servo effects can be ignored. The first measurement of the transfer function is used as a calibration by the HP4395. Using this calibration, the demodulation phase is varied by 1/10th turns of the dials, which corresponds to roughly 5° in demodulation phase. As the demodulation phase varies, the magnitude of the calibrated transfer function rises and drops according to the optical gain of the signal, which is being optimized. The demodulation phase which gives the strongest transfer function is used, and the

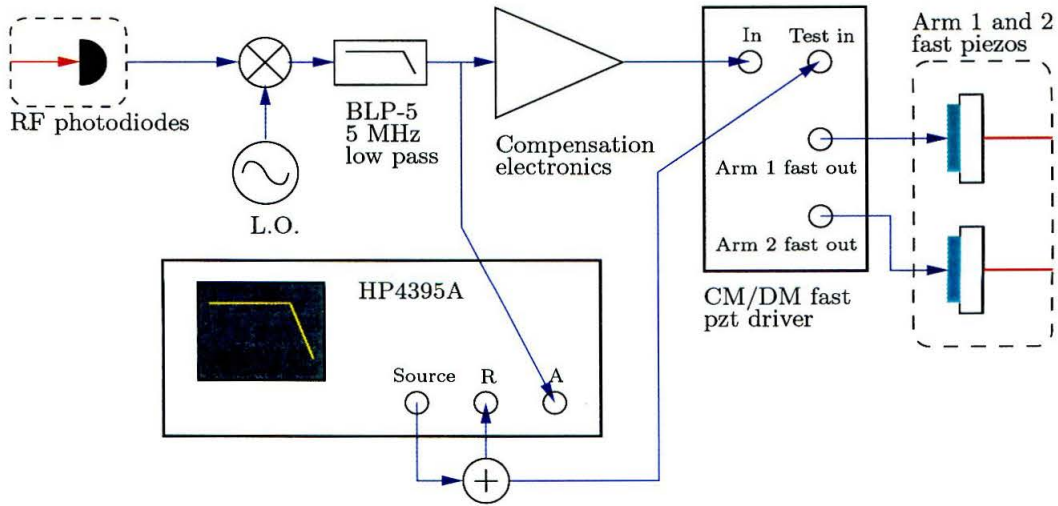


Figure 4.7: Experimental setup for the Φ_+ and Φ_- demodulation phase optimization. The HV PZT drivers between the CM/DM driver and the mirror actuators are not shown.

error is within \pm a 1/10 dial tick, or roughly $\pm 5^\circ$.

The demodulation phase for the ϕ_- degree of freedom is mainly optimized by maximizing the signal discriminant while sweeping the Michelson, with the arms blocked internally. The error here is a little bit larger, roughly $\pm 10^\circ$.

The demodulation phases for the 54 MHz signals are initially set by finding the phase at which the output of the mixer is at zero volts while the FPM is locked. The difficulty in this setting is that it's not easy to distinguish between an electronic offset and an offset generated by demodulation. The method used to deal with this was to vary the demodulation phase through its range, and to note the maximum and minimum voltages out of the mixer. Ideally, these should be equal, and any inequality would be due to offset. The offset adjust of the SR560 was tuned to equalize the maximum and minimum. The demodulation phase was then tuned to zero the output voltage.

One troublesome problem with the RF electronics is significant amounts of cross-coupling between the individual LO/mixer paths. For example, the offset out of one mixer can be seen to vary when the demodulation phase is varied on the LO for a

completely different mixer, and not at all in any sort of linear fashion. Various types of shielding, grounding, and isolating were tried out to find some way to minimize this, with some modest success. In the end, offsets still varied, at most, by a few mV out of the mixers, mostly in the 81 MHz mixers. This tends to throw a bit of uncertainty into this type of calibration of the phase, which is unfortunately an uncertainty which is very hard to characterize. The amount of phase tuning which generated the same levels of offset generated due to tuning other phase shifters was $\leq 10^\circ$.

The other important measurement made with this configuration is the calibration for the RSE measurement. As noted earlier, the detuned RSE Φ_- transfer function will be measured at high frequencies, where the piezos have resonances and the gains are difficult to reliably calibrate. In order to avoid this problem, the RSE transfer function will be normalized to the Fabry-Perot Michelson Φ_- transfer function, similar to the method used by Heinzl, *et al.*[31]

4.4.2 Dual-Recycled Michelson

The phases for Φ_+ and ϕ_- need to be changed when going from the Fabry-Perot Michelson to RSE. Finding these new phase settings is most easily done with the dual-recycled Michelson (DRM), in which the arms are internally blocked. Also, locking the dual-recycled Michelson gives a measure for the power levels expected in the various sidebands for the RSE experiment, which are measured by the optical spectrum analyzer at the power and signal cavity pickoffs. Last, measurement of the 3×3 matrix of discriminants is a useful characterization of the interferometer at this point, since the coupling of the minor degrees of freedom can more clearly be determined without the overwhelming contribution from the arm cavity signals (most notably in the 81 MHz demodulation signal ports).

The procedure to acquire lock begins with the arm cavities internally blocked, and the power and signal mirror grossly misaligned. The Michelson, ϕ_- , is aligned and locked with very low gain, and the SM1 mirror is swept through several fringes as the

PRM is manually brought into alignment. Low gain means the servo bandwidth is also low, and if the cavity is swept through resonance over a time scale faster than the inverse of the servo bandwidth, the ϕ_- servo remains relatively unperturbed by the power recycling cavity resonance. Both the camera and the DC power are monitored at the pickoff in the power recycling cavity. As the PRM is brought into alignment, the trace of the DC power on the oscilloscope shows the resonance peaks, and the modes resonating in the cavity clearly flash in the camera output. Good alignment is achieved when the peaks in the oscilloscope trace are clean, and the mode flashing in the camera is centered and has a good mode shape (no lobes).

Three signal ports are monitored in this sweep: the reflected 81 MHz, and both the reflected and pickoff 54 MHz. The phases of the 54 MHz signals are varied slightly to give the nice, bipolar signals expected from this sweep, and offsets are adjusted slightly to give the appropriate zero crossings. Ideally, the 54 MHz demodulation phases wouldn't have to be changed at all from the setting obtained in the Fabry-Perot Michelson; however, imperfect lengths of the power and signal cavities, even on the order of 1 cm, cause the zero-signal demodulation phase to shift by a few degrees from their settings in the FPM. The shifts in demodulation phase, as well as in offsets, were usually quite small.

The power recycled Michelson is then locked. ϕ_+ is initially locked using the reflected 81 MHz signal port, while ϕ_- uses the pickoff 81 MHz, both with fairly low gain as before. The signal cavity slow piezo, SM6, is swept over several fringes as the signal cavity mirror is manually brought into alignment. Alignment is primarily done by looking at the mode shape seen by the camera at the signal cavity pickoff, and aligning for best mode shape. Looking at the various DC powers, for example at the dark port, is only mildly helpful due to the stronger effect of the signal cavity resonance on the ϕ_+ and ϕ_- degrees of freedom. The pickoff 54 MHz signal is likewise monitored during the sweep, and its shape is also seen to be consistent with what is expected.

Lock is acquired in somewhat of a bootstrapping method. The power and signal cavity servos, using the reflected 54 and pickoff 54 signal ports respectively, are turned

on with minimal gain and using the fast path only, while the Michelson servo is turned off. The Michelson itself is tuned to a carrier dark fringe by hand using the bias of the slow HV PZT drivers. The optical spectrum analyzer output from the signal cavity pickoff (SEC OSA) clearly shows the carrier dark fringe. The power and signal cavities are brought into lock by hand, by tuning the slow power and signal mirrors, again using the bias knob of the slow HV PZT drivers. The guide for finding the right lock is the output of the SEC OSA. It's expected from modeling that no carrier should be seen in the SEC OSA, and the lower RF sideband should be around $5\times$ larger than the upper RF sideband. When this condition is met, the ϕ_+ and ϕ_s servos are turned all the way on, that is the slow path is engaged with its integrator and the overall gain is increased. The Michelson signal port, however, has a large offset, which is expected due to improper demodulation phase. While maintaining the dark fringe condition for the Michelson by hand, the demodulation phase for the pickoff 81 signal port is varied until its output is at 0 volts. The ϕ_- servo is then turned on, and the demodulation phase is fine tuned to best enforce the carrier darkness at the dark port as measured by the SEC OSA. The relative strengths of the carrier and the 81 MHz sidebands in the two OSA outputs is noted and compared with the model in order to give confidence that the interferometer is locked in the right place. The results are tabulated in Table 4.5. This particular metric, however, is only modestly reliable. The OSA response is quite sensitive to the alignment of the beam into it. Misalignment of the cavity, and the effect that has on the mode structure and alignment of every individual RF sideband would conspire to make the uncertainties in this measurement quite difficult to analyze.

The last task before going on to lock the RSE interferometer is to set the phase for the Φ_+ signal, which is the reflected 81 signal port. It's assumed that setting the phase of the reflected 81 signal port doesn't change in going from the dual-recycled Michelson to RSE, and so this is simply done by changing the phase such that the offset voltage in this signal port is 0. The Φ_- phase doesn't need to be changed, since there is no offset generated for the dark port signals at 81 MHz due to the lack of carrier.

	Pickoff	Signal
-81 MHz	1 1	1 1
-27 MHz	1.1 1.3	0.02 0.01
Carrier	3.0 2.9	0 0
+81 MHz	2.9 3.6	0.16 0.17

Table 4.5: Powers in dual-recycled Michelson as measured by the OSA. Experimental numbers are in normal text, *Twiddle* numbers are in bold text. This is a relative measurement, since the OSA output is not reliably calibrated. Hence, all modeled and measured powers are scaled to the -81 MHz RF sideband.

The following table summarizes the measured change in demodulation phase predicted by the *Twiddle* model between the DRM and FPM experiments. Given the un-

Signal Port	Measured phase change	Model prediction
Reflected 81 MHz (Φ_+)	+18.5°	+14°
Pickoff 81 MHz (ϕ_-)	-72°	-73°
Reflected 54 MHz (ϕ_+)	-5°	0°
Pickoff 54 MHz (ϕ_s)	+2°	-4°

Table 4.6: Demodulation phase changes for the dual-recycled Michelson experiment, relative to the Fabry-Perot Michelson experiment.

certainties in proper demodulation phase setting of roughly 10° due to cross-coupling offsets, these numbers agree with the model quite well.

4.4.3 RSE

Once the PRM and DRM have been locked, some confidence has been gained that the interferometer is aligned, demodulation phases are set, and that servo gains are somewhat appropriate for locking. Certainly, the gain for the Φ_+ and Φ_- servos in RSE will increase compared to the FPM due to power recycling, and so appropriate adjustments are made to allow for this.

Lock acquisition occurred by turning on the fast path feedback for all servos except

for the ϕ_- servo, hand tuning the ϕ_- for a carrier dark fringe, and hand tuning the ϕ_+ and ϕ_s slow piezos until the RF sideband powers in the SEC OSA looked about right. Beyond this, there was nothing particularly rigorous about the procedure. Typically, some cavity, or the Michelson, would be slowly tuned using the slow HV PZT bias until the interferometer locked. Usually lock would be acquired in a few minutes, which was noted by seeing the power in the arms increase simultaneously. All slow paths, integrators, and the boosts used would be quickly turned on (except for the ϕ_- servo, still), and then the ϕ_- slow HV PZT bias would be carefully tuned to make sure the ϕ_- servo was close to its lock point before it would be turned on as well.

Lock was usually robust, once acquired. Unless disturbed by a measurement, a particularly vigorous door slamming, or by construction which was occurring inside or outside the building, the interferometer would remain locked for anywhere from 5 minutes to an hour.

Offsets

Without any offsets added to signals, it was clear that the interferometer was not locked in the same place as in the dual-recycled Michelson. This was clear due to the difference in the RF sideband powers in the power and signal cavity compared to the DRM experiment, as measured by the OSA at these pickoffs. During lock acquisition it could be seen that the same powers for the RF sidebands as in the DRM could be attained using a modest offset (about 15 mV) added to the pickoff 54 MHz (ϕ_s) signal port. The source of this offset was never completely understood. Knowledge of the cross-coupling of the RF electronics, along with the fact that there would now be a significant amount of power at 81 MHz in the pickoff signal port, conspired to make this scenario not inconsistent. Even though the RF and LO inputs for the 54 MHz mixers were fairly well band-passed, there was still some power at 81 MHz present in each. It's not known if this alone would have been enough to generate this amount of offset.

Power

The RF sideband powers in the power and signal cavities were consistent with what they should be, compared to the DRM, where there was good confidence that that sub-configuration was properly locked. The carrier power, on the other hand, typically seemed to be about 15-20% low. The “dither/ $2f$ ” test was applied to test whether the arms were locked at the center of their fringes. This involved driving the piezos at some frequency above unity gain and looking at the power fluctuations on an oscilloscope. If the cavity is locked in the center of the fringe, the fluctuations will occur at twice the driving frequency, with equal excursions to each side of the fringe. In general, the arms were locked fairly close to the fringe center.

Attempts at increasing the power by alignment weren’t successful, mostly because the interferometer seemed to be very sensitive to alignment, and adjustments too far one way or another to the alignment piezos tended to cause the interferometer to lose lock. The reason for this isn’t well understood, since other disturbances (for example, the dither/ $2f$ test or transfer function measurements) were seemingly much more violent.

Excess power at the reflected photodiode was measured, so it was accepted that there was some combination of mode-matching and misalignment which contributed to the decrease in the expected carrier power in the interferometer. This is subsequently modeled as a coupling factor less than unity for the carrier.

4.4.4 Systematic Errors

For both the dual-recycled Michelson and RSE, measurements were made of the plant transfer functions. In comparing these measurements to the modeled prediction, parameters which represent the interferometer must be input to the model. These parameters have uncertainties, which generates uncertainties in the modeled prediction. The main parameters are the various path lengths, the optical parameters (transmittance and losses), the input powers of the RF sidebands and carrier, and demodulation phases. To attempt to quantify the sensitivity of the designed control

matrix to imperfections in these parameters, a program was written in *Mathematica* which generates the DC matrix as derivatives of the signals at the appropriate demodulation phase, and then takes derivatives of this matrix with respect to the parameters listed in Table 4.7. Each of these uncertainties generates an error matrix,

Parameter	Deviation
l_{prc}	0.005 m
l_{sec}	0.005 m
Asymmetry	0.005 m
Arm cavity losses	10%
Demodulation phases	5°
Mod. depths (81 and 27 MHz)	1%

Table 4.7: Uncertainties in parameters used in the model predictions of the matrix of discriminants.

which are then all summed in quadrature, assuming the parameter estimation errors are uncorrelated. Some parameters had a very small effect compared to the others, such as the beamsplitter mismatch ($R \neq T$) and losses in the power and signal mirrors, and were neglected. The table shows the parameters which tended to have the largest effect on the matrix predictions.

Application of a standard error analysis to the control matrix must be done very carefully, due to the fact that the interferometer is a very non-linear system. Some parameters are easily justified. Demodulation phase varies sinusoidally, and variations of 5° are easily approximated as linear. Length errors of the power and signal cavities on the order of 5 mm are less than a percent of the modulation wavelength, and so are likewise expected to be approximately linear. The magnitude of the matrix elements are linear with the field amplitudes, which is a function of the modulation depths. Other parameters, such as arm cavity loss or beamsplitter loss, are verified to behave approximately linearly with variation by running the model several times for different parameter errors.

4.5 Data and Results

Verification of the design of this interferometer is demonstrated by several metrics. First, simply acquiring and holding lock is considered a success. Second, measuring the control matrix and showing that it behaves as expected gives a measure of success. This is done for both the dual-recycled Michelson and the RSE interferometers. Third, and most important, showing agreement between the measured and modeled gravitational wave transfer function is considered a success.

4.5.1 Dual-Recycled Michelson

Success in locking and characterizing the dual-recycled Michelson is important in the sense that the signal ports used to control the interferometer depend on this sub-configuration being locked correctly. All signals depend on the RF sidebands which are only sensitive to their state in the dual-recycled Michelson. Verifying that the matrix of discriminants is what it is modeled to be is therefore of interest.

Matrix of Discriminants Measurement

The dual-recycled Michelson is a three degree of freedom system, comprised of ϕ_+ , ϕ_- , and ϕ_s . The three signal ports used to control these modes are the reflected 54 MHz, the pickoff 54 MHz, and the pickoff 81 MHz signals. A schematic of the measurement of this 3×3 matrix is shown in Figure 4.8. In order that the effect of the various servos can be neglected, the gains are all lowered as much as is possible while still maintaining a decent lock, and then the measurement is made at frequencies higher than the highest unity gain frequency. Unity gain frequencies around 5-10 Hz for the ϕ_+ and ϕ_s , and roughly 1 Hz for ϕ_- , keep the DRM locked sufficiently for this measurement. Data from 70 Hz to 200 Hz was used, the lower frequency set by a factor of 10 greater than unity gain, the upper frequency set by the point at which resonances in the actuators begin to corrupt the data and increase the uncertainties. For both the ϕ_+ and ϕ_s measurements, a drive is applied to the fast piezo, the input to the transfer function measurement is taken from the fast piezo high voltage

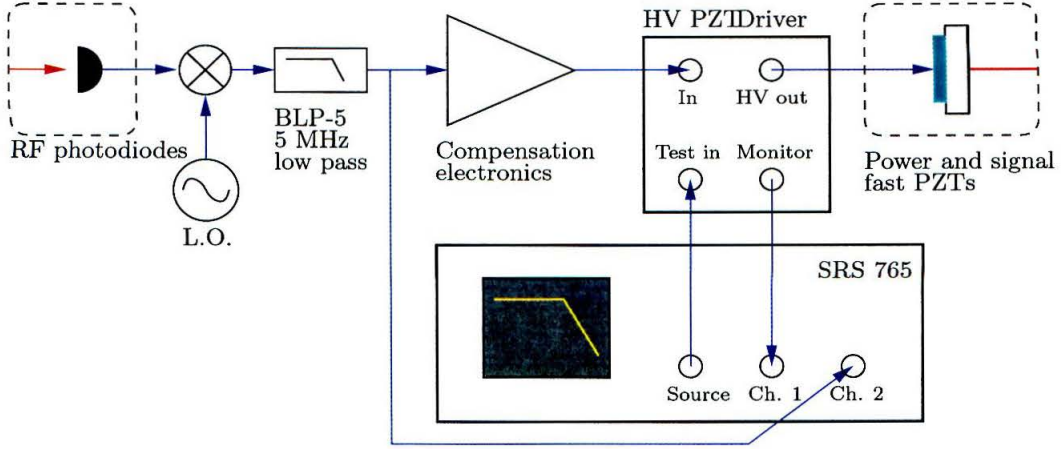


Figure 4.8: Experimental setup for transfer function measurements in the dual-recycled Michelson for the ϕ_+ and ϕ_s degrees of freedom. For measuring transfer functions from the ϕ_- degree of freedom, the source drives the second input in the compensation electronics, and the input to the transfer function measurement (Ch. 1) is taken from the slow PZT monitor.

monitor, while the output is taken at the output of the mixer, after the RF low-pass filter. For the ϕ_- degree of freedom, the drive is applied to the slow piezos. The summing electronics which drive the ϕ_- mirrors at SM2 and SM3 are built into the compensation electronics, so the source drive is applied to the second input to the compensation electronics. Explicitly, the measurement of the M_{ij} matrix element has the following form when the measurement is taken significantly above unity gain.

$$\frac{o_i}{i_j} = A_{pzt} P_{optics} S_{PD+Mixer} \quad (4.10)$$

The fraction o_i/i_j is the measured transfer function (output over input). The desired matrix element is represented by P_{optics} . The actuator gains A_{pzt} are scaled from the piezo responses given in Table 4.2, while the sensor gains $S_{PD+Mixer}$ are taken from Table 4.1. Note that this scales the measured data to the size of the signal at the point where the light is picked off, rather than at the photodiode, as shown in Figure 4.2. That is to say, the effect of the pickoff, attenuators, RF photodiode gain, cable and mixer losses are all contained in $S_{PD+Mixer}$. Also, the measured data is

further scaled to an input power of 1 watt, which is the assumption used in *Twiddle*. The transfer function measurements are shown in Figure 4.9, while the DC matrix is shown in Table 4.8, along with the prediction from *Twiddle*.

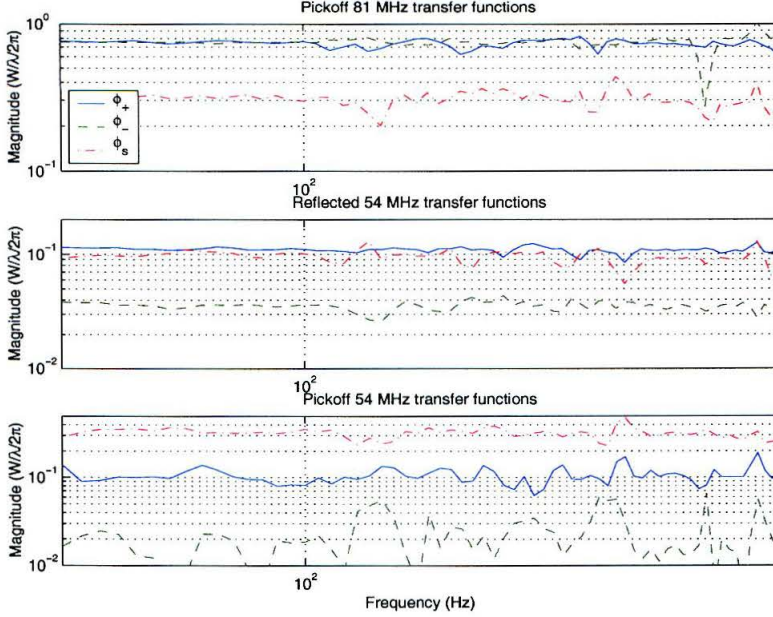


Figure 4.9: Dual-recycled Michelson transfer function measurements.

	ϕ_+	ϕ_-	ϕ_s
Pickoff 81 (ϕ_-)	0.73 ± 0.043 0.82 ± 0.019	-0.75 ± 0.081 -0.69 ± 0.068	-0.30 ± 0.041 -0.39 ± 0.017
Reflected 54 (ϕ_+)	0.11 ± 0.0066 0.12 ± 0.0089	-0.035 ± 0.0032 -0.057 ± 0.013	-0.094 ± 0.013 -0.11 ± 0.0078
Pickoff 54 (ϕ_s)	-0.11 ± 0.023 -0.069 ± 0.0056	0.023 ± 0.014 -0.0091 ± 0.036	-0.32 ± 0.042 -0.32 ± 0.023

Table 4.8: Dual-recycled Michelson matrix of discriminants. Measured values are in normal text, while the predicted *Twiddle* values are presented in bold text.

The measured values in Table 4.8 and the associated errors are derived from a fit to the data in Figure 4.9 along with the readout gain calibration errors. The errors in the model are taken from the known uncertainties of the parameters used to generate the model, discussed in Section 4.4.4. The largest contributors to uncertainties in the

modeled matrix are the demodulation phase and length errors.

The agreement here is reasonably good and most all elements are within their errors. Perhaps the worst agreement comes at the ϕ_+ signal in the pickoff 54 MHz port. The reason for this discrepancy isn't understood. The ϕ_- signal in the same port is likewise significantly different; however, the errors in the measured and modeled values are very large.

4.5.2 RSE

Matrix of Discriminants Measurement

A major difference in the measurement of the matrix of discriminants for RSE compared to the dual-recycled Michelson is the presence of the arm cavity signals. Most notably, the arm cavity common mode (Φ_+) couples very strongly in the pickoff 81 MHz signal port, which is the source of the control signal for ϕ_- . Also, the gains of the arm cavity servos must be kept very high, since the fringe is much narrower, so loop gain effects must be considered. Therefore, a more careful analysis of what actually is being measured is necessary. Analyzing more than a coupled 2×2 system rapidly loses any pedagogical value due to the complexity involved, so attention will be confined to this simple case. Its application will be to view how an individual measurement of the minor degrees of freedom (ϕ_+ , ϕ_- , and ϕ_s) in the pickoff 81 MHz signal port is affected by the strong presence of the Φ_+ signal, which derives its control through the reflected 81 MHz signal port. The basic analysis of this measurement is done in Appendix C, Section C.2, which assumes a 2×2 system in which one degree of freedom dominates both signal outputs. The equations which describe the four

transfer function measurements of this 2×2 system are given in Eq. (4.11).

$$\begin{aligned}
 \frac{o_1}{i_1} &\cong S_1 P_{11} (1 - \epsilon_1 H_2 P_{21}) A_1 \cong S_1 P_{11} A_1 \\
 \frac{o_2}{i_2} &\cong S_2 P_{22} (1 - \epsilon_1 / \epsilon_2) A_2 \\
 \frac{o_2}{i_1} &\cong S_2 P_{21} (1 - \epsilon_2 H_2 P_{21}) A_1 \cong S_2 P_{21} A_1 \\
 \frac{o_1}{i_2} &\cong 0
 \end{aligned} \tag{4.11}$$

It's assumed that the measurement is taken above the unity gain frequency for loop 2 ($H_2 P_{22} \ll 1$), which will correspond to the minor degrees of freedom, but below unity gain for loop 1 ($H_1 P_{11} \gg 1$), which will correspond to the Φ_+ degree of freedom.

The interesting thing in Eqs. (4.11) is that measurements of the small signals, that is the inputs into loop 2, are fraught with difficulty. Most notably, it's not really possible to measure the cross coupling from loop 2 into loop 1 at all. In loop 2, the output is corrupted by the cross-coupling of the two loops. This can be understood in the following way. The output of loop 2 has a large contribution due to the error in loop 1, e_1 . Since the loop gain in loop 1 is very high, it faithfully tracks the output of loop 1, which includes the small error from loop 2, e_2 . Therefore, for any drive into loop 2, the measured output will include the contribution from loop 2, as well as the contribution from loop 2 into loop 1. The end result is that it's very hard to separate the individual matrix elements.

The measurement of the matrix will be confined to the Φ_+ , ϕ_+ , ϕ_- , and ϕ_s degrees of freedom in the pickoff 81 MHz, and the reflected and pickoff 54 MHz signal ports. Measurement of the coupling of the minor degrees of freedom in the reflected 81 MHz signal port is nearly impossible, due to the presence of the high gain servo for the Φ_+ degree of freedom. Cross coupling of Φ_- in the pickoff 81 MHz signal is small and will likewise be ignored, since it's largely an artifact of a lousy beamsplitter, and not particularly interesting. Measurement of the Φ_- signal in the dark port 81 MHz signal port is left as the measurement of the gravitational wave transfer function.

Measurement of the transfer functions was more difficult with RSE than with

the dual-recycled Michelson. The amount of drive applied to the mirrors was a bit smaller, owing to the fact that the interferometer as a whole was more sensitive to disturbances. This made the measurements a bit noisier.

Figure 4.10 shows the data for the 3×3 submatrix associated with the minor degrees of freedom. Figure 4.11 includes the data from the Φ_+ degree of freedom in the pickoff 81 MHz signal port, as well as showing the rest of the data which was truncated in calculating the matrix elements. The decrease in magnitude of the Φ_+ transfer function below 2 kHz is mainly due to saturation effects in the electronics. At lower frequencies, the loop gain is quite high, and the electronics are easily driven into saturation by the addition of noise.

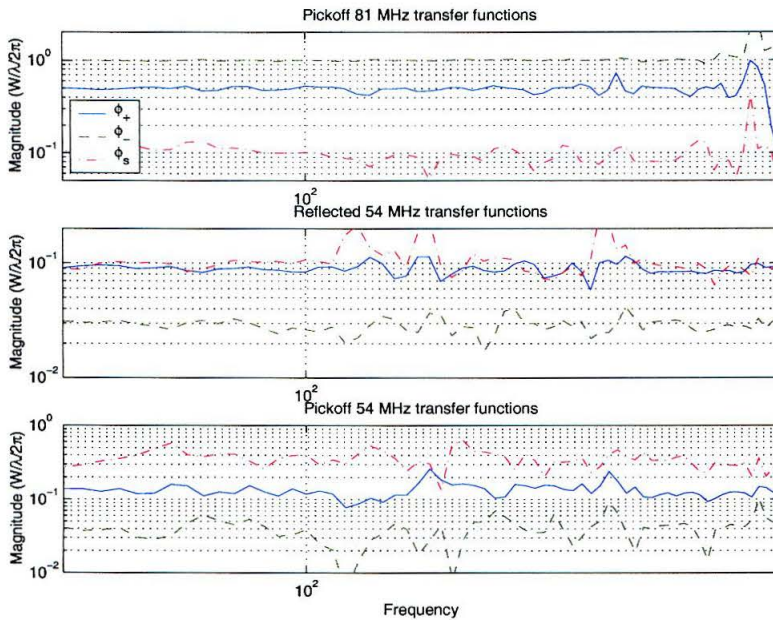


Figure 4.10: RSE transfer function data for the minor degrees of freedom. Note that because of the coupling indicated in Eq. (4.11), the data in the first plot does not indicate the actual matrix elements.

Table 4.9 shows the analysis of the data presented in the Figures 4.10 and 4.11. The measurements of ϕ_+ , ϕ_- , and ϕ_s in the pickoff 81 MHz signal port are not directly the matrix elements, but rather the combination due to the cross coupling as indicated in the second equation listed in Eq. (4.11). The agreement overall is modest, most

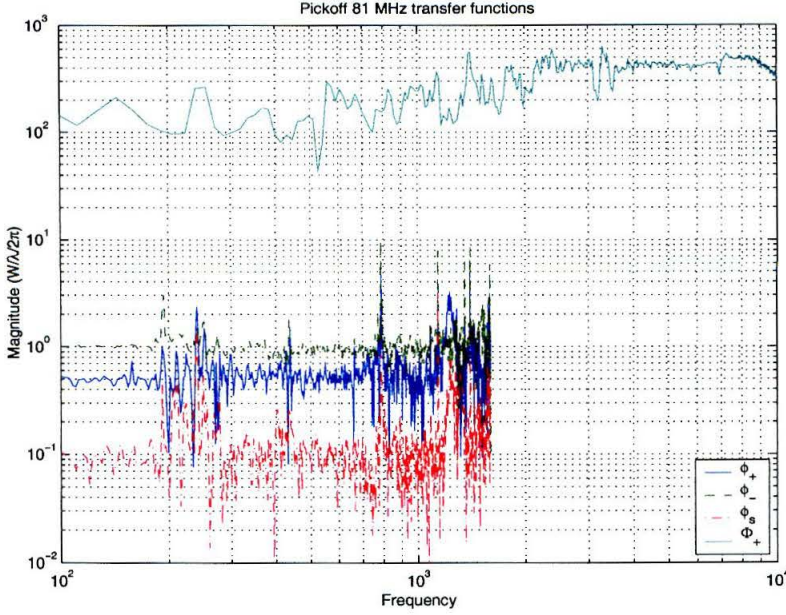


Figure 4.11: RSE transfer function data at the pickoff 81 MHz port. Included is the contribution from the arm cavity common mode, Φ_+ .

	Φ_+	ϕ_+	ϕ_-	ϕ_s
Pickoff 81 (ϕ_-)	410 ± 55 310 ± 25	0.50 ± 0.11 0.46 ± 0.16	-1.06 ± 0.29 -0.60 ± 0.14	-0.10 ± 0.046 -0.16 ± 0.03
Reflected 54 (ϕ_+)	0 0	0.090 ± 0.010 0.13 ± 0.010	-0.029 ± 0.0041 -0.060 ± 0.013	-0.11 ± 0.039 -0.12 ± 0.0084
Pickoff 54 (ϕ_s)	0 0	0.13 ± 0.031 0.070 ± 0.0058	0.041 ± 0.016 0.011 ± 0.037	0.35 ± 0.092 0.34 ± 0.024

Table 4.9: Matrix of discriminants for the RSE. Measured values are in normal text, while the predicted *Twiddle* values are presented in bold text. The ϕ_+ , ϕ_- , and ϕ_s elements in the pickoff 81 row are actually the cross-coupled matrix elements predicted by Eq. (4.11).

elements are either within the predicted errors, or if not, are close. The measured and modeled ϕ_- elements are the most disparate, although the errors in the reflected 81 and pickoff 54 elements are quite large. The most troubling elements are M_{r,ϕ_-}^S and, similar to the DRM experiment, M_{p,ϕ_+}^S . These discrepancies are not understood.

4.5.3 Gravitational Wave Transfer Function

Without very long arm cavities, measurement of the non-DC peak sensitivity of the detuned RSE transfer function is kept at fairly high frequencies. Unfortunately, at frequencies higher than 50 kHz, the mirror actuation assemblies have a forest of resonances. Making a measurement of the transfer function by excitation of the end mirror piezos is then best accomplished in a relative sense, as in Heinzel, *et al.*[31] This method uses a transfer function from a simpler configuration as a calibration, and divides the RSE transfer function by the calibration. This divides out the mirror actuation resonances, as well as the RF photodiode gains, mixer losses, etc. This also divides out some of the optical response. An approach which would allow an absolute measurement of the transfer function is to use a second laser which is directed through the end mirrors. The frequency of the second laser is swept through a large range around that of the initial laser, and measurements are made by doing a max-hold of the value at a particular frequency. This approach is used by the Daniel Shaddock in his thesis. [58] Without a second laser, however, this is prohibitively difficult, and so the relative measurement scheme was adopted.

The measurement with which to compare to the RSE transfer function was taken in the Fabry-Perot Michelson experiment. The experimental setup was identical to that of Figure 4.7, with the specific application that the input was the DM fast test input of the CM/DM driver box, and the output was the dark port 81 MHz signal port. The measurement was taken from 10 kHz to 1 MHz, so some care had to be taken to make sure no lingering servo effects were to be seen. This entailed simply lowering the gain of the Φ_- servo as much as possible while maintaining a good lock (typically the minimum bandwidth achievable was around 4-5 kHz). Five averages of the transfer function were taken, although the data usually looked good enough after one pass. Figure 4.12 shows a typical raw transfer function for the Fabry-Perot Michelson.

The same measurement was taken with the locked RSE interferometer. Since the same sensors and actuators are used in both measurements, dividing the complex-

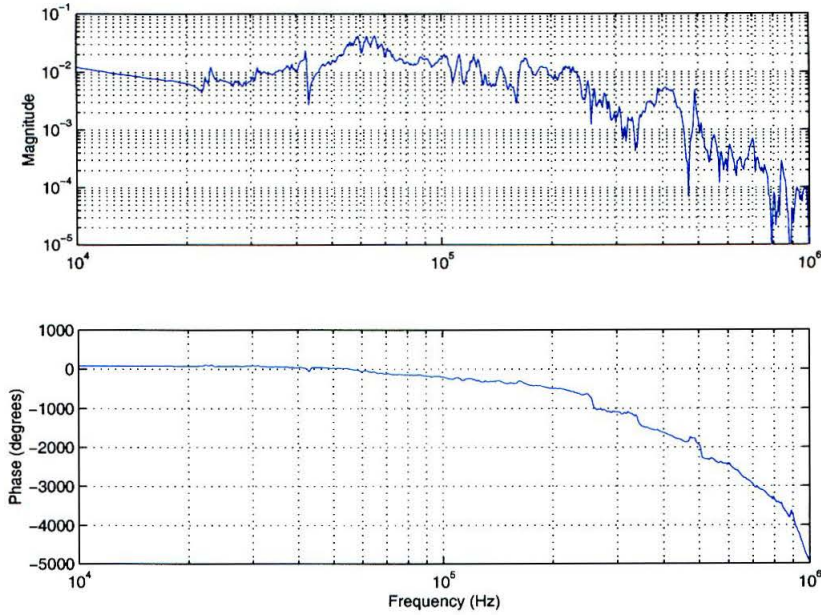


Figure 4.12: Raw data of the Φ_- transfer function measurement of the Fabry-Perot Michelson.

valued transfer functions cancels out these elements, leaving only the optical transfer function of RSE relative to the Fabry-Perot Michelson.

Twiddle is actually a bit cumbersome to use for the purpose of comparing the model to data. The model analysis was much more easily done in Matlab, so a script was written to generate the Φ_- transfer functions in Matlab. A good deal of effort was put into verifying agreement between Matlab model and *Twiddle* before it was used in doing a comparative analysis with the data.

The first measurement is simply that of the gravitational wave signal transfer function of RSE, shown in Figure 4.13. The modeled fit to the data uses all the measured parameters, with a few small deviations from the ideal case. First, the relative magnitude plots are scaled by a multiplicative factor. The justification for this can be found in the discussion regarding the carrier power buildup in the locked RSE interferometer. Either due to poor mode matching, misalignment, or a combination of both, the model magnitude data is scaled by some factor to match the experimental data; in this case, it's 90%. The model demodulation phase is varied by 4° from

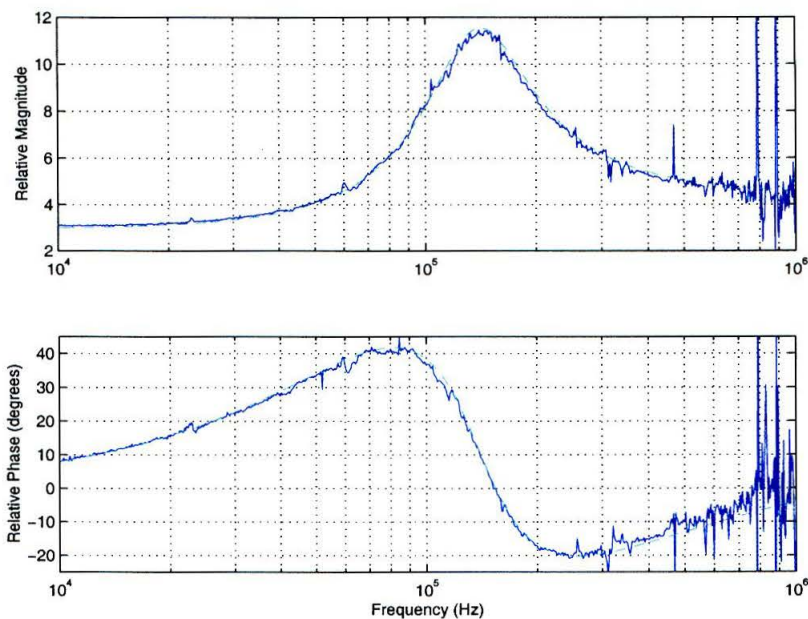


Figure 4.13: Measurement of the RSE gravitational wave transfer function, relative to the same measurement in the Fabry-Perot Michelson. The modeled prediction is the cyan dashed line.

the phase which maximizes the Φ_- degree of freedom in the Fabry-Perot Michelson case. This is consistent with the expected uncertainty in the demodulation phase of $\lesssim 10^\circ$. The modeled detuning is also offset by a small amount, about 5% from the designed detuning. The reason for this is believed to be related to the trouble with DC offsets in the signal ports (most notably, the pickoff 54 port), and the inability to adequately separate these offsets from errors in demodulation phase. It would be expected that with better real-time diagnostics of the transfer function, the state of the interferometer could be tweaked to the desired state. The real-time diagnostic available to this experiment was essentially to look at the phase and magnitude of the transfer function and estimate the peak frequency response by eye.

The fact that the detuning phase can be affected by offsets in the pickoff 54 (ϕ_s) signal port gives a method to detune the interferometer on the fly. This was done here by simply removing the 15 mV offset added to the ϕ_s signal port in the experimental setup mentioned earlier. The resulting shift in the transfer function due

to this phase shift is shown in Figure 4.14, which shows the data from Figure 4.13 also for comparison. For clarity, the additionally detuned magnitude data is shifted downward by 1.5. The modeled fit to the additionally detuned data only varied the

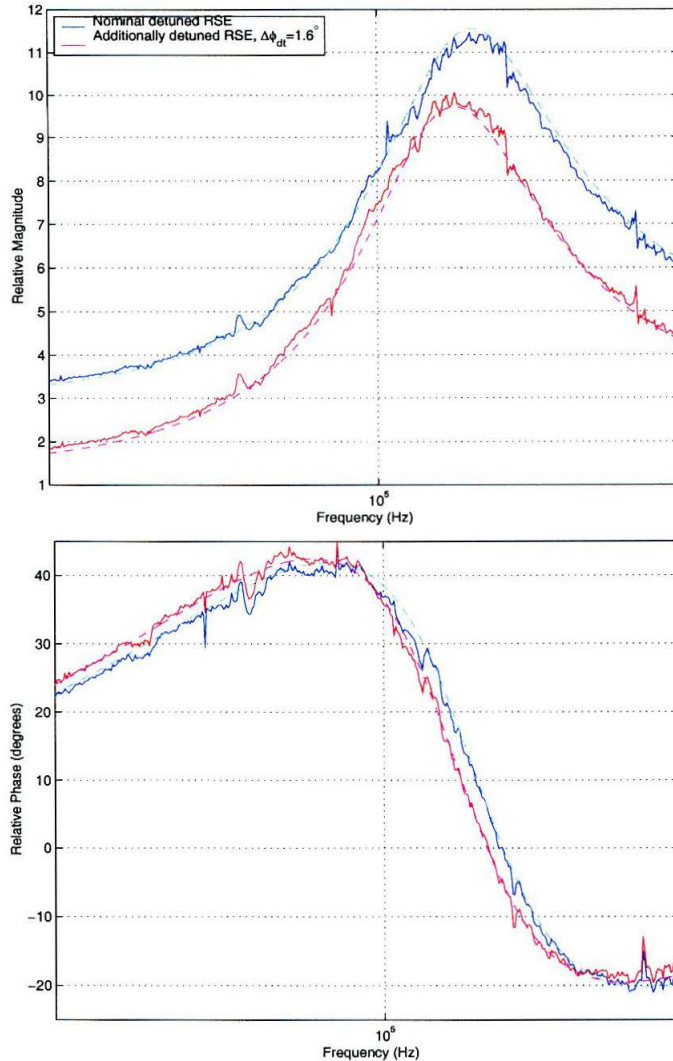


Figure 4.14: RSE transfer function of Figure 4.13, as well as one with an offset added to the ϕ_s signal. Model-predicted transfer functions are shown in lighter colors, as well as being dashed.

detuning phase. The scaling of the magnitude was the same as in the previous figure. The detuning represents a shift of 9 kHz, from 130 kHz to 121 kHz, corresponding to 1.7° of phase shift in the signal cavity. To check consistency, the phase shift for

an offset can be estimated. The DC gain of the ϕ_s signal is 0.34 W/rad, for 1 watt input power. Assume this is linear over the amount the cavity is shifted. Scale this by the measured input power of 36 mW, and take the measured readout gain at the pickoff 54 MHz of 6.33 V/W. The resulting phase shift of the cavity per volt is 3.1 rad/V. For 15 mV offset, this corresponds to a phase shift of 2.6° , which is a bit more than the 1.7° suggested by the fit. The assumption that the response is linear is perhaps a bit optimistic, which would lead to an over-estimation of the resulting phase shift. All in all, it's not a bad guess.

Sensitivity to demodulation phase is an obvious prediction of the modeled RSE transfer functions. In this case, a good comparison between modeled and measured values can be made, since the demodulation phase is easy to measure directly with little error. The demodulation phase was varied in the dark port 81 signal port (Φ_-) by an arbitrary amount, and then additional data was taken, the results shown in Figure 4.15. The new demodulation phase was then measured. The shift in demodulation phase was 46° , while the best fit to the data resulted in a phase shift of 43° , certainly within reason.

4.6 Conclusions

An experiment was designed to test both the tuning of the frequency response of RSE as discussed in Chapter 2, and the signal extraction scheme proposed for RSE in Chapter 3. The method of choosing optics, as well as setting cavity lengths and modulation frequencies, was discussed. There are several differences between this prototype and an advanced LIGO detector; however, it is felt that those differences do not greatly impact the main goal of this experiment, which was to demonstrate the ability to design, build, and lock a detuned RSE interferometer in which the RF sidebands used for signal extraction were unbalanced.

The detuning was tested by demonstrating the shift in the peak sensitivity of the gravitational wave transfer function away from DC by a detuning phase in the signal cavity. In particular, this was shown given the method proposed in this thesis

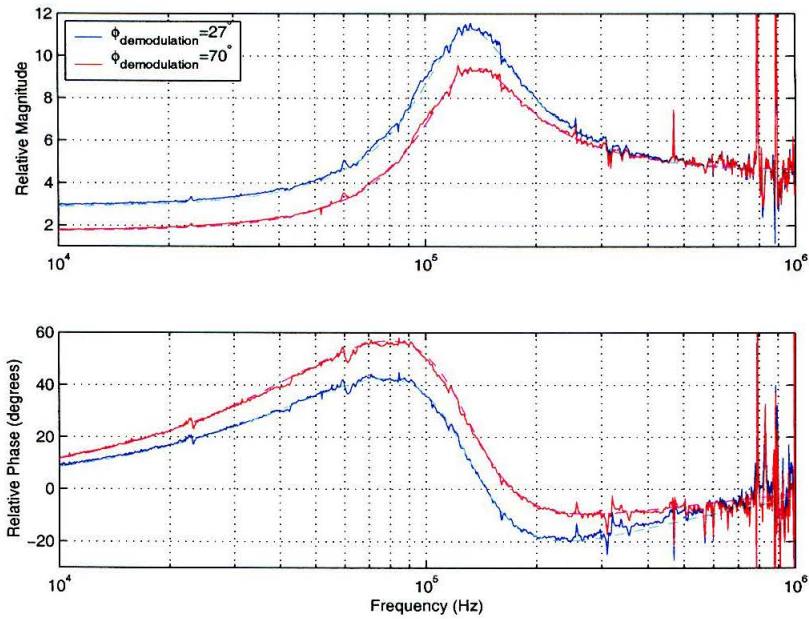


Figure 4.15: RSE transfer function sensitivity to demodulation phase. The measured change in demodulation phase from the curve in Figure 4.13 is 46° , while the modeled value which matches the data was 43° . Model-predicted curves are shown in dashed lighter colors.

to establish the signal extraction scheme; that is that detuning is accompanied by a macroscopic shift in the length of the signal cavity. Some other aspects of detuned RSE were demonstrated as well: sensitivity to demodulation phase, as well as offsets in the control of the signal cavity. The parameters used to fit the data were all within the measured parameters plus their known uncertainties.

The signal extraction scheme was tested by successfully locking the RSE interferometer in the first place, and demonstrating a reasonably good agreement between model and experiment for both the RSE transfer function as well as the measurable elements of the matrix of discriminants. This gives confidence in the use of the *Twiddle* model to design a control system for an RSE interferometer with unbalanced RF sidebands. Also, some indication was given that *Twiddle* is useful in determining approximately the relative shifts in demodulation phase in going from one configuration to another.

Many aspects of the process of locking the interferometer were demonstrated as well. It's not particularly clear how many of these might be useful for a suspended interferometer. It is expected it would be extremely useful if sub-configurations like the Fabry-Perot Michelson and the dual-recycled Michelson could be implemented and locked in order to establish some baselines for the expected state of the full RSE interferometer. As a matter of fact, perhaps the greatest difficulty in this experiment was the feeling of "flying blind." Until the final data was analyzed, there was always an uncertainty about whether the interferometer was in the right state. Better diagnostics would certainly be useful; for example, calibrated optical spectrum analyzers which weren't so touchy. Another diagnostic which could be useful might be electronic pickoffs with which to monitor the RF power incident on each photodiode in all of the beat frequencies. This could give a reasonably good prediction of the powers in each of the RF sidebands, which might be a more accurate diagnostic of the relative state of the RF sidebands and carrier in the interferometer than the output of the OSA.

Chapter 5

Laser Noise Couplings in RSE

Defining the sensitivity of the detector relative to the fundamental noise sources of seismic, thermal, and shot noise is valid only if the noise due to all other sources is less. Other sources of noise, such as the sensors, the actuators which control the positions of the mirrors, and the laser light itself must be taken into consideration. The dependence of the detector sensitivity to noise of the laser light, in particular, depends on the optical configuration and the method of gravitational wave readout, and will be investigated in this chapter.

The laser light incident on the power recycling mirror is composed of the carrier and two phase modulated RF sidebands.¹ Each of these components fluctuates with some small amount of amplitude and frequency noise.² The carrier and the RF sidebands, along with their noise spectra, are propagated from the input of the interferometer at the power recycling mirror to the dark port. The propagation is particularly dependent on some of the imperfections of the interferometer. The readout model Eq. (3.19) determines the measured output due to the noise, hereafter referred to as “measured noise” or “measured technical noise.” Reasonable estimations can be made regarding the magnitude of the coupling mechanisms (e.g., optical imperfections and feedback control limitations), and a comparison between the level of measured fundamental noise and the measured technical noise due to laser frequency and amplitude noise will set specifications on the required stabilization of the laser light.

Phasor diagrams are used to illustrate the various expected coupling mechanisms in Section 5.1. This is straightforward in a broadband RSE interferometer; however,

¹Only the sidebands used in gravitational wave readout are considered.

²Frequency noise is defined as the derivative of phase noise. Spectrally, then, frequency noise is $1/f$ times the phase noise. The two terms, “phase noise” and “frequency noise”, will occasionally be used interchangeably.

the detuned case is more complicated. Section 5.2 defines how the measured noise is to be compared to the gravitational wave signal sensitivity. The amplitudes of the noise sidebands at the input of the interferometer are derived in Section 5.3. It's assumed here that the source of the noise is the laser light itself, and that the modulation which generates the RF sidebands transfers the same relative noise spectra to the RF sidebands. Section 5.4 restates the optical heterodyne readout model given in Eq. (3.19). The noise sidebands, as well as the DC components of the carrier and RF sidebands, are propagated to the dark port using transmission functions derived in Section 5.5. The input noise is multiplied by the transmission functions, and then folded into the readout model to generate a spectrum of measured noise in Section 5.6. Finally, the figure of merit discussed in Section 5.2 is used in Section 5.7 to examine the noise coupling mechanisms and set specifications on the input laser noise, as well as residual length deviations of the Φ_- and ϕ_- degrees of freedom.

5.1 Conceptual Motivation

The use of phasor diagrams, which was outlined in Section 3.1.3, is very helpful to conceptually understand the mechanisms for the generation of the measured noise.

5.1.1 Balanced Sidebands

It's easiest to first consider the case when the RF sidebands are equal. The summed resultant RF sideband phasor is a swinging length phasor along the horizontal axis. The dark port is a special case where the carrier phasor is ideally null. The only light present is due to the two counter-rotating RF sideband phasors. A small differential phase modulation of the arms generates carrier light at the dark port which is orthogonal to the carrier axis, as shown in Figure 5.1. If the signal phasor is along the horizontal axis, the demodulation phase which generates the largest measured signal is the one at which the two RF sideband phasors are parallel, hence their sum is maximum. This is the inphase demodulation.

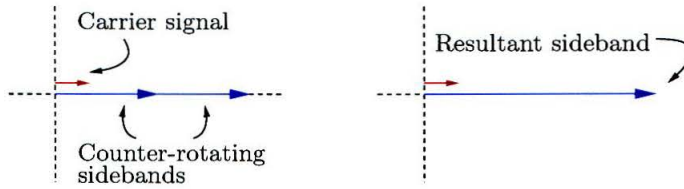


Figure 5.1: Phasor representation of gravitational wave signal generation.

When considering noise couplings, first imagine that the arm cavities are mismatched in reflectivity, due to differing losses in the cavities. This results in a contrast defect of carrier light at the dark port, since the two beams summed at the beamsplitter cannot completely cancel if their magnitudes are different. The relative phase of this “mismatch carrier defect” phasor is parallel to the carrier axis. In the static case, this still presents no signal, since the defect and resultant RF sideband vectors are orthogonal. Phase noise on the carrier and RF sidebands is decomposed into the nominal fixed phasor plus an orthogonal swinging length phasor, generating a measured signal as shown in the right-hand side of Figure 5.2. It can be easily shown

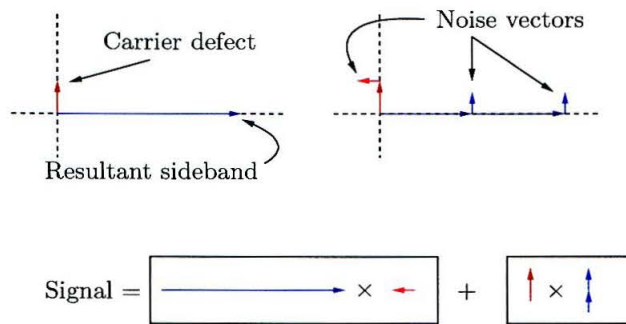


Figure 5.2: Phasor representation of frequency noise generation. The top left shows the static case, the top right shows the noise sidebands generated by frequency noise. The bottom diagram indicates the vector products which generate the measured noise.

that if the phase fluctuation of the carrier defect and resultant RF sideband were equal, the measured noise terms indicated in the bottom of Figure 5.2 would cancel. However, this typically is not the case. The carrier and RF sidebands propagate very differently through the interferometer. Hence, the relative amplitude of the phase fluctuations in the carrier and RF sidebands which reach the dark port tends to be

different, and these terms do not cancel. For LIGO I, this is the dominant form of coupling for frequency noise.[59]

Amplitude noise wiggles the length of each of these phasors. The noise phasors generated are parallel to the source phasors. For the mismatch carrier defect and the resultant RF sidebands, these remain orthogonal, and there is no measured signal due to amplitude noise. A different coupling mechanism is required. If either the Michelson (ϕ_-) or the arm cavity differential mode (Φ_-) are offset, there will be a small bit of “offset carrier defect” present which is parallel to the RF sidebands (similar to the measurement of the gravitational wave signal, but at DC). This bit of offset carrier defect provides a local oscillator for amplitude noise on the RF sideband, as shown in Figure 5.3. The amplitude noise of the carrier generates measured noise as well through the modulation of the offset carrier defect, although this is typically a much smaller term.

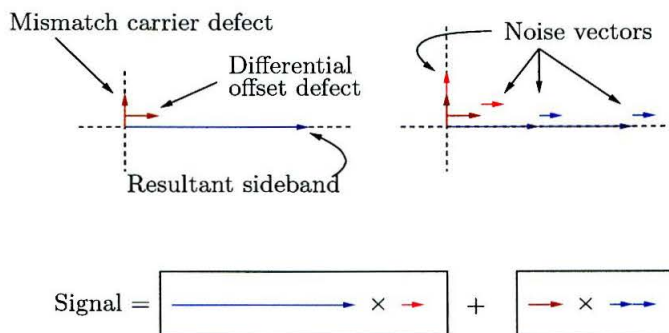


Figure 5.3: Phasor representation of amplitude noise generation.

The amplitude modulation of mismatch carrier defect doesn’t generate a signal. However, if any of the cavities are off resonant, then the resultant sideband vector can be rotated relative to the carrier. In this case, there will be a component of the RF resultant parallel to the mismatch carrier defect, which can now couple amplitude noise from the arm mismatch carrier defect as in Figure 5.4. This second order effect would tend to be the largest to be considered, due to the fact that the mismatch carrier defect tends to be much larger than any other coupling mechanism. Earlier work considered this coupling, which was typically found to contribute to the total

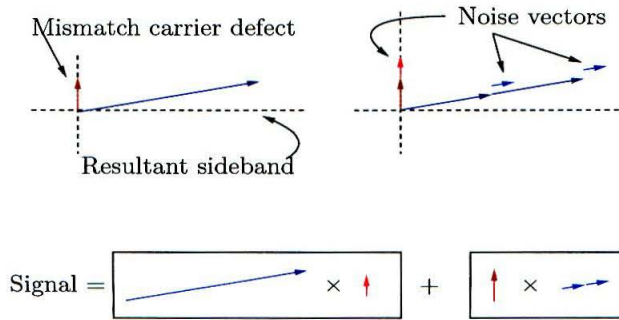


Figure 5.4: Phasor representation of second order amplitude noise generation.

noise by no more than 10%. [60] Since the point of this analysis is to set a specification, rather than determine an accurate prediction of measured noise, this mechanism will not be considered here.

Clearly, one could imagine all sorts of couplings involving various rotations, offsets, etc., but most will be second order and will be ignored.

As the demodulation phase is varied from inphase to quadrature, the length of the resultant RF sideband goes from maximum to zero. At the inphase demodulation, these couplings are maximum, while at the quadrature phase, other mechanisms would come into effect, for example differential amplitudes of the RF sidebands. In general, though, the size of these signals will be much smaller (second order) than in the inphase demodulation. For this reason, quadrature demodulation will not be considered in the balanced sideband case.

5.1.2 Unbalanced Sidebands

In the detuned RSE configuration, the RF sidebands become unequal when the interferometer is adjusted to maximize the transmission of one of the RF sidebands to the dark port. Since propagation of the upper and lower RF sidebands is unequal, the resultant RF sideband vector is no longer a swinging length vector along a fixed axis, but is rather a rotating vector which traces out an ellipse at the frequency of the RF modulation. In the reflected and pickoff ports, this forces the choice of demodulation phase such that there is no DC offset of an optical origin. However, at the dark port,

where there (ideally) is no carrier, the choice of demodulation phase is arbitrary.

The detuning of the signal cavity causes the upper and lower noise sidebands to propagate unequally as well. The resultant noise phasor also traces out an ellipse, but at the noise sideband frequency. Since demodulation can be thought of as the scalar product of the resultant RF sideband vector with the resultant noise sideband vector, the signal is seen to be the projection of the noise ellipse onto the axis defined by the demodulation phase. In general, since there is no axis where either the RF or the noise resultant phasor is null, the measured noise doesn't vanish at any demodulation phase. The analysis will have to include both quadratures.

Mismatch carrier defect typically has the largest magnitude of all the noise coupling mechanisms. Amplitude noise is free from this coupling mechanism in the balanced sideband case due to the orthogonality of the resultant phasors. This is no longer the case for unbalanced sidebands. An example of this is shown in Figure 5.5. In this case, the noise ellipse of the RF sidebands is projected onto the carrier mis-

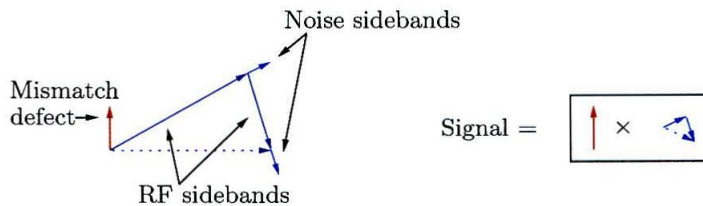


Figure 5.5: Amplitude noise coupling via mismatch carrier defect with unbalanced RF sidebands.

match contrast defect. The details of the amplitudes of all the phasors, their relative phases, as well as the appropriate demodulation phase, will need to be derived, of course. It should be quite apparent, however, that the description of coupling when the RF sidebands are unbalanced will be fairly complicated.

5.2 Figure of Merit

The goal here is to find specifications on the noise of the laser light and on the optics, such that the coupling of laser noise to the gravitational wave signal port is

significantly less (say, $\leq 1/10$) than the measured fundamental noise, which is due to shot noise at high frequencies, thermal noise at intermediate frequencies, and seismic noise at lower frequencies.

Shot noise is fundamentally different from either thermal or seismic noise. Both seismic and thermal noise are actually physical disturbances to the path lengths in the interferometer, whereas shot noise is a fundamental noise in the optical readout system. It has an equivalent displacement noise only by dividing it by the transfer function of the detector. The demodulated, low-pass filtered shot noise is derived in Regehr's thesis for inphase and quadrature demodulations only.[32] The same analysis is generalized here for arbitrary demodulation phase and arbitrary RF sideband amplitudes, and given by

$$i_{shot}(f)/\sqrt{\text{Hz}} = e\sqrt{\frac{\epsilon}{h\nu_0}(|E_{DC}|^2 + |E_+|^2 + |E_-|^2 + \Re\{E_+E_-^*e^{i2\beta}\})} \quad (5.1)$$

where e is the electric charge, ϵ is the photodiode quantum efficiency, $h\nu_0$ is the photon energy, and E_{DC} , E_+ , and E_- are the DC contrast, and upper and lower electric field amplitudes,³ respectively, and β is the demodulation phase. This is in units of amps/ $\sqrt{\text{Hz}}$, which is a current spectral density whose spectral shape is flat. This scales directly to the measured voltage spectral density, which is also flat, assuming a constant transimpedance over the bandwidth of interest.

The measured spectrum due to some displacement is given by

$$i_{signal}(f) = e\frac{\epsilon}{h\nu_0}T_{signal}(f)x_{signal}(f) \quad (5.2)$$

This is a displacement spectrum times the transfer function T_{signal} , which is units of watts per meter. $x_{signal}(f)$ is taken to be a spectral density of the source, in units of m/ $\sqrt{\text{Hz}}$. The displacement spectral density which would give a measured output

³Scaled to be in units of $\sqrt{\text{watts}}$

equivalent to shot noise, $i_{signal}(f) = i_{shot}(f)$, is given by

$$x_{shot}(f)/\sqrt{\text{Hz}} = \frac{i_{shot}}{e \frac{\epsilon}{h\nu_0} T_{signal}(f)} \quad (5.3)$$

If the seismic, thermal, and shot noises are the dominant noise sources in the detector, summing them in quadrature gives the detector sensitivity

$$x_{sens}(f)/\sqrt{\text{Hz}} = \sqrt{x_{shot}^2(f) + x_{thermal}^2(f) + x_{seis}^2(f)} \quad (5.4)$$

The measured photocurrent spectral density equivalent to this displacement can be written as

$$i_{sens}(f)/\sqrt{\text{Hz}} = e \frac{\epsilon}{h\nu_0} T_{signal}(f) x_{sens}(f) \quad (5.5)$$

It's desired that all other technical noise sources, such as laser amplitude and frequency noise, contribute to the measured photocurrent by some small fraction of this amount. The current spectral density due to either amplitude and frequency noise can be written as

$$i_{noise}(f)/\sqrt{\text{Hz}} = e \frac{\epsilon}{h\nu_0} T_{noise}(f) a_{noise}(f) \quad (5.6)$$

with $T_{noise}(f)$ the transfer function from the input of the noise to the demodulated output in units of watts per input noise unit, and $a_{noise}(f)$ being the magnitude of the input noise spectral density. Setting an equality

$$a_{noise}(f) = \mu \frac{T_{signal}(f) x_{sens}(f)}{T_{noise}(f)} \quad (5.7)$$

defines the limit of the input noise, where μ is the specified fraction of allowable noise due to technical sources, relative to the fundamental noise sources.

5.3 Input Noise

The noise is viewed in terms of its Fourier components. Each noise source is a modulation of the otherwise ideal input light, at a particular frequency, with a particular

magnitude. The input field can then be expanded to lowest order, which reveals the spectrum of the input light as the input carrier and RF sidebands components, each with a pair of corresponding noise sidebands, or nine frequency components in all. *It's assumed that the frequency and amplitude noises are on the laser light, before the phase modulator.* The consequence of this assumption is that there is coherence between the carrier and RF sideband noise terms, and that the noise amplitudes scale directly with the amplitudes of the carrier and RF sidebands. A requirement which must be satisfied to maintain this assumption is that none of the optics or electro-optics between the laser and interferometer add noise. This primarily drives the specifications on the mode cleaner and on the RF modulation oscillator.⁴

5.3.1 Laser Frequency Noise

The input light is ideally modeled as a single frequency, phase modulated field.

$$E_{laser} = E_i e^{i(\omega_0 t + \Gamma \cos(\Omega t))} \quad (5.8)$$

where the constants E_i and Γ are real. Frequency noise is defined such that its integral is the phase noise,[61] and is modeled as an additional phase term

$$\begin{aligned} \delta\phi(t) &= -2\pi \int \delta\nu \sin(2\pi ft) dt \\ &= \frac{\delta\nu}{f} \cos(2\pi ft) \end{aligned} \quad (5.9)$$

⁴This same approach can be used to set the limit of the amplitude of the RF oscillator, by neglecting the carrier noise terms. The phase noise of the RF oscillator requires a fundamentally different approach, as it adds noise to the demodulation phase, as well.

The laser field can be expanded to lowest order to generate the frequency noise spectra.

$$\begin{aligned}
E_{laser} &= E_i e^{i(\omega_0 t + \Gamma \cos(\Omega t) + \frac{\delta\nu}{f} \cos(2\pi f t))} \\
&= E_i e^{i\omega_0 t} e^{i\Gamma \cos(\Omega t)} e^{i\frac{\delta\nu}{f} \cos(2\pi f t)} \\
&\approx E_i e^{i\omega_0 t} (J_0(\Gamma) + iJ_1(\Gamma)e^{i\Omega t} + iJ_1(\Gamma)e^{-i\Omega t}) \left(1 + i\frac{\delta\nu}{2f}e^{i2\pi f t} + i\frac{\delta\nu}{2f}e^{-i2\pi f t}\right)
\end{aligned} \tag{5.10}$$

It is assumed that the modulation depth for the RF sidebands is much greater than the modulation depth which generates the frequency noise sidebands. Because of this, the usual expansion of $e^{i(\delta\nu/f)\cos(2\pi f t)}$ in terms of the Bessel functions J_i can be further simplified as $J_0(\delta\nu/f) \approx 1$ and $J_1(\delta\nu/f) \approx \delta\nu/(2f)$ for the noise sidebands. The final term in parentheses indicates that each RF sideband and the carrier are modified to be the original DC field plus upper and lower noise sidebands at the noise frequency f .

5.3.2 Laser Amplitude Noise

Amplitude noise is modeled as a modulation of the input field amplitude E_i

$$\begin{aligned}
E_i &\rightarrow E_i \left(1 + \frac{\delta E}{E_i} \cos(2\pi f t)\right) \\
&= E_i \left(1 + \frac{\delta E}{2E_i} e^{i2\pi f t} + \frac{\delta E}{2E_i} e^{-i2\pi f t}\right)
\end{aligned} \tag{5.11}$$

Substituting in Eq. (5.8), and expanding to low order as in the frequency noise case, gives

$$E_{laser} \approx E_i e^{i\omega_0 t} (J_0(\Gamma) + iJ_1(\Gamma)e^{i\Omega t} + iJ_1(\Gamma)e^{-i\Omega t}) \left(1 + \frac{\delta E}{2E_i} e^{i2\pi f t} + \frac{\delta E}{2E_i} e^{-i2\pi f t}\right) \tag{5.12}$$

Table 5.1 gives the various input amplitudes of the nine frequency components. The J_i 's are shorthand for the Bessel functions of the first kind which appear in the RF phase modulation, and are functions of the RF modulation depth Γ . The

first subscript indicates the carrier, upper and lower RF sideband by 0, +, and -, respectively. The second subscript indicates DC, upper and lower noise sideband by 0, +, and -, respectively.

	E_{--}	E_{-0}	E_{-+}	E_{0-}	E_{00}	E_{0+}	E_{+-}	E_{+0}	E_{++}
Laser frequency	$\frac{-J_1\delta\nu}{2f}$	iJ_1	$\frac{-J_1\delta\nu}{2f}$	$\frac{iJ_0\delta\nu}{2f}$	J_0	$\frac{iJ_0\delta\nu}{2f}$	$\frac{-J_1\delta\nu}{2f}$	iJ_1	$\frac{-J_1\delta\nu}{2f}$
Laser amplitude	$\frac{iJ_1\delta E}{2E_i}$	iJ_1	$\frac{iJ_1\delta E}{2E_i}$	$\frac{J_0\delta E}{2E_i}$	J_0	$\frac{J_0\delta E}{2E_i}$	$\frac{iJ_1\delta E}{2E_i}$	iJ_1	$\frac{iJ_1\delta E}{2E_i}$

Table 5.1: Spectral components of the input light due to frequency and amplitude noise.

5.4 Readout

The signal readout model used is from Chapter 3, Eq. (3.19), which is repeated here.

$$V_{noise}(t) = \Re\{[E_{00}^*(E_{++}e^{i\beta} + E_{-+}e^{-i\beta}) + E_{00}(E_{--}^*e^{i\beta} + E_{+-}^*e^{-i\beta}) + E_{0+}(E_{-0}^*e^{i\beta} + E_{+0}^*e^{-i\beta}) + E_{0-}^*(E_{+0}e^{i\beta} + E_{-0}e^{-i\beta})]e^{i\omega_n t}\} \quad (5.13)$$

The quantity of interest is the amplitude of this signal, given by

$$V_{noise} = |E_{00}^*(E_{++}e^{i\beta} + E_{-+}e^{-i\beta}) + E_{00}(E_{--}^*e^{i\beta} + E_{+-}^*e^{-i\beta}) + E_{0+}(E_{-0}^*e^{i\beta} + E_{+0}^*e^{-i\beta}) + E_{0-}^*(E_{+0}e^{i\beta} + E_{-0}e^{-i\beta})| \quad (5.14)$$

This is used in conjunction with the amplitudes of the input spectrum of Table 5.1 and the transmission functions of the next section in order to calculate the measured noise.

5.5 Transmission of Light

The model of the RSE interferometer is shown again in Figure 5.6.

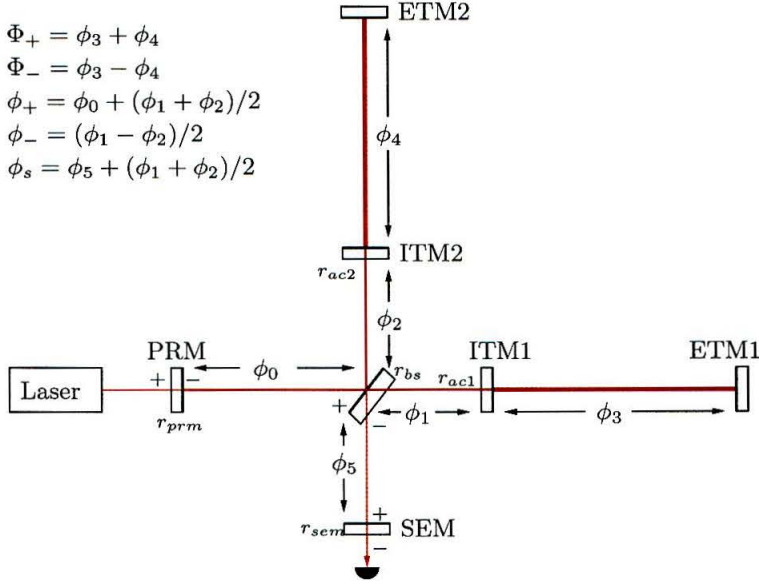


Figure 5.6: The RSE interferometer optical layout.

5.5.1 The General Transmission Function

The exact transmission function from the input of the power recycling mirror to the dark port is derived in Appendix B as

$$t = \frac{t_{prm} t_{m_f} t_{sem} e^{-i(\phi_+ + \phi_s)/2}}{1 + r_{prm} r_{m_f} e^{-i\phi_+} - r_{sem} r_{m_b} e^{-i\phi_s} - r_{prm} r_{sem} (r_c^2 - \delta r_c^2) A_{bs}^2 e^{-i(\phi_+ + \phi_s)}} \quad (5.15)$$

$$t_{m_f} = 2r_{bs} t_{bs} [\delta r_c \cos(\phi_-) + i r_c \sin(\phi_-)] \quad (5.16)$$

$$r_{m_f} = A_{bs} [(r_c + \delta r_c \Delta) \cos(\phi_-) + i(\delta r_c + r_c \Delta) \sin(\phi_-)] \quad (5.17)$$

$$r_{m_b} = A_{bs} [(r_c - \delta r_c \Delta) \cos(\phi_-) + i(\delta r_c - r_c \Delta) \sin(\phi_-)] \quad (5.18)$$

The arm cavities are modeled as the usual frequency dependent complex reflectivities. The two arm reflectivities are gathered into an average and differential arm reflectivity as follows.

$$r_c = (r_{c1} + r_{c2})/2 \quad (5.19)$$

$$\delta r_c = (r_{c2} - r_{c1})/2 \quad (5.20)$$

Implicit in the arm cavity reflectivities are the common and differential arm cavity phases.

$$\Phi_+ = \phi_3 + \phi_4 \quad (5.21)$$

$$\Phi_- = \phi_3 - \phi_4 \quad (5.22)$$

The beamsplitter is ideally 50% in reflectance (R_{bs}) and transmittance (T_{bs}). The mismatch (typically about 1%) and the loss (typically about 300 ppm) in these values are defined as

$$A_{bs} = R_{bs} + T_{bs} = 1 - L_{bs} \quad (5.23)$$

$$\Delta = (R_{bs} - T_{bs})/A_{bs} \quad (5.24)$$

In addition to optical imperfections, there will be imperfections in the phases in the interferometer. The degrees of freedom are held at their nominal phases against the natural disturbances of the environment by feedback control systems. The gains of these control systems will be finite, which means that the phase of the cavity will fluctuate around the nominal value by an amount characterized by the natural disturbance to the mirrors multiplied by the closed loop gain of the control system. Integrating this over the measurement bandwidth defines the RMS of the fluctuations about the desired phase. These fluctuations will be modeled as a DC offset equivalent to the RMS of the residual motion.

The approach to reducing Eq. (5.15) into something more usable will be to examine the carrier and the RF sidebands separately. For each, the nominal phases for the degrees of freedom will be defined for the DC component. RMS offsets will be added to this nominal value, as well as frequency dependence for the spectrum of noise sidebands accompanying the carrier or RF sidebands, in the following way.

$$\phi(f) = \phi_{\text{Nominal}} + \frac{(2\pi f)(2l)}{c} + d\phi \quad (5.25)$$

Eq. (5.15) will then be evaluated at these phases and expanded to first order in the optical imperfections and phase offsets.

5.5.2 The Carrier

Eq. (5.15) can be expanded to lowest order by first deriving appropriate expression for the arm cavity average and differential reflectivity. This is done in Appendix A, and given in Eq. (A.20) and Eq. (A.26).

$$r'_c(\omega) = r_c(\omega) + ig_a d\Phi_+ = \frac{r_c^0 + i(1 - L_{itm}/2)\frac{\omega}{\omega_c}}{1 + i\frac{\omega}{\omega_c}} + ig_a d\Phi_+ \quad (5.26)$$

$$\delta r'_c(\omega) = \delta r_c(\omega) + ig_a d\Phi_- = \frac{dLg_a}{4} \frac{1 - (dT/dL)\frac{\omega}{\omega_c}}{(1 + i\frac{\omega}{\omega_c})^2} + ig_a d\Phi_- \quad (5.27)$$

The following definitions are used, where it's been assumed that the end mirror reflectivity is unity, and so the losses and transmittance of the ETM must be included in the losses of the ITM in the calculation of r_{itm} .

$$g_a = \frac{2}{1 - r_{itm}} \quad (5.28)$$

$$\omega_c = \frac{c}{2l_{arm}} \frac{1 - r_{itm}}{\sqrt{r_{itm}}} \quad (5.29)$$

$$r_c^0 = r_{itm} - \frac{T_{itm}}{1 - r_{itm}} \quad (5.30)$$

The explicit frequency dependence will clutter the formulas, so a convention will be adopted that puts the frequency dependence into the superscript. A “+” will indicate a positive frequency component, “-” a negative one, and “0” for a DC component. In the case that a variable is used for both the carrier and RF sidebands, two superscripts will be used, the first indicating the carrier, upper, or lower RF sidebands by a c , $+$, or $-$ respectively, followed by the superscript which indicates the frequency of the noise component. Subscripts will typically be used to indicate degrees of freedom, or c for arm cavity. The one exception to this rule is in the t 's of the transmission functions, and E 's of the fields, where the frequency dependence is

in the subscript.

Appendix B.2 derives the relevant equation for the carrier from Eq. (5.15). Terms are kept to first order in the phase offsets. The DC carrier term is given by

$$t_{00} = t_{prm}A_{bs}t_{sem}g_{ifo}^{c0}[\delta r_c^0 + i(r_c^0 d\phi_- + g_a d\Phi_-)] \quad (5.31)$$

while the frequency dependent term is

$$t_{0\pm} = t_{prm}A_{bs}t_{sem}g_{ifo}^{c0}H^\pm(\delta r_c^\pm + ir_c^\pm(d\phi_- \pm (\omega\delta/c)) + ig_a d\Phi_-) \quad (5.32)$$

These use Eq. (5.26), Eq. (5.27), as well as the following definitions

$$g_{ifo}^{c0} = \frac{e^{-i\phi_{dt}/2}}{(1 + r_{prm}A_{bs}r_c^0)(1 - r_{sem}A_{bs}r_c^0 e^{-i\phi_{dt}})} \quad (5.33)$$

$$H^\pm = \frac{\left(1 \pm i\frac{\omega}{\omega_c}\right) \left(1 \pm i\frac{\omega}{\omega_c}\right)}{\left(1 \pm i\frac{\omega}{\omega_{cc}}\right) \left(1 \pm i\frac{\omega}{\omega_{sc}}\right)} \quad (5.34)$$

$$\omega_{cc} = (1 + r_{prm}r_c^0 A_{bs})\omega_c/2 \quad (5.35)$$

$$\omega_{sc} = \frac{1 - r_{sem}r_c^0 A_{bs}e^{-i\phi_{dt}}}{1 - r_{sem}A_{bs}e^{-i\phi_{dt}}}\omega_c \quad (5.36)$$

These last few equations define the frequency dependent interferometer gain, where the frequency dependence is carried in H^\pm . The shape of H^\pm has two zeros at the arm cavity pole ω_c and two poles which are the arm/power and arm/signal coupled cavity poles. A nice derivation of the poles and zeros of coupled cavities is done by Rahkmanov.[62]

As could be expected, the transmission at DC is strictly dependent on imperfections, either in differential mode offsets or arm mismatch, as seen by the terms in brackets of Eq. (5.31). This is nearly true for the transmission of the noise sidebands on the carrier as well, with the exception of the coupling via the asymmetry by $(\omega\delta/c)$ as seen in Eq. (5.32).

DC Carrier Term

It's useful to make a comparison of the sensitivity of the RSE interferometer with the initial LIGO I interferometer, in order to get a sense for how much the specifications might change. In the initial LIGO I configuration, with no signal mirror, it was noted that the largest source of noise was due typically to noise on the RF sidebands which beat against the carrier mismatch contrast defect.[59] The level of contrast can be compared in RSE to LIGO I by examining the ratio

$$\frac{|t_{prm}A_{bs}t_{sem}g_{ifo}^{c0}|}{t_{prm}A_{bs}g_{ifo,LIGO\ I}^{c0}} \quad (5.37)$$

These terms in the ratio are the interferometer-dependent gains for the amplitude of the mismatch carrier defect. The ratio then assumes the same input power and the same level of δr_c^0 . The LIGO I interferometer gain is given by

$$g_{ifo,LIGO\ I}^{c0} = \frac{1}{1 + r_{prm}A_{bs}r_c^0} \quad (5.38)$$

Figure 5.7 plots this ratio using the same optical parameters (except for the addition of the signal mirror, of course). Figure 5.7 shows that the signal tuned interferometer

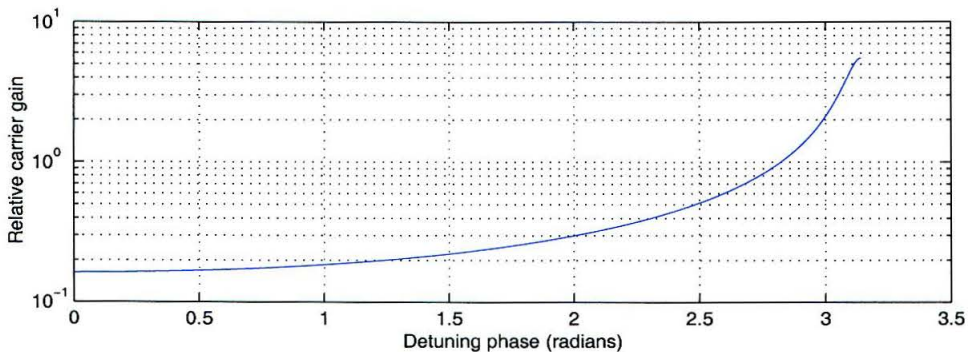


Figure 5.7: Ratio of the RSE DC carrier gain to that of the LIGO I configuration, as a function of detuning phase. The optical parameters are $T_{itm} = 3\%$, $T_{prm} = 1\%$, and $T_{sem} = 10\%$.

suppresses the contrast defect by nearly a factor of ten for most all detunings. The

source of the suppression has two factors. First is simply the amplitude transmissivity of the signal mirror, which in this case is 0.32. Second is the suppression due to the fact that the signal cavity is actually *anti-resonant* at the carrier frequency. The cavity phase itself is at a resonance condition for broadband RSE, but the fact that the arms are over-coupled adds a phase of π upon reflection, hence making the cavity anti-resonant. The transmissivity of an anti-resonant cavity is roughly 1/2 that of the transmissivity of the mirrors involved. The combination of these two factors suggests a transmissivity which is roughly 0.16 times that of LIGO I, which is what the figure shows. This degrades somewhat as the signal cavity is detuned away from the RSE point, although the mismatch carrier defect suppression remains fairly good for most detunings. At the dual-recycling point, however, it's seen that this defect is actually enhanced. This was a result also discovered by the modeling efforts of Bochner.[29]

Carrier Noise Sidebands

The comparison between an RSE interferometer and the LIGO I configuration for the transmission of the frequency dependent part of the carrier transmission can be made as well. Eq. (5.32) gives the equation for the transmissivity of the RSE interferometer for the carrier noise sidebands. Clearly, the noise sidebands couple through the imperfections via the gain of $t_{prm}A_{bs}t_{sem}g_{ifo}^{c0}H^{\pm}$. The only difference between this and the previous section is the frequency dependence contained in the interferometer gain term, H^{\pm} . The overall DC gain suppression factor for RSE will be the same. For LIGO I, without the signal cavity, the second pole and the second zero in Eq. (5.34) don't exist.

$$H_{\text{LIGO I}}^{\pm} = \frac{\left(1 \pm i \frac{\omega}{\omega_c}\right)}{\left(1 \pm i \frac{\omega}{\omega_{cc}}\right)} \quad (5.39)$$

LIGO I has a pole at the coupled cavity pole, which is typically about 1 Hz. The zero is the arm cavity zero, around 100 Hz. Thus, the frequency response for carrier noise sidebands in LIGO I rolls off at 1 Hz, then flattens out at 100 Hz. In the bandwidth

of interest, then, the noise sidebands are about a factor of 100 smaller than the DC term.

The RSE response is given in Eq. (5.34), and has two zeros at 100 Hz, the arm/power coupled cavity pole at 1 Hz, and the arm/signal cavity pole, which is characteristic of the frequency response of the arm/signal coupled cavity system. This is typically much larger than the arm cavity pole frequency in broadband. Even for a detuned interferometer, this will typically be larger than the arm cavity pole frequency, since the signals of interest are in the several hundred Hz range. The response is then expected to roll off at 1 Hz, as before, but at the arm cavity pole frequency, the two zeros cause the response to increase. The details of the signal cavity determine the overall coupling in the bandwidth of interest. In the broadband RSE case, this will be a simple pole at some fairly high frequency. For a detuned interferometer, the pole will be complex, and a somewhat more complicated response is expected.

An example using the same parameters as in the previous section is displayed in Figure 5.8, for a broadband RSE interferometer, and one detuned by $\phi_{dt} = 0.2$ radians. In each case, the gain reduction of roughly 0.16 is evident, as well as the presence of the extra zero in the RSE response. In the broadband case, the noise sidebands are actually enhanced over the LIGO I case above 600 Hz. It should be pointed out that, in all likelihood, this example interferometer is not practical, because the bandwidth is much too high to be of any use. However, the detuned case is perhaps more disturbing. The peak frequency here is around 900 Hz, which is also exactly where the carrier noise sidebands are being most effectively transmitted. It is expected that the carrier noise terms might be more of an issue in RSE than in LIGO I, where they were insignificant.

5.5.3 RF Sidebands

The treatment of the RF sidebands in the interferometer has two major simplifications over that of the carrier. First, the interferometer is designed to have high

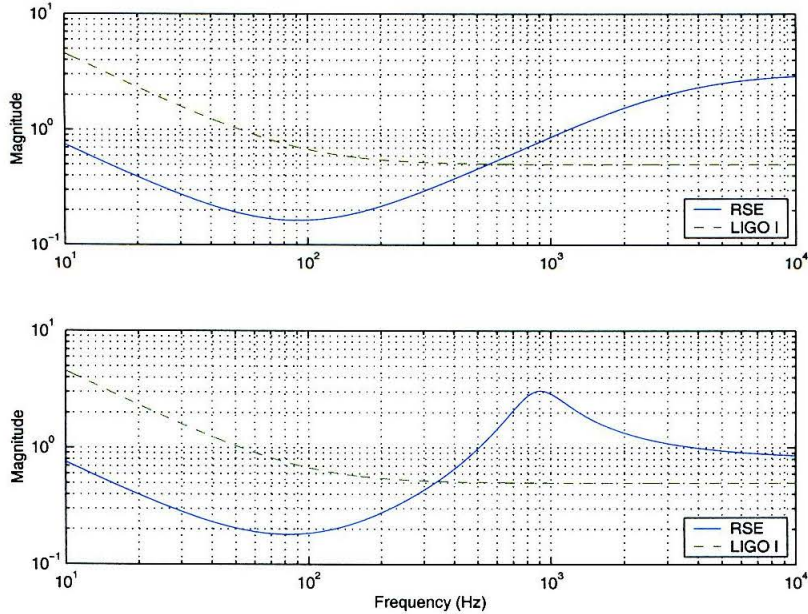


Figure 5.8: Carrier noise sideband transmission gain for RSE ($\phi_{dt} = 0$, top) and a detuned RSE ($\phi_{dt} = 0.2$, bottom) and LIGO I. The same optics are used, $T_{itm} = 3\%$, $T_{prm} = 1\%$, and $T_{sem} = 10\%$.

transmission to the dark port. Hence, first order terms due to imperfections are very small compared to the zeroth order term. Also, the calculation of the measured noise will use products of carrier and RF sideband terms. Since only first order terms exist in the carrier equations, any first order terms in the RF sideband equations would generate second order predictions, which are not being considered here. As a result, the interferometer imperfections and phase offsets can be ignored.

Second, since the RF sidebands are non-resonant in the arm cavities, all references to arm cavity phases and mismatches are neglected, and the arm cavity reflectivity is set to unity.⁵ However, the physical Michelson asymmetry included in the Michelson degree of freedom will keep the sines and cosines in the Michelson reflectivity and

⁵This approximation breaks down at frequencies in the many kHz, as the frequencies get closer to a resonant condition (18.75 kHz for 4 km arms).

transmissivity terms. Eq. (5.15) simplifies in the following way.

$$t = \frac{it_{pr m}A_{bs}t_{sem} \sin(\phi_-)e^{-i(\phi_++\phi_s)/2}}{1 + r_{pr m}A_{bs} \cos(\phi_-)e^{-i\phi_+} - r_{sem}A_{bs} \cos(\phi_-)e^{-i\phi_s} - r_{pr m}r_{sem}A_{bs}^2e^{-i(\phi_++\phi_s)}} \quad (5.40)$$

Defining the phases for the RF sidebands requires more care. At issue is the method of optimizing the transmission of one RF sideband to the dark port when the interferometer is detuned. As the detuning changes, there are two methods of re-optimizing the RF sideband transmission – either the length of the signal cavity can be changed to null the effect of the detuning, or else the frequency of the modulation can be changed, to re-optimize the RF sideband transmission.

It will be assumed that a configuration is chosen such that the RF sidebands resonate within the power and signal cavities, individually, at the broadband RSE tuning. The RF sideband frequency for the broadband interferometer is Ω_{bb} , so that

$$\phi_{bb}^{\pm} = \frac{2l}{c}(\omega_0 \pm \Omega_{bb}) \quad (5.41)$$

will be the nominal broadband phase for the three degrees of freedom that the RF sidebands are sensitive to: ϕ_+ , ϕ_- , and ϕ_s . The length l then refers to the degree of freedom length, and ω_0 is the carrier frequency. Detunings will be accommodated by introducing a phase η , such that

$$\eta = \frac{2l}{c}d\Omega + \frac{2\Omega_{bb}}{c}dl \quad (5.42)$$

where a length change is indicated by dl and a frequency shift in the RF modulation frequency is indicated by $d\Omega$. This allows for either of the methods for optimization of RF sideband power at the dark port to be used in the equations. The general RF sideband phase will then be written as

$$\phi^{\pm} = \frac{2l}{c}(\omega_0 \pm \Omega_{bb}) + \eta^{\pm} \quad (5.43)$$

The broadband RF sideband phases are then (modulo 2π)

$$\phi_+^\pm = \pm\pi \quad (5.44)$$

$$\phi_s^\pm = \pm 2\pi \quad (5.45)$$

$$\phi_-^\pm = \pm\alpha = \pm \frac{\Omega_{bb}\delta}{c} \quad (5.46)$$

where δ is the macroscopic asymmetry $l_1 - l_2$.

The power and signal cavities are both relatively short (of order 10 m), which corresponds to a free spectral range of roughly 10 MHz. Even with an unlikely finesse of 1000, the bandwidth of these cavities wouldn't be much less than 10 kHz (for typical numbers, the bandwidth of the power/signal coupled cavity tends to be roughly 100 kHz). This allows the assumption that the transmission for the DC RF sidebands and their noise sidebands is constant over the bandwidth of interest, so the dependence on the frequency of the noise sideband $\pm\omega$ can be ignored.

The transmissivity for the RF sidebands is derived in Appendix B.3.

$$t_\pm = \pm t_{prm} A_{bs} t_{sem} \sin(\alpha') g_{ifo}^\pm \quad (5.47)$$

$$g_{ifo}^\pm = \frac{e^{-i(\phi_{dt} + \eta_s^\pm + \eta_+^\pm)/2}}{t_{D\pm}} \quad (5.48)$$

$$t_{D\pm} = 1 - r_{prm} A_{bs} \cos(\alpha') e^{-i\eta_+^\pm} - r_{sem} A_{bs} \cos(\alpha') e^{-i(\eta_s^\pm + \phi_{dt})} + r_{prm} r_{sem} A_{bs}^2 e^{-i(\eta_+^\pm + \eta_s^\pm + \phi_{dt})} \quad (5.49)$$

where the primed α is defined to include the η phase as

$$\alpha' = \alpha \mp \eta_-^\pm \quad (5.50)$$

The approach used in this thesis is to modify the length of the signal cavity to

match the detuning phase for the lower RF sideband, that is

$$\eta_s^- = -\phi_{dt} = \frac{-\Omega 2\delta l_{sec}}{c} \quad (5.51)$$

$$\eta_s^+ = +\phi_{dt} = \frac{+\Omega 2\delta l_{sec}}{c} \quad (5.52)$$

All other η 's are zero.

5.6 Calculation of the Measured Noise

The input spectrum of Table 5.1 is propagated to the dark port via Eqs. (5.31), (5.32), and (5.47). The measured noise is given by the product of these terms using Eq. (5.14).

5.6.1 Broadband RSE

In the broadband RSE interferometer, both RF sidebands are designed to transmit equally to the dark port. Section 5.1.1 discussed conceptually the methods of noise coupling, which are borne out in the calculation of the noise signals. As mentioned earlier, only the inphase demodulation is considered.

Frequency Noise

The largest coupling mechanism for frequency noise is through the arm cavity mismatch. The level of noise is given by

$$V^{freq} = 4|E_i|^2 J_0 J_1 \frac{\delta\nu}{2f} T_{prm} T_{sem} A_{bs}^2 g_{ifo}^{c0} g_{ifo}^+ r_c^0 \sin(\alpha) |-\delta r_c^0 + H^+ \delta r_c^+| \quad (5.53)$$

The first term in the absolute value indicates the coupling of RF sideband noise terms which beat against the mismatch carrier DC defect, while the second term is due to the carrier noise terms which beat against the DC RF sidebands.

Amplitude Noise

Amplitude noise couples predominantly through offsets in the differential modes, ϕ_- and Φ_- .

$$V^{amp} = 4|E_i|^2 J_0 J_1 \frac{\delta E}{2E_i} T_{prm} T_{sem} A_{bs}^2 g_{ifo}^0 g_{ifo}^+ r_c^0 \sin(\alpha) |(r_c^0 + H^+ r_c^+) d\phi_- + g_a d\Phi_-| \quad (5.54)$$

Again, the way to interpret these terms is to look at whether there is frequency dependence in the coupling mechanism. A DC term ($r_c^0 d\phi_-$ or $g_a d\Phi_-$) indicates a coupling mechanism for the noise on the RF sidebands, while a frequency dependent term, such as $H^+ r_c^+ d\phi_-$, is due to noise on the carrier which have the RF sidebands as its local oscillator.

5.6.2 Detuned RSE

The corresponding equations for detuned RSE will be much more complicated due to the fact that the upper and lower RF sidebands, as well as the upper and lower noise audio sidebands, must each be handled individually. Furthermore, the dependence on demodulation phase needs to be considered. To simplify the calculation of the measured noise, the inphase and quadrature demodulations will be calculated separately, and summed as in Eq. (5.55).

$$V_{noise} = |V_I \cos(\beta) + V_Q \sin(\beta)| \quad (5.55)$$

Furthermore, the output signal will be separated into the contributions due to RF sideband noise which beats against the carrier contrast defects, and the contributions due to carrier noise which beats against the DC RF sidebands. Subscripts will indicate the noise term, V_{sb} for RF sideband noise, V_{car} for carrier noise.

$$V_{sb} = E_{00}^*(E_{++}e^{i\beta} + E_{-+}e^{-i\beta}) + E_{00}(E_{--}^*e^{i\beta} + E_{+-}^*e^{-i\beta}) \quad (5.56)$$

$$V_{car} = E_{0+}(E_{-0}^*e^{i\beta} + E_{+0}^*e^{-i\beta}) + E_{0-}^*(E_{+0}e^{i\beta} + E_{-0}e^{-i\beta}) \quad (5.57)$$

A second subscript, I or Q, will indicate the demodulation quadrature.

The RF sideband gains can be brought together with the following definitions.

$$\bar{g} = g_{ifo}^+ + g_{ifo}^- \quad (5.58)$$

$$\Delta g = g_{ifo}^+ - g_{ifo}^- \quad (5.59)$$

These terms will occur in the formulas as either their $\Re\{\}$ or $\Im\{\}$ parts. It should be noted that the resonant, lower RF sideband interferometer gain is real, so couplings which depend on $\Im\{g\}$ depend only on the non-resonant upper RF sideband. Furthermore, this suggests that $\Im\{\bar{g}\} = \Im\{\Delta g\}$. Also, Δg is nominally zero in the balanced RF sideband case, so it's a measure of the imbalance of the RF sidebands in the interferometer as well.

Frequency Noise

The inphase demodulation noise couplings due to frequency noise are given in the following equations.

$$V_{sb,I}^{freq} = -2|E_i|^2 J_0 J_1 \frac{\delta\nu}{2f} T_{prm} T_{sem} g_{ifo}^{c0} \sin(\alpha) [\delta r_c^0 \Re\{\bar{g}\} + \Im\{\bar{g}\} (r_c^0 d\phi_- + g_a d\Phi_-)] \quad (5.60)$$

$$V_{car,I}^{freq} = |E_i|^2 J_0 J_1 \frac{\delta\nu}{2f} T_{prm} T_{sem} g_{ifo}^{c0} \sin(\alpha) \left[((H^- \delta r_c^-)^* \bar{g} + H^+ \delta r_c^+ \bar{g}^*) + i r_c^+ [(H^- \bar{g} - H^+ \bar{g}^*) d\phi_- - (H^- \bar{g} + H^+ \bar{g}^*) (\omega \delta / c)] \right] \quad (5.61)$$

Likewise the quadrature demodulation noise couplings are given below.

$$V_{sb,Q}^{freq} = 2|E_i|^2 J_0 J_1 \frac{\delta\nu}{2f} T_{prm} T_{sem} g_{ifo}^{c0} \sin(\alpha) [\delta r_c^0 \Im \{\Delta g\} - \Re \{\Delta g\} (r_c^0 d\phi_- + g_a d\Phi_-)] \quad (5.62)$$

$$V_{car,Q}^{freq} = i|E_i|^2 J_0 J_1 \frac{\delta\nu}{2f} T_{prm} T_{sem} g_{ifo}^{c0} \sin(\alpha) \left[((H^- \delta r_c^-)^* \Delta g - H^+ \delta r_c^+ (\Delta g)^*) - i r_c^+ [(H^{-*} \Delta g + H^+ \Delta g^*) d\phi_- - (H^{-*} \Delta g - H^+ \Delta g^*) (\omega\delta/c)] \right] \quad (5.63)$$

Amplitude Noise

Amplitude noise couplings in the inphase quadrature are given by

$$V_{sb,I}^{amp} = i2|E_i|^2 J_0 J_1 \frac{\delta E}{2E_i} T_{prm} T_{sem} g_{ifo}^{c0} \sin(\alpha) [\delta r_c^0 \Im \{\bar{g}\} - \Re \{\bar{g}\} (r_c^0 d\phi_- + g_a d\Phi_-)] \quad (5.64)$$

$$V_{car,I}^{amp} = |E_i|^2 J_0 J_1 \frac{\delta E}{2E_i} T_{prm} T_{sem} g_{ifo}^{c0} \sin(\alpha) \left[((H^- \delta r_c^-)^* \bar{g} - H^+ \delta r_c^+ \bar{g}^*) + i r_c^+ [(H^{-*} \bar{g} + H^+ \bar{g}^*) d\phi_- - (H^{-*} \bar{g} - H^+ \bar{g}^*) (\omega\delta/c)] \right] \quad (5.65)$$

The quadrature demodulation amplitude noise couplings are given by

$$V_{sb,Q}^{amp} = i2|E_i|^2 J_0 J_1 \frac{\delta E}{2E_i} T_{prm} T_{sem} g_{ifo}^{c0} \sin(\alpha) [\delta r_c^0 \Re \{\Delta g\} + \Im \{\Delta g\} (r_c^0 d\phi_- + g_a d\Phi_-)] \quad (5.66)$$

$$V_{car,Q}^{freq} = i|E_i|^2 J_0 J_1 \frac{\delta E}{2E_i} T_{prm} T_{sem} g_{ifo}^{c0} \sin(\alpha) \left[((H^- \delta r_c^-)^* \Delta g + H^+ \delta r_c^+ (\Delta g)^*) - i r_c^+ [(H^{-*} \Delta g - H^+ \Delta g^*) d\phi_- - (H^{-*} \Delta g + H^+ \Delta g^*) (\omega\delta/c)] \right] \quad (5.67)$$

There is a great deal of similarity in all these equations. Essentially, the equations permute the combinations of $\Re \{\}$ and $\Im \{\}$ along with \bar{g} and Δg . It's also noted that the one term which would survive in the broadband RSE interferometer, $\Re \{\bar{g}\}$, picks out the coupling mechanisms for frequency and amplitude noise found in the previous section. In general, though, it's seen that every coupling mechanism now exists for

each noise source.

5.7 Analysis

The mismatch carrier defect δr_c is the coupling mechanism which is a constant of the interferometer, being a function of the difference in losses and transmittances of the optics. The specifications on amplitude and frequency noise set by this coupling mechanism will define a fiducial level of coupling that control systems can't improve. Acceptable residual RMS phase fluctuations of the other two coupling mechanisms, $d\phi_-$ and $d\Phi_-$, will be set at a level which degrades the fiducial specifications on the laser amplitude and frequency due to mismatch carrier defect noise by a factor of 2.

Two methods are used to do this analysis. First, the full, general equations of Eq. (5.15) are used to propagate the terms in Table 5.1 to the dark port, which are folded into the readout equation. Second, the analytical expressions derived in Section 5.6 are also evaluated and compared to the "exact" results using Eq. (5.15).

A Matlab code was written to do this comparison, *rsenoise.m*, which calculates the level of input frequency and amplitude noise equivalent to the expected fundamental noise sources, as in Eq. (5.7). This code is available through the STAIC webpage.[63] The interferometers discussed in this thesis, the optimized broadband and the 1 kHz narrowband interferometer of Chapter 2, are analyzed in this section. In general, though, *rsenoise.m* can be used for any configuration. The code uses a separate configuration file which inputs all the physical parameters of the interferometer so the engine code, *rsenoise.m*, doesn't have to be edited.

Sapphire optics are assumed, which contribute 480 ppm loss in substrate absorption. Coating losses are assumed to be 37.5 ppm per optic. AR coating loss is assumed to be 300 ppm. Mismatch of the ITM transmittance is assumed to be 1% of the nominal value. Mismatch of arm losses is assumed to be 30 ppm. The input power is assumed to be 120 watts. The specifications placed on the laser frequency and amplitude noise will be 10% of the input spectrum which is equivalent to the measured fundamental noise.

5.7.1 Optimized Broadband RSE

The interferometer which was optimized for binary inspiral sources in Section 2.3.2 has ITM transmittances of 0.5% and a SEM transmittance of 5%. The power recycling mirror is calculated by *rnoise.m*. The modulation frequency is assumed to be 81 MHz, similar to the work in this thesis. Lengths chosen for the power and signal cavities are the shortest to be consistent with the resonance conditions for those cavities. The asymmetry is taken from the analysis of Section 3.4.1 which most effectively diagonalizes the control matrix.

First, the noise coupling is evaluated at a single frequency as a function of demodulation phase. The optimized broadband configuration has a peak sensitivity at roughly 300 Hz. Figure 5.9 is the output of a version of *rnoise.m*, which shows the level of amplitude and frequency noise equivalent to the quadrature sum of thermal and shot noise at 300 Hz as a function of demodulation phase. The strain sensitivity at 300 Hz is also shown. The interesting thing here is the strong dependence on

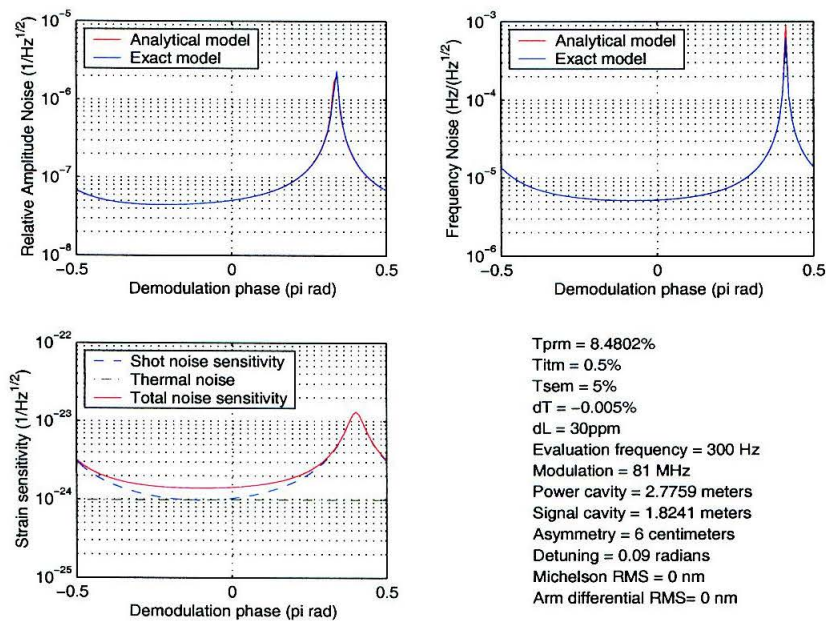


Figure 5.9: Optimized broadband noise coupling as a function of demodulation phase, evaluated at 300 Hz.

the demodulation phase. This is perhaps not unexpected. In the broadband RSE interferometer, the signal and RF sidebands are swinging length phasors, such that their scalar product varies from a maximum value to 0 with the change in demodulation phase. In a strongly detuned case, where one of the RF and one of the signal sidebands have been nearly suppressed, the resultant phasors are very nearly rotating circles. Hence the scalar product would be relatively constant as a function of demodulation phase. The optimized broadband case has only a weak suppression of the second signal or RF sideband, and so more closely resembles the balanced sideband case. It's to be expected that the 1 kHz narrowband interferometer will more closely be approximated by the strongly detuned limiting case.

Using the demodulation phase which maximizes the sensitivity at 300 Hz, the noise coupling due to arm mismatch is shown in Figure 5.10. This figure defines the fiducial level of laser amplitude and frequency noise. The contributions to the

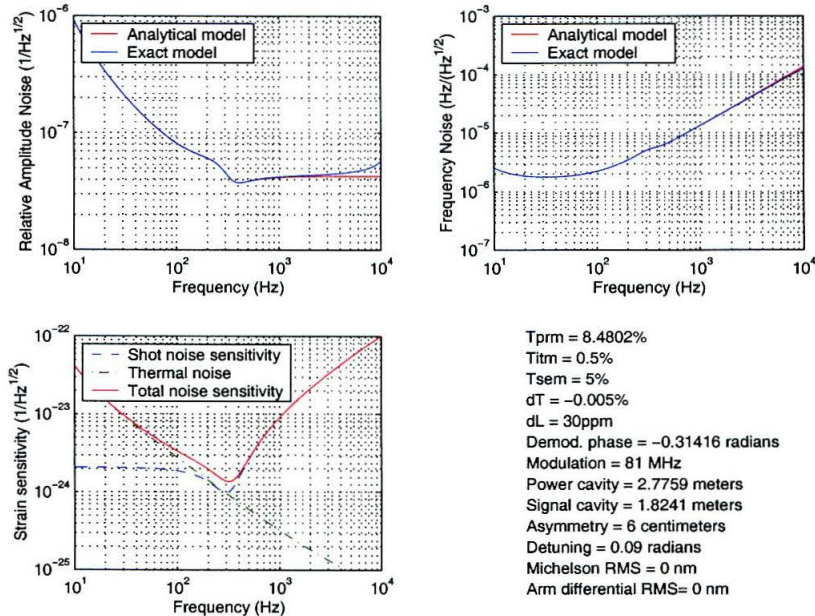


Figure 5.10: Optimized broadband noise coupling. The demodulation phase is chosen to optimize signal sensitivity at 300 Hz, from Figure 5.9.

total measured noise due to carrier noise and RF sideband noise can be decoupled to indicate the dominant coupling mechanism. This is shown in Figure 5.11. This

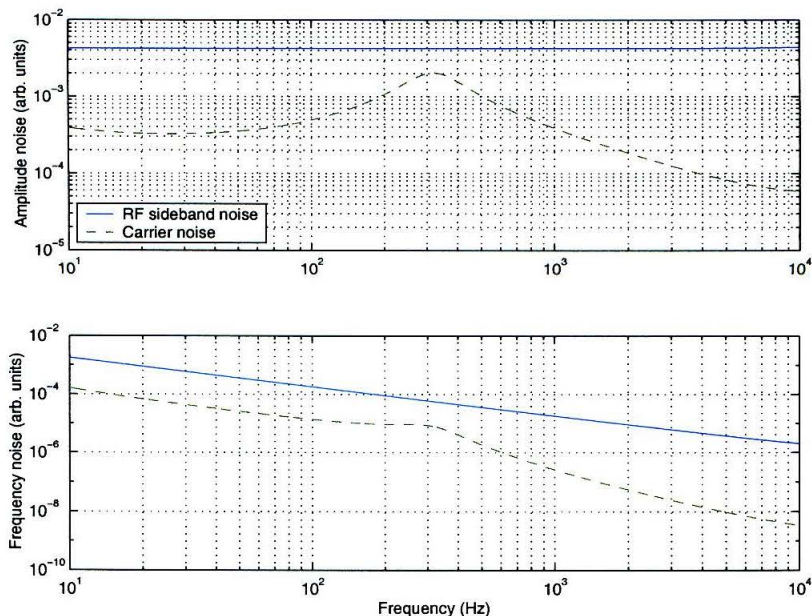


Figure 5.11: Contributions from carrier noise and RF sideband noise to the total measured noise in the optimized broadband interferometer.

clearly shows that the noise on the RF sidebands which couples to the mismatch carrier defect generates the strongest noise coupling, but only by a factor of 2 around the frequency of peak sensitivity.

The RMS differential phase fluctuations which increase the amplitude coupling by a factor of 2 are $d\phi_- = k(5 \times 10^{-10} \text{ m}_{RMS})$ and $d\Phi_- = k(5 \times 10^{-13} \text{ m}_{RMS})$ at 300 Hz, where k is the wavenumber. For comparison, the LIGO I requirements on differential length fluctuations are $\lesssim 10^{-9} \text{ m}_{RMS}$ and $\lesssim 10^{-13} \text{ m}_{RMS}$, respectively.[53] These length fluctuations are quite similar, and should be attainable. The amplitude noise at the input of the interferometer needs to be less than $2 \times 10^{-9} / \sqrt{\text{Hz}}$, which is a much more stringent requirement than the LIGO I requirement of $10^{-7} / \sqrt{\text{Hz}}$. [59] The coupling of amplitude noise to the mismatch carrier defect, as well as the increased laser power, are the main factors which drive the tightening of this specification.

The frequency noise specification, as in LIGO I, is dominated by mismatch defect and is relatively insensitive to the differential mode fluctuations. Due to the carrier defect suppression of RSE over LIGO I, which is the dominant coupling for frequency

noise, the frequency noise specification remains the same as LIGO I at $10^{-7}\text{Hz}/\sqrt{\text{Hz}}$ at 100 Hz, despite the fact that the input power has increased by a factor of 20.

5.7.2 Narrowband RSE

The narrowband interferometer optimized at 1 kHz from Section 2.3.1 has an ITM transmittance of 2% and a signal mirror transmittance of 0.25%. The asymmetry, found from the analysis in Section 3.4.2, is 1 cm.

The analysis is first done at the target frequency of 1 kHz, as a function of demodulation phase. As mentioned in Section 3.3, the narrowband interferometer tends

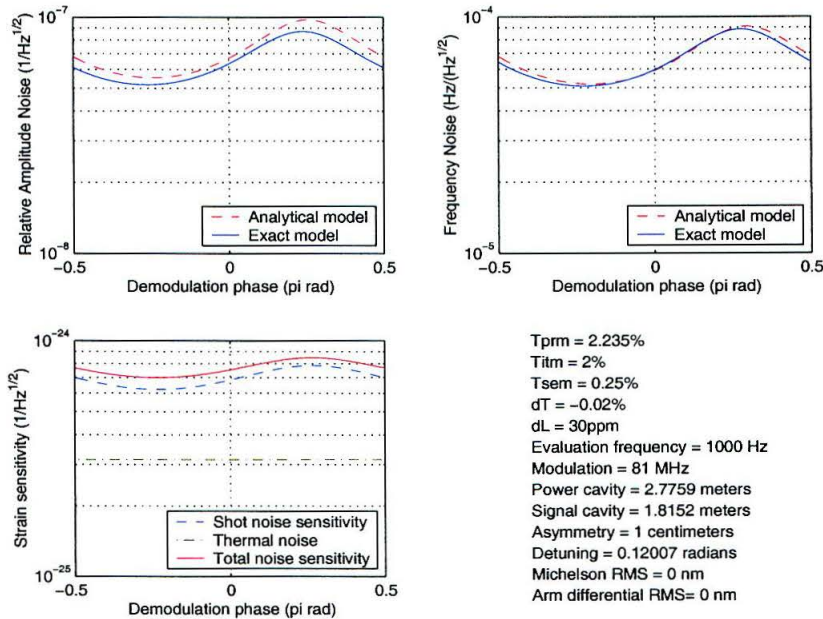


Figure 5.12: Noise coupling of a 1 kHz narrowband RSE interferometer evaluated at 1 kHz, as a function of demodulation phase.

to strongly suppress one of the signal and one of the RF sidebands, so the dependence on demodulation phase is much less at the targeted frequency. It should be noted that this would not be the case at other frequencies, since the relatively strong suppression of the signal sideband is only maximum around the target frequency. At lower and higher frequencies, the resultant signal sideband phasor is more elliptical

than circular.

Figure 5.13 is the analysis performed at the demodulation phase which maximizes the sensitivity at 1 kHz. The first thing evident is the fact that, away from 1 kHz, the

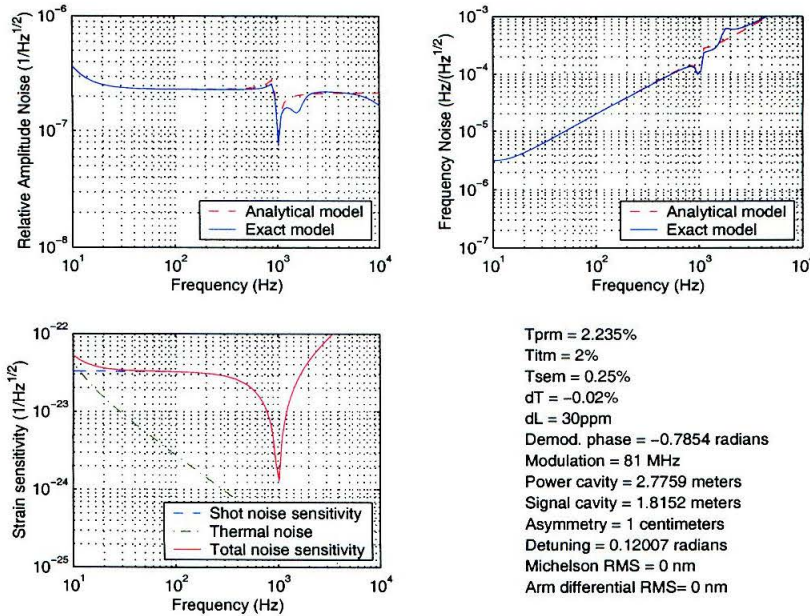


Figure 5.13: Noise coupling of a 1 kHz narrowband RSE interferometer, evaluated at the demodulation phase which maximizes the 1 kHz sensitivity.

noise coupling has dropped nearly an order of magnitude compared to the optimized broadband case. As in LIGO I, the strongest coupling in these frequency regions are from noise on the RF sidebands beating against the carrier defect. The stronger suppression of the carrier defect due to the lower transmittance of the signal mirror reduces this coupling mechanism, as discussed in Section 5.5.2. But, as also pointed out in that section, the carrier noise terms will be enhanced around the peak frequency in a detuned interferometer. This is what causes the dips in the spectra of amplitude and frequency noise around 1 kHz, and is clearly shown in Figure 5.14.

Using Figure 5.13 as a fiducial, the residual differential RMS fluctuations which are found to increase the sensitivity to laser amplitude noise by a factor of 2 are $d\phi_- = k(10^{-10} \text{ m}_{RMS})$ and $d\Phi_- = k(3 \times 10^{-12} \text{ m}_{RMS})$. The change in these numbers relative to the optimized broadband reflect the lower finesse of the arm cavities (which

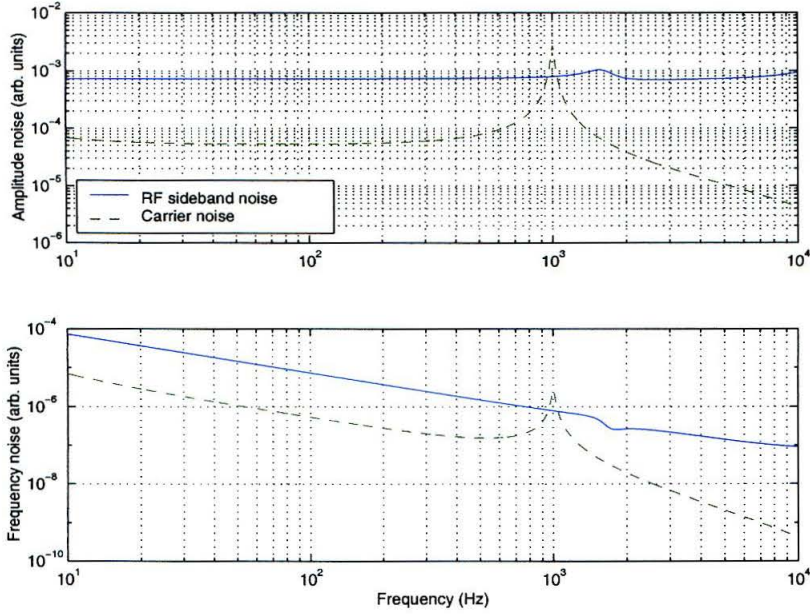


Figure 5.14: Contributions from the carrier noise and RF sideband noise to the total measured noise in the 1kHz narrowband interferometer.

affects $d\Phi_-$), and the higher finesse of the power recycling cavity (which affects $d\phi_-$). Again, both should be attainable, although the RMS for ϕ_- has decreased by an order of magnitude, compared to LIGO I.

Amplitude noise specifications are similar to those for the optimized broadband interferometer, at $\lesssim 2 \times 10^{-9}/\sqrt{\text{Hz}}$. As noted, this is mainly due to the enhanced transmission of carrier noise around the peak frequency. The specification for frequency noise is relaxed considerably. The narrowband interferometer requires sensitivity only at high frequencies, so it's clear that a fairly easily attainable level of $\lesssim 10^{-5}\text{Hz}/\sqrt{\text{Hz}}$ should be sufficient. It's most likely, however, that the laser will have a general design for use in any type of interferometer, so the more stringent requirements of the optimized broadband interferometer should be used.

5.7.3 Conclusion

The factors which influence noise coupling in RSE are somewhat more complicated than in the LIGO I configuration. A simple estimation based on the increased laser power (a factor of 20) clearly doesn't give proper specifications on acceptable laser noise levels.

Surprisingly, the specifications for frequency noise stay the same, or are even relaxed somewhat in the case of the narrowband interferometer. This is primarily due to its dependence on the mismatch contrast defect, which is more strongly suppressed in RSE relative to LIGO I.

Amplitude noise, on the other hand, has a much more stringent requirement. In the case of the optimized broadband interferometer, this is mainly due to its coupling to the mismatch carrier defect. The narrowband interferometer, on the other hand, shows the enhanced transmission of carrier noise sideband terms, as in the bottom Figure 5.8. It's worth investigating this a little further. Eq. (5.27) is the mismatch contrast defect, and is repeated here.

$$\delta r_c(\omega) = \frac{dLg_a}{4} \frac{1 - (dT/dL)\frac{\omega}{\omega_c}}{(1 + i\frac{\omega}{\omega_c})^2}$$

The DC term, which scales as the loss mismatch, dL , is the dominant coupling mechanism for the optimized broadband interferometer. The amplitude noise scales directly with this factor, so improving dL relaxes the amplitude noise specification by the same factor. The narrowband interferometer, on the other hand, is more sensitive to the frequency dependent part of this expression. The two poles at the cavity pole frequency aren't affected by the mismatch, but the frequency of the zero, $\frac{dT}{dT}\omega_c$, is. Loss mismatch is typically much smaller than transmittance mismatch, dT , so the zero frequency will usually be much less than the cavity pole, below the frequencies of interest. Decreasing dL decreases the zero frequency, but also decreases the gain, so there's no effect at frequencies above the zero. Decreasing dT increases the zero frequency, which reduces the factor δr_c at the carrier noise sideband frequency. Of course, in both cases, this level of coupling is what drove the specification of the dif-

ferential length RMS fluctuations, so an improvement in dL and/or dT would result in a tightening of the length control specifications.

There's one more factor which should be considered. Amplitude noise has another effect on the interferometer, known as "technical radiation pressure noise." Intensity fluctuations translate into force fluctuations on the test masses due to the recoil of the photons reflecting from them. An estimation of acceptable amplitude noise such that this is similarly a factor of 10 below the fundamental noise sensitivity is also roughly $\lesssim 10^{-9}/\sqrt{\text{Hz}}$. [64] In the end, these specifications appear to be fairly solid.

Appendix A

The Fabry-Perot Cavity

The Fabry-Perot cavity is just about the most fundamental building block of the Michelson-based gravitational wave interferometer. This Appendix will derive some useful formulas.

Figure A.1 shows the model of the Fabry-Perot cavity used in this Appendix, and the fields which will be of interest: the reflected, pickoff, and transmitted fields. The

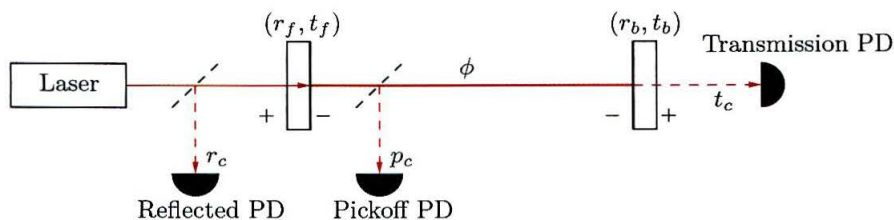


Figure A.1: The model of a Fabry-Perot cavity. The three fields of interest are marked by pickoffs and respective photodiodes. These are the reflected, pickoff, and transmitted fields. The mirror reciprocity convention used is the real, anti-symmetric convention, and the signs for the mirror reflectivities are indicated. The phase of the cavity, ϕ , is taken to be round trip.

fields at the reflected and pickoff photodiodes both have some method of guiding the light to the photodiode, such as a low reflectance pickoff optic placed in the beam. The efficiency of this cavity field-to-photodiode mechanism is usually less than one (especially for the pickoff field). In this Appendix the efficiency will be assumed to be unity, that is the fields discussed are the direct, inline fields of the cavity.

Probably the most cited characteristic of a cavity is the finesse, \mathcal{F} . This is given in any standard optics text,[65] although the typical assumption is that the reflectivity of the front and back mirrors are equal. Removing this assumption, the finesse, which

characterizes the fringe width relative to the spacing of the fringes, is

$$\mathcal{F} = \frac{\pi\sqrt{r_f r_b}}{1 - r_f r_b} \quad (\text{A.1})$$

The behavior of the cavity is a function of the mirrors and the round trip phase of the light. The cavity is periodic in its behavior as the phase increments by 2π radians. This defines a quantity known as the free spectral range, which is the frequency at which the phase changes by 2π for a given length.

$$f_{fsr} = \frac{c}{2l} \quad (\text{A.2})$$

where l is the one way length of the cavity, and the phase is given by $\phi = 2\pi 2lf/c$.

A.1 The Reflected Field

The reflectivity, as a function of the mirror parameters and the round trip phase is given by

$$r_c = r_f - \frac{T_f r_b e^{-i\phi}}{1 - r_f r_b e^{-i\phi}} \quad (\text{A.3})$$

$$= \frac{r_f - A_f r_b e^{-i\phi}}{1 - r_f r_b e^{-i\phi}} \quad (\text{A.4})$$

Lower case r 's and t 's will be used for amplitude reflectivity and transmissivity, while upper case R 's and T 's will be used for power reflectance and transmittance. The quantity A_f is given by

$$A_f = R_f + T_f = r_f^2 + t_f^2 = 1 - L_f \quad (\text{A.5})$$

and is associated with the losses of the front mirror. Resonance is satisfied for an integer 2π propagation phase. The reflectivity of the cavity, which is a complex

number, can be represented in a magnitude and phase form.

$$r_c = |r_c|e^{-i\phi_c} \quad (\text{A.6})$$

$$|r_c| = \sqrt{\frac{R_f + R_b A_f^2 - 2r_f r_b A_f \cos(\phi)}{1 + R_f R_b - 2r_f r_b \cos(\phi)}} \quad (\text{A.7})$$

$$\phi_c = \arctan\left(\frac{r_b T_f \sin(\phi)}{r_f(1 + R_b A_f) - r_b(2R_f + T_f) \cos(\phi)}\right) \quad (\text{A.8})$$

Examples of the cavity reflectivity are shown in Figure A.2. The two curves in the

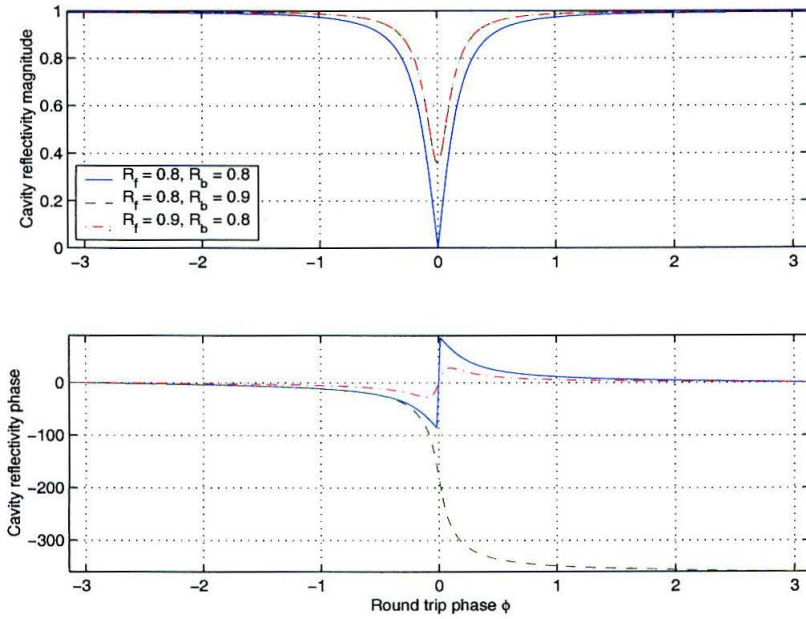


Figure A.2: Examples of cavity reflectivity for the cases where the mirrors are matched $T_f = T_b$, the front mirror has higher transmission than the back $T_f > T_b$, and when these mirrors are reversed.

magnitude plot which correspond to $R_f = 0.8$ and $R_b = 0.9$ and the converse are identical. Clearly, however, their phases are not. It needs to be noted that, on resonance, the cavity reflectivity is less than either of the individual cavity mirrors, whereas the reflectivity is greater than either of the individual cavity mirrors for most of the phase range away from resonance. This is a general feature of all cavities.

A.1.1 Cavity Coupling

One of the curves shows the reflectivity going to zero at the resonance point. From Eq. (A.3), this happens when

$$r_f = (1 - L_f)r_b \quad (\text{A.9})$$

One way to view this is that the reflectivity of the front mirror is equal to a modified back mirror whose reflectivity is decreased by a factor due to losses. Another, perhaps more enlightening approach, is to first assume the losses are small. Then Eq. (A.3) can be solved for the transmittance of the front mirror which satisfies this condition.

$$T_{f_{opt}} = T_b + L_f + L_b \quad (\text{A.10})$$

This condition is called “optimally coupled,” or “impedance matched.” Stated verbally, this condition says the transmittance of the front mirror is equal to the sum of the losses of the cavity, which includes the transmittance of the back mirror.

The optimally coupled point is a discontinuity in the reflectivity of a cavity, as a function of the front mirror parameters. For values $T_f > T_{f_{opt}}$, the cavity is referred to as “over-coupled.” Contrariwise, a cavity with $T_f < T_{f_{opt}}$ is referred to as “under-coupled.” The reflectivity of the cavity on resonance as a function of the front mirror parameters is shown in Figure A.3. As the front mirror departs from the optimally coupled point, the cavity reflectivity increases to either the reflectivity of the back or front mirror, whichever is highest. Perhaps the most interesting thing is the discontinuity in phase. The phase of the reflectivity of a resonant under-coupled cavity is positive, and the reflectivity phase of the over-coupled cavity is negative.

Figure A.2 can also be re-visited in this context. The two cases, $R_f = 0.8\%$, $R_b = 0.9\%$, and $R_f = 0.9\%$, $R_b = 0.8\%$ correspond to over- and under-coupled cavities, respectively. As noted earlier, the magnitude of the reflectivity is the same as a function of the cavity phase. However, the phase of the reflectivities are very different. For an under-coupled cavity, the phase of the reflectivity only wiggles a little around 0 radians as the cavity phase is swept through resonance. The over-coupled

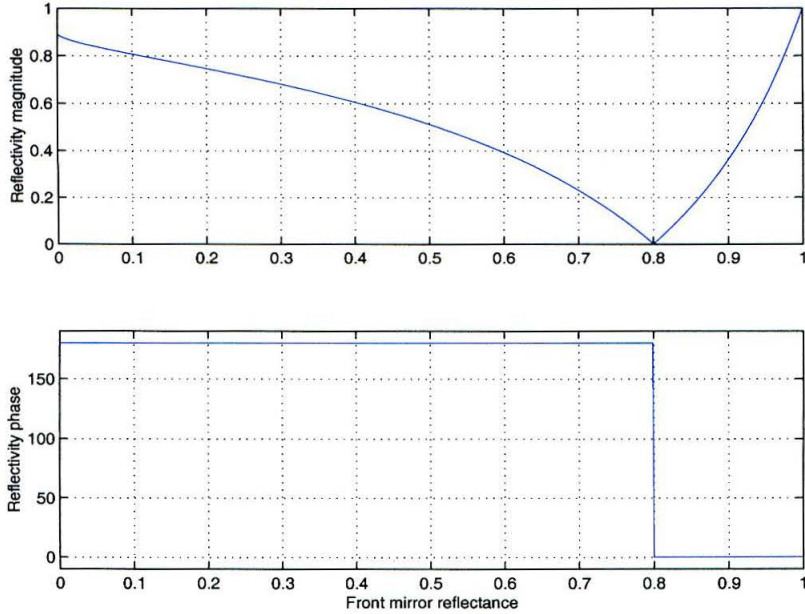


Figure A.3: Resonant cavity reflectivity as a function of the front mirror reflectance. The back mirror has reflectance of $R_b = 80\%$.

cavity reflectivity, on the other hand, goes through 2π phase as the the cavity phase is swept through resonance.

One way to approach this issue of the coupling is to refer back to Eq. (A.3). On resonance, this is a sum of two components, r_f and $-T_f r_b / (1 - r_f r_b)$, where the first term is positive, the second negative. These two terms refer to the prompt field, and the leakage field, respectively. This is because the reflected field is clearly a sum between the light which promptly reflects from the front mirror the first time it encounters the mirror, and the field which transmits, or “leaks out” through the front mirror from the cavity. Optimal coupling occurs when the magnitude of these two fields is equal. The limit of over-coupling occurs when the leakage field is nearly twice the amplitude of the prompt field, for mirrors of low transmittance. In the limit of under-coupling, almost all of the light is promptly reflected.

A.1.2 Cavity Approximations

The fundamental assumption for all approximations is that the cavity phase deviation from resonance, frequency dependent or DC offset, is small compared to π . In frequency terms, this is equivalent to saying the frequency is small compared to the free spectral range of the cavity. Typical RMS offsets from resonance for the arm cavities are small, maybe at most 10^{-5} radians. On the other hand, given arm lengths of 4 km, the minimum phase due to frequency dependent offset at 10 Hz is roughly 2×10^{-3} radians. This allows a reasonable assumption that the effect of the RMS offset can be dealt with separately from the frequency dependence.

First, the effect of offset is considered. Eq. (A.3) can be expanded in a Taylor series to first order as

$$r_c \approx \frac{r_f - A_f r_b e^{-i\phi}}{1 - r_f r_b e^{-i\phi}} + i \frac{T_f r_b e^{-i\phi}}{(1 - r_f r_b e^{-i\phi})^2} d\phi \quad (\text{A.11})$$

The back mirror typically has nearly unity reflection ($\approx .99997$ for the LIGO arm cavities), and so can be assumed to be 1. The front mirror also has high reflectivity, although the transmittance typically is much larger than the losses, so r_f can be expanded.

$$r_f = \sqrt{1 - T_f - L_f} \approx 1 - T_f/2 \quad (\text{A.12})$$

Making this approximation in the coefficient of $d\phi$ and evaluating at resonance, $\phi = 0$, gives

$$r_c \approx r_c^0 + i g_c d\phi \quad (\text{A.13})$$

$$r_c^0 = \frac{r_f - A_f r_b}{1 - r_f r_b} \quad (\text{A.14})$$

$$g_c = \frac{2}{1 - r_f} \quad (\text{A.15})$$

Thus the effect of an offset on the reflected field is a phase shift g_c times the offset.

The frequency dependent reflectivity for the cavity is best derived in a different fashion. The reflectivity of a 4 km long cavity as a function of frequency displaced

from the resonant frequency is shown in the following Figure A.4. The front mirror has $T = 3\%$, the back mirror has near unity reflectance, and the cavity losses are 75 ppm. The shape of this curve is very suggestive of a pole-zero response, where the

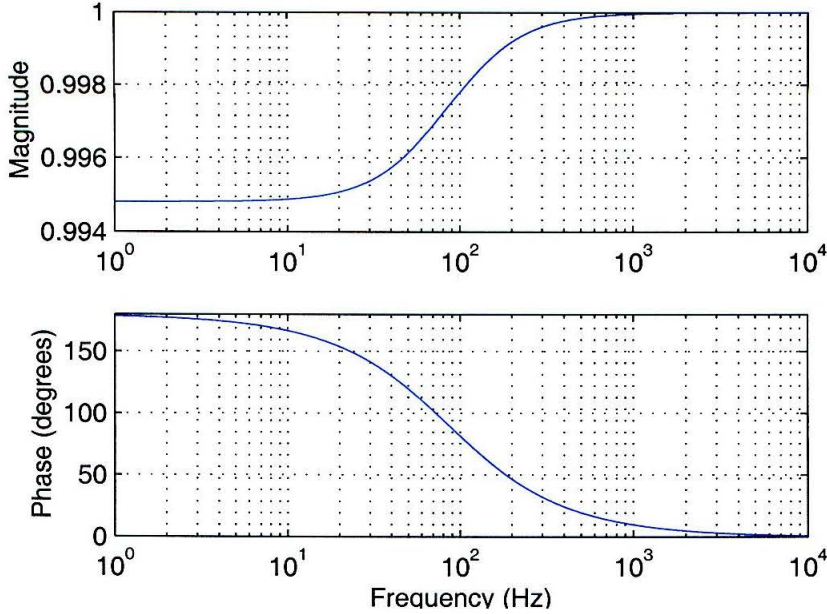


Figure A.4: Arm cavity reflectivity as a function of frequency. The cavity is 4 km long, so the free spectral range is about 37.5 kHz.

zero is non-minimum phase.¹ The reflectivity can be modeled as such, requiring three pieces of information: the DC gain, and the frequencies of the pole and zero. The DC gain is simply the cavity reflectivity on resonance, as expressed in Eq. (A.14). The pole should be the well-known cavity pole, given in Eq. (A.37), due to energy conservation arguments.

$$\omega_c = \frac{c}{2l} \frac{1 - r_f r_b}{\sqrt{r_f r_b}} \quad (\text{A.16})$$

The zero isn't obvious, but can be deduced from the fact that the cavity reflectivity should asymptote, at high frequency, to the value of the cavity reflectivity at anti-

¹If the cavity had been arranged to be under-coupled, the reflectivity would have a minimum phase zero.

resonance.

$$r_{canti-res.} = \frac{r_f + A_f r_b}{1 + r_f r_b} \quad (\text{A.17})$$

$$\approx 1 - \frac{L_f}{2} \quad (\text{A.18})$$

Putting these three bits of information together gives an approximation to the cavity reflectivity as

$$r_c(\omega) = \frac{r_c^0 + i(1 - \frac{L_f}{2})(\omega/\omega_c)}{1 + i(\omega/\omega_c)} \quad (\text{A.19})$$

Combining this with the phase offset term will define

$$r'_c(\omega) = \frac{r_c^0 + i(1 - \frac{L_f}{2})(\omega/\omega_c)}{1 + i(\omega/\omega_c)} + i g_a d \Phi_+ \quad (\text{A.20})$$

A comparison of this formula with the exact formula of Eq. (A.3) is shown in the following Figure A.5. The difference is seen to be a part in 10^{-7} in magnitude, and a

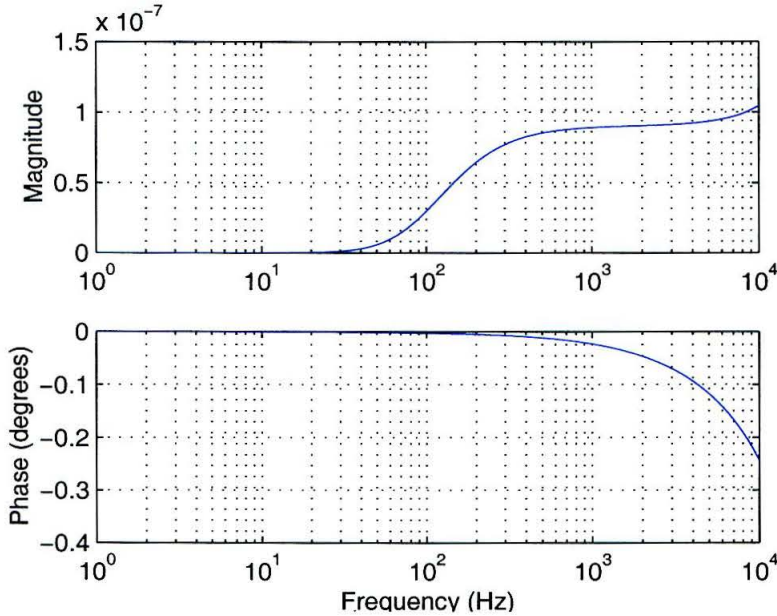


Figure A.5: Difference between Eq. (A.3) and Eq. (A.19).

part in 1000 in phase, so the approximation in Eq. (A.19) is quite good.

A.1.3 Fabry-Perot Cavity Difference

The inability to match the Fabry-Perot cavities in the arms of the interferometer leads to a strong term in the evaluation of noise couplings. The differences are characterized by three things: the difference in the losses of the two arms, the difference in the transmittance of the ITMs, and the individual offsets of the two cavities. Although Eq. (A.19) could be used with different parameters to calculate the difference in cavity poles, etc., a fresh equation with explicit dependence on mismatch of the losses and transmittances, as well as the phase offsets, can be derived. It is assumed that the mismatches are small.

The back mirrors of the cavities will be neglected, assuming they are very low loss and have very high reflectivity. The arm cavity difference dr_c is defined as

$$2\delta r_c = \frac{r'_f - (1 - L'_f)e^{-i\phi'}}{1 - r'_f e^{-i\phi'}} - \frac{r_f - (1 - L_f)e^{-i\phi}}{1 - r_f e^{-i\phi}} \quad (\text{A.21})$$

Another approximation will be made to the front mirror reflectivities, assuming they're close to unity, so that

$$\begin{aligned} r &= \sqrt{1 - L - T} \\ &\approx 1 - L/2 - T/2 \end{aligned} \quad (\text{A.22})$$

The various quantities in Eq. (A.21) are defined according to the following relations,

where the primed parameters refer to the first cavity, unprimed to the second.

$$\begin{aligned}
T'_f &= T + dT/2 \\
T_f &= T - dT/2 \\
L'_f &= L + dL/2 \\
L_f &= L - dL/2 \\
\phi' &= \phi + d\phi \\
\phi &= \phi - d\phi \\
R &= 1 - T - L \\
g_a &= 2/(1 - \sqrt{R})
\end{aligned} \tag{A.23}$$

T , L , and R are all seen to be the nominal, specified values for the front mirror, while dT and dL indicate the difference in loss and transmittance. ϕ will be the frequency dependent round trip cavity phase plus the common mode RMS offset, while $d\phi$ is the differential mode RMS offset (making the assumption that the arms are of equal length).

$$\phi = \omega \frac{2l_{arm}}{c} + d\Phi_+ \tag{A.24}$$

$$d\phi = d\Phi_- \tag{A.25}$$

A further assumption about the RMS phase offset, relative to the frequency dependent phases, allows the differential arm cavity RMS phase to be analyzed separately. Substitutions, and lots of tedious algebra, keeping terms to first order, gives the following approximation to Eq. (A.21).

$$\delta r'_c(\omega) = \frac{g_a dL}{4} \frac{1 - i \frac{\omega}{(dL/dT)\omega_c}}{(1 + i \frac{\omega}{\omega_c})^2} + i g_a d\Phi_- \tag{A.26}$$

A small sleight of hand: as with the single cavity, the difference due to phase offset is assumed to be a small perturbation on the frequency dependent phases. Hence,

when considering frequency dependence, the equation used will be

$$\delta r_c(\omega) = \frac{g_a dL}{4} \frac{1 - i \frac{\omega}{(dL/dT)\omega_c}}{(1 + i \frac{\omega}{\omega_c})^2} \quad (\text{A.27})$$

and when considering the DC arm cavity difference,

$$\delta r_c^0 = \frac{g_a dL}{4} + i g_a d\Phi_- \quad (\text{A.28})$$

will be used.

Eq. (A.28) illustrates explicitly that the carrier defect term comes from the difference in losses of the arms for the real part, and the arm differential mode offset for the imaginary part. Eq. (A.27) shows that the difference in transmittance only couples to the frequency dependent part of the function. Because of this, the difference in transmittance has more of an effect on carrier noise coupling, while the difference in losses impacts the RF sideband noise coupling.

Figure A.6 compares this approximation to the exact solution. The arm cavities modeled have $T = 3\%$ front mirrors with a mismatch of 10% in transmittance. The losses are nominally 50 ppm, and the difference in losses is also taken to be 50 ppm.

A.2 The Pickoff Field

There are two internal fields of interest: the field returning to the input mirror, and the field leaving the input mirror inside the cavity. These equations relating the input field to these fields are

$$p_{c1} = \frac{-t_f r_b e^{-i\phi}}{1 - r_f r_b e^{-i\phi}} \quad (\text{A.29})$$

$$p_{c2} = \frac{t_f}{1 - r_f r_b e^{-i\phi}} \quad (\text{A.30})$$

The equation for p_{c1} gives the field most commonly used (in this thesis) to derive signals for control. It's also the source of the leakage field in the reflected port.

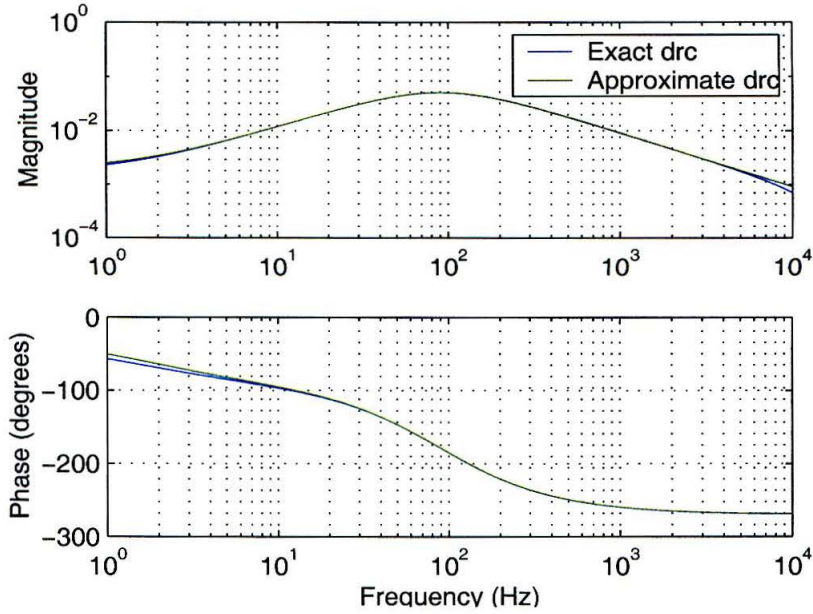


Figure A.6: Comparison of approximation Eq. (A.26) with the exact equation Eq. (A.21).

The equation for p_{c2} is seen to give the amplitude of the field inside the cavity relative to the input field, otherwise known as the cavity amplitude gain. The power gain of the cavity is simply the magnitude of this, squared. An example of the dependence of the power gain on the input mirror is shown in Figure A.7. Taking the derivative of $|p_{c2}|^2$ on resonance with respect to r_f and finding the maximum gives the following relation to optimize the power in the cavity.

$$r_f = (1 - L_f)r_b \quad (\text{A.31})$$

It's seen that the same condition which optimally couples the cavity also gives the largest power gain. If the back mirror has a reflectance near unity (such as in the arm cavities), and the front mirror has fairly high reflectivity (but losses are negligible),

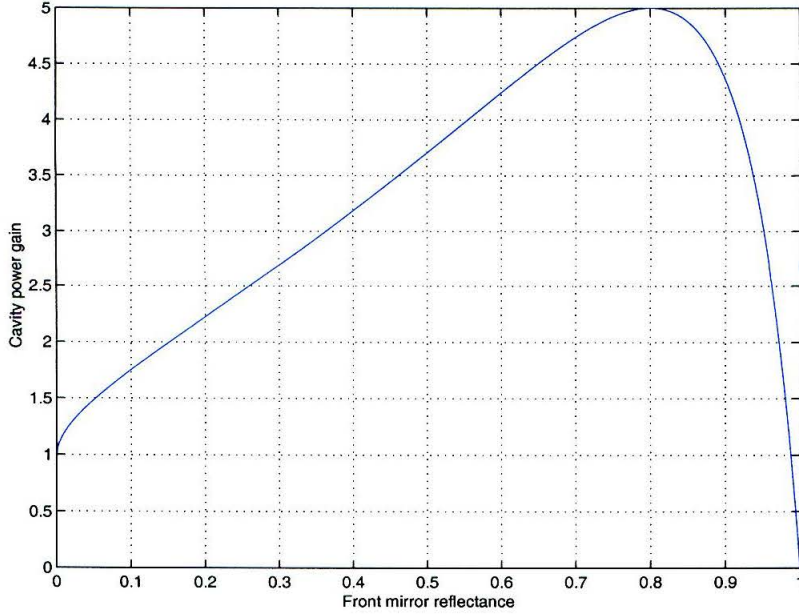


Figure A.7: Cavity power gain as a function of the front mirror reflectance. In this case, $R_b = 0.8$.

then

$$\begin{aligned}
 p_{c2} &\approx \frac{t_f}{1 - r_f} \\
 &\approx \frac{2t_f}{T_f + L_f} \\
 &\approx \frac{2}{t_f}
 \end{aligned} \tag{A.32}$$

using the approximation $r_f \approx 1 - T_f/2 - L_f/2$. The power gain of the cavity is seen to be $4/T_f$.

A.3 The Transmitted Field

The field transmitted through the cavity propagated by the equation

$$t_c = \frac{t_f t_b e^{-i\phi/2}}{1 - r_f r_b e^{-i\phi}} \tag{A.33}$$

The magnitude of the transmitted power is related to the input power by

$$T_c = \frac{T_f T_b}{1 + R_f R_b - 2r_f r_b \cos(\phi)} \quad (\text{A.34})$$

The phase at which the magnitude is at half maximum can be found by expanding the cosine to lowest order

$$\phi_{3 \text{ dB}} = \frac{1 - r_f r_b}{\sqrt{r_f r_b}} \quad (\text{A.35})$$

The full width at half-maximum is twice this. The width of the transmittance relative to the spacing of these peaks every 2π radians is the definition of the finesse \mathcal{F} .

$$\mathcal{F} = \frac{\pi \sqrt{r_f r_b}}{1 - r_f r_b} \quad (\text{A.36})$$

For a cavity of a given length l , the phase associated with the half-maximum defines the cavity pole,

$$\phi_{3 \text{ dB}} = \omega_{3 \text{ dB}} \frac{2l}{c} \quad (\text{A.37})$$

$$\omega_{3 \text{ dB}} = \frac{c}{2l} \frac{1 - r_f r_b}{\sqrt{r_f r_b}} = \frac{c}{2l} \mathcal{F} \quad (\text{A.38})$$

This is also referred to as the bandwidth of the cavity.

A.4 Derivatives

Sensitivity to a change in phase is one of the features of Fabry-Perot cavities that is most widely used. This sensitivity can be shown by noting that the formula

$$\frac{1}{-iE} \frac{\partial E}{\partial \phi} = \frac{1}{-i|E|e^{-i\theta(\phi)}} \frac{\partial}{\partial \phi} |E|e^{-i\theta(\phi)} = \frac{\partial}{\partial \phi} \theta(\phi) \quad (\text{A.39})$$

gives the derivative of the phase θ of the complex quantity E with respect to the parameter ϕ . This is of most interest for the reflected and pickoff fields, and has been defined in the past as the ‘‘augmented bounce number’’ N' and ‘‘bounce number’’ N

[32], due to analogy with the quantities of similar meaning in delay line interferometers.

In reflection, Eq. (A.3) gives the relevant field equation, and the reflected phase gain evaluated at resonance is given by

$$N' = \frac{r_b T_f}{(1 - r_f r_b)(r_f - r_b A_f)} \quad (\text{A.40})$$

When the end mirror has very nearly unity reflection, and the input mirror likewise has high reflectivity, this can be approximated by

$$N' \approx \frac{2}{1 - r_f} \quad (\text{A.41})$$

The internal field returning to the input mirror, p_{c1} , has the following phase gain.

$$N = \frac{2}{1 - r_f r_b} \quad (\text{A.42})$$

A.5 Additional Losses

The addition of an element in the cavity which contributes a loss, but no reflectivity,² can be incorporated into the formulas in a straightforward way. Expressed exactly, the various fields are

$$r_c = r_f - \frac{T_f A_s r_b e^{-i\phi}}{1 - r_f A_s r_b e^{-i\phi}} \quad (\text{A.43})$$

$$p_{c1} = \frac{-t_f A_s r_b e^{-i\phi}}{1 - r_f A_s r_b e^{-i\phi}} \quad (\text{A.44})$$

$$p_{c2} = \frac{t_f}{1 - r_f A_s r_b e^{-i\phi}} \quad (\text{A.45})$$

$$t_c = \frac{t_f \sqrt{A_s} t_b e^{-i\phi/2}}{1 - r_f A_s r_b e^{-i\phi}} \quad (\text{A.46})$$

²More precisely, any reflectivity associated with the lossy element reflects out of the cavity. For example, if a pickoff is placed in the cavity, or mirrors with AR coatings have the AR coating inside the cavity, etc. The reflectance, in this case, counts as an additional loss.

Where A_s is $1 - L_s$, or one minus the additional loss. By examination, these are equivalent to the original equations with the substitutions

$$r'_b = r_b A_s \tag{A.47}$$

$$t'_b = t_b \sqrt{A_s} \tag{A.48}$$

This is easy to arrive at conceptually, as well. If the reflectivity is zero, then the quantity $A_s = 1 - L_s = T_s$ is the transmittance of the element for the cavity field. Since fields that reflect off the back mirror, and return to the front, pass through this twice, the amplitude is reduced by a factor of $t_s^2 = A_s$, hence the reflectivity can be modified in such a way. For the transmission, the field passes through one (more) time, hence the transmission of the back mirror is modified by $\sqrt{A_s}$.

Appendix B

Transmission of the RSE Interferometer

B.1 The General Transmission Equation

Deriving the transmission of the carrier and the RF sidebands as well as their noise sidebands from the input of the RSE interferometer to the dark port is necessary to derive analytical formulas which predict laser noise coupling in RSE. The equations for a dual-recycled Michelson are useful for the RSE interferometer since they're much simpler. The assumption is that the arms of the RSE interferometer are treated as complex, frequency dependent reflectivities. In this Appendix, the necessary transmission functions are derived.

Referring to Figure 5.6, the equation for the transmissivity from the input of the power recycling mirror to the dark port is

$$t = \frac{t_N}{t_D} \quad (\text{B.1})$$

$$t_N = t_{prm} r_{bs} t_{bs} t_{sem} (r_{c2} e^{i(\phi_1 - \phi_2)/2} - r_{c1} e^{-i(\phi_1 - \phi_2)/2}) e^{-i(\phi_0 + \phi_1 + \phi_2 + \phi_5)/2} \quad (\text{B.2})$$

$$\begin{aligned} t_D = & 1 + r_{prm} (r_{bs}^2 r_{c2} e^{i(\phi_1 - \phi_2)/2} + t_{bs}^2 r_{c1} e^{-i(\phi_1 - \phi_2)/2}) e^{-i(\phi_0 + (\phi_1 + \phi_2)/2)} \\ & - r_{sem} (t_{bs}^2 r_{c2} e^{i(\phi_1 - \phi_2)/2} + r_{bs}^2 r_{c1} e^{-i(\phi_1 - \phi_2)/2}) e^{-i(\phi_5 + (\phi_1 + \phi_2)/2)} \\ & - r_{prm} r_{sem} r_{c1} r_{c2} (r_{bs}^2 + t_{bs}^2)^2 e^{-i(\phi_0 + \phi_1 + \phi_2 + \phi_5)} \end{aligned} \quad (\text{B.3})$$

This is not a particularly useful equation. It can be re-cast with several definitions. First, the degrees of freedom can be used.

$$\phi_+ = \phi_0 + (\phi_1 + \phi_2)/2 \quad (\text{B.4})$$

$$\phi_s = \phi_5 + (\phi_1 + \phi_2)/2 \quad (\text{B.5})$$

$$\phi_- = (\phi_1 - \phi_2)/2 \quad (\text{B.6})$$

The beamsplitter is typically very nearly 50/50, so the mismatch can be defined as

$$A_{bs} = r_{bs}^2 + t_{bs}^2 \quad (\text{B.7})$$

$$\Delta = (r_{bs}^2 - t_{bs}^2)/A_{bs} \quad (\text{B.8})$$

The mismatch Δ is typically around 0.01, while A_{bs} , which is equivalent to 1 – losses, is very nearly unity.

The arms likewise are usually very similar, and the mismatch can be defined as

$$r_c = (r_{c1} + r_{c2})/2 \quad (\text{B.9})$$

$$\delta r_c = (r_{c2} - r_{c1})/2 \quad (\text{B.10})$$

These must be evaluated carefully, as they are complex, frequency dependent quantities. These are examined in Appendix A.

Eq. (B.1) can be simplified through some tedious algebra, to be

$$t = \frac{t_{prm} t_{m_f} t_{sem} e^{-i(\phi_+ + \phi_s)/2}}{1 + r_{prm} r_{m_f} e^{-i\phi_+} - r_{sem} r_{m_b} e^{-i\phi_s} - r_{prm} r_{sem} (r_c^2 - \delta r_c^2) A_{bs}^2 e^{-i(\phi_+ + \phi_s)}} \quad (\text{B.11})$$

$$t_{m_f} = 2r_{bs} t_{bs} [\delta r_c \cos(\phi_-) + i r_c \sin(\phi_-)] \quad (\text{B.12})$$

$$r_{m_f} = A_{bs} [(r_c + \delta r_c \Delta) \cos(\phi_-) + i(\delta r_c + r_c \Delta) \sin(\phi_-)] \quad (\text{B.13})$$

$$r_{m_b} = A_{bs} [(r_c - \delta r_c \Delta) \cos(\phi_-) + i(\delta r_c - r_c \Delta) \sin(\phi_-)] \quad (\text{B.14})$$

B.1.1 Dual-Recycled Michelson – Coupled Cavity

Eq. (B.11) has a marked similarity to the equation for the transmissivity of a three mirror coupled cavity. In the limit that the imperfections vanish, that is $\delta r_c = 0$, $\Delta = 0$, and $2r_{bs} t_{bs} = A_{bs}$, Eq. (B.11) simplifies to

$$t = \frac{i t_{prm} A_{bs} r_c \sin(\phi_-) t_{sem} e^{-i(\phi_+ + \phi_s)/2}}{1 + r_{prm} A_{bs} r_c \cos(\phi_-) e^{-i\phi_+} - r_{sem} A_{bs} r_c \cos(\phi_-) e^{-i\phi_s} - r_{prm} r_{sem} r_c^2 A_{bs}^2 e^{-i(\phi_+ + \phi_s)}} \quad (\text{B.15})$$

The transmissivity of a three mirror coupled cavity is given by

$$t = \frac{t_1 t_2 t_3 e^{-i(\phi_1 + \phi_2)/2}}{1 + r_1 r_2 e^{-i\phi_1} + r_2 r_3 e^{-i\phi_2} + r_1 r_3 (r_2^2 + t_2^2) e^{-i(\phi_1 + \phi_2)}} \quad (\text{B.16})$$

The optical subscripts 1, 2, and 3 refer to the input, coupling, and output mirrors respectively, while the phase subscripts 1 and 2 refer to the cavities formed by mirrors 1 and 2, and 2 and 3, respectively. These are equivalent with the following associations

$$r_2 = r_c A_{bs} \cos(\phi_-) \quad (\text{B.17})$$

$$t_2 = r_c A_{bs} \sin(\phi_-) \quad (\text{B.18})$$

$$L_2 = 1 - r_2^2 - t_2^2 = 1 - r_c A_{bs} \quad (\text{B.19})$$

$$\phi_2 = \phi_s - \pi \quad (\text{B.20})$$

An interesting feature is the real phase shift of π that shows up in the signal cavity. This is simply an artifact of the fact that the equivalent “coupling mirror” of the dual-recycled Michelson is not actually a mirror, but rather is a Michelson interferometer.

B.2 The Carrier Equation

Eq. (B.11) can be evaluated for the carrier in the interferometer. The nominal phases for the carrier in the interferometer are (modulo 2π)

$$\begin{aligned} \phi_+ &= 0 \\ \phi_- &= 0 \\ \phi_s &= 0 + \phi_{dt} \end{aligned} \quad (\text{B.21})$$

The interferometer will be held at these nominal phases against the natural disturbances of the environment by feedback control systems. The gains of these control systems will be finite, which means that the exact phase of the cavity will not be precisely the nominal value, but will fluctuate around the nominal value, characterized by a RMS equal to the integrated disturbance to the mirrors multiplied by the

closed loop gain of the control system. The non-zero fluctuations will be modeled as a DC offset equivalent to the RMS fluctuations. The phases will also be expressed as functions of frequency shifted from the carrier frequency.

$$\phi_+ = d\phi_+ + \frac{\omega 2l_{pre}}{c} \quad (\text{B.22})$$

$$\phi_- = d\phi_- + \frac{\omega\delta}{c} \quad (\text{B.23})$$

$$\phi_s = \phi_{dt} + d\phi_s + \frac{\omega 2l_{sec}}{c} \quad (\text{B.24})$$

where the asymmetry δ is defined

$$\delta = l_1 - l_2 \quad (\text{B.25})$$

Eq. (B.11) is expanded in the phase offsets and arm cavity mismatches to first order. This expansion has the form of

$$t \approx t^0 + \delta t \quad (\text{B.26})$$

where t^0 represents the ideal carrier transmission function (which is 0), and δt is the perturbation to t due to the imperfections.

$$\delta \left(\frac{t_N}{t_D} \right) \approx \frac{t_D(\delta t_N) - t_N(\delta t_D)}{t_D^2} \quad (\text{B.27})$$

For the carrier, which is held on the dark fringe, $t_N = 0$ so $t^0 = 0$, and the dual-recycled Michelson transmission equation can be approximated as

$$t \approx \frac{\delta t_N}{t_D} \quad (\text{B.28})$$

The denominator and numerator are examined separately.

The Denominator

The ideal carrier denominator is quite simple to represent.

$$t_D = 1 + r_{prm}A_{bs}r_c e^{-i\phi_+} - r_{sem}A_{bs}r_c e^{-i\phi_s} - r_{prm}r_{sem}r_c^2 A_{bs}^2 e^{-i(\phi_+ + \phi_s)} \quad (\text{B.29})$$

The arm cavity reflectivity is general at this point, as are the phases. Evaluation of this equation at DC and at frequencies away from DC will pull out the dependence on these factors.

This simplifies at DC with the use of the nominal phases of Eq. (B.21). The DC arm cavity reflectivity Eq. (A.14) is also used.

$$t_{D00} = 1 + r_{prm}A_{bs}r_c^0 - r_{sem}A_{bs}r_c^0 e^{-i\phi_{dt}} - r_{prm}r_{sem}(r_c^0)^2 A_{bs}^2 e^{-i\phi_{dt}} \quad (\text{B.30})$$

The DC interferometer gain for the carrier will be defined as

$$g_{ifo}^{c0} = \frac{e^{-i\phi_{dt}/2}}{t_{D00}} = \frac{e^{-i\phi_{dt}/2}}{1 + r_{prm}A_{bs}r_c^0 - r_{sem}A_{bs}r_c^0 e^{-i\phi_{dt}} - r_{prm}r_{sem}(r_c^0)^2 A_{bs}^2 e^{-i\phi_{dt}}} \quad (\text{B.31})$$

As a function of frequency, the explicit dependence on frequency of the arm cavity reflectivity as well as the power and signal cavity phases needs to be considered. First, it is noted that the power and signal cavities are typically of order 10 m in length. At frequencies as high as 1 kHz, the phase in these cavities will not exceed 1 mrad. The arm cavities, however, are quite long (4 km), and the phase due to the arm cavity reflectivity is quite large compared to the power and signal cavity phases. Hence, the frequency dependence of the power and signal cavities will be ignored.

$$\begin{aligned} t_{D0\pm} &= 1 + r_{prm}A_{bs}r_c^\pm - r_{sem}A_{bs}r_c^\pm e^{-i\phi_{dt}} - r_{prm}r_{sem}(r_c^\pm)^2 A_{bs}^2 e^{-i\phi_{dt}} \\ &= (1 + r_{prm}A_{bs}r_c^\pm)(1 + r_{sem}A_{bs}r_c^\pm e^{-i\phi_{dt}}) \end{aligned} \quad (\text{B.32})$$

The arm cavity reflectivity from Appendix A.1, Eq. (A.19), is given here again.

$$r_c^\pm = \frac{r_c^0 + i(1 - L_{itm}/2)\frac{\pm\omega}{\omega_c}}{1 + i\frac{\pm\omega}{\omega_c}} \quad (\text{B.33})$$

Substitution and some algebra molds $e^{-i\phi_{dt}/2}/t_{D0\pm}$ into the frequency dependent interferometer gain for the carrier,

$$g_{ifo}^{c\pm} = g_{ifo}^{c0} H^\pm \quad (\text{B.34})$$

where the frequency dependence is entirely wrapped up in H^\pm .

$$H^\pm = \frac{\left(1 + i\frac{\pm\omega}{\omega_c}\right) \left(1 + i\frac{\pm\omega}{\omega_c}\right)}{\left(1 + i\frac{\pm\omega}{\omega_{cc}}\right) \left(1 + i\frac{\pm\omega}{\omega_{sc}}\right)} \quad (\text{B.35})$$

$$\omega_{cc} = (1 + r_{prm} r_c^0 A_{bs}) \frac{\omega_c}{2} \quad (\text{B.36})$$

$$\omega_{sc} = \frac{1 - r_{sem} r_c^0 A_{bs} e^{-i\phi_{dt}}}{1 - r_{sem} A_{bs} e^{-i\phi_{dt}}} \omega_c \quad (\text{B.37})$$

The Numerator

The numerator of Eq. (B.11) is expanded to first order at DC.

$$\begin{aligned} t_{N00} &= t_{prm} t_{m_f} t_{sem} e^{-i(\phi_+ + \phi_s)/2} \\ &\approx t_{prm} A_{bs} t_{sem} e^{-i\phi_{dt}/2} (\delta r_c'^0 + i r_c'^0 d\phi_-) (1 - id\phi_+/2 - id\phi_s/2) \end{aligned} \quad (\text{B.38})$$

The arm cavity difference $\delta r_c'^0$ has a nominal arm difference term, and a part due to phase offset, $\delta r_c'^0 = \delta r_c^0 + i g_a d\Phi_-$. Keeping terms to first order, the phase offsets from the power and signal cavities disappear.

$$t_{N00} = t_{prm} A_{bs} t_{sem} e^{-i\phi_{dt}/2} (\delta r_c^0 + i(r_c^0 d\phi_- + g_a d\Phi_-)) \quad (\text{B.39})$$

As a function of frequency, the Michelson transmission needs to be expanded more carefully.

$$\begin{aligned} t_{m_f} &= 2r_{bs} t_{bs} [\delta r_c \cos(\phi_-) + i r_c \sin(\phi_-)] \\ &\approx A_{bs} (\delta r_c'^\pm + i r_c'^\pm (d\phi_- \pm \omega\delta/c)) \end{aligned} \quad (\text{B.40})$$

The frequency dependent numerator is then expressed as

$$t_{N0\pm} = t_{prm}A_{bs}t_{sem}e^{-i\phi_{dt}/2}(\delta r_c^\pm + ir_c^\pm(d\phi_- \pm \omega\delta/c) + ig_ad\Phi_-) \quad (\text{B.41})$$

The Carrier Transmission Functions

These results are easily combined to approximate the DC carrier transmission function

$$t_{00} \approx t_{prm}A_{bs}t_{sem}g_{ifo}^{c0}(\delta r_c^0 + i(r_c^0 d\phi_- + g_ad\Phi_-)) \quad (\text{B.42})$$

as well as the transmission function for the noise sidebands of the carrier.

$$t_{0\pm} \approx t_{prm}A_{bs}t_{sem}g_{ifo}^{c0}H^\pm(\delta r_c^\pm + ir_c^\pm(d\phi_- \pm (\omega\delta/c)) + ig_ad\Phi_-) \quad (\text{B.43})$$

B.3 The RF Sideband Equation

Contrary to the carrier, the interferometer is designed to have high transmission of the RF sidebands to the dark port. As a result, the effects of the interferometer imperfections are small corrections on a large zeroth order term. In addition, the calculation of noise coupling forms products of the carrier terms with the RF sideband terms. Since all the carrier terms are first order in imperfections, including such terms in the equations for the RF sidebands would simply generate second order terms in the measured noise. Hence, only the zeroth order terms for the RF sidebands are derived.

The first assumption made about the RF sidebands in the interferometer is that $r_{c1} = r_{c2} \approx 1$, since they aren't resonant in the arm cavities. For the audio sidebands of the RF sidebands, this approximation begins to break down at frequencies in the high kHz, which is beyond the frequency of interest. Eq. (B.11) simplifies for the RF sidebands as

$$t_\pm = \frac{it_{prm}A_{bs}t_{sem} \sin(\phi_-)e^{-i(\phi_+ + \phi_s)/2}}{1 + r_{prm}A_{bs} \cos(\phi_-)e^{-i\phi_+} - r_{sem}A_{bs} \cos(\phi_-)e^{-i\phi_s} - r_{prm}r_{sem}A_{bs}^2 e^{-i(\phi_+ + \phi_s)}} \quad (\text{B.44})$$

Defining the phases for the RF sidebands is more complicated. At issue is the method of optimizing the transmission of a RF sideband to the dark port when the interferometer is detuned. As detuning changes, or is shifted from broadband, there are two methods of re-optimizing the RF sideband transmission – either the length of the signal cavity can be changed to null the effect of the detuning, or else the frequency of the modulation can be changed, to re-optimize the RF sideband transmission.

It will be assumed that a configuration is chosen such that the RF sidebands resonate within the power and signal cavities, individually, at the broadband RSE tuning. The RF sideband frequency for the broadband interferometer is Ω_{bb} , so that

$$\phi_{bb}^{\pm} = \frac{2l}{c}(\omega_0 \pm \Omega_{bb}) \quad (\text{B.45})$$

will be the nominal broadband phase for the three degrees of phase that the RF sidebands are sensitive to: ϕ_+ , ϕ_- , and ϕ_s . The length l then refers to the degree of freedom length, and ω_0 is the carrier frequency. Detunings will be accommodated by introducing a phase η , such that

$$\eta = \frac{2l}{c}d\Omega + \frac{2\Omega_{bb}}{c}dl \quad (\text{B.46})$$

where a length change is indicated by dl and a frequency shift in the RF modulation frequency is indicated by $d\Omega$. This allows for either of the methods for optimization of RF sideband power at the dark port to be used in the equations. The general RF sideband phase will then be written as

$$\phi^{\pm} = \frac{2l}{c}(\omega_0 \pm \Omega_{bb}) + \eta \quad (\text{B.47})$$

Note that the carrier phase $2\omega_0 l/c$ will also contain the same RMS offset phase that the carrier has.

The next assumption is that the frequency response of the dual-recycled Michelson for the RF sidebands is flat. The finesse of the combined power/signal cavity will typically not be terribly high, say 100, and the lengths of the cavities will typically

be fairly short. An estimate of the bandwidth of the coupled cavity system would then be around 100 kHz or so, much higher than the bandwidth of interest.

The nominal phases for the RF sidebands are

$$\phi_{\pm}^{\pm} = \pm\pi + \eta_{\pm}^{\pm} \quad (\text{B.48})$$

$$\phi_s^{\pm} = \pm 2\pi + \eta_s^{\pm} + \phi_{dt} \quad (\text{B.49})$$

$$\phi_{\pm}^{\pm} = \pm\alpha + \eta_{\pm}^{\pm} = \pm\alpha' \quad (\text{B.50})$$

The phase α is the asymmetry phase, defined as $\alpha = \Omega_{bb}\delta/c$.

These phases can be substituted into Eq. (B.44). First the RF sideband gain term is defined, analogous to Eq. (B.31), by evaluating the denominator.

$$g_{ifo}^{\pm} = \frac{e^{-i(\phi_{dt} + \eta_s^{\pm} + \eta_{\pm}^{\pm})/2}}{t_{D\pm}} \quad (\text{B.51})$$

$$t_{D\pm} = 1 - r_{prm}A_{bs} \cos(\alpha')e^{-i\eta_{\pm}^{\pm}} - r_{sem}A_{bs} \cos(\alpha')e^{-i(\eta_s^{\pm} + \phi_{dt})} + r_{prm}r_{sem}A_{bs}^2 e^{-i(\eta_{\pm}^{\pm} + \eta_s^{\pm} + \phi_{dt})} \quad (\text{B.52})$$

The numerator, sans the exponential which is absorbed into g_{ifo}^{\pm} , is quite simple.

$$t_{N\pm} \approx \pm t_{prm}A_{bs}t_{sem} \sin(\alpha') \quad (\text{B.53})$$

so that the equation for the transmission of the DC RF sidebands as well as their noise sidebands is given by

$$t_{\pm} \approx \pm t_{prm}A_{bs}t_{sem} \sin(\alpha')g_{ifo}^{\pm} \quad (\text{B.54})$$

Appendix C

Cross-Coupled 2×2 Plant

The RSE interferometer plant is a five degree of freedom system which has a significant amount of cross coupling. In this Appendix, some analysis is done of a simpler 2×2 plant, with regards to the effects of cross-coupling.

A block diagram of the 2×2 system is given in Figure C.1. This figure shows

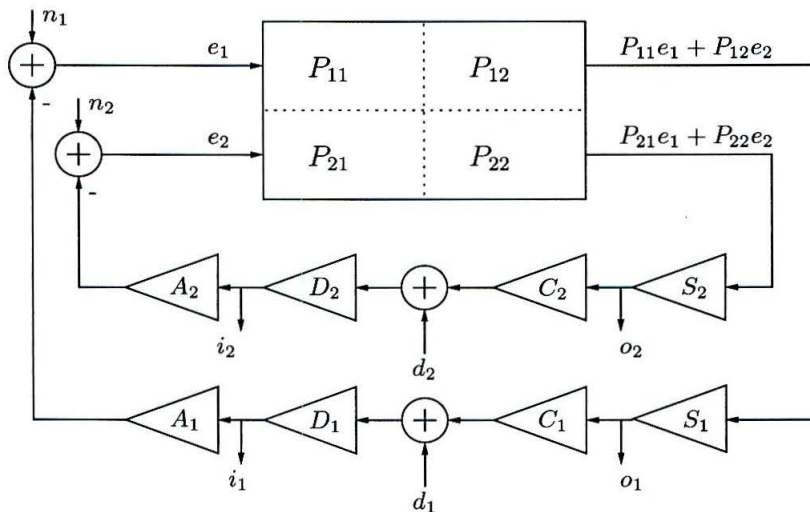


Figure C.1: Block diagram of a 2×2 control system.

two loops, loop 1 and loop 2, which are closed. Two inputs into the loops are shown, n_i which is assumed to be the environmental disturbance that the feedback system is attempting to correct, and d_i , which could either be noise of the electronics, or an input for a transfer function measurement. The plant is general – nothing is assumed about the relative sizes of the four elements. The feedback includes the sensor S , the compensation C , the actuator driver D , and the actuator itself, A . The points i_i and o_i indicate useful places to define an “input” and “output” for a measurement of the loops. In general, a system cannot be realistically monitored after the actuator

or before the sensor. The quantity H_i is defined by $H_i = A_i D_i C_i S_i$. The plant and feedback can be expressed in matrix form as

$$H = \begin{pmatrix} H_1 & 0 \\ 0 & H_2 \end{pmatrix} \quad (\text{C.1})$$

$$P = \begin{pmatrix} P_{11} & P_{12} \\ P_{21} & P_{22} \end{pmatrix} \quad (\text{C.2})$$

The error e and the noise n can be expressed as vectors.

$$\vec{e} = \begin{pmatrix} e_1 \\ e_2 \end{pmatrix} \quad (\text{C.3})$$

$$\vec{n} = \begin{pmatrix} n_1 \\ n_2 \end{pmatrix} \quad (\text{C.4})$$

With the loops closed, the resulting error \vec{e} with input disturbance n is given by

$$\vec{e} = (1 + H \cdot P)^{-1} \vec{n} \quad (\text{C.5})$$

The closed loop gain matrix is

$$S = (1 + H \cdot P)^{-1} = \frac{1}{\Delta} \begin{pmatrix} 1 + H_2 P_{22} & -H_1 P_{12} \\ -H_2 P_{21} & 1 + H_1 P_{11} \end{pmatrix} \quad (\text{C.6})$$

$$\Delta = 1 + H_1 P_{11} + H_2 P_{22} + H_1 H_2 (P_{11} P_{22} - P_{12} P_{21})$$

The closed loop matrix S describes how the disturbances from d_1 and d_2 are affected by the feedback control system which is attempting to minimize the error at \vec{e} .

The following equations relate the inputs i_i to the outputs o_j . The first two equations examine the input/output relationship for one loop, taking into account

the coupling due to the second loop, which is closed.

$$P'_{11} = \frac{o_1}{i_1} = S_1 \left(P_{11} - \frac{P_{12}H_2P_{21}}{1 + H_2P_{22}} \right) A_1 \quad (\text{C.7})$$

$$P'_{22} = \frac{o_2}{i_2} = S_2 \left(P_{22} - \frac{P_{21}H_1P_{12}}{1 + H_1P_{11}} \right) A_2 \quad (\text{C.8})$$

These equations define an effective plant, around which the loop is closed. That is to say, the loop gain for loops 1 and 2 are given by

$$L_1 = P'_{11}C_1D_1 \quad (\text{C.9})$$

$$L_2 = P'_{22}C_2D_2 \quad (\text{C.10})$$

The closed loop gains for each loop are given by

$$G_1 = \frac{1}{1 + L_1} \quad (\text{C.11})$$

$$G_2 = \frac{1}{1 + L_2} \quad (\text{C.12})$$

These next two equations give the coupling from one loop into the other.

$$P'_{12} = \frac{o_2}{i_1} = S_2 \left(P_{21} - \frac{P_{22}H_2P_{21}}{1 + H_2P_{22}} \right) A_1 \quad (\text{C.13})$$

$$P'_{21} = \frac{o_1}{i_2} = S_1 \left(P_{12} - \frac{P_{11}H_1P_{12}}{1 + H_1P_{11}} \right) A_2 \quad (\text{C.14})$$

C.1 Diagonal Plant

In a diagonal plant, it's assumed that $P_{11} > P_{12}$ and $P_{22} > P_{21}$. The rows of the plant P can be normalized to the largest element, with the normalization constant absorbed in the feedback H .

$$P = \begin{pmatrix} 1 & \epsilon_1 \\ \epsilon_2 & 1 \end{pmatrix} \quad (\text{C.15})$$

The closed loop gain matrix S becomes

$$S = \frac{1}{\Delta} \begin{pmatrix} 1 + H_2 & -H_1\epsilon_1 \\ -H_2\epsilon_2 & 1 + H_1 \end{pmatrix} \quad (\text{C.16})$$

$$\Delta = 1 + H_1 + H_2 + H_1H_2(1 - \epsilon_1\epsilon_2)$$

The error in loop 1 is seen to be

$$e_1 = S_{11}n_1 + S_{12}n_2 \quad (\text{C.17})$$

The effect of the cross-coupling of n_2 into loop 1 by the control system is

$$\frac{S_{12}}{S_{11}} = \frac{H_1\epsilon_1}{1 + H_2} \quad (\text{C.18})$$

It's more useful to cast this in terms of the loop gains.

$$L_1 = H_1 \left(1 - \frac{\epsilon_1\epsilon_2H_2}{1 + H_2} \right) \approx H_1(1 - \epsilon_1\epsilon_2) \quad (\text{C.19})$$

$$L_2 = H_2 \left(1 - \frac{\epsilon_1\epsilon_2H_1}{1 + H_1} \right) \approx H_2(1 - \epsilon_1\epsilon_2) \quad (\text{C.20})$$

The approximations assume $H_1 \gg 1$ and $H_2 \gg 1$, or that the loops are closed. Given this, the effect of the cross coupling is seen to be

$$\frac{S_{12}}{S_{11}} = \frac{L_1\epsilon_1}{L_2} \quad (\text{C.21})$$

Hence, given equivalent loop gains in loops 1 and 2, the coupling between the two loops is simply the coupling element ϵ_1 .

C.2 Ill-Conditioned Plant

In an ill-conditioned plant, it's assumed that the plant elements P_{11} and P_{21} are the dominant terms in their rows, so that the plant output in both loops is due mostly

to the disturbance at d_1 .

$$P = \begin{pmatrix} 1 & \epsilon_1 \\ 1 & \epsilon_2 \end{pmatrix} \quad (\text{C.22})$$

This case was specifically analyzed in M. Regehr's thesis.[32] His results, and some other comments, are given here. It should be noted that the feedback sign is different between this analysis and Regehr's thesis. This is simply a matter of convention.

The closed loop gain matrix is given by

$$S = \frac{1}{\Delta} \begin{pmatrix} 1 + H_2\epsilon_2 & -H_1\epsilon_1 \\ -H_2 & 1 + H_1 \end{pmatrix} \quad (\text{C.23})$$

$$\Delta = 1 + H_1 + H_2\epsilon_2 + H_1H_2(\epsilon_2 - \epsilon_1)$$

In this case, clearly loop 2 is the most problematic.

C.2.1 System Performance

The coupling of loop 1 into the error of loop 2 is seen to be

$$\frac{S_{21}}{S_{22}} = \frac{H_2}{1 + H_1} \quad (\text{C.24})$$

The control system does not degrade the loop 2 error e_2 significantly if

$$|H_2| \ll |1 + H_1| \quad (\text{C.25})$$

To cast this in terms of the loop gains, the effective plant elements become

$$L_1 = H_1 \left(1 - \frac{\epsilon_1 H_2}{1 + H_2\epsilon_2} \right) \approx H_1 \left(1 - \frac{\epsilon_1}{\epsilon_2} \right) \quad (\text{C.26})$$

$$L_2 = H_2 \left(\epsilon_2 - \frac{H_1\epsilon_1}{1 + H_1} \right) \approx H_2(\epsilon_2 - \epsilon_1) \quad (\text{C.27})$$

The approximations are taken assuming the loops are closed and the gains are $\gg 1$. Also assuming $H_1 \gg 1$, the coupling of loop 1 to loop 2 can be seen to be

$$\frac{S_{21}}{S_{22}} = \frac{L_2}{\epsilon_2 L_1} \quad (\text{C.28})$$

This states that the performance in loop 2 is not degraded much if the loop gain L_1 is greater than L_2 by the inverse of the coupling factor, $1/\epsilon_2$. Perhaps a way to understand this, is that, given equivalent disturbances in the two loops, if the loop gain in loop 1 is so large that it reduces the residual disturbances at e_1 by a factor larger than the increased coupling factor $1/\epsilon_2$, then the performance of loop 2 is not significantly degraded. This is typically referred to as the “gain hierarchy.”

A similar analysis in loop 1 shows the coupling to be

$$\left| \frac{S_{12}}{S_{11}} \right| = \left| \frac{H_1}{1 + \epsilon_2 H_2} \right| \quad (\text{C.29})$$

$$\approx \left| \frac{L_1 \epsilon_1}{L_2} \right| \quad (\text{C.30})$$

Clearly there is a potential degradation in loop 1 as well. If the two ϵ 's are roughly equivalent, then increasing the gain L_1 decreases the degradation of loop 2's performance, but loop 1 suffers somewhat. Reducing the gain, on the other hand, reduces the degradation of loop 1's performance, at the expense of loop 2. Regehr points out, however, that the degradation of loop 1's performance with increasing L_1 saturates at some level, that is, it doesn't become worse. In essence, the increased noise due to the coupling is suppressed by the increased loop gain. The best situation, of course, is if $\epsilon_2 \gg \epsilon_1$. In this case, it's possible that the disturbances in both loops can be adequately reduced.

C.2.2 Transfer Function Measurement

The measurement of the transfer functions of such a plant are also quite problematic. It's assumed the transfer function measurement is taken at the o and i points in the loop. Given the above criteria, the loop gain L_1 is assumed to be much larger than L_2 .

The measurement is also assumed to be taken above unity gain for loop 2 ($L_2 \ll 1$), but below unity gain for loop 1 ($L_1 \gg 1$). The input/output relations of Eq. (C.7), (C.8), (C.13), and (C.14) become

$$\frac{o_1}{i_1} \cong S_1 P_{11} (1 - \epsilon_1 H_2 P_{21}) A_1 \cong S_1 P_{11} A_1 \quad (\text{C.31})$$

$$\frac{o_2}{i_2} \cong S_2 P_{22} (1 - \epsilon_1 / \epsilon_2) A_2 \quad (\text{C.32})$$

$$\frac{o_2}{i_1} \cong S_2 P_{21} (1 - \epsilon_2 H_2 P_{21}) A_1 \cong S_2 P_{21} A_1 \quad (\text{C.33})$$

$$\frac{o_1}{i_2} \cong 0 \quad (\text{C.34})$$

For input into loop 1, the measurements are fairly clean. However, both measurements of loop 2 are difficult, if not impossible. o_2/i_2 does not cleanly give the matrix element P_{22} , and the measurement of P_{12} doesn't appear to be possible at all, in this regime.

Appendix D

Schematics of the Prototype Electronics

There are two main components to the electronics used in the RSE tabletop prototype experiment. The first are the feedback electronics, which are the analog electronics designed to provide filtering and gain for the control system, as well as the drivers for the piezo actuators. The second set of electronics are the RF electronics. These generate the three RF frequencies used in modulation as well as demodulation.

D.1 Feedback Electronics

The PZT compensation electronics were given to this experiment by Nergis Mavalala, who used them in her fixed mass interferometer.[56] An overview of the block components of the electronics is shown in Figure D.1, while the actual schematics are given in Figures D.2 through D.6.

There are several modifications that should be mentioned. R14, R15, R21 and R22 are all removed from the input stages. R23 is replaced with a 100k Ω resistor in the adder stage. The fast network has several modifications. First, C13 is removed in some cases. This forms a 10 Hz pole which was implemented, in some cases, in the fast PZT drivers. The universal filter IC7 is disconnected in most cases. This was used as a notch filter for the fast PZT resonance at 50 kHz. It was found that this was not particularly bothersome in this experiment, and furthermore it degraded the phase margin of the loops. The output stage of the fast network around the IC5 op-amp is heavily modified. First, C18 is replaced by a 22 nF capacitor in series with a 1500 Ω resistor. A switch is placed across the capacitor. R38 is replaced with a 750 k Ω resistor. R37 is replaced with a 511 Ω resistor. This circuit forms the boost stage, which is turned on with the switch. There are several changes in the slow network as well. The relay is disconnected. R8 is replaced by a 100 k Ω resistor. C10

is replaced with a 1 μF capacitor, and R28 is replaced with a 150 k Ω resistor. A switch is added in series with R28, which is the integrator switch.

The feedback compensation for the Michelson (ϕ_-) was designed specially, and shown in Figure D.7. This has a 10 Hz pole that can be switched to an integrator. The output is split into two paths, and switches are included to output the signal in common or differential mode, as well as change the sign.

The fast PZT HV driver is shown in Figure D.8. This is a fairly simple circuit, using a high voltage PA-85 op-amp. This is shown with a 10 Hz pole in its feedback; however, this is disconnected in the drivers for the arm cavity ETMs. The reason is that these PZTs need to be driven at high frequency for the gravitational wave transfer function measurement. The 10 Hz pole is moved into the fast PZT network in the PZT compensation modules.

The slow PZT HV driver is largely inspired by a circuit from Horowitz and Hill and is shown in Figure D.9.[61] This can output 0 to +1000 V, and has two inputs, a $\div 100$ monitor, and a 10-turn pot to set the bias of the HV output.

D.2 RF Electronics

A deep debt of gratitude is owed to Rich Abbott for his help in designing and laying out the two RF electronics boards. The first board is used to generate the three frequencies required of this experiment, 27 MHz, 54 MHz, and 81 MHz, and is shown in Figure D.10.

The second board was used to take the 54 and 81 MHz outputs from the frequency generation board, split it four ways, phase shift each path with a voltage controlled phase shifter, and amplify each path. In reality, only three of the four paths were phase shifted. The schematic is shown in Figure D.11. As a future suggestion, it is strongly recommended that the phase shifting and amplification for each LO which goes to a mixer be done on separate boards. It's believed that the large amount of cross-talk seen in the mixer outputs was due to having all four of these on a single board.

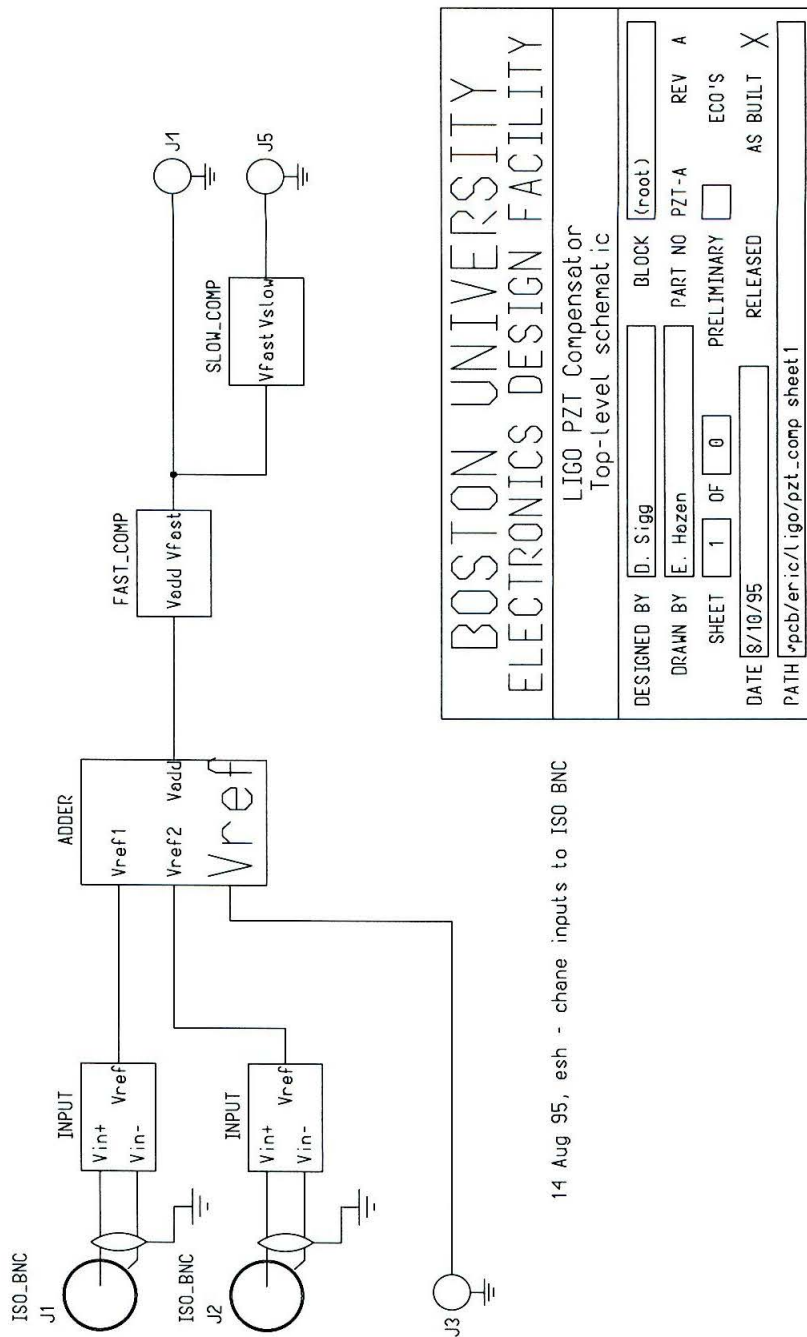


Figure D.1: PZT compensation schematics: Overview.

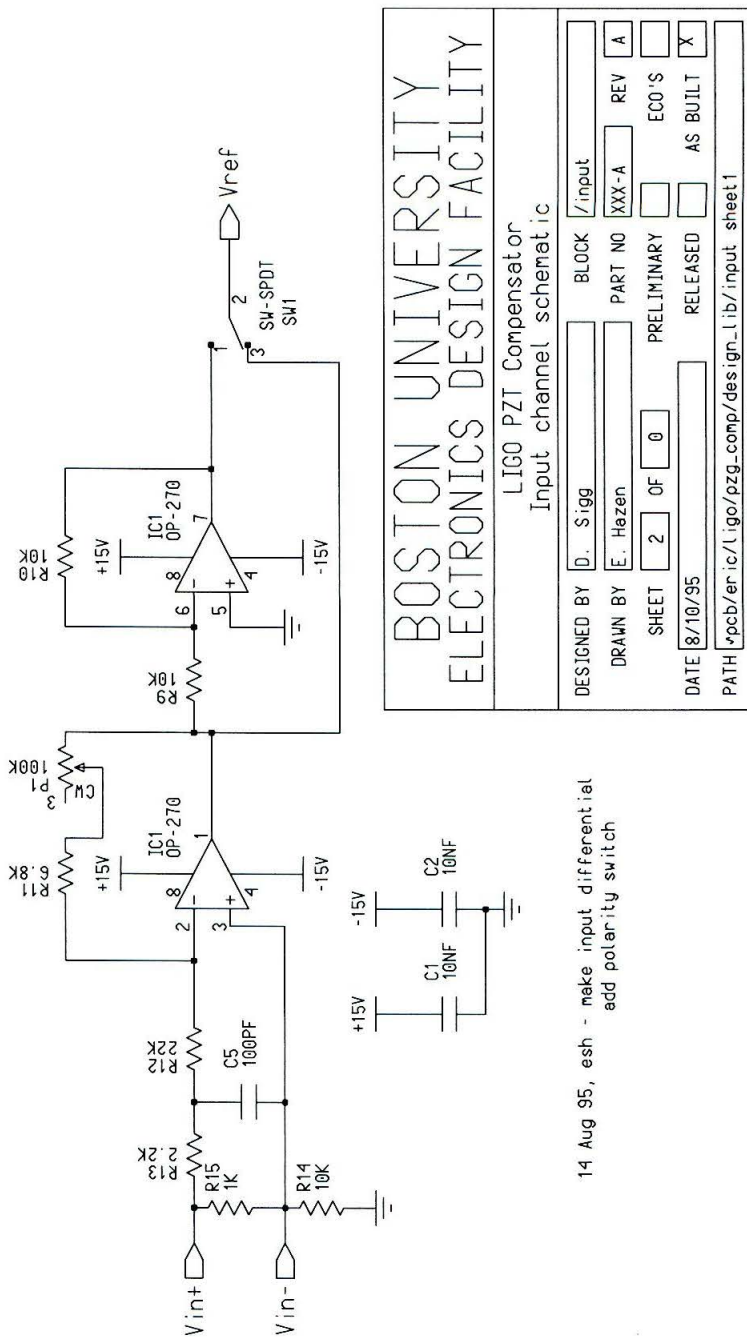
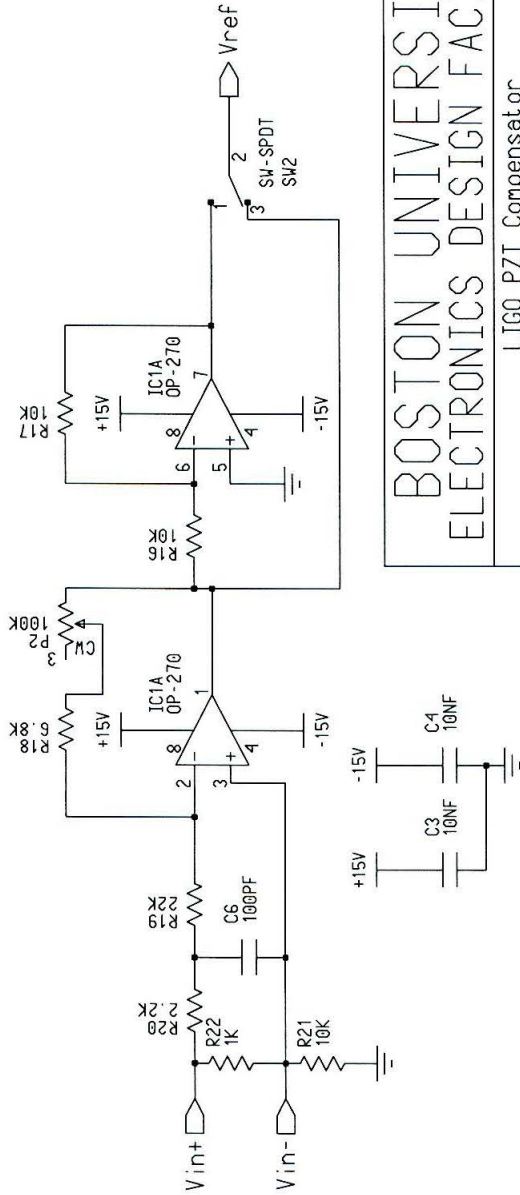


Figure D.2: PZT compensation schematics: Channel 1 input.



BOSTON UNIVERSITY
ELECTRONICS DESIGN FACILITY

LIGO PZT Compensator
Input channel schematic

DESIGNED BY	D. Sigg	BLOCK	/input
DRAWN BY	E. Hazen	PART NO	XXX-A
SHEET	2	OF	0
DATE	8/10/95	PRELIMINARY	<input type="checkbox"/>
PATH	[pcb/enr/ic/ligo/pzg_comp/design_lib/input_sheet1		
		RELEASED	<input type="checkbox"/>
		AS BUILT	<input checked="" type="checkbox"/>

14 Aug 95, esh - make input differential
add polarity switch

Figure D.3: PZT compensation schematics: Channel 2 input.

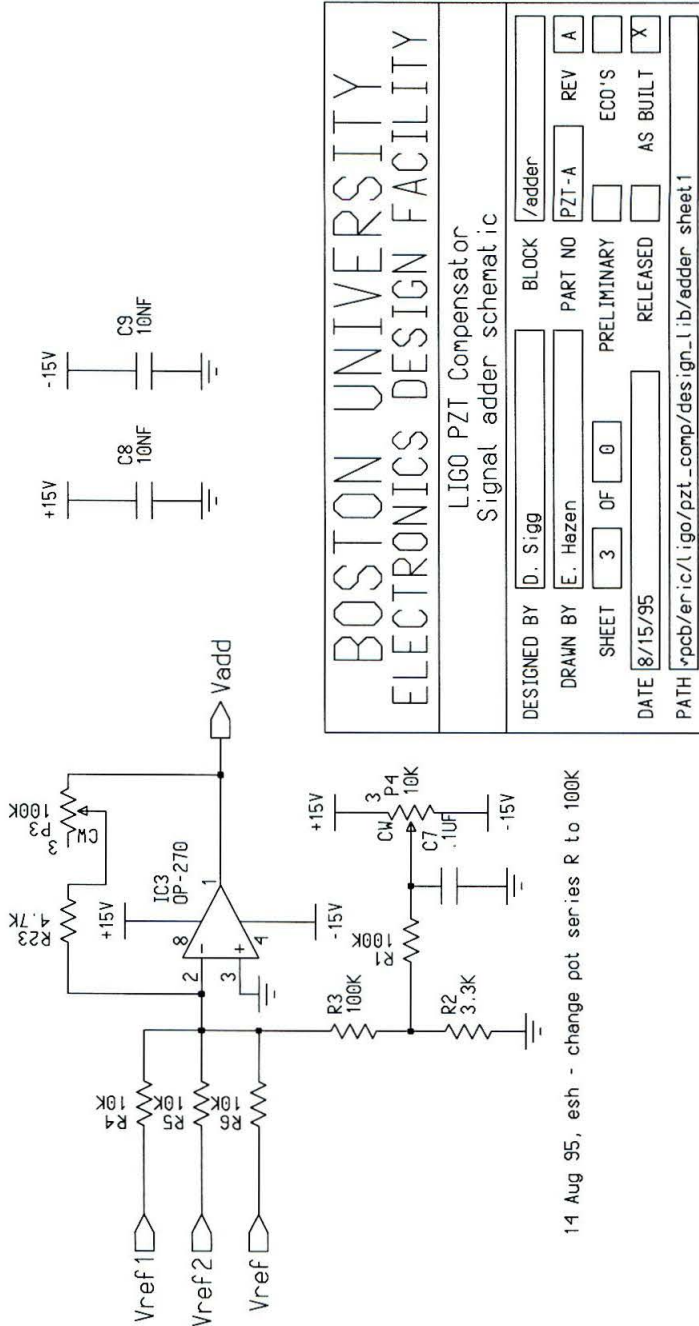
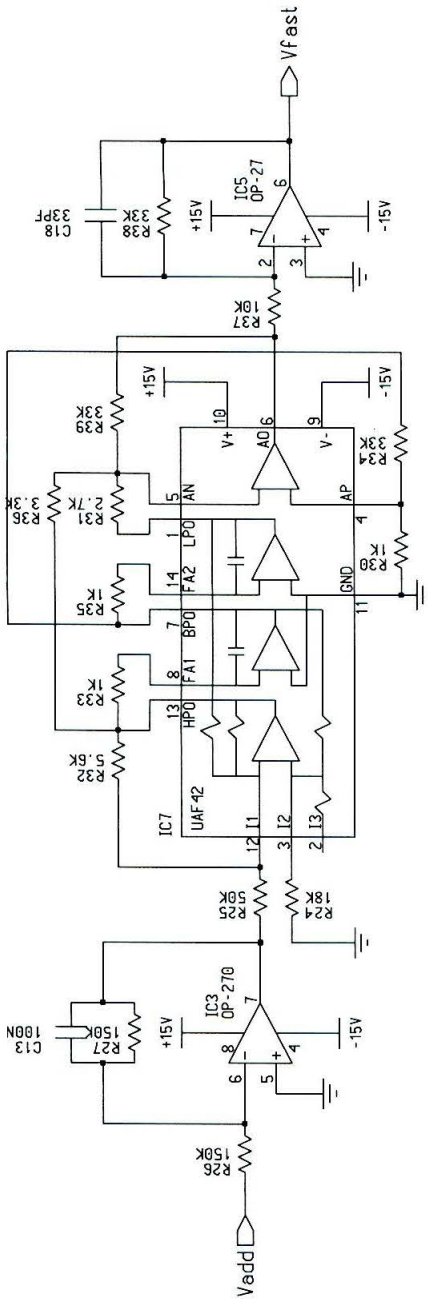
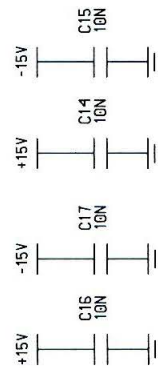


Figure D.4: PZT compensation schematics: Adder.



BOSTON UNIVERSITY ELECTRONICS DESIGN FACILITY			
LIGO PZT Compensator Fast PZT Compensation schematic			
DESIGNED BY	D. Sigg	BLOCK	/Fast
DRAWN BY	E. Hezen	PART NO	PZT-A
SHEET	4	OF	8
DATE	8/18/95	PRELIMINARY	<input type="checkbox"/>
PATH	*pcb/er/ic/ligo/pzt-comp/design.lib/fast sheet 1		
		RELEASED	<input type="checkbox"/>
		AS BUILT	<input checked="" type="checkbox"/>
		ECO'S	<input type="checkbox"/>
		REV	A



14 Aug 95, esh - fix pin no's on UAF42
 16 Aug 95, esh - add 33k feedback on amp#4

Figure D.5: PZT compensation schematics: Fast PZT network.

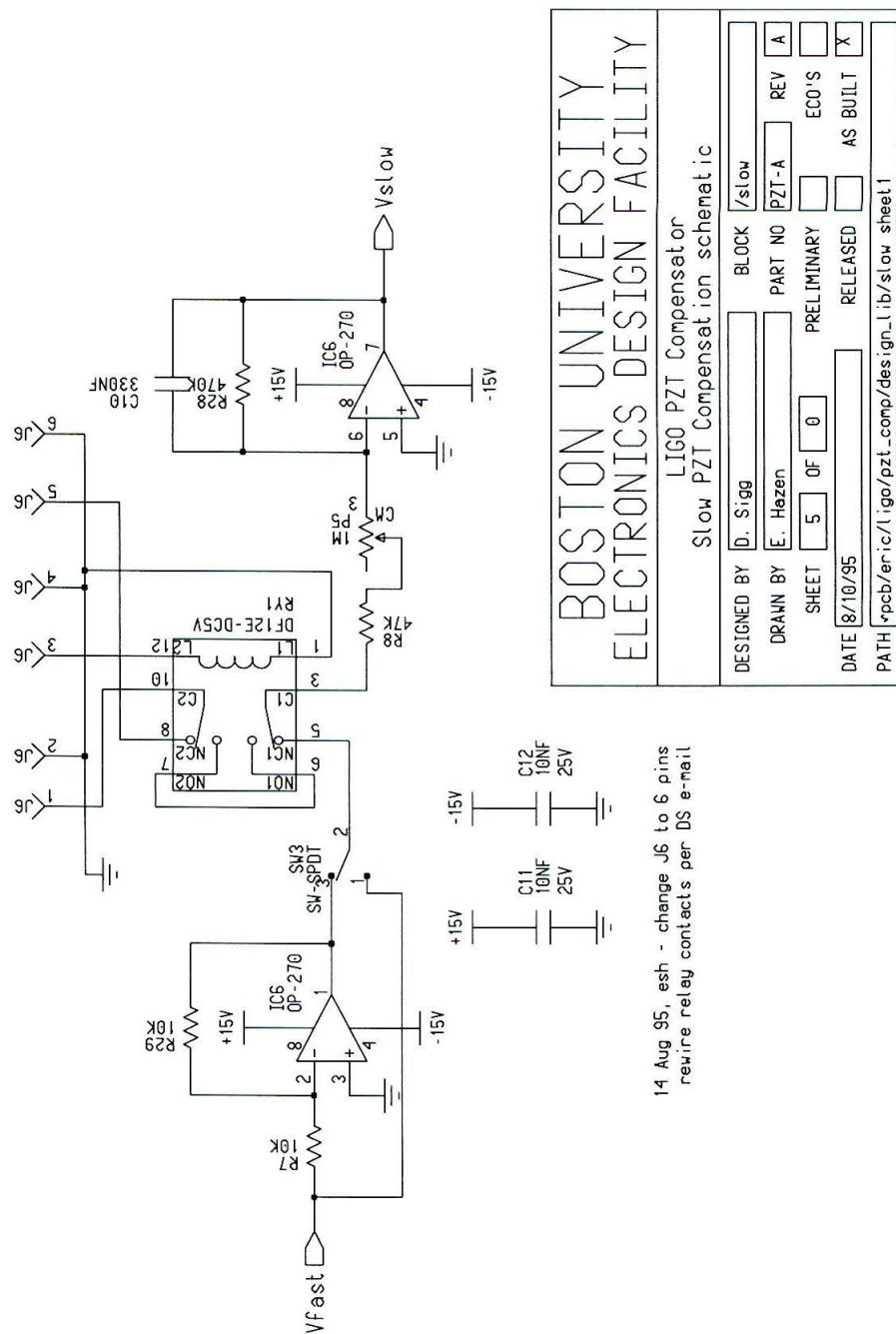


Figure D.6: PZT compensation schematics: Slow PZT network.

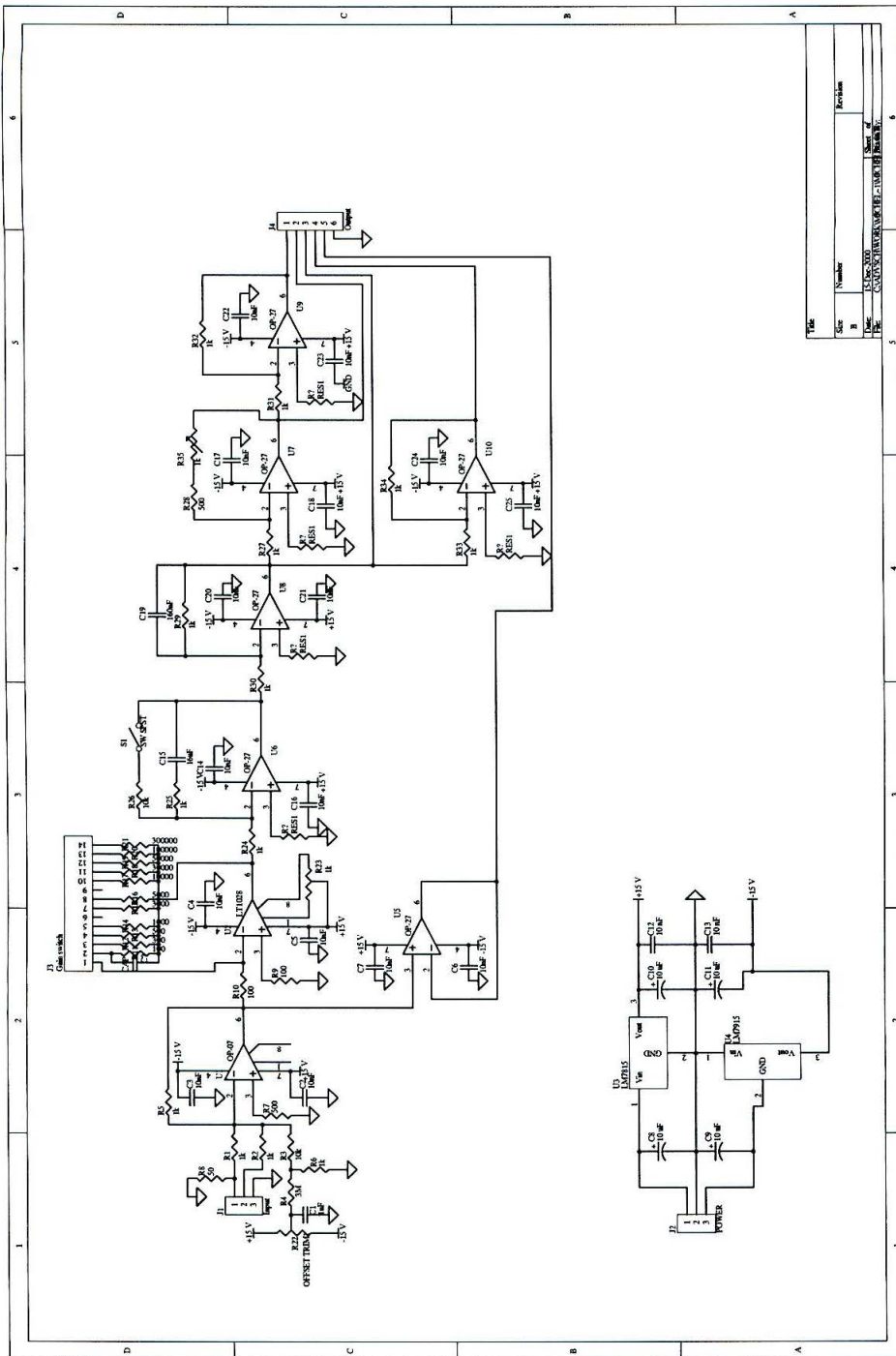


Figure D.7: Michelson degree of freedom compensation board.

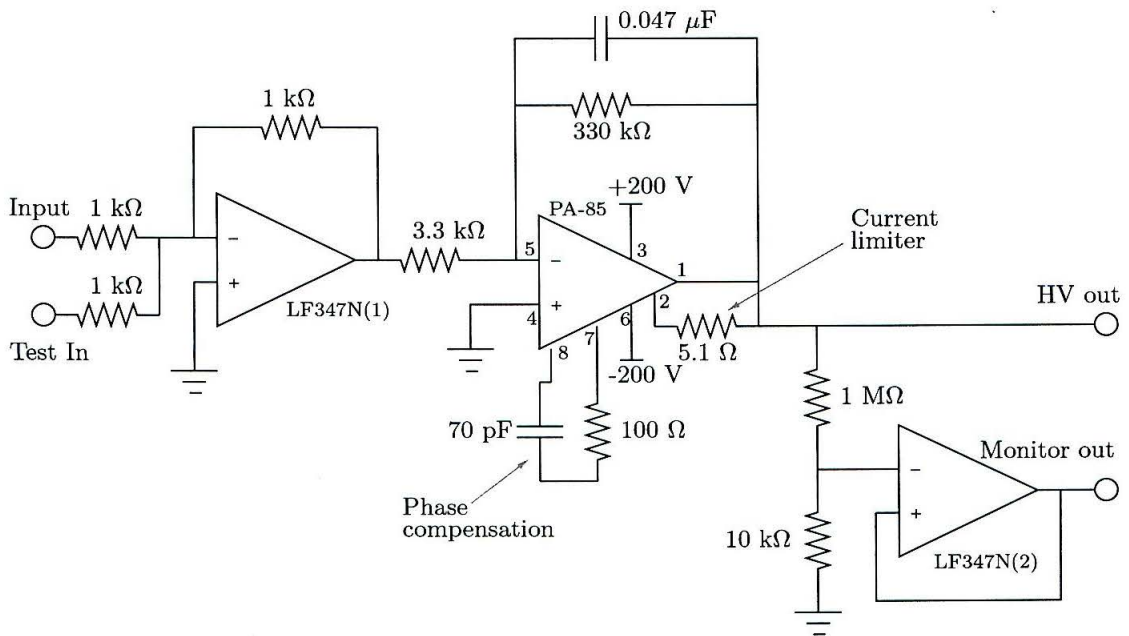
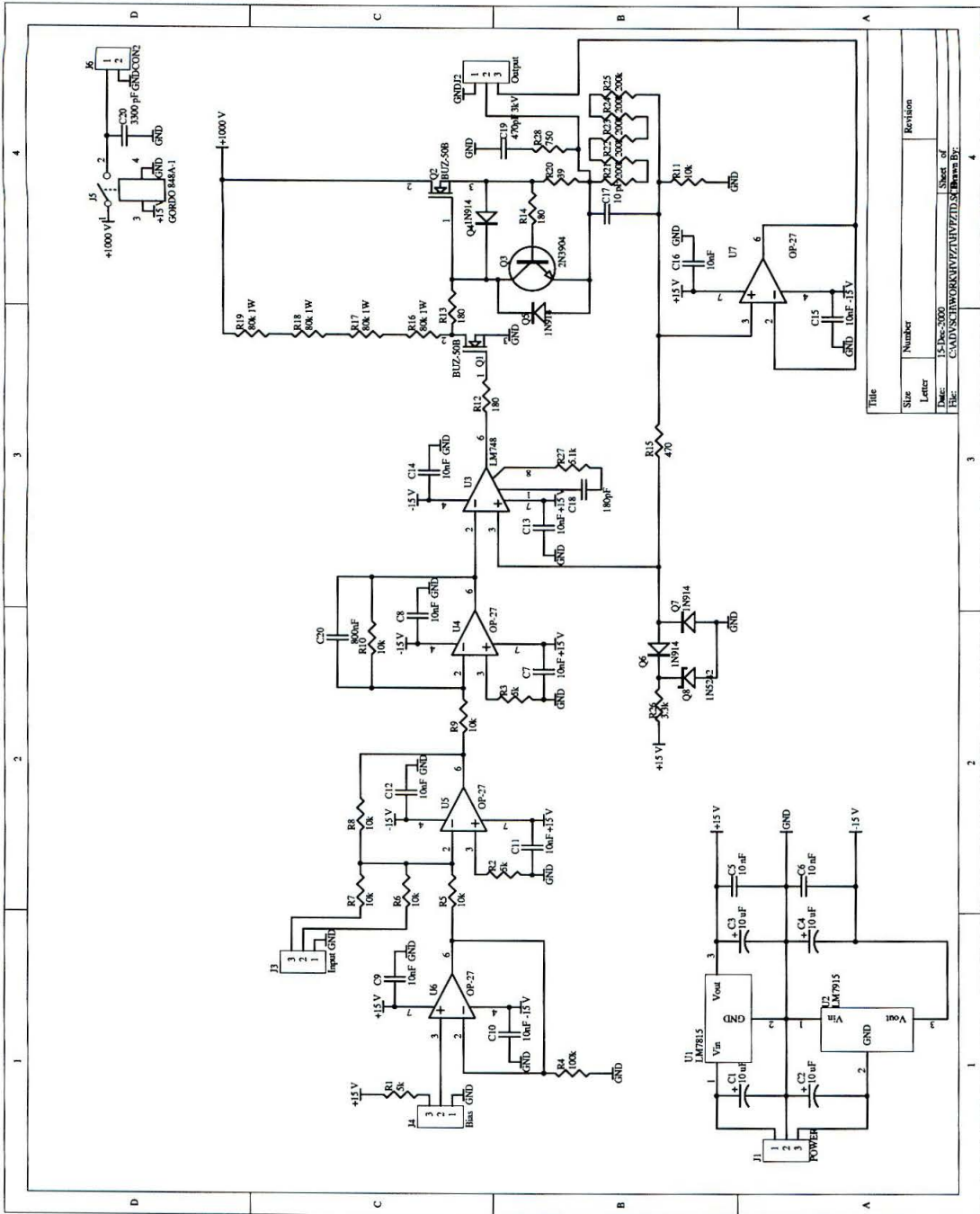


Figure D.8: High voltage fast PZT driver. Output is ± 200 V. The bandwidth without the 10 Hz pole in the PA-85 feedback is roughly 1 MHz.



File	Size	Number	Revision
15-Pez-3000			
Doc:		Sheet of	
File:		C:\AD\WORK\KAWAUFZ\U7\FZD5E\Brow.Bcr	

Figure D.9: High voltage slow PZT driver. Output is 0-1000 V, bandwidth roughly 3 kHz.

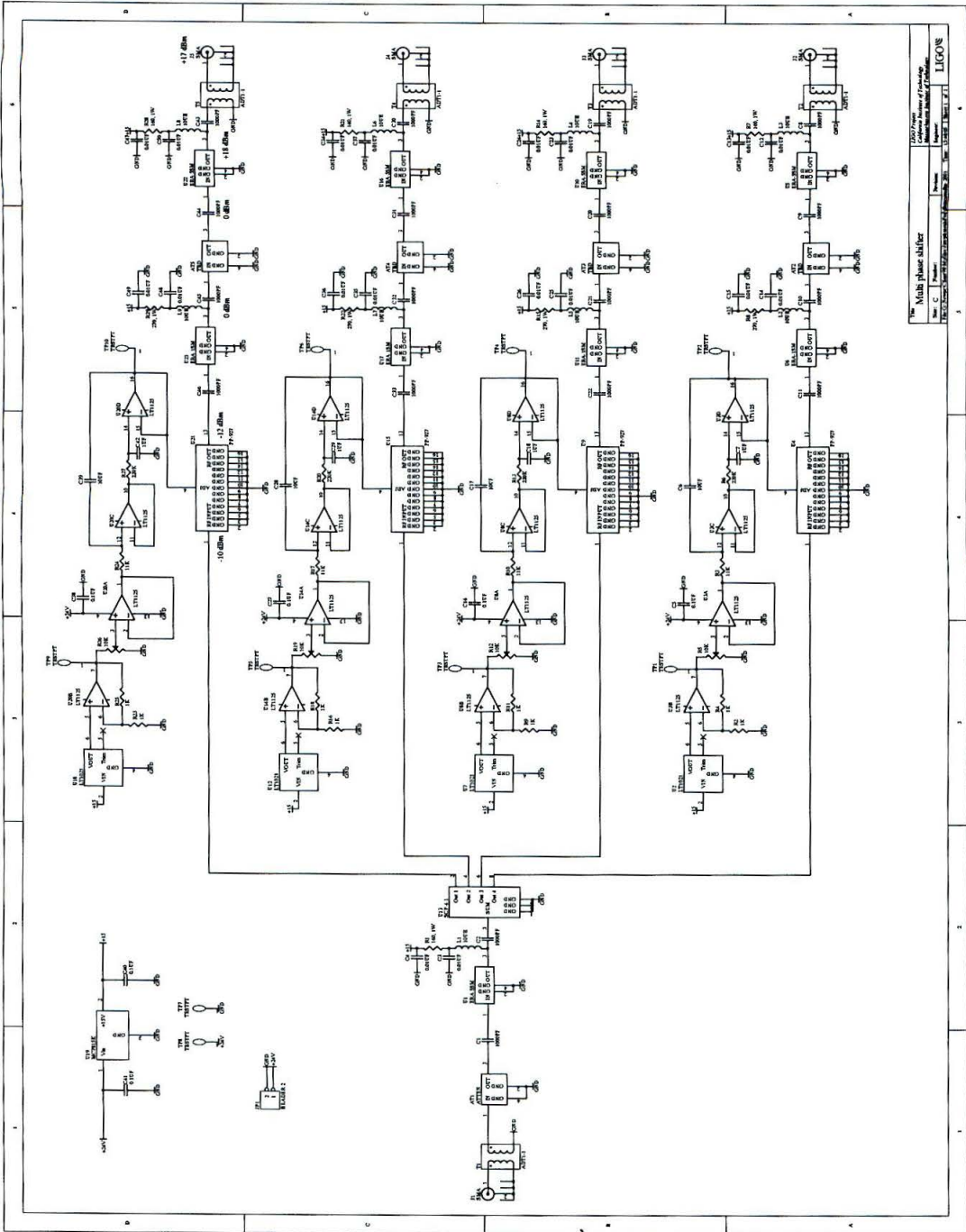


Figure D.11: 4-way voltage controlled phase shifter and amplification board.

Bibliography

- [1] J. Weber. Detection and generation of gravitational waves. *Physical Review*, 117(306), 1960.
- [2] M.E. Gertsenshtein and V.I. Pustovoit. On the detection of low-frequency gravitational waves. *Soviet Physics - JETP*, 16:433, 1963.
- [3] Kip S. Thorne. *Black Holes and Time Warps: Einstein's Outrageous Legacy*. W.W. Norton & Co., 1994.
- [4] R. Weiss. Electromagnetically coupled broadband gravitational antenna. Research Laboratory of Electronics, Massachusetts Institute of Technology, Quarterly Progress Report No. 105, 1972.
- [5] G.E. Moss, L.R. Miller, and R.L. Forward. Photon-noise-limited laser transducer for gravitational antenna. *Appl. Opt.*, 10:2495–2498, 1971.
- [6] Robert L. Forward. Wideband laser-interferometer gravitational-radiation experiment. *Phys. Rev. D*, 17(2):379–390, 1978.
- [7] A. Abramovici, W. Althouse, J. Camp, D. Durance, J.A. Giaime, A. Gillespie, S. Kawamura, A. Kuhnert, T. Lyons, F.J. Raab, R.L. Savage, D. Shoemaker, L. Sievers, R. Spero, R. Vogt, R. Weiss, S. Whitcomb, and M. Zucker. Improved sensitivity in a gravitational wave interferometer and implications for LIGO. *Phys. Lett. A*, 218:157–163, 1996.
- [8] M.W. Coles. The Status of LIGO. In Syd Meshkov, editor, *Gravitational Waves*, Third Edoardo Amaldi Conference, pages 101–109, 1999.
- [9] Frédérique Marion for the VIRGO collaboration. Status of the VIRGO Experiment. In Syd Meshkov, editor, *Gravitational Waves*, Third Edoardo Amaldi Conference, pages 110–119, 1999.

- [10] Masaki Ando and Kimio Tsubono. TAMA Project: Design and Current Status. In Syd Meshkov, editor, *Gravitational Waves*, Third Edoardo Amaldi Conference, pages 128–139, 1999.
- [11] H. Lück and et al. The Status of GEO600. In Syd Meshkov, editor, *Gravitational Waves*, Third Edoardo Amaldi Conference, pages 120–127, 1999.
- [12] E. Gustafson, D. Shoemaker, K. Strain, and R. Weiss. LSC white paper on detector research and development. Technical Report LIGO-T990080, LIGO Project/California Institute of Technology, 1999.
- [13] A. Bertolini, G. Cella, E. D’Ambrosio, R. DeSalvo, V. Sannibale, A. Takamori, and H. Yamamoto. New seismic attenuation system (SAS) for the advanced LIGO configurations (LIGO2). In Syd Meshkov, editor, *Gravitational Waves*, pages 320–324. Third Edoardo Amaldi Conference, 1999.
- [14] J. Giaime, B. Lantz, D. DeBra, J. How, C. Hardham, S. Richman, and R. Stebbins. Active seismic isolation for enhanced LIGO detectors. In Syd Meshkov, editor, *Gravitational Waves*, pages 300–305. Third Edoardo Amaldi Conference, 1999.
- [15] Peter R. Saulson. *Fundamentals of Interferometric Gravitational Wave Detectors*. World Scientific, 1994.
- [16] P.R. Saulson. Thermal noise in mechanical experiments. *Phys. Rev. D*, 42(8):2437–2445, 1990.
- [17] V.B. Braginsky, M.L. Gorodetsky, and S.P. Vyatchanin. Thermodynamical fluctuations and photo-thermal shot noise in gravitational wave antennae. *Phys. Lett. A*, 264:1–10, 1999.
- [18] Y. Levin. Internal thermal noise in the LIGO test masses: A direct approach. *Phys. Rev. D*, 57(2):659–663, 1988.

- [19] Yuk Tung Liu and Kip S. Thorne. Thermoelastic noise and homogeneous thermal noise in finite sized gravitational-wave test masses. *Phys. Rev. D*, 2000.
- [20] R. Weiss. In L. Smarr, editor, *Sources of Gravitational Radiation*, page 7. Cambridge University Press, Cambridge, 1979.
- [21] Carlton M. Caves. Quantum-mechanical radiation-pressure fluctuations in an interferometer. *Phys. Rev. Lett.*, 45(2):75–79, 1980.
- [22] Vladimir B. Braginsky and Farid Ya. Khalili. *Quantum Measurement*. Cambridge University Press, 1992.
- [23] Alessandra Buonanno and Yanbei Chen. Optical noise correlations and beating the standard quantum limit in LIGO II. *submitted to Phys. Rev. Lett.*, 2000.
- [24] Alessandra Buonanno and Yanbei Chen. Quantum noise in second generation laser interferometric gravitational wave detectors. *In Preparation*, 2000.
- [25] Jun Mizuno. *Comparison of Optical Configurations for Laser-Interferometric Gravitational Wave Detectors*. PhD thesis, Max Plank Institute for Quantum Optics, 1995.
- [26] B.J. Meers. Recycling in laser-interferometric gravitational-wave detectors. *Phys. Rev. D*, 38(8):2317–2326, 1988.
- [27] J. Mizuno, K.A. Strain, P.G. Nelson, J.M. Chen, R. Schilling, A. Rüdiger, W. Winkler, and K. Danzmann. Resonant sideband extraction: A new configuration for interferometric gravitational wave detectors. *Phys. Lett. A*, 175:273–276, 1993.
- [28] W. Winkler, K. Danzmann, A. Rüdiger, and R. Schilling. Heating by optical-absorption and the performance of interferometric gravitational-wave detectors. *Phys. Rev. A*, 44(11):7022–7036, 1991.

- [29] Brett Bochner. *Modelling the Performance of Interferometric Gravitational-Wave Detectors with Realistically Imperfect Optics*. PhD thesis, Massachusetts Institute of Technology, 1998.
- [30] G. Heinzel, K.A. Strain, J. Mizuno, K.D. Skeldon, B. Willke, W. Winkler, R. Schilling, A. Rüdiger, and K. Danzmann. Experimental demonstration of a suspended dual recycling interferometer for gravitational wave detection. *Phys. Rev. Lett.*, 81(25):5493–5496, December 1998.
- [31] G. Heinzel, J. Mizuno, R. Schilling, A. Rüdiger, and K. Danzmann. An experimental demonstration of resonant sideband extraction for laser-interferometric gravitational wave detectors. *Phys. Lett. A*, 217:305–314, 1996.
- [32] Martin Regehr. *Signal Extraction and Control for an Interferometric Gravitational Wave Detector*. PhD thesis, California Institute of Technology, 1995.
- [33] C.N. Man, D. Shoemaker, M. Pham Tu, and D. Dewey. External modulation technique for sensitive interferometric detection of displacements. *Phys. Lett. A*, 148:8–16, 1990.
- [34] L. Schnupp. A talk delivered at *European Collaboration Meeting on Interferometric Detection of Gravitational Waves*. Sorrento, 1988.
- [35] H.J. Kimble, Yuri Levin, Andrey B. Matsko, Kip S. Thorne, and Sergey P. Vyatchanin. Conversion of conventional gravitational-wave interferometers into QND interferometers by modifying their input and/or output optics. *Phys. Rev. D*, 2000.
- [36] T.M. Niebauer, R. Schilling, K. Danzmann, A. Rüdiger, and W. Winkler. Non-stationary shot noise and its effect on the sensitivity of interferometers. *Phys. Rev. A*, 43(9):5022–5029, 1991.
- [37] Brian J. Meers and Kenneth A. Strain. Modulation, signal, and quantum noise in interferometers. *Phys. Rev. A*, 44(7):4693–4703, 1991.

- [38] T.T. Lyons, M.W. Regehr, and F.J. Raab. Shot noise in gravitational-wave detectors with Fabry-Perot arms. *Optics Letters*, 2000.
- [39] R.W.P. Drever. Interferometric detectors for gravitational radiation. In N. Deruelle and T. Piran, editors, *Gravitational Radiation*, pages 321–338. North Holland, Amsterdam, 1983.
- [40] private communication Jordan Camp.
- [41] Ken Strain. Personal communication.
- [42] K.S. Thorne. Probing Black Holes and Relativistic Stars. In R.M. Wald, editor, *Proceedings of a Conference in Memory of S. Chandrasekhar*, pages 41–78. University of Chicago Press, Chicago, 1988.
- [43] A. Krolak, J.A. Lobo, and B.J. Meers. Optimization of laser interferometers for the detection of gravitational-waves from coalescing binaries. *Phys. Rev. D*, 43(8):2470–2483, 1991.
- [44] Curt Cutler and Éanna E. Flanagan. Gravitational waves from merging compact binaries: How accurately can one extract the binary’s parameters from the inspiral waveform? *Phys. Rev. D*, 49(6):2658–2697, March 1994.
- [45] Lee Samuel Finn. LIGO Science Benchmarks. Technical Report LIGO-T970167, LIGO Project/California Institute of Technology, 1997.
- [46] L.S. Finn and et al. Toward gravitational wave detection. In S. Meshkov, editor, *Gravitational Waves: Third Edoardo Amaldi Conference*, 1999.
- [47] Ken Strain. AIC update July 2000. Report to the Advanced Interferometer Configuration (AIC) working group of the LSC.
- [48] Ray Beausoleil. Melody – Thermal distortions in LIGO interferometers. On the STAIC web page. <http://www.phys.ufl.edu/LIGO/LIGO/STAIC.html#2>.

- [49] Martin Regehr, James Mason, Hiro Yamamoto, and Osamu Miyakawa. Twiddle – A program for analyzing interferometer frequency response. On the STAIC web page. <http://www.phys.ufl.edu/LIGO/LIGO/STAIC.html#9>.
- [50] Gehard Heinzel. *Advanced optical techniques for laser interferometric gravitational wave detectors*. PhD thesis, University of Hannover, 1999.
- [51] Brian J. Meers, Andrzej Krolak, and J. Alberto Lobo. Dynamically tuned interferometers for the observation of gravitational waves from coalescing compact binaries. *Phys. Rev. D*, 47(6):2184–2197, March 1993.
- [52] Laurent Derome. *Le système de détection de l'expérience VIRGO dédiée à la recherche d'ondes gravitationnelles*. PhD thesis, l'Université de Savoie, 1999.
- [53] Peter Fritschel. Length sensing & control (LSC) design requirements. Technical Report LIGO-T960058-03, LIGO Project/California Institute of Technology, 1997.
- [54] ISC team. Length sensing & control subsystem final design. Technical Report LIGO-T980068-00, LIGO Project/California Institute of Technology, 1998.
- [55] Rich Abbott, James Mason, and Rick Savage. NPRO frequency stabilization. Technical Report LIGO-T970051-00-R, LIGO Project/California Institute of Technology, 1997.
- [56] Nergis Mavalvala. *Alignment Issues in Laser-Interferometric Gravitational Wave Detectors*. PhD thesis, Massachusetts Institute of Technology, 1997.
- [57] Hiro Yamamoto. Personal communication.
- [58] Daniel Shaddock. *Advanced Interferometry for Gravitational Wave Detection*. PhD thesis, Australian National University, 2000.
- [59] J.B. Camp, H. Yamamoto, S.E. Whitcomb, and D.E. McClelland. Analysis of light noise sources in a recycled Michelson interferometer with Fabry-Perot arms. *J. Opt. Soc. Am. A*, 17(1):120–128, 2000.

- [60] J.E. Mason. Noise coupling in RSE. Technical Report In preparation, LIGO Project/California Institute of Technology, 2001.
- [61] Paul Horowitz and Winfield Hill. *The Art of Electronics*. Cambridge University Press, 1989.
- [62] Malik Rakhmanov. Transfer function for fields in a 3-mirror nested cavity. In Syd Meshkov, editor, *Gravitational Waves*, Third Edoardo Amaldi Conference, pages 204–207, 1999.
- [63] James Mason. rsenoise.m – A program for analyzing sensitivity to amplitude and frequency noise in RSE interferometers. On the STAIC web page. <http://www.phys.ufl.edu/LIGO/LIGO/STAIC.html#11>.
- [64] Peter Fritschel. Personal communication.
- [65] Max Born and Emil Wolf. *Principles of Optics*. Pergamon Press, sixth edition, 1980.